Mechanisms of functional MRI based decoding of oriented grating stimuli: analysis based on functional imaging of the cat visual cortex

Zeshan Yao

Biomedical Engineering, McGill University, Montreal

December 2015

A thesis submitted to McGill University in partial fulfillment of the requirements of the degree of Doctor of Philosophy

Table of Contents

Abstract

Recent studies have demonstrated that multivariate machine learning algorithms can decode the orientation of grating stimuli from coarsely sampled ($3\times3\times3$ mm^3) functional magnetic resonance imaging (fMRI) data. Unraveling the mechanisms underlying decoding of information conveyed in the fine scale cortical organization of orientation preference will enable informed search for other fine scale organizations in relatively unknown areas such as the frontal cortex. We therefore aimed to analyze the mechanisms underlying decoding of information conveyed by orientation columns and maps. To this end, we have analyzed contributions from four out of the six hypothesized mechanisms as candidate contributors to the decoding of information encoded in fine-scale orientation maps: (I) random local irregularities in the functional organization, (II) very low spatial frequencies reflecting large-scale components of the organization, (III) orientation selective responses of macroscopic blood vessels, and (IV) complex spatiotemporal sampling of neuronal activity by fMRI voxels, that transforms high spatial frequency cortical responses to responses of macroscopic vessels.

To evaluate mechanisms underlying decoding of oriented grating, we utilized an animal model, allowing for high-resolution contrast-agent based cerebral blood volume (CBV)-fMRI and invasive optical imaging. We first determined whether local irregularities and low-frequency components in cat area 17 contribute to decoding, by analyzing CBV-fMRI data that do not contain contributions from macroscopic blood vessels nor from complex spatio-temporal sampling. We then evaluated contributions from local irregularities and low spatial-frequency responses from gray matter (GM) and macroscopic vessels. To this end, we directly visualized responses in cat area 18 using wide-field optical imaging of intrinsic signals (OI-IS) and computing relative changes in deoxy- (HbR) and total- hemoglobin (HbT), that are analogous to blood-oxygen-level-dependent (BOLD) and CBV-fMRI measurements, respectively. In addition, we tested whether decoding based on the spatiotemporal evolution of the hemodynamic response results in higher success rates than those obtained from the spatial response averaged over time. To make our findings from the cat visual cortex applicable to fMRI in human subjects, we defined voxels homologous in size to those used in fMRI-based decoding in humans, by comparing the main frequency of the orientation map in cat to that in human V1. Using the homologous voxel, low-frequency organizations in cat area 17 contribute to decoding. In contrast, irregularities in the fine-

scale organization do not contribute to the decoding of oriented gratings. Responses to oriented gratings in cat area 18 showed that the lower-end of the irregularities spread in the frequency domain can be captured by the homologous voxel; no clear contributions from low-frequency organizations were observed. Using the homologous voxel, macroscopic vessel responses showed decoding accuracies higher than chance level but lower than those obtained from GM regions, and redundant when combined with contributions from GM. Lastly, spatiotemporal time-series do not improve decoding accuracies compared to those obtained from the spatial response averaged over time. We therefore conclude that: 1) whether irregularities contribute to decoding of a fine scale organization depends on the features of the specific organization; 2) the contributions of macroscopic vessels and complex spatiotemporal filtering to decoding of information conveyed in fine scale organizations are insignificant.

Furthermore, detailed knowledge on the spatial specificity of hemodynamic responses in GM and vessels can guide data acquisition, data analysis and interpretation of high-resolution fMRI and fMRI-based decoding studies. We therefore used OI-IS to quantify the functional selectivity and spatial specificity of HbR and HbT responses from blood vessels as a function of their diameters. In addition, we used concurrent OI-IS and extracellular electrophysiology (EP) to quantified the hemodynamic point spread function (PSF) relative to the underlying neurophysiological activities. HbR responses in veins with diameter smaller than or equal to 0.12 mm showed orientation selectivity to noise ratio and decoding accuracy comparable to those obtained from GM regions. HbT responses in veins and arteries of all tested diameters showed decreased orientation selectivity measures relative to those obtained from GM regions. Lastly, the spatial spread of HbT responses is comparable to those shown by low-gamma and high-gamma neurophysiological responses. Thus, CBV responses reflect fine scale organization at high fidelity. Our findings predict that the PSF of fMRI response in humans is expected to be smaller than what has been reported thus far, consistent with the feasibility of fMRI at the resolution scale of cortical columns.

Résumé

Des études récentes ont démontré que les algorithmes multivariés de classification automatique peuvent décoder l'orientation des mires de traits en utilisant des données d'imagerie par résonance magnétique fonctionnelles (IRMf) échantillonnées grossièrement ($3\times3\times3$ mm^3). Démêler les mécanismes sous-jacents de décodage de l'information contenue dans l'organisation cérébrale fine des orientations préférées permettra de la recherche éclairé sur d'autres organisations fines dans des zones relativement inconnues telles que le cortex frontal. Nous avons donc analysé les mécanismes sous-jacents de décodage de l'information contenue dans les colonnes et les cartes d'orientation. À cette fin, nous avons analysé quatre des six mécanismes proposés dans la littérature scientifique pouvant contribuer au décodage de l'informations contenues dans les cartes d'orientation à fine échelle: (i) les irrégularités locales aléatoires dans l'organisation fonctionnelle, (II) les fréquences spatiales très basses reflétant les composantes à grande échelle de l'organisation, (III) l'orientation des réponses sélectives des vaisseaux sanguins macroscopiques, et (iv) l'échantillonnage spatio-temporelle complexe de l'activité neuronale par les voxels IRMf, qui transforme les réponses corticales haute fréquence spatiale à des réponses de vaisseaux macroscopiques.

Pour évaluer les mécanismes de décodage de réseaux orientés, nous avons utilisé un modèle animal, permettant l'IRMf haute résolution du volume sanguin cérébral (VSC) par agent de contraste et d'imagerie optique invasive. Nous avons d'abord déterminé si des irrégularités locales et les composantes de fréquence très basse dans l'aire 17 de chat contribuent à décoder, en analysant les données IRMf-VSC qui ne contiennent pas de contribution des vaisseaux sanguins macroscopiques ni de l'échantillonnage spatio-temporelle complexe. Nous avons ensuite évalué les contributions des réponses d'irrégularités locales et de la fréquence spatiale basse dans la matière grise (GM) et les vaisseaux macroscopiques. À cette fin, nous avons visualisé directement les réponses dans l'aire 18 du chat en utilisant l'imagerie optique des signaux intrinsèques (IO-SI) et calculé les changements relatifs de l'hémoglobine-désoxygénée (HbR) et -totale (HBT), qui sont analogues aux mesures IRMf dépendant du niveau d'oxygène sanguin (BOLD) et VSC. En outre, nous avons testé si le décodage basé sur l'évolution spatio-temporelle de la réponse hémodynamique résulte avec un taux de réussite plus élevés que ceux obtenus à partir de la réponse spatiale moyennée dans le temps. Afin de rendre nos découvertes du cortex visuel du chat

applicable à IRMf chez les humains, nous avons défini notre mesure des voxels homologues à ceux utilisés dans le décodage IRMf chez l'humain, en comparant la fréquence principale de la carte d'orientation du chat à celle de V1 chez l'humain. Utilisant le voxel homologue, les organisations de fréquence basse dans l'aire 17 du chat contribuent au décodage. Par contre, les irrégularités dans l'organisation fine ne contribuent pas au décodage des mires de traits. Les réponses aux mires de traits dans l'aire 18 du chat ont montré que le bas d'échelle des irrégularités réparties dans le domaine fréquentiel peut être capturé par le voxel homologue; aucune contribution claire de la part des organisations de fréquence basse n'a été observée. Utilisant le voxel homologue, les réponses des vaisseaux macroscopiques ont montré un décodage plus précis que la chance, mais inférieur à ceux obtenus à partir des régions de GM, et redondantes lorsqu'elles sont combinées avec la contribution de GM. Enfin, l'évolution spatio-temporelle des séries temporelles n'améliore pas les précisions de décodage par rapport à celles obtenues à partir de la réponse spatiale moyennée dans le temps. Nous concluons donc que: 1) si les irrégularités contribuent au décodage d'une organisation fine ou ne dépend pas sur des caractéristiques de l'organisation spécifique; 2) les contributions des vaisseaux sanguins macroscopiques et l'échantillonnage spatio-temporelle complexe sont insignifiants pour le décodage de l'information contenus dans les organisations fines.

En supplément, une connaissance approfondie de la spécificité spatiale des réponses hémodynamiques dans la GM et les vaisseaux peut guider l'acquisition des données, l'analyse des données et l'interprétation de l'IRMf à haute-résolution et des études de décodage basées sur l'IRMf. Nous avons donc utilisé IO-SI pour quantifier la sélectivité fonctionnelle et la spécificité spatiale des réponses d'HbR et d'HbT à partir de vaisseaux sanguins, en fonction de leur diamètre. De plus, nous avons simultanément utilisé IO-SI et l'électrophysiologie (EP) extracellulaire pour quantifier la fonction d'étalement du point (PSF) hémodynamique par rapport aux activités neurophysiologiques sous-jacents. Les réponses de HbR dans les veines d'un diamètre inférieur ou égal à 0,12 mm ont montré de la sélectivité d'orientation par rapport au bruit et la précision de décodage qui sont comparables à ceux obtenus à partir de régions de GM. Les réponses d'HbT de tous les diamètres testés en veines et artères ont montré une diminution des mesures de sélectivité d'orientation par rapport à celles obtenues à partir des régions de GM. Enfin, la propagation spatiale des réponses HbT est comparable à celle présenté par les réponses neurophysiologiques de bas-gamma et de haut-gamma. Ainsi, les réponses VSC reflètent l'organisation fine avec une haute

précision. Nos résultats prédisent que la PSF de réponse IRMf chez les humains devrait être inférieure à ce qui a été rapporté à ce jour, en accord avec la faisabilité de l'IRMf à l'échelle de la résolution de colonnes corticales.

Acknowledgment

First and foremost, I would like to show my sincere gratitude to my supervisor, Dr. Amir Shmuel, for his unwavering mentorship throughout the course of my graduate training. I received countless advices and feedbacks towards not only my critical thinking as a scientist, but also towards my personal growth during this pinnacle period of my career. The time we spent together conducting the long experiments that last for several days is now a fond memory of mine. I am forever in debt for his devotion as an advisor in realizing the work presented here and it is not an overstatement that I am proud to be his apprentice.

I would also like to express my appreciation to my supervisory committee: Drs. Robert Kearney, Bruce Pike, Doina Precup, and Curtis Baker, for their enthusiasm, guidance, and patience in going through all my documents and presentations.

I thank Samuel Belanger and Frederic Lesage for the design and implementation of the apparatus for illumination using LEDs, Alexandre Hutton for implementation of the Monte-Carlo simulation of photon path lengths, and David Levi for histology of cortical layers.

I am grateful to all the members of Amir Shmuel's laboratory for creating a wonderful and dynamic environment to work in. In particular, I would like to acknowledge Martin Villeneuve, Pascal Kropf, and Ajay Venkateswaran for their scientific expertise and collaborative spirit. I extend my gratitude to Dr. Clotilde Lecrux from Dr. Edith Hamel's laboratory, André Cormier and his team of the BIC-MRI imaging technologists, Cathy Hunt and her colleagues from the MNI's Animal Care Facility, Toula Papadopoulos and Pina Sorrini whom are both outstanding department administrators, for their friendship, kindness, and assistance. I am grateful for being able to interact during my graduate studies with all the people I have mentioned above; these interactions allowed me to refine myself.

Most importantly, I cannot thank enough all my family members and friends for their endless patience and support. My mother and father saw my ups and downs and cheered me whenever I experienced hardships. My friends who listened through my ranting showed much empathy and at the same time, commented humorously to ease my stress. I stand this far today thanks to the steady environment provided by all my family members and friends.

Lastly, the research presented in this thesis would not have been possible without the financial support from Natural Science and Engineering Research Council of Canada (NSERC), Canadian Institutes of Health Research (CIHR), NSERC CREATE Program in Medical Imaging Analysis, and the excellence awards granted to me by the Department of Biomedical Engineering of McGill University.

Original contributions to knowledge

My thesis is the first to address the concurrent debate on the mechanisms underlying decoding of oriented gratings using coarse fMRI voxels, while employing high-resolution contrast-agent based cerebral blood-volume fMRI. Since the MION contrast agent-based fMRI shows better spatial specificity than BOLD fMRI does, and since it excludes contributions from blood vessels, my study is the first to test whether the functional anatomy of orientation selective columns with no blood vessel contributions enables decoding of oriented grating stimuli (Chapter 3). Our findings from this original work clearly rule out, for the first time, any contributions from irregularities in the organization of orientation preference to decoding in a primary visual area (Chapter 3).

My thesis is also the first to directly compare contributions from gray matter regions and blood vessels to decoding of oriented gratings using coarse voxels. It is the first to demonstrate that contributions from macroscopic vessels to decoding orientation are lower than those from gray matter regions, and redundant when contributions from gray matter regions are considered (Chapter 4). It is the first work that shows that whether irregularities contribute to the decoding of the fine scale organization for orientation depends on the features of the organization, including the main frequency of the organization and the width of elevated amplitudes in the frequency domain around the main frequency (Chapters 3 and 4). It is the first to show that considering the spatiotemporal response rather than the spatial patterns of the response averaged over time does not improve orientation decoding accuracy (Chapter 4). The combined results on redundant information from macroscopic vessels and no added information from the spatiotemporal responses strongly indicate that spatiotemporal filtering of neuronal activity by fMRI voxels does not contribute to decoding information conveyed by fine scale organizations.

My thesis is the first to introduce the concept of a voxel size homologous to that used in human studies, based on the ratio of the main frequencies of the fine-scale organizations in humans and an animal model (Chapters 3 and 4). This creates a framework with which the mechanisms of fMRI-based decoding in humans can be investigated by invasive measurements in animal models.

My thesis is the first to measure the functional (and, indirectly spatial) specificity of metabolic (deoxy-hemoglobin) and hemodynamic (total hemoglobin) responses in arteries and veins as a function of blood vessel' diameter (Chapters 5). To date, only one theoretical model has evaluated the draining of deoxy-hemoglobin in veins, based on a still image (Turner, 2002). Several high-resolution studies investigated the responses of veins (Hillman et al., 2007); however, the functional/spatial specificities of responses of veins or arteries relative to the site of increased neurophysiological responses have not been quantified yet.

Lastly, my thesis is the first to measure the spatial specificity of hemodynamic responses relative to the neuronal responses using well controlled retinotopic stimuli. The only previous study that estimated the spatial specificity of hemodynamic relative to neurophysiological responses used forelimb stimulation in mice and multiple penetrations with electrodes at various sites relative to the center of the hemodynamic response (Chapters 6).

Author contributions

Chapter 2: Literature review

Zeshan Yao wrote the literature review, and Amir Shmuel edited it. Denis Chaimow contributed to the part on fMRI-based decoding.

Chapter 3: Cerebral blood volume function MRI with no contributions from macroscopic vessels rules out the decoding of oriented grating stimuli through local irregularities in cat area 17

Zeshan Yao, Seong-Gi Kim and Amir Shmuel set the aims of the study.
Mitsuhiro Fukuda, Chan-Hong Moon and Seong-Gi Kim acquired the data.
Zeshan Yao and Amir Shmuel outlined the analysis.
Zeshan Yao performed the analysis.
Zeshan Yao wrote and Amir Shmuel edited the manuscript.

Chapter 4: Mechanisms underlying decoding the orientation grating stimuli investigated by optical imaging of cat area 18

Zeshan Yao and Amir Shmuel set the aims of the study.
Zeshan Yao acquired the data; Pascal Kropf and Martin Villeneuve contributed to the data acquisition.
Zeshan Yao and Amir Shmuel outlined the analysis.
Denis Chaimow and Javeed Shaikh contributed to the frequency-based analysis of an irregularly shaped region of interest and to the fMRI-like sampling, respectively.
Zeshan Yao performed the analysis.
Zeshan Yao wrote and Amir Shmuel edited the manuscript.

Chapter 5: Spatial specificity of blood-oxygenation and blood volume signals in pial vessels and gray matter: implications for high-resolution fMRI

Zeshan Yao and Amir Shmuel set the aims of the study.
Zeshan Yao acquired the data; Pascal Kropf and Martin Villeneuve contributed to the data acquisition.
Zeshan Yao and Amir Shmuel outlined the analysis.
Zeshan Yao, Alexander Peplowski and Amir Shmuel designed and implemented the segmentation of blood vessels from gray matter regions.
Zeshan Yao performed the analysis.
Alexandre Hutton contributed to the Monte-Carlo simulation.
Zeshan Yao wrote and Amir Shmuel edited the manuscript.

Chapter 6: Spatial specificity of hemodynamic response relative to neuronal response in cat area 18: implication for high-resolution fMRI

Zeshan Yao and Amir Shmuel set the aims of the study.
Zeshan Yao acquired the data; Victor Mocanu and Niladri Mohanty contributed to the data acquisition.
Zeshan Yao and Amir Shmuel outlined the analysis.
Zeshan Yao performed the analysis.
Zeshan Yao wrote and Amir Shmuel edited the manuscript.

List of acronyms

ASE:	asymmetric spin echo
BOLD:	blood oxygen level dependent
CBV:	cerebral blood volume
CNR:	contrast to noise ratio
DOG:	difference of Gaussian
EP:	electrophysiology
FDR:	false discovery rate
FFT:	fast Fourier transform
fMRI:	functional magnetic resonance imaging
FOV:	field of view
FWHM:	full width at half max
Gd-DTPA:	gadolinium diethylenetriaminepenta-acetic acid
GE:	gradient echo
GM:	gray matter
HbO:	oxy-hemoglobin
HbR:	deoxy-hemoglobin
HbT:	total-hemoglobin
LDA:	linear discriminant analysis
LED:	light emitting diode
LFP:	local field potential
LV:	large vein
MRI:	magnetic resonance imaging
MVP:	multivariate pattern analysis
MUA:	multiunit activity
MION:	monocrystalline iron oxide nanoparticle
ODC:	ocular dominance column
OI-IS:	intrinsic optical imaging
PSF:	point spread function
PSTH:	peristimulus time histogram
RF:	receptive field
ROI:	region of interest
SE:	spin echo
SI:	selectivity index
SiNR:	selectivity index to noise ratio
SLR:	sparse logistic regression
SVM:	support vector machine
TE:	echo time
TR:	repetition time
VASO	vascular space occupancy
VCI:	vessel caliber index

List of figures

List of tables

Chapter 1. Overview of the thesis

The topics covered in this thesis consist of several aspects of functional and spatial specificity of hemodynamic signals commonly used for non-invasive brain imaging of human subjects and patients. Chapter 1 (this Chapter) presents the overview of my thesis, including a brief introduction and the rationale of the research. Chapter 2 includes a comprehensive review of the relevant literature. The first part of this Chapter reviews the basics, history, and advances of functional magnetic resonance imaging (fMRI). The second and third parts of Chapter 2 present a specific gap in knowledge that motivates three specific aims that follow. My findings obtained while addressing the first aim are presented in two manuscripts (Chapters 3 and 4), whereas my findings with regard to the second and third aims are presented by one manuscript per aim (Chapters 5 and 6). Chapter 7 is a discussion that connects and bridges findings from the four separate manuscripts.

1.1 Problem statement

FMRI allows non-invasive dynamic measurements of brain activity. This method has been commonly used for linking subjective experience with the corresponding physical neural response, e.g. the response of the brain to visual stimuli. Also, fMRI is an indirect measure of neuronal activity, based on changes in blood oxygenation, cerebral blood flow and cerebral blood volume. Hence, it is expected that fMRI data is only a coarse representation of the underlying neuronal activities. However, recent studies have demonstrated that multivariate machine learning algorithms can decode visual stimuli from coarse fMRI data (Haxby et al., 2001; Haynes and Rees, 2005; Kamitani and Tong, 2005). Using gradient-echo (GE) blood-oxygenation-level-dependent (BOLD) fMRI at 3T, these algorithms decoded information thought to be mediated by cortical columns. This result is surprising given the large size of the voxels ($3\times3\times3$ mm^3) relative to the mean cycle length of columns (2 mm or less for ocular dominance columns (ODC) and orientation columns along the cortical manifold in humans; Fig. 1-1). This result is even more surprising considering the relatively wide PSF of GE BOLD-fMRI signals at 3T (~3.5 mm; Engel et al., 1997 Parkes et al., 2005) and even that demonstrated at 7T (~2.3 mm; Shmuel et al., 2007). The mechanisms with which low-resolution imaging decodes information represented at a fine scale relative to the voxel size are unclear. Decoding analysis of signals potentially conveyed at the fine scale of cortical columns drew substantial interest of the neuroimaging community (Boynton, 2005; Kriegeskorte et al., 2010; Mannion et al., 2010; Op de Beeck, 2010; Shmuel et al., 2010; Swisher et al., 2010; Chaimow et al., 2011; Freeman et al., 2011; Carlson, 2014). In sharp contrast to this growing interest, to date there has been only one study (Swisher et al., 2010) devoted to understanding the mechanisms underlying fMRI-based decoding of information thought to be conveyed by cortical columns in an animal model, in which the functional organization of the columns is well known.

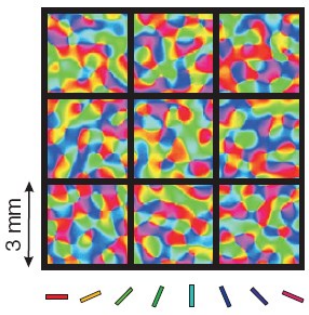

Figure 1-1. Pattern of preferred orientation sampled by fMRI. The color bars represent preference of neurons to specific orientation of the gratings. The black squares represent the size of coarse fMRI voxels, with the edge being longer than 1 cycle of orientation columns. Note that this image demonstrates the problem, but the relative scales are not precise (Image modified from Boynton, 2005).

1.2 Main hypothesis and specific aims

The central theme of my thesis is the spatial specificity of hemodynamic responses in cortex, with emphasis on understanding of how hemodynamic responses underlie fMRI-based decoding of information conveyed in fine scale organizations. I will address this theme in three specific aims.

1.2.1 Aim 1. To unravel the mechanisms underlying hemodynamic-response based decoding of oriented grating stimuli using coarse voxel sampling

The majority of neurons in the primary visual area show orientation selectivity: they respond at a higher amplitude to gratings of a specific orientation than to others (Hubel and Wiesel, 1959). These neurons are clustered together according to their preferred orientation, thus creating cortical columns of neurons with similar preference.

Low-resolution functional imaging can decode information thought to be represented at a fine scale relative to the voxel size (Haynes and Rees, 2005; Kamitani and Tong, 2005). The mechanisms with which low-resolution imaging decodes information represented at a fine scale relative to the voxel size is not clear. Six alternative mechanisms have been hypothesized as candidates to contribute to decoding of information encoded in fine scale structures. The first suggested hypothesis posited that aliasing of high spatial-frequency components of the columnar organization by the large voxels gives rise to decoding rate higher than chance level (Boynton, 2005). This hypothesized "aliasing" mechanism, also termed the "hyperacuity" mechanism involves components of the columnar organization with frequencies higher than the Nyquist frequency, which were thought to contribute to the sampled voxels. This hypothetical mechanism has been ruled out (Chaimow et al., 2011), based on the fact that fMRI samples data in the frequency space, with the highest frequency in the k-space being the highest frequency available to the sampling process.

Therefore, there are five remaining hypothetical mechanisms. (I) It was hypothesized that random, local variations and irregularities in the functional organization contribute to decoding (Kamitani and Tong, 2005; Haynes and Rees, 2006; Kriegeskorte and Bandettini, 2007; Swisher et al., 2010). The argument is that due to irregularities in columnar patterns, each voxel overlaps columns with different preferences unequally, resulting in biases towards specific preferences. (II) Very low spatial frequencies reflecting large-scale components of the organization with no

contributions from cortical columns were proposed to play a role (Op de Beeck, 2010; Freeman et al., 2011; Freeman et al., 2013; Wang et al., 2014).These include the oblique effect (Furmanski and Engel, 2000; Sun et al., 2013) and the radial bias effect (Sasaki et al., 2006; Clifford et al., 2009; Mannion et al., 2010; Freeman et al., 2011; Sun et al., 2013) associated with the representation of orientation. For decoding the stimulated eye, a relevant large scale organization is formed by the higher amplitude response to stimulation of the contra-lateral eye (Tychsen and Burkhalter, 1997). (III) An alternative mechanism to the large-scale organization (item II above) has been recently proposed. Observations made by Carlson (2014) and Wardle et al. (2015) suggest that the edges of oriented grating stimuli elicit responses that are orientation specific. Similarly, Wang et al. (2014) identified a direction-selective response bias in human visual cortex that predicted motion-decoding accuracy; and depended on the shape of the stimulus aperture rather than the absolute direction of motion. The response amplitudes gradually decreased with distance from the stimulus aperture edge corresponding to motion origin in V1, V2, V3, thus explaining the higher motion-decoding accuracies reported previously in early visual cortex. Alternatively (IV), draining regions that cover cortical maps and columns non-homogeneously may cause selective responses of their corresponding draining veins (Kamitani and Tong, 2005; Gardner et al., 2006; Kamitani and Tong, 2006; Kriegeskorte and Bandettini, 2007; Gardner, 2010; Thompson et al., 2011). In this scenario, selective signals from macroscopic blood vessels can be captured by large voxels; therefore, they can contribute to the decoding of stimuli encoded at the resolution of cortical columns. Evidence in support of this phenomenon was provided by (Gardner et al., 2006; Shmuel et al., 2010; Thompson et al., 2011). Lastly (V), Kriegeskorte et al. (2010) introduced a model in which fMRI voxels sample neuronal activity as complex spatiotemporal filters. These authors described how such a model can account for representation of high-frequency components of the cortical maps by the sampled voxels and for decoding of information conveyed by fine structures.

We hypothesize that **the successful decoding of information conveyed on the orientation of visual stimuli relies on a combination of the mechanisms (I)-(V) mentioned above**. We further hypothesize that **the contributions of each of these mechanisms depend on the features of the specific fine-scale organization**.

Although five hypothetical mechanisms are still considered, the contribution of each of these mechanisms and the possible redundancy of information across them have yet to be

determined. My first aim is to decipher the mechanisms underlying fMRI-based decoding of information thought to be conveyed by cortical columns. Specifically, I will determine which components of the hemodynamic response that carry information on the orientation of grating stimuli are preserved when sampled by coarse voxels. I will specifically evaluate contributions from irregularities in the fine scale organization of orientation preference, contributions of low-frequency components of the organization, contributions from macroscopic blood vessels, and whether the evolution of the spatiotemporal hemodynamic responses is more informative of the presented orientation than the static pattern of the response averaged over time.

1.2.2 Aim 2. To determine the functional and spatial specificity of deoxy- and total-hemoglobin response in blood vessels as a function of vessel diameter

Since one of the proposed mechanisms for successful decoding is defined as contributions from macroscopic blood vessels, it is important to further quantify the selectivity of blood vessels in response to the presented stimulus. The spatial specificity of draining veins relative to the site of increased neuronal activity is expected to vary as a function of their diameter. It is widely accepted that cortical capillaries provide the highest specificity of hemodynamic signals relative to the site of neuronal activation. However, capillaries show the lowest functional contrast to noise ratio (CNR) of all currently used fMRI signals. It is further expected that macroscopic veins show high CNR in fMRI, but since they drain blood, including deoxy-Hemoglobin, from relatively large regions, their response is not expected to carry information on fine scale organizations. Therefore, functional signals from blood vessels show a trade-off between spatial specificity and CNR. In order to image relatively fine functional organizations, one can optimize the spatial specificity and CNR by maximizing the relative contribution of vessels of certain diameters and suppressing contributions of veins with other diameters. This can be indirectly done during data acquisition, by determining the level of asymmetry in asymmetric spin-echo sequences (Boxerman et al., 1995; Brewer et al., 2009). An alternative, indirect means of selecting contributions from a certain range of vessels is by tuning the duration of the readout window around the top of the echo in spin-echo sequences (Goense and Logothetis, 2006). This can also be done during the data processing stage, by combining techniques for determining mean vessel diameter (for a review, see Tropres et al., 2015) with fMRI. In other words, one can increase the CNR of the sampled voxel with no significant loss of spatial specificity by allowing contributions from capillaries and veins of certain sizes. The spatial specificity of medium size sub-voxel level blood vessels remains unknown. In

my second aim I will determine the functional and spatial specificity of deoxy- and total hemoglobin responses from vessels as a function of their diameters relative to that of aggregates of capillaries in gray matter. This will not only further our understanding of the potential contributions of vessels to decoding information conveyed by fine scale organizations, it will also guide the use of fMRI for high-resolution applications with balanced spatial specificity and contrast to noise. I will determine the spatial specificity of hemodynamic signals obtained from pial blood vessels with different diameters compared to the spatial specificity shown by the aggregates of cortical capillaries.

1.2.3 Aim 3. To analyze the spatial specificity of the hemodynamic response from aggregates of capillaries within the gray matter relative to the site of increased neurophysiological responses.

Another aspect that challenges successful decoding of orientation stimuli is the spatial spread of the hemodynamic response. This spread has been modeled as a hemodynamic point spread function (PSF) which is thought to represent the upper bound on how spatially precise fMRI response is to a point-like or a line-like increase in neuronal activity. There have been several studies that investigated the PSF using Optical Imaging of Intrinsic Signals (OI-IS) (Sheth et al., 2004; Fukuda et al., 2006; Sirotin et al., 2009) or fMRI response (Engel et al., 1997; Olman et al., 2003; Kim et al., 2004; Parkes et al., 2005; Shmuel et al., 2007). The estimated hemodynamic PSFs were in the order of 2-3.5mm. However, as has been shown by Chaimow et al. (2011), a PSF with full width at half max (FWHM) of 2 mm is inconsistent with successful decoding of orientation stimuli and with imaging of ODCs, although reliable decoding (Kamitani and Tong, 2005) and imaging of ODCs (Cheng et al., 2001a; Yacoub et al., 2007) have been achieved.

Of note, the studies mentioned above that have quantified the PSF did not consider the neurophysiological spread. Thus the reported hemodynamic PSFs include the component of the spatial spread of neural activity, including the size of receptive fields, the spatial extent of the scatter of receptive-fields, integration by the dendritic fields and long range horizontal connection. My third aim is to determine the hemodynamic point spread function relative to that of the neuronal response. The findings from my third aim may reconcile the contradictory large PSF and the measurement of columnar level activities in the visual cortex. Importantly, they can be considered in modeling and planning of high-resolution fMRI and fMRI-based decoding of fine-scale organizations

1.3 General experimental procedure

In order to realize the thesis aims, we based our research on experiments in early visual cortex of anesthetized cats. We focused on A18 of the cat visual cortex since it has well organized orientation map and columns. In addition, it is located at the dorsal surface of cortex, thus it is accessible for high-resolution, wide field optical imaging.

In addition to probing A18, we have imaged responses of cat A17 in aim 1. We obtained data from both A17 and A18 in order to test whether the relative contributions of different mechanisms of fMRI based decoding depend on the features of the probed functional organization.

1.4 Significance of my scientific contributions

Unraveling the mechanism of fMRI-based decoding of information conveyed by a fine scale organization using coarse voxels will allow improved planning, optimization and interpretation of fMRI studies that employ decoding of fine scale organizations. Furthermore, it will facilitate the use of decoding for discovering currently unknown fine scale organizations in relatively unknown areas of the brain, such as the parietal and frontal cortices. Detailed knowledge of blood vessels' spatial specificity as a function of vessel diameter will facilitate the optimization of fMRI data acquisition parameters and analysis for balanced spatial specificity and CNR. Determining the point spread function of hemodynamic responses sets refined expectations of the limits of high-resolution fMRI. My work will therefore provide guidance for future studies that will employ decoding paradigms for discovering unknown fine-scale representations in higher areas of the brain and/or high-resolution fMRI.

Chapter 2. Literature Review

Functional MRI (Bandettini et al., 1992; Kwong et al., 1992; Ogawa et al., 1992) is the most commonly used non-invasive functional imaging method for probing normal brain function. With the emergence of resting-state functional connectivity (Biswal et al., 1995; Fox and Raichle, 2007), functional MRI (fMRI) is expected to find its way to the clinic. Its popularity stems from advantages it proposes relative to other functional brain imaging methods: it does not involve radiation, and it has the best spatial resolution among all non-invasive functional imaging methods. In this chapter we will describe the emergence of Blood-Oxygen-Level-Dependent (BOLD) fMRI and analysis techniques applied in conjunction with fMRI.

2.1 Review of fMRI

2.1.1 History of development of fMRI

Understanding how the brain functions has been of great interest since the beginning of the 19th century under the form of a pseudoscience termed phrenology, developed by Franz Joseph Gall (for review see Clarke and Jacyna, 1988). Gall's studies were based on the concept that the brain is the organ of the mind and localized brain areas have specific functions. Despite the fact that it is now regarded as obsolete, this discipline has been greatly influential in psychiatry and modern neuroscience.

Much effort was put into probing the function of the brain. In the late 19th century, it was already known (Roy and Sherrington, 1890**)** that changes in cerebral blood flow are closely linked to changes in the underlying neuronal activities. The production of energy for neurons is supported by glucose and by oxygen molecules. Oxygen is transported via the hemoglobin residing in the red blood cells (Sokoloff, 1981). When a neuron is active, i.e. once it releases neurotransmitters, it uses more energy than during its basal state. Local blood flow increases, by what currently is expected to be a feedforward mechanism involving neurotransmitters and neuromodulators which dilate the arterioles and arteries concurrently with increases in neuronal activity (Attwell et al., 2010; Cauli and Hamel, 2010; Devor et al., 2012). This response, the hemodynamic response, also termed hyperemia, overcompensates the tissue with excess of oxygen (Figure 2-1). The fractional increase in CBF is approximately 2-3 fold relative to the increase in oxygen consumption (Fox and Raichle, 1986; Hoge et al., 1999; Buxton, 2009).

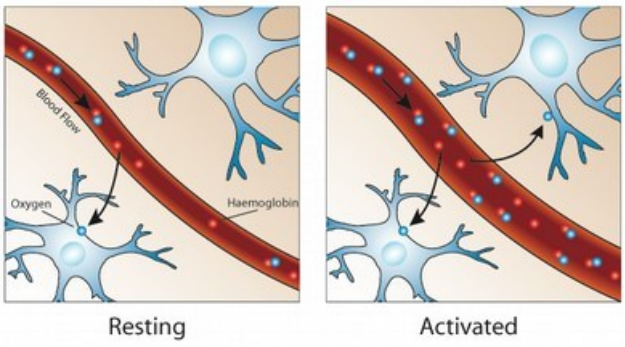

Figure 2-1. Overcompensation of tissue with excess oxygen. (Image from FMRIB Centre, Department of Clinical Neurology, University of Oxford). Upon activation, more oxygen is consumed by the neurons. However, the total amount of oxygen within the same region increases.

However, only in the late 20th century did fMRI become possible. Earlier, MRI made a considerable impact by enabling non-invasive visualization of the structure of the brain. In 1971, it was discovered that the hydrogen signal in cancerous tissue was different from that of healthy tissue using a nuclear magnetic resonance (NMR) machine (Damadian, 1971). In 1977, the first MR image of the whole body was produced (Damadian, 1977). In 1990, it was discovered that the difference in magnetic properties of oxy-hemoglobin (HbO) and deoxy-hemoglobin (HbR) can be used to localize the activated regions of the brain (Ogawa et al., 1990). Finally, in 1992, BOLD functional MRI was introduced (Bandettini et al., 1992; Kwong et al., 1992; Ogawa et al., 1992).

2.1.2 Physics of fMRI

Our body is composed of protons**,** electrically charged particles in the nuclei of hydrogen atoms that are abundant in water. In the presence of a magnetic field, hydrogen atoms align both with and against the field. However, at any given instant, aligned molecules slightly outnumber anti-aligned molecules. The difference in the numbers gives the net magnetization. An MRI scanner releases a short burst of radio waves which knocks the protons out of alignment. Application of a radio pulse can tip this net polarization vector sideways (90° pulse) or reverse it (180° pulse). After the radio burst has ended, the protons fall back gradually in line while three things happen simultaneously: 1) the absorbed radio-wave energy is retransmitted as a decaying sinusoidal signal termed FID; 2) the excited spins begin to return to the original orientation; this process is termed 'T1 relaxation', and 3) initially in phase, the excited protons begin to de-phase, a process termed 'T2 relaxation'. In an ideal experiment, the signal decays approximately exponentially with a time constant T2. However in practical MRI, there are small differences in the static magnetic field at different spatial locations ("inhomogeneities"). This creates destructive interference, which shortens the signal decay. The time constant for the observed decay of the signal in the presence of inhomogeneities is called T2*; it is always shorter than T2. The presence of deoxy-Hemoglobin, a paramagnetic molecule, causes more distortions and shortens the T2* of the deoxygenated blood in the veins. BOLD-fMRI takes advantage of the difference in magnetic properties between oxy-Hemoglobin (longer T2*) and deoxy-Hemoglobin (shorter T2*) to capture the activated brain regions where local deoxy-Hemoglobin is washed out by the overcompensation of the cerebral arterial blood flow response during hyperemia.

2.1.3 Basic analysis of fMRI

Several techniques for analyzing fMRI data voxel-by-voxel have been proposed. The simplest method tests for every voxel the null hypothesis that there was no change in blood-oxygenation between the baseline state and following the presentation of a stimulus or a task. In case a t-test is used, high t-scores indicate large differences and possibly small standard deviations; and low t-scores indicate small differences with standard deviations that may be too large to reject the null hypothesis (Kwong et al., 1992).

Correlation techniques improve the previously mentioned t-test method by taking into account the temporal evolution of BOLD responses from the stimulus paradigm (Bandettini et al., 1993). One can expect smoother and delayed rising (and falling) of the hemodynamic responses subjected to a square-wave like on/off stimulation. The correlation coefficient is calculated between the response time-course and a model constituting the stimulus time-course convolved with the hypothetical average BOLD response. The justification for such analysis stems from the fact that the BOLD response to relatively long stimuli, such as those used in block paradigms, reflects a linear transformation of the stimulus duration (Boynton et al., 1996).

The extension of the correlation method is the general linear model. It aims to explain the BOLD time course as a linear combination of different variables and an error term. It provides a general framework for modelling of the data, and can eliminate effects that may confound the analysis, such as drift or respiration, provided that they can be modelled (Friston et al., 1994; Friston et al., 1995).

Finally, ANOVA (i.e., the analysis of variance) techniques do not assume the shape of activation (Clare et al., 1999). The analysis of variance measures the change in variance upon averaging. For example, take a BOLD time course where the same stimulus was presented 100 times. In the region of purely random intensity variations, the ratio of variance of averaged time course to raw time course is 1/100. Activated regions, however, will have a significantly higher ratio than this, since the variance of both raw and averaged data is dominated by the stimulus triggered BOLD time course.

2.2 Advances in high-resolution fMRI

Because fMRI proved to be a promising scientific tool, researchers have made substantial efforts in extending the physical limits of fMRI, as well as in better understanding of the obtained fMRI data. In this section I will summarize advances in fMRI and challenges that came with new discoveries in the 21st century. One of the main focuses of current fMRI developments is on functional imaging of cortical columns and layers. The uniformity of the mammalian cortex has led to the proposition that there exist elementary cortical units of operation, consisting of several hundred or thousand neurons that are repeated within and across cortical areas (Lorente de Nó, 1938). Cortical columns and layers of neocortex are prominent examples of such structurally and functionally specialized units. Functional properties and connectivity are similar for neurons within a column but are known to vary between columns. It can therefore be argued, based on information-theory, that the optimal spatial scale for studying the relationship between brain function and behavior is that of cortical columns (and layers, for similar reasons). This explains the need for functional imaging of cortical columns and layers, and for reliable techniques for decoding information conveyed by these fine scale structures.

2.2.1 Data mining and MVPA; mechanisms underlying orientation decoding

In section 2.1.3 I briefly described the traditional univariate voxel-by-voxel analysis of the fMRI data. One limitation of the mass-univariate approach is the assumption that the covariance across neighboring voxels has no meaningful information, that it shows uncorrelated noise which can be reduced by spatial smoothing. The multivariate pattern analysis (MVPA) however, is a promising technique to overcome such limitations by extracting the subtle neuronal patterns while considering a volume of voxels as a whole. MVPA has become a popular analysis method among FMRI users.

Interestingly, recent MVPA studies have indicated the feasibility of decoding of information conveyed by neuronal populations organized in structures thought to be smaller than a single voxel (Haxby et al., 2001; Haynes and Rees, 2005; Kamitani and Tong, 2005). That is to say, with a conventional fMRI voxel of size 3x3x3 mm in human studies, it was shown that one can decode the orientation of gratings presented to the subject out of a group of 2 orthogonally oriented or even 8 differently oriented gratings. It is an intriguing phenomenon since, just as in the cat visual cortex (Hubel and Wiesel, 1959; Swindale et al., 1987; Bonhoeffer and Grinvald, 1991;

Shmuel and Grinvald, 2000) neurons that are tuned to a specific orientation in the visual cortex are arranged in a semi-cyclic manner with an interval of 2 mm or even shorter (Yacoub et al., 2008). Furthermore, the large hemodynamic PSF of ~3 mm (Engel et al., 1997; Parkes et al., 2005; Shmuel et al., 2007) should render the data impossible to decode orientations. Six mechanisms have been proposed in search of an answer to this intriguing phenomenon, including the exciting possibility that MVPA is capable of probing sub-voxel level information without the need for the difficult to achieve high-resolution fMRI. However, which mechanisms contribute to decoding orientation is still unclear, in part because of insufficient invasive studies for validation in animal models.

One school explains fMRI-based decoding based on contributions from signals of certain cortical frequencies (Boynton, 2005; Kamitani and Tong, 2005; Op de Beeck, 2010; Swisher et al., 2010; Chaimow et al., 2011; Freeman et al., 2011). Boynton (2005) argued that classifying such activity is only possible due to aliasing. Aliasing occurs when the sampling rate of a recording is relatively low, such that the high frequency components of signals are reflected in the lower frequencies, and produce a mixed lower frequency components. However, Chaimow et al. (2011) showed that aliasing is not a possible mechanism, because fMRI is sampled in the frequency space, and the sampling is limited by the highest frequency available in the K-space. The same authors pursued a simulation of ocular dominance column fMRI, showing that the only information available locally is of a very low contrast to noise ratio, and that it arises from local irregularities that are associated with frequencies lower than the main frequency of the organization.

Experimental evidence that supports contributions of irregularities was shown by the only work (thus far) conducted in an animal model (Swisher et al., 2010). They used high-field, high-resolution functional magnetic resonance imaging (fMRI) and multivariate pattern analysis to determine the spatial scales at which orientation-selective information can be found in the primary visual cortex (V1) of cats and humans. Cat visual cortex, imaged at 0.3125 mm resolution, showed a strong orientation signal at the scale of individual columns. Nonetheless, reliable orientation bias could still be found at spatial scales of several millimeters. In the human visual cortex, imaged at 1 mm resolution, a majority of orientation information was found on scales of millimeters, with small contributions from global spatial biases exceeding approximately 1 cm. Swisher and colleagues concluded that there exists a reliable millimeters-scale orientation signal, likely emerging from irregular spatial arrangements of orientation columns and their supporting

vasculature. Thus, fMRI pattern analysis methods are likely to be sensitive to signals originating from other irregular columnar structures elsewhere in the brain.

Several other studies suggested that fMRI-based decoding of orientation is made possible by large scale organizations rather than local random irregularities in the orientation map. Op de Beeck (2010) pursued spatial low-pass filtering, and showed that the filtering did not hurt classification accuracy. He therefore suggested that fMRI based decoding relies on large scale organizations that are associated with very low-frequencies. The same type of conclusion, that voxel averaging does not hurt decoding performance, was also observed for responses to visual stimuli and decoding of direction of motion (Beckett et al., 2012). These authors tested how classification accuracy varied across subsets of voxels for classification of motion-direction. They combined voxels with similar visual field preference as determined in separate retinotopy measurements in areas V1, V2 and V3. They observed that classification accuracy was preserved when averaging in this 'retinotopically restricted' way, compared to random averaging of voxels. They concluded that this insensitivity to averaging of voxels (with similar visual angle preference) across substantial distances in cortical space suggests that there are large-scale biases at the level of retinotopic maps underlying classification of direction of motion based on fMRI.

However, Kamitani and Sawahata (2010) showed that spatial smoothing hurts localization but not information. They concluded that classification of spatially smoothed fMRI data is not an effective means to probe into information sources for multi-voxel decoding, since smoothing does not hurt the information contents of multi-voxel patterns. They further concluded that Op de Beeck's results provide no evidence against the hypothesis of fMRI-based decoding of orientation based on irregularities in the organization. Of note, their work did not refute contributions from large scale organization: it showed that smoothing is not sufficient to rule out contributions from irregularities.

Other studies suggested that specific large-scale organizations inherent to the functional architecture of V1 may underlie orientation decoding. The oblique effect is an example of a large scale organization: both in humans and non-human primates, vertical and horizontal orientations either show higher responses or occupy larger cortical territories than oblique orientations (Mansfield and Ronner, 1978; LeVay and Nelson, 1991; Furmanski and Engel, 2000). The radial effect is yet another example for a large scale organization: there is a global bias in the orientation map because the neurons are more sensitive to the orientation that is radially collinear with the

center of gaze (Sasaki et al., 2006; Clifford et al., 2009; Mannion et al., 2010; Freeman et al., 2011; Sun et al., 2013). Freeman et al. (2011) confirmed Sasaki's observations of a topographic map of orientation preference in human V1 at a much coarser scale than that of orientation columns, in register with the angular-position component of the retinotopic map of V1. They suggested that this coarse-scale orientation map provides a parsimonious explanation for why multivariate pattern analysis methods succeed in decoding stimulus orientation from fMRI measurements, challenging the widely held assumption that decoding results reflect sampling of spatial irregularities in the fine-scale columnar architecture. Sun et al. (2013) confirmed that there are more voxels preferring horizontal and vertical orientations, a physiological substrate underlying the oblique effect, and that these over-representations of horizontal and vertical orientations are prevalent in the cortical regions near the horizontal- and vertical-meridian representations, a phenomenon related to the radial bias. A recent study by Freeman et al. (2013) measured fMRI responses in human V1 to both oriented gratings and spirals. Responses to oriented gratings exhibited a complex topography, including a radial bias that was most pronounced in the peripheral representation. Responses to clockwise and counter-clockwise spirals also exhibited coarse-scale organization. The preference of each voxel for clockwise or counter-clockwise spirals was predicted from the preferences of that voxel for orientation and spatial position. Freeman et al. (2013) conclude that a bias exists for local stimulus orientation that has a coarse spatial scale, is robust across stimulus classes (spirals and gratings), and suffices to explain decoding from fMRI responses in V1.

However, recent studies challenged the hypothesis on contributions of large-scale organization, and suggested that irregularities underlie orientation decoding even after contributions from large scale organizations are filtered out (Alink et al., 2013; Misaki et al., 2013b). Alink and colleagues used opposite-orientation gratings (balanced about the cardinal orientations) and spirals (balanced about the radial orientation), along with patch-swapped variants of these stimuli. They showed that all stimulus pairs are robustly decodable, demonstrating that fMRI orientation decoding does not require globally coherent orientation stimuli. Furthermore, decoding remained robust after spatial high-pass filtering for all stimuli, showing that fine-grained components of the fMRI patterns reflect visual orientations. While they did observe evidence for global radial and vertical preference maps in V1, these were weak or absent for patch-swapped stimuli, suggesting that global preference maps depend on globally coherent orientations and might arise through recurrent or top-down processes related to the perception of global form. Misaki et

al. (2013b) tested the effect of smoothing in an fMRI experiment of decoding ocular dominance responses. Their results of across group statistics showed that large smoothing reduced decoding accuracies while the smoothing effect at the individual subject level were not the same for all subjects. Their results suggest that spatial smoothing can have a major effect on decoding performance, and that although the effect is variable across subjects, the informative pattern for columnar level decoding resides in higher frequencies.

More recent studies challenge the previously suggested contributions from large-scale organizations, supporting mechanisms other than irregularities. Carlson (2014) and Wardle et al. (2015) propose that what was thought as contributions from the radial bias can be explained by orientation selective responses near the contour edges of oriented grating stimuli that are spatially limited in the visual space. Similarly, Wang et al. (2014) identified a direction-selective response bias in human visual cortex that predicted motion-decoding accuracy, and depended on the shape of the stimulus aperture rather than the absolute direction of motion.

A second school supported contributions from cortical blood vessels to decoding (Gardner et al., 2006; Gardner, 2010; Kriegeskorte et al., 2010; Shmuel et al., 2010). One reason for justifying such an approach is the 3T BOLD-fMRI's increased sensitivity to intra-vascular BOLD compared to signals from capillaries. Gardner (2010) suggested that cortical columns that share tuning for stimulus features like orientation may often be active together and thus require oxygen and metabolic nutrients together. He hypothesized that the cortical vasculature is built to serve these needs, tending to aggregate and amplify orientation specific signals, thus explaining why they are available in fMRI data at very low resolution. Thus, the ability of classifiers to work at very low spatial resolutions, may be a consequences of a well-structured vasculature aligned to the functional architecture of the cortex. Shmuel et al. (2010) showed that the arrangement of macroscopic blood vessels observable in fMRI voxels contributes to the segregation of the stimulated eye. This claim is further endorsed by the work of Thompson et al. (2011) which compared pattern classification between gradient echo and spin echo. It is also possible that a similar mechanism is in effect for orientation stimuli. Kriegeskorte et al. (2010) postulated that MVPA hyper-acuity can be made possible through a complex spatio-temporal filtering kernel model applied by fMRI voxels. It may be possible that the way one voxel samples the local hemodynamic response is not through a simple box-like kernel, as the CCD of a digital camera does, but rather through a space-time variant complex kernel. According to Kriegeskorte's

hypothesis, such spatio-temporal information may allow high-cortical frequency information to be coded in lower frequencies, and thus remain robust to head motions during fMRI scans, and eventually contribute to decoding. This concept was further endorsed by subsequent findings in subtle onset variability of hemodynamic responses from sub-TR differences (Misaki et al., 2013a).

Ten years after the first demonstration of the power of multivariate pattern analysis to decode functional imaging data, the debate on the involved mechanisms remains hot. It is not trivial to assess the contributions of each proposed mechanism relative to others. Feasibility of one does not disprove the validity of others. Moreover, the cortical responses obtained in fMRI are often the combined results of the intertwined mechanisms. Hence it is necessary to conduct high-resolution imaging studies that will capture hemodynamic responses at spatial resolutions allowing for the direct functional imaging of responses from cortical columns.

2.2.2 Pulse sequences and functional contrasts of fMRI; selectivity vs. data amplitude

Two of the popular standard BOLD-fMRI sequences are gradient-echo (GE) and spin-echo (SE). GE is the simplest procedure that measures the T2* properties of different brain tissue (explained in Chapter 2.1.2). GE-BOLD-fMRI directly measures the changes in HbR content (Ogawa et al., 1990). It is sensitive to changes in HbR in draining veins. However, draining veins may carry changes in HbR content undiluted to regions remote from the site of increased neuronal activity (Kim et al., 1994; Turner, 2002).

Such phenomena cause uncertainties in localizing brain regions that responded to the stimulus or task. SE-BOLD-fMRI can partially overcome the influence of veins at the data acquisition stage. It applies a refocusing 2^{nd} pulse, focusing the signal only onto the cortical microvessels (Ogawa et al., 1993; Kim and Ogawa, 2002; Lee et al., 2002). However, it is not always practical to apply this sequence due to its significantly low signal-to-noise ratio compared to the GE sequence (Uludag et al., 2009). Among the numerous studies conducted to date for improving the spatial resolution and specificity of the data acquisition, an asymmetric spin echo (ASE) sequence provides partial nullification of veins leading to a middle ground between spin echo and gradient echo sequence: the more asymmetrical acquisition of the pulse, the closer to GE the resultant signal is (Boxerman et al., 1995). It is therefore possible that one particular asymmetry parameter of ASE is optimal for managing the trade-off between the spatial specificity shown by SE sequences and the T2 contrast and the increased contrast to noise ratio inherent to GE sequences and T2* contrasts. In other words, it might be possible to increase the acquired signal strength

without losing its spatial specificity, by incorporating contributions from relatively small vessels. Also, a different way of reducing the non-spatially specific contributions of larger venules to the SE-BOLD functional signal is by shortening the duration of the readout window (Goense and Logothetis, 2006). Increasing the read out duration to include signals away from the peak increases T2* contributions that emerge from larger vessels, while increasing image SNR.

Another means of capturing similar, yet more spatially specific hemodynamic changes than GE-BOLD-fMRI, is that of GE cerebral blood volume (CBV) fMRI. CBV fMRI has been applied to detect brain activation based on changes in the blood volume in active brain areas (Smirnakis et al., 2007). It was less widely used in human subjects, due to the need for an invasive contrast agent injection, such as gadolinium diethylene-triamine-penta-acetic acid (Gd-DTPA) or monocrystalline-iron-oxide-nanoparticles (MION) to amplify the detected signal (Belliveau et al., 1991; Vanduffel et al., 2001). The emergence of a new technique called vascular space occupancy (VASO) fMRI (Lu and van Zijl, 2012) has made CBV-fMRI feasible in human subjects, since it does not require any injection of contrast agents. VASO-fMRI utilizes T1 differences between blood and tissue to distinguish between these two compartments within a voxel, and employs a blood-nulling inversion recovery sequence to yield an MR signal proportional to 1 - CBV. As such, vasodilatation will result in a VASO signal decrease, while vasoconstriction will have the reverse effect.

The CBV method can be applied in conjunction with GE/SE/ASE. GE BOLD vs. SE BOLD vs. GE CBV vs. SE CBV showed different spatial specificity of fMRI responses (Zhao et al., 2006). However, all studies mentioned above used coarse fMRI voxels and their conclusions were based on the amplitude of the response to a single stimulus per study. In addition, the concept that the larger a vessel is the less specific its metabolic (HbR) and hemodynamic (CBF or CBV) responses is to the site of increased neuronal activity is widely accepted (Turner, 2002). However, all previous studies that demonstrated fMRI responses from draining veins remote from the site of increased neuronal responses have not quantified the spatial specificity of vessels as a function of their diameters. Direct, high-resolution physiological investigations of the spatial specificity of blood vessels while using several stimuli have yet to be performed. The findings from such investigations will make it possible to take advantage of data acquisition (Boxerman et al., 1995; Goense and Logothetis, 2006) and data analysis methods capable of including and/or excluding contributions from specific voxels based on the dominant vessel size (Jochimsen and Moller, 2008).

2.2.3 High-resolution fMRI at high-magnetic field: on the spatial specificity of hemodynamic responses

The ultimate goal for any functional imaging method is to achieve the spatial resolution and specificity which is limited only by the limits of the biological system it images. In case of BOLD-fMRI, the objective is to obtain the limit of spatial resolution of hemodynamic based mapping. Over the past 10 years, there has been a growing interest in imaging the cortex at a high spatial resolution with high magnetic-field fMRI (Shmuel et al., 2007; Yacoub et al., 2007). The reason for this interest is that fMRI at high-field can potentially image the function of fine-scale anatomical constructs, i.e. cortical columns and layers.

High resolution functional imaging enables more precise brain probing and more accurate data acquisition. However, the higher sampling resolution inherently lowers the signal-to-noise ratio of fMRI (Triantafyllou et al., 2005). The SNR of an fMRI voxel is linearly proportional to the magnetic field, and linearly proportional to the voxel's volume. Simply reducing the size of a voxel from 3x3x3mm to 1x1x1mm while increasing the field strength from 3T to 7T decreases the voxel SNR by approximately 12-fold. In addition, a smaller voxel volume leads to attenuated partial volume effects and intra-voxel de-phasing, allowing draining veins to have a greater influence on the signal of downstream voxels (Nencka and Rowe, 2007).

Nevertheless, with advances in fMRI technologies and with improved SNR it was shown possible to image functional structures such as ocular dominance columns in humans (Cheng et al., 2001b; Goodyear and Menon, 2001; Yacoub et al., 2007). Interestingly, the possibility of imaging ODCs in humans challenges the previously reported hemodynamic PSF width. In general, it is expected that hemodynamic responses are a smoother version of neuronal responses. The width of the smoothing kernel of the PSF was reported as FWHM of 3-3.5 mm at 3 Tesla and ~2 mm at 7 Tesla (Engel et al., 1997; Parkes et al., 2005; Shmuel et al., 2007). The ocular dominance arrangement in humans has a semi-cyclic structure with a cycle equal to or smaller than 2 mm. Simulations (Chaimow et al., 2015) show that imaging ODCs with a method whose PSF's FWHM is 2 mm is impractical. In order to be able to model, plan and interpret high-resolution fMRI, one needs to correctly quantify the hemodynamic PSF. In order to solve this problem, an important factor to be considered is the need for a technique that is not affected by the magnet field strength.

2.3 OI-IS and EP: methods for evaluating and validating mechanisms underlying fMRI

Throughout Chapter 2.2, I mentioned that the lack of invasive animal studies utilizing means other than fMRI has left a gap in our understanding of the mechanisms of fMRI-based decoding of fine-scale organizations. In this section, I review the OI-IS and EP techniques that have been used in conjunction, and subsequently with, fMRI to study general mechanisms underlying fMRI, not necessarily for understanding decoding.

2.3.1 Intrinsic Optical Imaging

OI-IS has been extensively used to analyze the functional architecture of the visual cortex in several species (Swindale et al., 2003; Villeneuve and Casanova, 2003; Vanzetta et al., 2004; Gias et al., 2005). A typical set-up of an OI-IS experiment requires a high-definition camera, computer screen for visual stimuli (when imaging the visual cortex), illumination with monochromatic light or band-limited light, and a sealed chamber that is cemented onto the animal's surgically exposed cortex (Ts'o et al., 1990; Grinvald et al., 1999). OI-IS takes advantage of hemoglobin absorption under visible light to assess hemodynamic responses. Because HbO and HbR have different absorption spectra, and one of the wavelengths where this difference is most prominent is 605 nm, using a wavelength of 605 nm can allow for capturing changes in blood oxygenation (Frostig et al., 1990). The important premise is that the absorption of HbO is relatively negligible between 600-630nm allowing the measurement to be dominated by changes in HbR. Light scattering due mainly to cell swelling dominates over blood oxygenation and blood volume signals for illumination wavelengths that are longer than 630nm (Frostig et al., 1990; Blasdel, 1997; Grinvald et al., 1999; Zhan et al., 2005). OI-IS with such long wavelengths shows functional selectivity (720 nm; Zhan et al., 2005) and possibly better spatial specificity relative to HbR or HbT responses (Frostig et al., 1990; Grinvald et al., 1999). Early OI-IS experiments studied well-known structural elements such as ocular dominance columns or orientation columns (Bonhoeffer and Grinvald, 1991, 1993a; Das and Gilbert, 1995; Shmuel and Grinvald, 1996; Das and Gilbert, 1997; Shmuel and Grinvald, 2000; Zhan et al., 2005).

The concern that HbO is 'negligible' under 600-630nm has led to recent improvement in optical imaging using multi-wavelength illumination, and more flexible decomposition of HbR, HbO, and also total hemoglobin (HbT) from a combination of wavelengths (Devor et al., 2005;

Dunn et al., 2005; Hillman et al., 2007; Sirotin et al., 2009). Adapted from the functional near-infrared spectroscopy community, this novel technique utilizes the Modified-Beer Lambert law to spectrally decompose two illumination wavelengths following changes in HbO and HbR, while taking into account the path-length of the photon. Given an estimate of baseline HbO/HbR concentration and brain tissue properties, one can simulate the appropriate path-length (Kohl et al., 2000).

In summary, an multi-wavelength illumination system (such as the one employed by Bouchard et al., 2009) allows for high-resolution imaging of the responses of hemoglobin species (HbR, HbO, and HbT). It is superior to fMRI in spatial and temporal resolution, signal to noise ratio and the possibility of detecting responses of Hemoglobin species.

2.3.2 Electrophysiology

Electrophysiology (EP) has been extensively used to probe neuronal activity by detecting the electrical changes associated with ion flow in biological tissues. EP is a very wide field ranging from intracellular recording (Hodgkin and Huxley, 1952) to extracellular recording. Either with intra- or extra-cellular recordings, one can measure single unit activity (Hubel and Wiesel, 1959). With extra-cellular recordings, one can measure, in addition, multiunit activity and local field potentials (LFP). The LFP is believed to be the result of synchronous synaptic potentials (Logothetis, 2002). LFP constitutes neuronal fluctuations that are reflected in different band-limited components (the delta, theta, alpha, beta and gamma bands). Accumulating evidence suggests that oscillations in these different bands originate in different pathways and/or different cellular mechanisms.

For my thesis, the LFP is of particular interest, because it shows the highest correlation to the BOLD signal (Logothetis et al., 2001). The hemodynamic response accompanies neuronal activation and therefore it is important to assess which measure or combination of measures of neuronal activity can be used for modeling the BOLD signal. Studies employing simultaneous measurements of fMRI and EP show that BOLD is better correlated with the LFP in the gamma band than with MUA (Logothetis et al., 2001; Magri et al., 2012).

In conjunction with recent advance in high-resolution fMRI, the possibility of imaging cortical layers, and multichannel depth electrodes have been widely used to probe layer specific neuronal activity (Goense and Logothetis, 2006; Zhao et al., 2006; Smirnakis et al., 2007; Xing et al., 2009; Spaak et al., 2012). Precise localization of layers across depth is important in

understanding the layer specific neurovascular coupling. However, LFPs are vulnerable to volume-conducted far-field effects. The second spatial derivative of LFPs, called the current source density (CSD), reduces this problem and has the ability of more precisely localizing transmembrane currents than LFPs (Sotero et al., 2015).

2.3.3 Combined techniques

OI-IS is physiologically equivalent to fMRI. Both measure hemodynamic signals, although they employ different principles of measurements. While fMRI is based on the magnetic properties of deoxy-Hemoglobin and oxy-Hemoglobin, OI-IS is based on the differences in light absorption of these two molecules.

Because fMRI voxels are too coarse to probe specific cortical activities, invasive techniques such as optical imaging are used in conjunction with fMRI in animal models for in depth understanding of the BOLD response. In one case, OI-IS measured HbT responses correlated well with CBV-fMRI in the superficial layers of gray matter (Kennerley et al., 2005). Another study from the same group showed the feasibility of using OI-IS to study the mechanism of negative BOLD responses (Kennerley et al., 2012). OI-IS can be also used to validate the results obtained in high-resolution fMRI (Fukuda et al., 2006).

OI-IS and EP have been used for quantifying neurovascular coupling. Studies involving these combined measurements assessed the dependence of orientation tuning of single neurons on the structure of the orientation map in their local vicinity (Schummers et al., 2002, 2004; Nauhaus et al., 2008), measured the hemodynamic point spread (Vazquez et al., 2014), or looked at the temporal relationship between the two (Sirotin and Das, 2009; Sirotin et al., 2012).

2.4 Summary

The work presented in this thesis takes advantage of techniques alternative to conventional BOLD fMRI, including CBV-fMRI, OI-IS and EP, that offer higher resolution and SNR. They allow the exploration of the mechanisms of BOLD-fMRI based decoding of information conveyed by fine scale organizations.

Preface to Chapter 3

Chapter 3 is the first of two chapters that address aim 1: 'to unravel the mechanisms underlying hemodynamic-response based decoding of oriented gratings using coarse voxel sampling'. This chapter uses contrast-agent-based CBV-fMRI data that have minimal contributions from large blood vessels. In addition, the data were acquired while stimulating the cat continuously, using oriented grating stimuli with the orientation changing gradually and slowly. Therefore, the responses of the larger vessels were practically in steady state. Therefore, this data-acquisition paradigm allows evaluating contributions from local irregularities and low-frequency components of the organization while contributions from macroscopic blood vessels and complex spatiotemporal filtering by fMRI voxels are eliminated. To analyze contributions from local irregularities and low-frequency components of the organization, spatial filtering and binning were performed on the cortical responses to different orientations.

Cerebral blood volume functional MRI with no contributions from macroscopic vessels rules out the decoding of oriented grating stimuli through local irregularities in cat area 17

Zeshan Yao[1], Mitsuhiro Fukuda[2], Chan-Hong Moon[2], Seong-Gi Kim[2], Amir Shmuel[1]

[1]McConnell Brain Imaging Centre, Montreal Neurological Institute,
Departments of Neurology, Neurosurgery, Physiology and Biomedical Engineering
McGill University, Montreal, QC, Canada

[2]Departments of Radiology, Neurobiology and Bioengineering
University of Pittsburgh, Pittsburgh, PA, USA

Correspondence:

Amir Shmuel, Ph.D.

3801 University, room NW109

Montreal, QC, Canada H3A 2B4

E-mail: amir.shmuel@mcgill.ca

Keywords: High-resolution functional MRI, Blood oxygenation level dependent, BOLD, Cerebral blood volume, CBV, Cortical columns, Orientation map, Decoding.

Acknowledgements: We thank Kelly Hennegan for her scientific English editing of the manuscript, and Drs. Doina Precup, Curtis Baker and Robert Kearney for very helpful discussions. This work was supported by grants from the Natural Sciences and Engineering Research Council of Canada (NSERC Discovery grants RGPIN 375457-09 and RGPIN-2015-05103) and the Human Frontier Science Program (RGY0080/2008) awarded to AS.

Abstract

Recent studies have demonstrated that multivariate machine learning algorithms can decode the orientation of grating stimuli from coarsely sampled ($3\times3\times3$ mm^3) fMRI data. Six alternative mechanisms have been hypothesized as candidate contributors to the decoding of information encoded in fine-scale orientation maps: (I) aliasing of high spatial-frequency components of the columnar organization by large voxels, (II) random local irregularities in the functional organization, (III) very low spatial frequencies reflecting large-scale components of the organization, (IV) orientation selective responses near the retinotopic edge of the orientation stimuli, (V) selective responses of macroscopic blood vessels, and (VI) fMRI voxel complex spatiotemporal sampling transforming finely organized neuronal activity into more coarsely organized vessels. Unraveling the mechanisms underlying decoding of fine scale organizations will enable informed search for such organizations in relatively unknown areas such as the frontal cortex. Here we aimed to determine whether local irregularities and low-frequency components contribute to decoding. To this end, we eliminated contributions from macroscopic vessels, by employing monocrystalline iron oxide nanoparticle (MION)-based cerebral blood volume fMRI, and quantifying the responses in cat area 17 to continuously rotating drifting gratings. We defined voxels homologous in size to those used in fMRI-based decoding in humans, by comparing the main frequency of the orientation map in cat area 17 to that in human V1. Our results show that low-frequency organizations likely contribute to decoding. In contrast, irregularities in the fine-scale organization do not contribute to the decoding of oriented gratings. Taking into account a BOLD point-spread function wider than that of cerebral blood volume responses, BOLD imaging is even less likely to reflect direct contributions of irregularities in the fine-scale organization to decoding.

Introduction

Recent studies have demonstrated that multivariate machine learning algorithms can decode visual stimuli from fMRI data (Haynes and Rees, 2005; Kamitani and Tong, 2005). Using gradient-echo (GE) blood oxygenation level dependent (BOLD) functional MRI (fMRI) at 3 Tesla (T), these algorithms have decoded information thought to be encoded in fine-scale structures, i.e. orientation columns. This result is surprising given the large size of the voxels ($3\times3\times3$ mm^3) relative to the expected mean cycle length of the orientation map in human area V1 (~2 mm; see Methods). This result is even more surprising considering the relatively wide point-spread function (PSF) of GE BOLD-fMRI signals at 3T (~3.5 mm, Engel et al., 1997; Parkes et al., 2005) and even that estimated at 7T (~2 mm, Shmuel et al., 2007). The mechanism by which low-resolution imaging decodes information represented at a fine scale relative to the voxel size is presently unclear. Here we aim to determine the mechanisms that could potentially contribute to the decoding of information conveyed by cortical columns, based solely on the functional architecture of orientation maps in cat area 17.

Six alternative mechanisms have been hypothesized as candidate contributors to the decoding of information encoded in fine-scale structures. The first proposed that the aliasing of high spatial-frequency components of the columnar organization by large voxels gave rise to a higher than chance level decoding rate (Boynton, 2005). This "aliasing" mechanism, also termed the "hyperacuity" mechanism (Op de Beeck, 2010), involves components of the columnar organization with frequencies higher than the Nyquist frequency, which had been thought to contribute to the sampled voxels. However, we have since ruled out this proposed mechanism (Chaimow et al. 2011), based on the fact that fMRI samples data in the frequency space, with the highest frequency in the k-space being the highest frequency available to the sampling process.

Therefore, there are five remaining possible mechanisms. (I) It was hypothesized that random local variations and irregularities in the functional organization contribute to decoding (Kamitani and Tong, 2005; Haynes and Rees, 2006; Kriegeskorte and Bandettini, 2007; Swisher et al., 2010). The argument is that due to irregularities in columnar patterns, each voxel overlaps columns with different preferences unequally, thereby resulting in biases towards specific preferences. (II) Very low spatial frequencies have also been proposed to play a role, reflecting large-scale components of the organization (Op de Beeck, 2010; Freeman et al., 2011; Freeman et al., 2013; Wang et al., 2014). These include the oblique effect (Furmanski and Engel, 2000; Sun

et al., 2013) and the radial bias effect (Sasaki et al., 2006; Clifford et al., 2009; Mannion et al., 2010; Freeman et al., 2011; Freeman et al., 2013; Sun et al., 2013) associated with the representation of orientation (see also Carlson (2014) for an alternative mechanism associated with the radial-specific responses). For decoding the stimulated eye, a relevant large scale organization is formed by the higher amplitude response to stimulation of the contra-lateral eye (Tychsen and Burkhalter, 1997). (III) A mechanism alternative to the large-scale organization (item II above) has been recently proposed. Observations made by Carlson (2014) suggest that the edges of oriented grating stimuli elicit responses that are orientation specific. Similarly, Wang et al. (2014) identified a direction-selective response bias in human visual cortex that predicted motion-decoding accuracy; and it depended on the shape of the stimulus aperture rather than the absolute direction of motion. The response amplitudes gradually decreased with distance from the stimulus aperture edge corresponding to motion origin in V1, V2, V3, thus explaining the higher motion-decoding accuracies reported previously in early visual cortex.

Alternatively, (IV) draining regions that cover cortical maps and columns non-homogeneously may cause selective responses of their corresponding blood vessels (Kamitani and Tong, 2005; Gardner et al., 2006; Kamitani and Tong, 2006; Kriegeskorte and Bandettini, 2007; Gardner, 2010; Shmuel et al., 2010; Thompson et al., 2011). In this scenario, selective signals from macroscopic blood vessels can be captured by large voxels; therefore, they can contribute to the decoding of stimuli encoded at the resolution of cortical columns. Evidence in support of this phenomenon has been provided by (Gardner et al., 2006; Shmuel et al., 2010; Thompson et al., 2011). Lastly, (V) Kriegeskorte et al. (2010) introduced a model in which fMRI voxels sample neuronal activity as complex spatiotemporal filters. These authors described how such a model can account for representation of high-frequency components of the cortical maps by the sampled voxels and for the decoding of information conveyed by cortical columns.

Unraveling the mechanisms underlying decoding of information conveyed by fine scale organizations is of high interest. It will allow informed search of fine scale organizations in relatively unknown cortical areas, such as the frontal cortex. Thus, it can greatly support the mapping of function in the human brain at a scale finer than that of cortical areas.

In using BOLD-fMRI, it is not straightforward to assess the importance of contributions from each of these proposed mechanisms, because cortical fMRI responses likely encompass the combined contributions of these intertwined mechanisms. In the current study, we specifically aim

to determine whether the functional architecture of orientation maps supports contributions from irregularities and/or large-scale organizations to the successful decoding of oriented grating stimuli. Importantly, in order to focus on contributions from irregularities and/or large-scale organizations alone, we exclude contributions from all other proposed mechanisms, including draining veins and complex spatiotemporal filters. To this end, we analyzed monocrystalline iron oxide nanoparticle (MION)-based cerebral blood volume (CBV) fMRI responses in cat area 17 to continuously rotating drifting gratings. It has been shown that the fMRI-based cortical CBV response is more spatially-specific than the BOLD response and shows a higher SNR (Kennan et al., 1998; Mandeville et al., 1998; van Bruggen et al., 1998; Mandeville et al., 2001; Keilholz et al., 2006; Zhao et al., 2006; Smirnakis et al., 2007; Poplawsky and Kim, 2014). In addition, MION-based CBV-fMRI has no signal contributions from macroscopic blood vessels (Mandeville and Marota, 1999; Zhao et al., 2006). Hence, by using MION-based CBV-fMRI, we can focus on cortical responses from micro-vessels while excluding the contributions of macroscopic blood vessels. Our results show that low-frequencies in the regime of large-scale organizations likely contribute to decoding. In contrast, irregularities in the fine-scale organization of orientation maps in cat area 17 likely do not contribute to the decoding of oriented gratings. Our CBV MION measurements show no contributions of irregularities in the organization to decoding. Therefore, taking into account a non-zero, expected BOLD PSF, BOLD imaging is even less likely to reflect direct contributions of irregularities in the fine-scale organization to decoding.

Methods

A more detailed description of the animal preparation, anaesthesia, and data acquisition can be found in (Fukuda et al., 2006). All data analysis was carried using custom-made MATLAB code.

Animal preparation

All experiments were approved by the Institutional Animal Care and Use Committee of the University of Pittsburgh. Five cats (1.3–2.5 kg; 13.6–21.7 weeks of age) were used for the fMRI scans. Each cat was initially treated with atropine sulfate (0.05 mg/kg, i.m.). Anaesthesia was induced by a mixture of ketamine (10–20 mg/kg, i.m.) and xylazine (1 mg/kg, i.m.); the surgery was performed under a mixture of air and O2 (maintaining a 30–35% O2 level) with 2% isoflurane. The cat was placed in a cradle and secured in a normal postural position by a custom-

designed head frame. The cranium was exposed for placement of a surface coil. The cat was paralyzed with pancuronium bromide (0.2 mg/kg/hr, i.v.). The eyes were focused on the stimulation screen using appropriate contact lenses. Data was acquired at a 0.8–1.2% isoflurane level.

Visual stimulation

Visual responses were elicited by binocularly presenting 100% contrast square-wave gratings, which were generated using either Cogent Graphics (John Romaya, Wellcome Department of Imaging Neuroscience, London, UK; http://www.vislab.ucl.ac.uk/Cogent/index.html) or with a VSG2/5 (Cambridge Research Systems, Kent, UK). The spatial frequency of the gratings was 0.1 cycle/°. The gratings drifted at 2 cycles/s, with the direction of motion reversed every 0.5 s. Stimulation was synchronized with image acquisition in fMRI experiments. An 80 s cyclical continuous stimulation paradigm was used, during which eight orientations were presented [0° (horizontal) to 157.5°, 22.5° increments, 10 s each] with no gaps between stimuli. Ten repetitions of an 80-s long full stimulation cycle were performed, for a total presentation time of 800 s in one scan.

MRI

All MRI experiments were performed on a 9.4T horizontal magnet with a clear bore size of 31 cm (Varian, Palo Alto, CA), using a surface radio frequency coil with an inner diameter of 25 mm placed over the primary visual cortex. The position of the functional imaging slice was determined based on flow-compensated, gradient-recalled, three-dimensional (3-D) venographic images [repetition time (TR), 50 ms; echo time (TE), 20 ms; data matrix, 512×256×256; field of view (FOV), approximately 4.0×2.0×2.0 cm; isotropic resolution, approx. 78 μm] (Park and Kim, 2005). Based on the vascular patterns and gyral curvatures from the 3-D venogram, a 1-mm thick fMRI slice was positioned in the visual cortex such that the vessels were perpendicular to the slice. For a direct comparison of functional and anatomical data, a two-dimensional (2-D) gradient-recalled anatomic image was also acquired (TR, 50 ms; TE, 15–20 ms; data matrix, 256×256; typical FOV, 2.0×2.0cm) with the same FOV, slice thickness, and position as those used for fMRI.

For CBV-weighted fMRI, a bolus of dextran-coated MION contrast agent (typically 10 mg Fe/kg body weight; obtained from the laboratory of Dr. Ralph Weissleder, Massachusetts General Hospital, Boston, MA) was injected into either the femoral or cephalic vein. The intravascular

injection of MION contrast agent enhances the sensitivity of fMRI in microvessels and induces a high susceptibility effect in large vessels, which reduces large vessel contributions (Kennan et al., 1998; Mandeville et al., 1998; van Bruggen et al., 1998). MION has a long intravascular half-life and distributes throughout the blood plasma in the cortical vessels; the fMRI signal with iron oxide is mainly weighted by changes in plasma CBV within microvessels (Kennan et al., 1998; Mandeville et al., 1998; van Bruggen et al., 1998). All functional images were obtained from the medial bank of the primary visual cortex, which allowed imaging a wide area of gray matter overlapping with the selected slice (see also 'Delineation of ROI' below). A GE four-shot echo planar imaging sequence was used, with typical imaging parameters as follows: FOV, 2.0×2.0 cm; data matrix, 128×128 (i.e., in-plane resolution of 156×156 μm/voxel), slice thickness, 1 mm; TR, 2 s; TE, 10 ms for CBV-weighted fMRI.

Delineation of the ROI

We defined our ROI as the region where the cortical surface was approximately parallel to the anatomical MRI slice and overlapping it. To this end, the initial ROI was manually drawn, such that it approximately overlapped with area 17 and encompassed all circular point-like penetrating veins (white curve in Fig. 3-1A). It approximately traversed the regions where transitions from perpendicularly to obliquely penetrating veins were observed. The delineation of the final ROI was based on quantitative assessment of the density of veins that penetrated orthogonally to the slice, thus indicating that the slice was parallel to the gray matter. To this end, we convolved the anatomical image with a Gaussian kernel ($\sigma = 5$ voxels) and applied a threshold, in order to localize the circular penetrating vessels (red dots in Fig. 3-1B; appearing as circular drops in signal in Fig. 3-1A) across the anatomical image, within and outside the preliminary ROI (Figures 3-1A and 1B). We then computed the density map of the penetrating vessels by convolving the result with a Gaussian kernel ($\sigma = 30$ voxels; Fig. 3-1C). The penetrating vessel density map was then thresholded, in order to define the ROI with an approximately homogeneous density of penetrating veins (Fig. 3-1D), thus ensuring that the ROI was approximately parallel to the gray matter. This prevented the inclusion of regions where the cortex was curved relative to the slice, thus analyzing orientation columns that were not orthogonal to the slice (such as at the bottom of Fig. 3-2C, where the colored regions showing orientation preference are elongated because cortex in this region is not parallel to the slice). The final ROI was the conjunction of the initial ROI and the ROI processed for an approximately homogeneous density of penetrating veins.

To summarize, given the procedure we applied for delineating the ROI, we expect that the orientation columns we analyzed were approximately orthogonal to the slice.

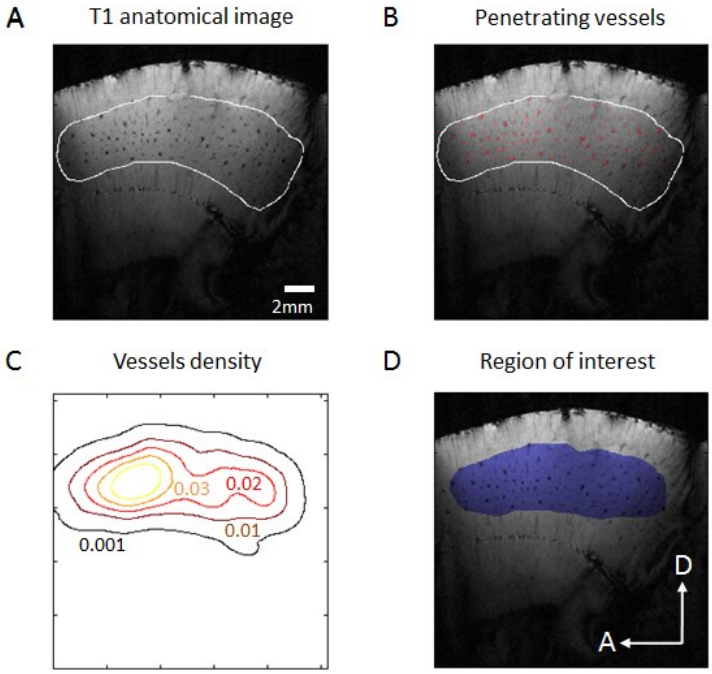

Figure 3-1. Delineation of the ROI from anatomical MRI.
A) Anatomical MRI slice with the preliminary hand-drawn boundary delineating the region where blood vessels run perpendicularly to the slice. **B)** The vessels that were identified by thresholding a convolution of the T1 image with a Gaussian kernel are marked in red. **C)** Contour plot of the density of the red-marked vessels in B. A cut-off of 0.01 was used to eliminate any region with density lower than the threshold. **D**) Final ROI. The conjunction of the preliminary ROI and the thresholded density cloud was taken as the final ROI for further analysis. A, Anterior; D, Dorsal.

Response to oriented gratings

One run of the phase-encoding fMRI consisted of a continuous recording of 820 s (TR = 2 s, 410 volumes). To relate a specific volume to a specific orientation, the time-series was shifted backwards (the first 6 volumes following the onset of the stimulus were discarded). This accounted for the typical 13 seconds CBV delay relative to the stimulus in MION-based phase-encoding fMRI (Fukuda et al. 2006). To generate temporally encoded maps for evaluating the data quality, Fourier analysis was applied to signals continuously recorded over the following 400 volumes on a voxel-by-voxel basis (Engel et al. 1997; Kalatsky and Stryker 2003) (Figures 3-2A and 3-2B). Data were qualitatively checked by observing the Fourier spectrum (Fig. 3-2B, upper panel) and the raw time course (Fig. 3-2B, bottom panel) at representative voxels within the slice (Fig. 3-2A).

A polar map was computed, with the color and brightness representing the voxel's preferred orientation and selective response, respectively (Fig. 3-2C).

Within 1 stimulation cycle (TR = 2 s, 40 volumes), there were 8 different orientations presented. Hence, we computed the average of 3 consecutive volumes within every 5 consecutive volumes, yielding 8 volumes associated with the 8 different oriented gratings. Note that for our analysis we neither used the phase map nor the polar map. Instead, we averaged 3 consecutive volumes to represent the response to each orientation. A 4-dimentional data matrix of 128 by 128 voxels by 10 trials by 8 orientations was obtained for each hemisphere. We normalized the data by dividing all 10 trials and 8 orientations values associated with a voxel by their mean value, thereby transforming the fMRI intensity into relative change.

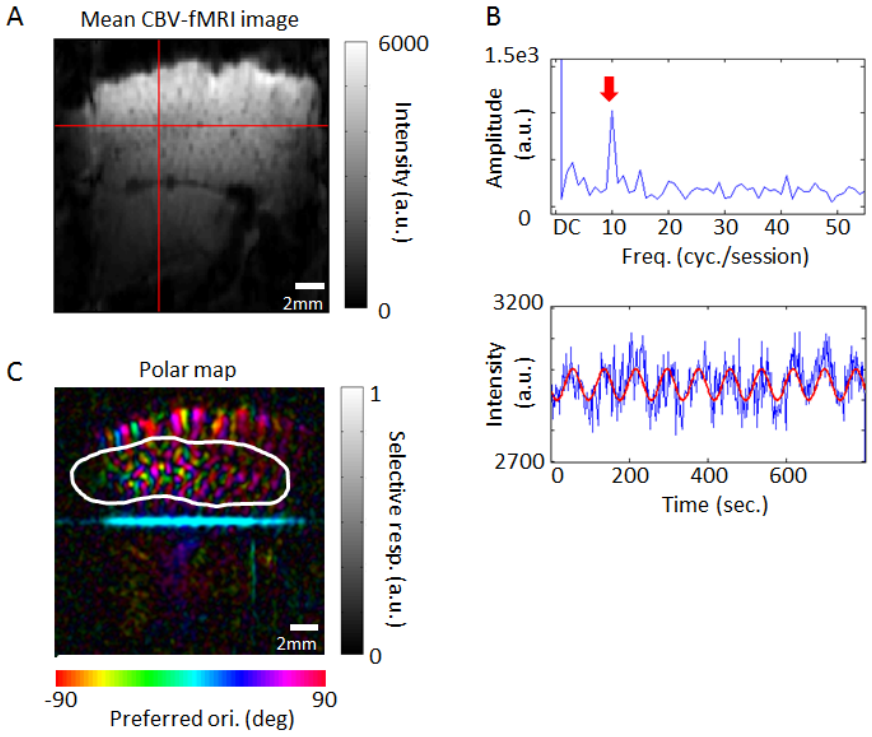

Figure 3-2. fMRI data: phase encoding in the orientation domain. **A)** Mean intensity image of MION-based CBV-weighted fMRI computed over one session (slice thickness, 1 mm; TR, 2 s; TE, 10 ms; data acquisition over 800 s). **B)** Raw time course and Fourier spectrum using MATLAB's FFT from the voxel corresponding to the crossing point of red lines in the mean fMRI image presented in B. The red sinusoidal wave and red arrow in the FFT represent the stimulus frequency. **C**) Polar map of preferred orientation obtained from the phase of the time course at the stimulus frequency. The color indicates the preferred orientation (phase of FFT) and the brightness indicates the orientation selective response (magnitude of FFT). The final ROI determined previously (see Fig. 1) is superimposed.

Fig. 3-3A presents a typical differential orientation map obtained within the ROI from responses to two orthogonal gratings. In addition to computing the differential contrast, we also computed the corresponding noise and contrast-to-noise ratio (CNR). We defined the voxel-by-voxel differential contrast as the difference in cortical responses to orthogonal stimuli, of which we had 4 pairs from each dataset. We defined the noise as the standard deviation of differential contrast across trials. We defined the voxel-by-voxel CNR as the ratio of absolute differential contrast to noise.

In order to determine the main cycle length of the differential orientation map, we computed the mean CNR as a function of spatial cortical frequency. We first computed the 2D fast Fourier transform (FFT) spectrum for each of the normalized differential response maps in the 4-dimensional normalized data matrix (see previous section). The filtering was performed on the response maps limited within the delineated ROI and zero-padded to have a rectangular output of 25×25 mm. We then masked the FFT for point-pass filtering (point-pass: 1 frequency passing band-pass) at cut-off frequencies from 0 to 2.40 cycle/mm, with a step size of 0.04 cycle/mm. The masked FFT was transformed back to image space. We then computed the differential contrast map, noise map, and CNR map for each pair of orthogonal orientation stimuli from each animal (Fig. 3-3B). Finally, a mean of absolute CNR was calculated spatially across the CNR map, as a function of center frequency. Next, in order to determine the peak frequency of the organization separately for each map, we fitted a Gaussian curve to the data points between 0.52 and 2.40 cycles/mm (Fig. 3-3C). Finally, we determined the main frequency of the orientation map as the center of the Gaussian curve. We performed this process separately for each map obtained from a pair of orthogonal orientations for each animal. The average peak was at 0.99 ± 0.05 cycle/mm (Fig. 3-3D; n = 19; 4 differential contrast maps per animal, 5 animals, 1 outlier).

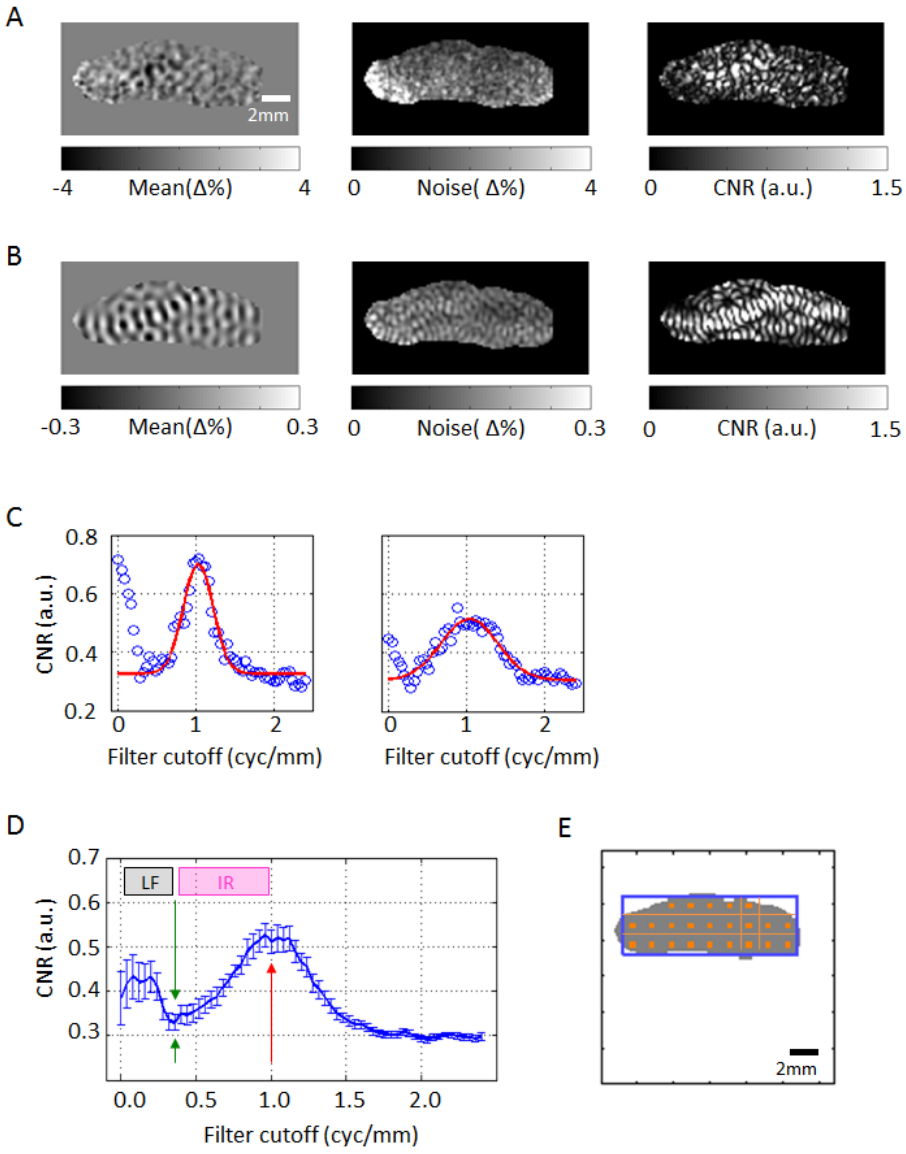

Figure 3-3. Main frequency of the orientation map.
A) Differential orientation map, Noise map, and CNR map within the ROI. **B)** Differential orientation map, Noise map, and CNR map obtained following point-pass filtering of the response maps with center frequency of 1 cycle/mm. Prior to filtering, zero-padding completed the image to a 25×25 mm region in order to have a square output. **C)** Two examples from 2 different animals of the CNR as a function of point-pass cut-off frequencies. A Gaussian curve was fitted to the segment between 0.52 and 2.40 cycle/mm to avoid the initial peak. **D)** The mean and standard error of the mean (SEM) of the raw CNR values. The average cycle length computed over all 4 pairs of orthogonal orientations and 5 animals (N = 19, 1 outlier) was 0.99 ± 0.05 cycle/mm (red arrow). The green arrow points to the trough at 0.36 cycle/mm, which we define as the separating point between the irregularities and low-frequencies regimes. IR, irregularities. LF, low-frequencies. **E)** Loci of homologous voxels that maximally overlapped with the ROI. The centers of voxels that defined the ROI used for further analysis are marked by a solid orange square.

Previous studies that decoded oriented gratings in humans (Haynes and Rees, 2005; Kamitani and Tong, 2005) used 3×3×3 mm^3 voxels. In order to compare our findings to those obtained in human studies, we resampled the data with voxels of various sizes including the size homologous to that used in human studies. The average cycle of ocular dominance maps in human area V1 is ~2 mm (Cheng et al., 2001a; Adams et al., 2007; Yacoub et al., 2007). By analogy to the monkey visual cortex, we can expect that the average cycle length of orientation maps in human V1 is also approximately 2 mm. Therefore, the ratio between the voxel edge used by Kamitani and Tong (2005) and Haynes and Rees (2005) and the cycle of orientation is ~1.5. We defined the homologous voxel size as 1.5 times the average length of the orientation cycle, i.e. 1.5 × (1 ÷ 0.99 cycle/mm) ≈ 1.50 mm. Since the standard deviation of the peak orientation cycle across animals was small (0.05 cycle/mm), we applied one standard homologous voxel of size 1.50 mm across all datasets.

Lastly, we placed a rectangular ROI using a group of these large voxels, after determining their loci such that there was a maximal overlap between the homologous voxel matrix and the previously defined ROI (Fig. 3-3E). The orange dots within the homologous voxel matrix in Fig. 3-3E highlight those voxels whose spatial overlap with the ROI was ≥ 75%. These voxels defined the area used for the analysis, including the input to the Support Vector Machine (SVM) decoding.

Data pre-processing: filtering and binning

Following the determination of the homologous voxel size (1.50 mm), we pre-processed the normalized data in two stages: filtering and binning. The first stage, spatial filtering, allows for the evaluation of the frequency components that contribute to decoding (Shmuel et al., 2010; Swisher et al., 2010). We zero-padded the ROI, transforming it into a square with each side equal to 12-homologous-voxel edges (12 × 1.50 mm = 18 mm). The lowest frequency obtainable, and the step size (frequency resolution in the FFT), was then: 1 ÷ 18 = 0.056 cycle/mm. We then filtered the data using an ideal spatial 2D FFT low-pass or point-pass filter with the following frequency cut-offs (Fig. 3-4A): [0 (=mean response); 1; 2; 3; 4; 5; 6; 7; 8; 9; 10; 12; 14; 16; 18; 20; 24; 28; 32; 36; infinite (= no filtering)] ÷ 1.50 ÷ 12 cycles per mm.

Thus, the highest frequency cut-off was 36 ÷ 1.50 ÷ 12 = 2.00 cycle/mm (cycle length = 0.50 mm). We selected the frequency cut-offs as the integer multiples of the lowest frequency obtained by FFT, in order to apply point-pass filtering effectively.

In the second stage of data pre-processing, we applied spatial binning: we simulated larger fMRI voxels of several sizes, including the size of the homologous voxel. MRI samples the data in the k-space frequency domain. Therefore, mimicking larger voxels acquired at a coarser resolution cannot be done by simply averaging neighbouring voxels in the image domain. One can simulate the coarser voxel sampling in two different ways: 1) by convolving the original voxels with a cardinal sinusoidal kernel (= sinc function) in the image space, followed by point sampling with an interval equal to twice the sinc function's standard deviation; or 2) by first applying an ideal low-pass filter in the Fourier domain with a certain cut-off frequency, followed by point sampling in the image domain with an interval equal to half the length of the inverse of the low-pass filter's cut-off frequency. In this work, we applied the second approach with bin sizes that were fractional to the homologous voxel size (Fig. 3-4B): [0 (= no binning); 1/6; 3/16; 1/4; 1/3; 3/8; 1/2; 2/3; 3/4; 6/7; 1] × 1.50 mm.

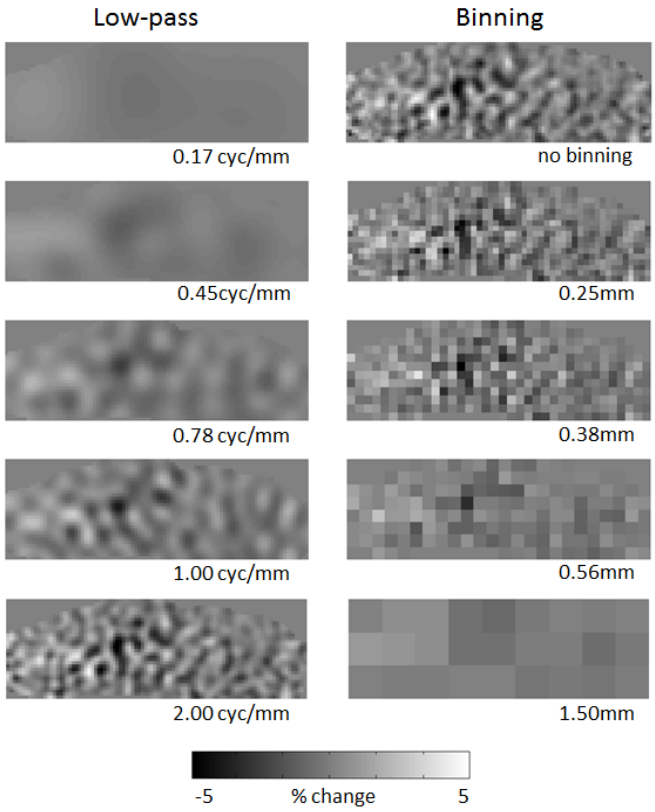

Figure 3-4. Spatial manipulation of orientation maps.
A) Examples of 2D ideal FFT low-pass filtering at several cut-off frequencies. **B)** Examples of fMRI-like voxel sampling at various binning sizes, applied to non-filtered fMRI data.

Data analysis: differential contrast and decoding measures

Following the pre-processing, we evaluated the information conveyed by the response map about the orientation of the stimulus. To this end, we first computed the differential contrast, noise, and CNR as described above. We then summarized the CNR level across voxels within the ROI by computing the mean CNR across the entire map. Since the CNR determines success rate with linear decoders (Chaimow et al., 2011), the quantification of the CNR allows us to compare the information provided by maps obtained by the various filtering and voxel-sampling parameters towards decoding (Fig. 3-5).

In addition, we used linear SVM for decoding analysis (Weston and Watkins, 1998; Misaki et al., 2010). Three SVM decoding analyses were pursued: using 4 pairs of 2 orientations, 2 groups of 4 orientations, and one 8 orientations decoding (Fig. 3-6). Because the number of voxels used as input can influence the overall accuracy (Chaimow et al., 2011), we randomly sampled 21 voxels within the ROI, and used 21 of them as the input feature for the SVM decoding learning stage. This number was chosen because the minimal number of the largest (i.e. homologous) voxels available when considering all 5 datasets was 21 (Table 3-III). To evaluate orientation decoding performance, we performed leave-one-trial-out cross-validation. We used this procedure in order to avoid using the same samples for both training and testing (Kamitani and Tong, 2005). The general decoding procedure was as follows:

1. Choose a binning size
2. Randomly sample 21 voxels
3. Choose a frequency cut-off
4. Perform decoding with leave-one-trial-out cross-validation
5. Obtain one mean decoding accuracy from all the 10 validation datasets
6. Repeat steps 3-5 for each of the defined frequency cut-offs
7. Repeat steps 2-6 ten times (i.e. randomly sample a different set of 21 voxels in each iteration)
8. Do the whole process (steps 1-7) for each of the defined binning sizes

The statistical significance of the overall decoding rate against chance level, and across spatial manipulations, was computed with a two-tailed Student's t-test with false-discovery-rate (FDR) correction (Benjamini and Hochberg, 1995). The total number of samples was 50 (n = 5 animals × 10 repetitions, where 10 repetitions was obtained from Step 7 above).

Results

Main frequency of orientation maps

To determine the main frequency of the organization, the CNR map, obtained by dividing the absolute mean of the differential contrast map within the ROI by its standard deviation (Figure 3-3A), was subjected to a 2D FFT. The image was zero-padded to a size of 25 mm so that the frequency resolution was 0.04 cycle/mm in the FFT domain. For each of the 20 CNR maps obtained from the 5 animals and 4 stimuli-pairs, we applied point-pass filtering at various center frequencies in the FFT domain. The filtered FFT was transformed back to the image domain and the CNR was obtained at each center frequency (Fig 3-3C shows two examples from 2 different animals). We then fitted a Gaussian distribution to the data within the 0.52 to 2.40 cycle/mm segment (Fig. 3-3C). The mean frequency computed over all peaks of the fitted Gaussians from 19 differential maps was 0.99 ± 0.05 cycle/mm (Table 3-I; Fig. 3-3D, red arrow; n = 19; 4 differential contrast maps per animal × 5 animals, 1 outlier; see Table 3-II for the mean FWHM of the fitted Gaussians). Hence, the voxel size homologous to that used in human studies of orientation decoding was 1.5 × 1 ÷ 0.99 cycle/mm = 1.50 mm. The highest frequency that can be captured by such a voxel is 0.333 cycle/mm (Fig 3-3D).

Table 3-I. Center of the Gaussian fit on the CNR as a function of point-pass cutoff frequencies

Center of fit (mm)	Animal A	Animal B	Animal C	Animal D	Animal E
Orientation-pair 1	0.973	1.027	1.035	0.970	0.964
Orientation-pair 2	1.008	0.973	1.100	1.044	0.913
Orientation-pair 3	0.923	0.946	0.986	0.958	0.806*
Orientation-pair 4	1.006	0.952	1.095	0.951	1.027

The average of the centers is 0.99(0.05) cycle/mm, n = 19, outlier (denoted by *) was not taken into account.

Table 3-II. FWHM of the Gaussian fit on the CNR as a function of point-pass cutoff frequencies

FWHM (mm)	Animal A	Animal B	Animal C	Animal D	Animal E
Orientation-pair 1	1.013*	0.448	0.848	0.369	-0.434*
Orientation-pair 2	0.554	0.658	0.473	0.445	0.385
Orientation-pair 3	0.667	0.623	0.780	0.561	1.340*
Orientation-pair 4	0.709	0.469	0.658	0.541	0.486

The average of the FWHM is 0.57(0.14) cycle/mm, n = 17, outlier (denoted by *) was not taken into account.

From the peak towards lower frequencies, the average CNR monotonously decreased until it reached a minimum at 0.36 cycle/mm (Fig. 3-3D, green arrow). From this minimum towards lower frequencies, the CNR increased. We here define "irregularities" as the band of frequencies such that 0.36 < irregularities < 1.0 cycle/mm (Fig. 3-3D, magenta rectangle). We will use the term "low-frequencies" to describe the band of frequencies such that low-frequencies < 0.36 cycle/mm (Fig. 3-3D, gray rectangle).

CNR as a function of spatial filtering and binning

Figure 3-5 presents the results of evaluating the CNR available for decoding orientation following low-pass or point-pass filtering and binning. The white dotted lines represent the main orientation cycle (0.99 cycle/mm) and the largest voxel size (0.50 mm) that, based on the sampling theorem, effectively captures such a frequency. The white dashed lines represent the homologous voxel size (1.50 mm) that is comparable to voxels used in human studies of orientation decoding, and the highest frequency that can be captured by this voxel size (0.333 cycle/mm).

Following low-pass filtering, the CNR matrix showed a rectangular plateau region (between cut-off frequencies of 1.0-2.0 cycle/mm and bin size < 0.5 mm) of relatively high CNR values (Fig. 3-5 left; CNR > 0.44). We observed the highest CNR (0.48) along the 1.33 cycle/mm frequency cut-off, with no binning. Although the CNR at the homologous voxel size was relatively low, it was significantly higher than the CNR obtained using the mean response (CNR with cut-off of 0.056, 0.111, 0.167, 0.222, 0.278, and 0.333 cycle/mm > CNR with cut-off of 0 cycle/mm; $p < 0.001$, two-tailed t-test). Of note, the CNR obtained with the homologous voxel size and cut-off frequencies higher than 0.36 cycle/mm (that is, the "irregularities" frequency regime) was not different from the CNR obtained with the same voxel size and cut-off frequency of 0.333 cycle/mm.

Following point-pass filtering, a wide peak (cut-off 0.78 – 1.33 cycle/mm) was observed in the CNR, centered near the main frequency of the orientation map (Fig. 3-5 right; CNR > 0.55). This peak was present irrespective of the sampling bin size, as long as the bin size conformed to the sampling theorem relative to the point-pass frequency (regions not shaded in gray). The CNR at the homologous voxel size showed values similar to the CNR obtained using the mean response (CNR with point-pass frequency of 0.056, 0.111, 0.167, and 0.222 cycle/mm ~ CNR with cut-off of 0 cycle/mm $p > 0.05$, two-tailed t-test) and values lower than that of mean responses (0.278 and 0.333 cycle/mm < CNR with cut-off of 0 cycle/mm; $p < 0.05$, two-tailed t-test).

Decoding analysis directly tests the predictability of the orientation stimuli from cortical responses. We used 20 randomly sampled voxels as the input features to the SVM decoder with leave-one-trial-out cross-validation. Statistical tests showed that for both the low-pass and point-pass filtering, and for 2-orientations, 4-orientations, and 8-orientations decoding, only the mean response showed non-statistically significant decoding accuracy compared to chance level ($p > 0.05$ for 0 cycle/mm cut-offs, two-tailed t-test, FDR corrected, $n = 50$; Fig. 3-6). All other combinations of filtering and binning showed higher decoding accuracy compared to chance level ($p < 0.001$, two-tailed t-test, FDR corrected, $n = 50$; entries corresponding to statistically significant decoding accuracy are colored; non-significance is presented in white).

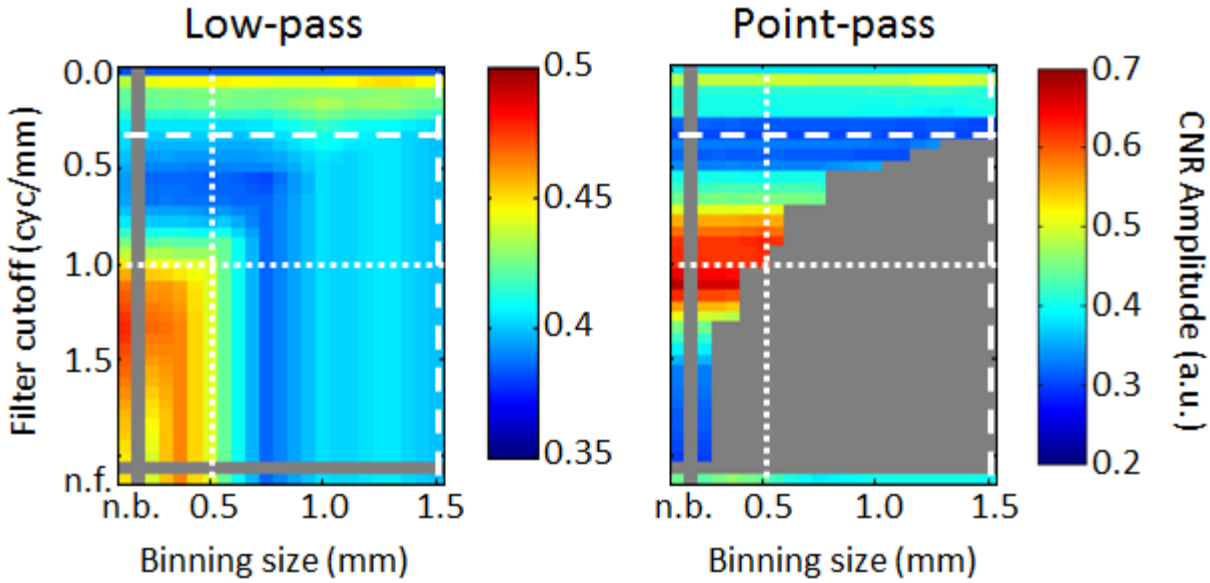

Figure 3-5. CNR as a function of spatial filtering and binning.
A) Mean absolute CNR under low-pass filtering and point-pass filtering as a function of filter cut-off frequency (vertical-axis), and voxel binning size (horizontal-axis; n = 5 animals × 4 orientation pairs). The white dotted lines represent the main orientation cycle (0.99 cycle/mm) and the largest voxel size that can effectively capture this frequency (0.50 mm). The white dashed lines represent the voxel size (1.50 mm) that is comparable to voxels used in human decoding studies (3 mm) and the highest frequency that can be captured by this voxel size (0.333 cycle/mm). The dark gray regions in the matrix showing CNR following point-pass filtering represent parameters for which no information is available because the filtering cut-off is higher than the frequencies that can be captured by the corresponding voxel size. n.b., no binning; n.f., no filtering.

SVM-based decoding following spatial filtering and binning

Following low-pass filtering, the 2-orientations decoding rate was higher than chance level (50%) for all cut-off frequencies (except for mean response) and bin size combinations, including the homologous voxel size (Fig. 3-6 top left). The decoding rate obtained using the mean response only (low-pass with a cut-off of 0 cycle/mm) was in the range of 49-52% for all voxel sizes, and thus not significantly different from chance level ($p > 0.05$; two-tailed t-test; FDR corrected). There was a visible rectangular plateau of higher decoding accuracy, similar to that observed for the CNR. Peak decoding accuracy was obtained at a cut-off frequency of 1.33 cycles/mm, higher than the main frequency of the organization, using a voxel edge of 0.39 mm. The highest value of decoding accuracy within the region enclosed by the horizontal and vertical dotted lines was 78.6%. The decoding accuracy using the homologous voxel size was significantly higher than chance level (e.g. accuracy with cut-off of 0.167 cycle/mm = 68.2%, two-tailed t-test, FDR corrected, $n = 50$, $p < 0.001$, Table 3-III). It was also higher than the decoding accuracy obtained using the mean response (accuracy with a cut-off of 0 cycle/mm: 50.5%). However, the decoding accuracies obtained with the homologous voxel size and cut-off frequencies higher than 0.36 cycle/mm (the frequency regime that underlies irregularities in the organization) were not different from the accuracy obtained with the same voxel size and cut-off frequency of 0.333 cycle/mm. We therefore concluded that the low-frequency regime contributed to successful decoding when sampled with the homologous voxel size, whereas irregularities in the organization did not.

Following point-pass filtering, the 2-orientations decoding showed elevated success rates (80 – 87%) with a peak centered on the main frequency of the orientation map (Fig. 3-6 top right). There was a pronounced decrease at the trough between 0.3-0.4 cycle/mm, where the CNR reaches a minimum (see also Fig. 3-3D). Hence, the inclusion of frequencies around the trough as an input for decoding produces reduced decoding accuracies. The decoding accuracies obtained with the homologous voxel size and point-pass frequencies of 0.333 cycle/mm or lower (except for the mean response) were higher than chance level ($p < 0.01$, two-tailed t-test; FDR; 54.3 – 67.6%, Table 3-IV).

Similar results were obtained for the 4- and 8-orientations decoding, relative to chance levels of 25% and 12.5%, respectively (Fig. 3-6 middle and bottom rows).

Table 3-III. Number of voxels available as the input feature for the SVM decoding

# of voxels	Animal A	Animal B	Animal C	Animal D	Animal E
0.38mm binning	384	352	368	336	336
0.75mm binning	96	88	92	84	84
1.50mm binning	24	22	23	21	21

Table 3-IV. Decoding accuracy using homologous voxel following low-pass or point-pass filtering

Filter cut-off frequency		**0.000**	**0.056**	**0.111**	**0.167**	**0.222**	**0.278**	**0.333**
Filtering	**# stimuli**							
Low-pass	**2-ori**	51.8	64.1	65.3	67.8	68.2	67.6	67.3
	4-ori	25.0	36.5	36.5	40.4	44.5	43.2	42.3
	8-ori	12.1	21.4	20.1	23.4	26.0	24.9	23.7
Point-pass	**2-ori**	51.8	64.1	67.6	66.6	63.9	55.7	54.3
	4-ori	24.9	37.3	37.8	42.9	39.9	33.4	29.8
	8-ori	12.1	21.5	22.0	25.3	24.0	20.2	17.9

Success rate of decoding (in %) using the homologous voxel following low-pass or point-pass filtering. Chance level is 50%, 25% and 12.5% for 2, 4, and 8 orientation gratings, respectively.

Figure 3-6. Decoding as a function of spatial filtering and binning. (See next page for figure) We present here 2-, 4- and 8-orientations decoding accuracy under low-pass filtering, and under point-pass filtering. The white dotted lines represent the main orientation cycle (0.99 cycle/mm) and the largest voxel size that can effectively capture this frequency (0.50 mm). The white dashed lines represent the voxel size (1.50 mm) that is comparable to voxels used in human studies (3 mm) and the highest frequency that can be captured by this voxel size (0.333 cycle/mm). The dark gray regions in the matrix showing decoding accuracy following point-pass filtering represent parameters for which no information is available because the filtering cut-off is higher than the frequencies that can be captured by the corresponding voxel size. The 0 cycle/mm (mean response) level showed decoding success rates no different than chance level (presented in white; $p > 0.05$, two-tail t-test, FDR corrected, $n = 50$).

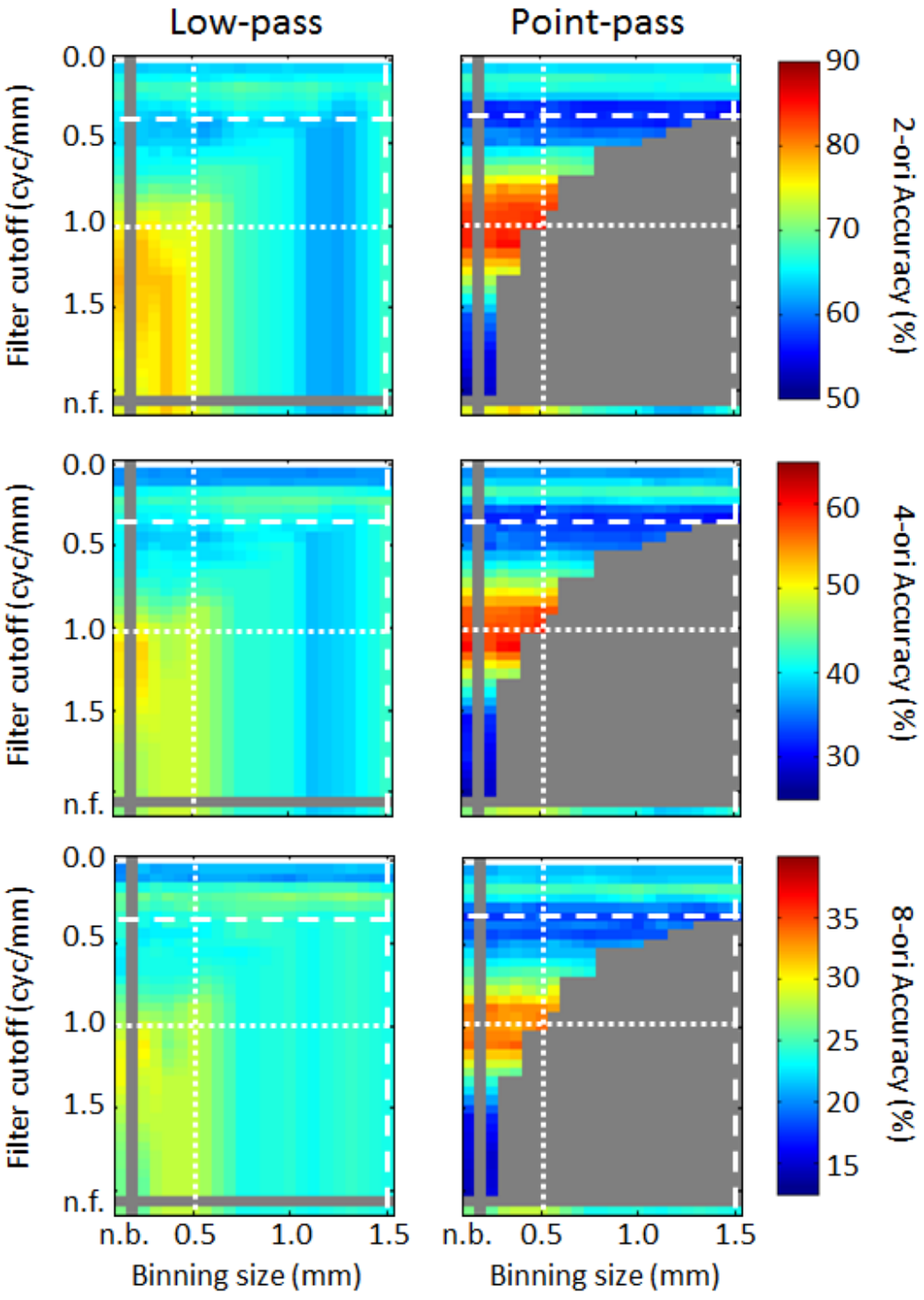

Figure 3-6. Decoding as a function of spatial filtering and binning. (See previous page for legend)

Voxels homologous to those used in human studies at a resolution higher than 3×3×3 mm^3

In the previous section we observed the general pattern of decoding performance as a function of binning size and filtering cut-off. In their prior studies, Kamitani and Tong (2005) and Haynes and Rees (2005) used 3×3×3 mm^3 voxels. However, more recent decoding studies of human subjects sample voxels at a higher resolution (1.0×1.0×1.0 mm3, Swisher et al., 2010; 1.5×1.5×1.5 mm3, Mannion et al., 2010; 2.0×2.0×2.0 mm^3, Alink et al., 2013; Freeman et al., 2013). To match our results to those presented by these studies, we need to reanalyze our data while considering new homologous voxel sizes.

Figure 3-7 presents decoding success rate as a function of filtering cut-off while considering different sizes of homologous voxels. Similarly to previous results, within the frequency range that can be captured by a homologous voxel, the voxel's size does not substantially influence the general shape of the curve for decoding rate as a function of filter cut-off. This is true following both low-pass and point-pass filtering. Under low-pass, the decoding rate remains unchanged beyond a certain frequency that depends on the size of the homologous voxel. Under point-pass filtering, the voxels cannot capture frequencies higher than their Nyquist sampling frequency. Homologous voxel sizes that can capture information from the irregularity regime include 0.25, 0.50, and 0.75 mm in cat area 17, corresponding to 0.5, 1.0, and 1.5 mm in human area V1.

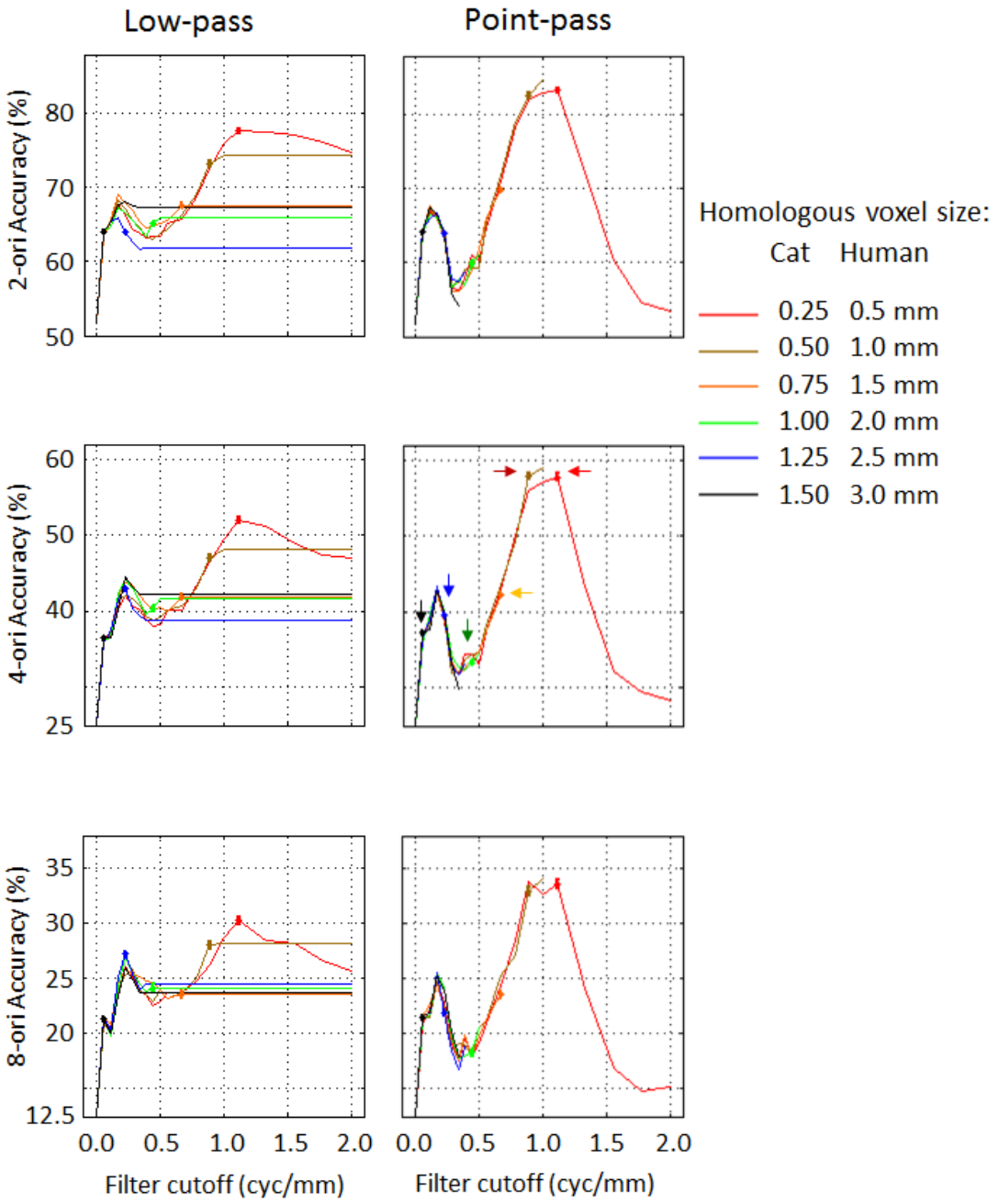

Figure 3-7. Decoding using homologous voxel sizes different from that for 3×3×3 mm^3. Decoding accuracy of 2-, 4-, and 8-orientations following low-pass filtering and point-pass filtering with different hypothetical homologous voxel sizes. The plotted curves are 1D presentations of data extracted from Fig. 3-6. The black curve here presents the data for the homologous voxel size considered throughout the previous sections and figure, also designated by the vertical dashed line in Fig. 3-6. The error bars, one per voxel size and indicated by the arrows in the middle-left panel, show the SEM (n = 50). Following low-pass, the decoding rate remains unchanged beyond a certain frequency that depends on the size of the voxel. Following point-pass, the voxels cannot capture frequencies higher than their Nyquist sampling frequency.

Discussion

Summary of the results

The main frequency of the organization in cat area 17 is 0.99 ± 0.05 cycle/mm (Table 3-I; Fig. 3-3D). The voxel size homologous to that used in human studies of orientation decoding is 1.50 mm, making it possible to capture frequencies of 0.333 cycle/mm or lower. Two bands of cortical frequencies showed elevated selective response to oriented gratings, one around the main frequency of the organization, and the other at frequencies lower than 0.36 cycle/mm. Following low-pass filtering, the CNR (Fig. 3-5) and successful decoding rate (Fig. 3-6) obtained with the homologous voxels and cut-off frequencies higher than 0.36 cycle/mm were not different from those obtained with the same voxel size and cut-off frequency of 0.333 cycle/mm. Following point-pass filtering, the decoding accuracies obtained with the homologous voxel size and point-pass frequencies of 0.333 cycle/mm or lower were higher than chance level (Fig. 3-6). Homologous voxel sizes that can capture information from the irregularity regime include 0.25, 0.50, and 0.75 mm in cat area 17, corresponding to 0.5, 1.0, and 1.5 mm in human area V1.

Decoding of orientation based on MION CBV with no contribution from large blood vessels

One of the mechanisms proposed to underlie the decoding of information in fine structures by relatively large voxels is the contribution of macroscopic blood vessels. The idea is that draining regions that cover cortical maps and columns non-homogeneously may cause selective responses of their corresponding blood vessels (Kamitani and Tong, 2005; Gardner et al., 2006; Kamitani and Tong, 2006; Kriegeskorte and Bandettini, 2007; Gardner, 2010; Shmuel et al., 2010; Thompson et al., 2011). By employing MION-based CBV-fMRI, we can rule out any contribution of macroscopic vessels to our data. Macroscopic vessels contain a high density of MION, which causes much faster dephasing and a significantly shorter T2* than those in gray matter regions. If a voxel lies entirely within a blood vessel, it shows virtually no functional signal and therefore no signal change in response to stimuli. Our study was performed using high-resolution fMRI (in-plane voxel size of ~156 μm), thus any large blood vessel appears as a drop in the MRI signal (Fig. 3-2A) and shows no change in fMRI signal across stimuli. Because of these reasons, the results we demonstrate here arise from contributions other than those of macroscopic blood vessels.

Yet another mechanism proposed to account for the decoding of fine-scale organizations is vasculature-based complex spatiotemporal filtering of neuronal activity (Kriegeskorte et al., 2010). In part, this concept proposes that information on fine-scale functional organizations transforms into signals in larger vessels that can be captured by large voxels. However, MION CBV reflects responses from tissue, arterioles, and venules, all belonging to fine-scale vasculature. In addition, the continuous, sequential presentation of grating stimuli with no control period in between effectively sets the blood volume in large vessels to a steady-state level, which likely eliminates any residual information on fine-scale organizations. Therefore, by similar reasoning that we ruled out contributions from macroscopic vessels, the possible contributions of complex spatiotemporal filtering of neuronal activity to our results can also be ruled out to a large extent. Possible mechanisms left to consider include irregularities in columnar organization and low-frequency/large-scale organizations.

Because MION CBV maps the fine-scale organization with high SNR and spatial specificity, it is optimal in terms of spatial specificity of the functional imaging response relative to the site of increased neurophysiological measures (Fukuda et al., 2006). Therefore, we consider that the functional maps that we analyze accurately reflect the underlying neurophysiological responses. In other words, factors such as the BOLD PSF do not play a significant role in shaping our results. Because of this, our present study is close to reflect the question of whether decoding based on voxels homologous to those used in human decoding studies can decode the fine-scale organization of neurophysiological activity, with no confounds of smoothing or contributions from macroscopic blood vessels. Because of the above-mentioned reasons, our study tests whether irregularities of the columnar organization or low spatial frequency responses in maps that reflect the organization of neuronal responses in a more precise manner than BOLD responses do contribute to the decoding of oriented gratings. Therefore, since the contribution of irregularities to decoding is negligible in our MION CBV data, irregularities are even less likely to contribute to decoding based on BOLD-fMRI responses measured with large voxels.

Low spatial frequency responses contribute to decoding orientation using large voxels; local irregularities likely do not

If irregularities in the map do not exist, then the cortical orientation preference map constitutes one single spatial frequency. Therefore, by definition of irregularities, if irregularities exist the columnar organization involves a distribution of frequencies, including frequencies lower

than the main frequency of the organization (Rojer and Schwartz, 1990; Chaimow et al., 2011). Indeed, in Fig. 3-3 we show that the CNR of differential orientation maps shows a peak at 0.99±0.05 cycles/mm and a distribution of frequencies around the peak with an FWHM of 0.56±0.14 cycles/mm. Therefore, with an appropriate voxel size, irregularities in the orientation map within cat area 17 may contribute to decoding. Indeed, using voxels with 0.5 mm edges, Shmuel et al. (2010) demonstrated contributions to the decoding of the stimulated eye in human subjects from frequency components lower than the main frequency of the organization (~0.5 cycle/mm).

However, do irregularities in the organization contribute to orientation decoding using voxels that are 1.5 times larger than the average cycle length of the organization? The critical factor in addressing this question is the width of the distribution of frequencies around the main frequency of the organization. If this distribution is wide enough, low-frequencies that still belong to it can possibly be captured by voxels that are 1.5 times larger than the average cycle length of the organization.

For orientation maps in cat area 17, the curve of mean CNR (Fig. 3-3D) shows a local maximum at 0.99 cycle/mm, which represents the main cycle of the orientation map. Based on considerations including the spatial frequency of human ocular dominance column (ODC) maps (~2 mm/cycle) and the similar cycle length of ODC and orientation maps in macaque V1 (~0.8mm,Bartfeld and Grinvald, 1992), we expect that the main cycle length of human orientation maps is ~2 mm or even shorter (Yacoub et al., 2008). Therefore, the 3×3×3 mm^3 voxels used by Kamitani and Tong (2005) and Haynes and Rees (2005) were 1.5 times larger than the main cycle of the orientation map in humans (3 mm voxels / 2 mm cycle = 1.5). We defined the size of the voxel homologous to that used by Kamitani and Tong (2005) and Haynes and Rees (2005) in human subjects to be 1.5 times larger than the main cycle of the orientation map in our cat area 17 data (1.5×1 mm = 1.5 mm). The largest frequency that can be captured by such a voxel is 0.33 cycle/mm, which is slightly lower than the frequency at the trough (0.36 cycle/mm).

The curve of mean CNR (Fig. 3-3D) also shows a local minimum at 0.36 cycle/mm. It is reasonable to define this trough as the frequency that separates the distribution of frequencies that underlie local irregularities in the organization (frequencies higher than the trough frequency) and lower-frequencies. We consider this trough frequency or a frequency slightly higher to be the lowest frequency belonging to the distribution of frequencies that constitute the local irregularities.

The largest frequency that can be captured by the homologous voxel is 0.33 cycle/mm, which is lower than the frequency at the trough (0.36 cycle/mm). We therefore conclude that local irregularities in the organization do not contribute to the CNR and to successful decoding when sampled using a homologous voxel size.

An argument can be made based on expected continuity of the organization in the frequency space, suggesting that the trough cannot represent an all-or-none change from the irregularity regime to the low-frequency regime. In other words, part of the power of frequencies lower than the trough frequency could belong to the irregularities. To evaluate whether the CNR curve possibly reflects superimposed contributions from local irregularities and from lower frequencies, we fitted the curve with two overlapping Gaussian curves. We show here the combined fit, including a baseline CNR of 0.3 (Fig. 3-8A) and the individual fit with the baseline removed (Fig. 3-8B). The trough of the combined CNR curve corresponds to the intersection between the two individual curves. Similarly, Figure 3-8C shows the combined fit to the average decoding accuracy, including a baseline accuracy of 53%, whereas Figure 3-8D presents the individual fit with the baseline removed. This analysis shows that even if one assumes a model where part of the power in frequencies below the trough frequency is considered as part of an extended irregularities regime, the contribution of the irregularities to low-frequencies is negligible.

We have shown that the CNR curve shows two frequency regimes with elevated power: one associated with the main frequency of the organization and the other at low-frequencies. An argument can theoretically be made that the increased low-frequency power is possibly an artefact of the point-pass FFT filtering performed on the masked region zero-padded to a rectangular region. In other words, rather than observing true low-frequencies of the neuronal organization, introducing the ROI mask into the otherwise homogenous zero-padded rectangle may create these low-frequencies. In order to evaluate such an argument, we computed the autocorrelation involving voxels strictly within the masked ROI, effectively eliminating the concern of employing any zero-padded voxels.

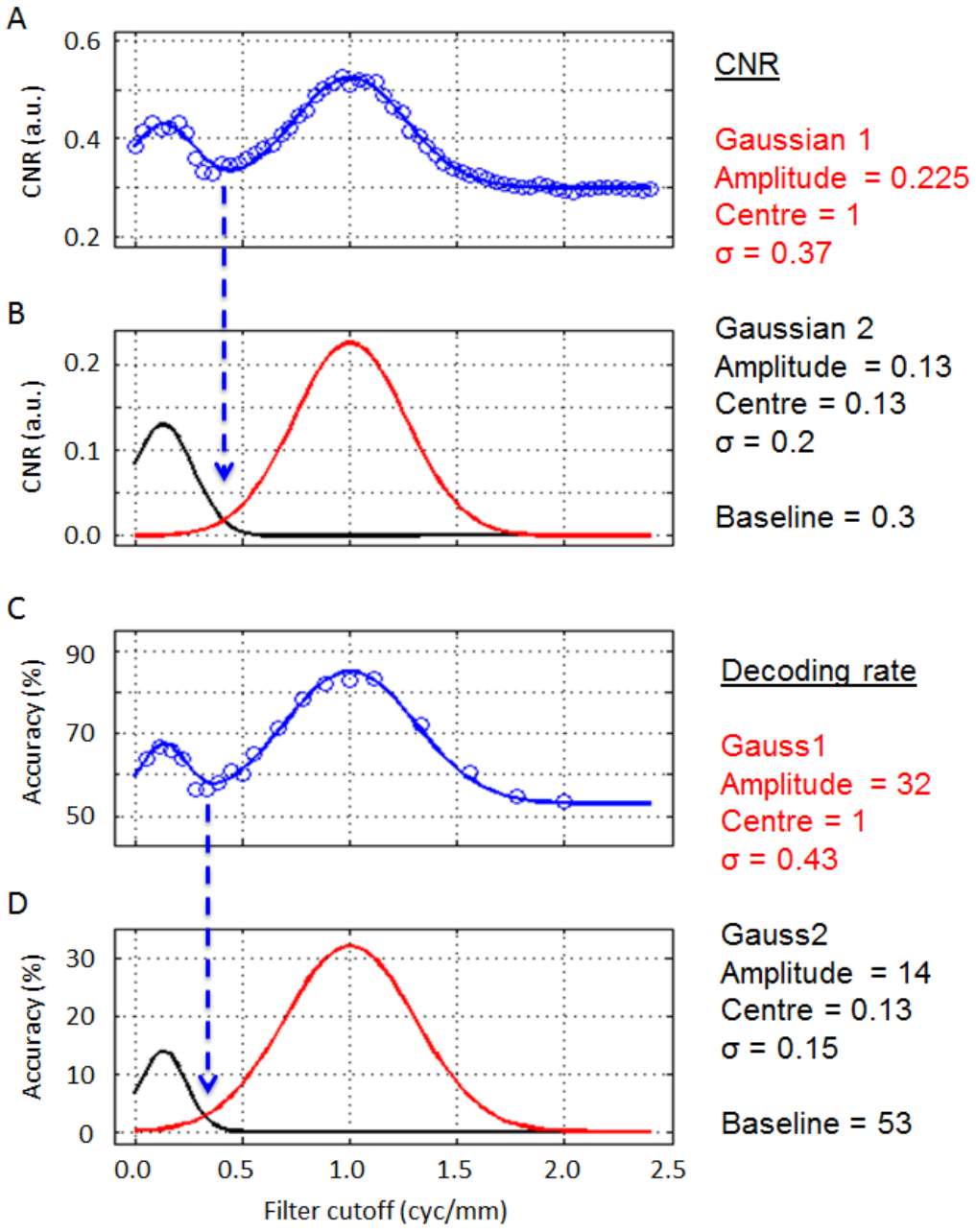

Figure 8. Evaluating the possibility of overlapping regimes of irregularities and low-frequencies.

A) The mean CNR as a function of frequency from Fig. 3-3D was fitted with two Gaussians, one centered on the local irregularity band (amplitude = 0.225, mean = 1.00, sigma = 0.37) and the other centered on the low-frequency regime (amplitude = 0.130, mean = 0.13, sigma = 0.20). **B)** The two Gaussian curves plotted separately. The Gaussian associated with the local irregularities is plotted in red and the one centered on the low-frequency regime is plotted in black. **C)** and **D)** show the mean decoding accuracy for 2 orientations from Fig. 3-6 fitted with two Gaussians similarly to the fit presented in **A)** and **B)**. The Gaussian centered on the local irregularity band has amplitude = 32%, mean = 1.00, and sigma = 0.43. The Gaussian centered on the low-frequency regime has amplitude = 14%, mean = 0.13, and sigma = 0.15.

The auto-correlation of the CNR maps was computed by multiplying the CNR from each pair of voxels within the ROI, and averaging the results in bins as a function of the cortical distance separating the two voxels. In this manner, the 2D autocorrelation collapses into 1D (Fig. 3-9A). We then resampled the 1D auto-correlation from 0 to 14 mm with a step-size of 0.01 mm. Finally, the spectral density was computed by taking the absolute of the Fourier transform of the resampled autocorrelation (Fig. 3-9B). We show here that the regimes of elevated power, one around the main frequency of the organization and the other at low-frequencies, and the trough between them can be observed even with the autocorrelation not involving any zero-padding voxels. We therefore conclude that the increased power at low-frequencies is inherent to the neuronal organization.

Importantly, the low-frequencies could not take on an important role simply because of an artefact of point-pass FFT filtering performed on the masked region zero-padded to a rectangular region. The reason is that the masked region was applied in an identical manner to all orientation maps and conditions, including 2-, 4-, and 8- orientations decoding. All decoding performed on maps that exclusively contained frequencies lower than the trough frequency showed decoding success rates that were higher than chance level. This cannot be explained by the point-pass or the low-pass filtering of the maps masked by the ROI, since the mask was identical for all conditions.

Therefore, the homologous voxel size, which can capture frequencies of 0.33 cycles/mm or lower, can capture frequencies in the low-frequency regime but it is too large to capture any frequency in the irregularities domain. This is indeed reflected in the CNR (Fig. 3-5) and in the successful decoding rate obtained by the homologous voxels (Fig. 3-6). Following point-pass filtering (that is, of information specific to the frequency), the successful decoding rate using the homologous voxel size showed values higher than chance level for the low-frequencies regime (0.333 cycle/mm or lower, except for the mean response). Following low-pass filtering, the decoding accuracy using the homologous voxel size was significantly higher than chance level for all frequency cut-offs, even for frequency cut-off within the low-frequency regime. These findings show that the low-frequency regime carries information about the stimulus orientation. Importantly, both the CNR and the decoding success rates obtained with the homologous voxel size and cut-off frequencies higher than 0.36 cycle/mm (the “irregularities” frequency regime) were not different from those obtained with the same voxel-size and cut-off frequency of 0.333 cycle/mm. These results further support our conclusion that when sampling with the homologous

voxel size, the low-frequency regime contributes to successful decoding, whereas irregularities in the organization do not.

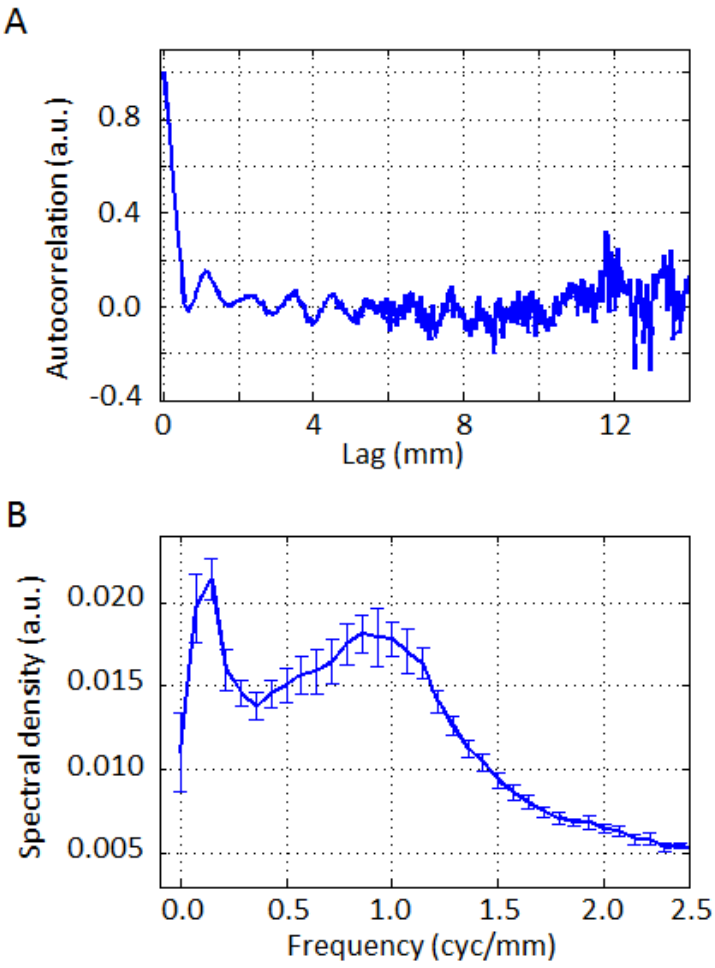

Figure 3-9. Autocorrelation-based spectrum analysis of the ROI.
A) 1D autocorrelation of a 2D CNR map. The 1D autocorrelation of the CNR was computed by multiplying the CNR of each pair of voxels in the ROI, and averaging the results as a function of distance between the 2 voxels. In other words, the x-y voxel shift between each pair of voxels was projected into 1D by taking the absolute distance. **B)** Average of spectral density across 20 CNR maps (5 cats x 4 orientation pairs). The spectral density was computed by averaging the absolute value of the Fourier transform of the 1D autocorrelation obtained from each of the CNR maps. It was smoothed with a moving average kernel of 3 points.

As discussed above, our MION CBV-fMRI measurements reflect the neuronal orientation preference map better than BOLD measurements do (Mandeville et al., 2001; Keilholz et al., 2006; Zhao et al., 2006; Smirnakis et al., 2007; Poplawsky and Kim, 2014). Our MION CBV measurements show no contributions of irregularities in the organization to decoding. Therefore,

by taking into account the fact that BOLD response is expected to be less spatially specific than the MION BOLD-fMRI response, BOLD imaging is even less likely to reflect the direct contributions of irregularities in the fine-scale organization to decoding.

Our conclusion, ruling out contributions from local irregularities in the columnar organization to decoding, is at odds with the conclusion made by Swisher et al. (2010). These authors used high-field, high-resolution (0.3125 mm) BOLD-fMRI and multivariate pattern analysis to determine the spatial scales at which orientation-selective information can be found in cat area 18. Similarly to our results, they used high-resolution data to show a strong orientation signal at the scale of individual columns and reliable orientation bias at spatial scales of several millimeters. They concluded that their results demonstrate a reliable millimeters-scale orientation signal, likely emerging from irregular spatial arrangements of orientation columns and their supporting vasculature. There are several possible reasons that could account for the discrepancy between our conclusions and those made by Swisher et al. (2010) with regard to contributions from local irregularities. Firstly, while we obtained our data from cat area 17, Swisher et al. (2010) obtained theirs from area 18. Area 18 possibly features a broader elevated frequency band around the main frequency of the organization, allowing for the capture of information from frequencies lower than the main frequency of the organization, but higher than the large-scale organization regime. In addition, although Swisher et al. (2010) applied low-pass and high-pass spatial filtering, they used small voxels that could capture the main frequency of the organization. In contrast, we base our conclusion on voxels homologous in size to those used in human decoding studies. In addition, we simulated fMRI k-space sampling, which eliminates contributions from frequencies higher than its Nyquist frequency (half of the inverse of the sampling interval).

Voxels homologous to those used in human studies at a resolution higher than 3×3×3 mm^3

Recent decoding studies employ higher resolution (1.5×1.5×1.5 mm3, Mannion et al., 2010; 1.0×1.0×1.0 mm3, Swisher et al., 2010; 2.0×2.0×2.0 mm^3, Alink et al., 2013; Freeman et al., 2013) than the 3×3×3 mm^3 previously applied by Kamitani and Tong (2005) and Haynes and Rees (2005). Considering the corresponding homologous voxels in our data, we expect that fMRI of human area V1 using voxels no larger than 1.5×1.5×1.5 mm^3 and suppression of signals from macroscopic vessels as is in our data could theoretically capture information from the local irregularities of the orientation map. In practice, the capacity to capture such information also depends on the SNR, subject movement, and various other factors crucial to high-resolution fMRI.

Effect of spatial filtering

Our findings show the effect of spatial filtering on the success rate of orientation decoding. Although low-frequencies indeed contribute to successful decoding, when using voxels small enough to capture the main frequency of the organization, the best performance can be obtained when one isolates the information around that same frequency. Under these conditions, the success rate obtained following point-pass filtering around the main frequency of the organization is higher than the success rate following any low-pass filtering. In addition, decoding following low-pass filtering performs best when the filtering cut-off is at the main cycle of organization, or slightly higher.

Although our conclusions with regard to the contributions of irregularities differ from those made by Swisher et al. (2010), the observations we report here on the effect of spatial filtering are nevertheless consistent with their results. Swisher et al. (2010) used BOLD-fMRI at a sampling resolution sufficiently high for capturing orientation columns in cat area 18. These authors indicate that when using high-resolution imaging, the orientation-selective signal peaks at the frequency of the cortical columns, but includes a coarse-scale, broad-spectrum bias component extending to a millimeters-scale. Furthermore, our results are consistent with their observation that the information available on scales of several millimeters is largely redundant with that present at columnar levels. Hence, acquiring data at a resolution higher than the Nyquist sampling frequency associated with the main frequency of the organization allows for a quantum leap in the success rate of decoding information conveyed by fine-scale organizations.

Conclusions

We previously ruled out aliasing contributions to the decoding of fine-scale organization by large voxels (Chaimow et al., 2011). In addition, we estimated that the contributions from local irregularities in V1 are very small, i.e. insufficient to account for the classification performance reported at 3 T using 3×3×3 mm^3 voxels (Chaimow et al., 2011). Here we rule out contributions from local irregularities in the cortical orientation map of cat area 17. Hypothesized mechanisms that may still contribute to successful decoding using BOLD-fMRI include low-frequency responses (Figures 3-3, 3-5, and 3-6), functionally biased responses of macroscopic blood vessels, and complex spatiotemporal filtering of neurophysiological activity.

Preface to Chapter 4

Chapter 4 is the second of two chapters that address aim 1: 'to unravel the mechanisms underlying hemodynamic response based decoding of oriented gratings using coarse voxel sampling'. In Chapter 3 we used contrast-agent-based CBV-fMRI data that were acquired with continuous stimulation, eliminating possible contributions from both macroscopic vessels and complex spatiotemporal filtering by fMRI voxels. Using this data acquisition paradigm, we demonstrated that in cat area 17, contributions from macroscopic vessels or from complex spatiotemporal filtering are not necessary for decoding orientation. In addition, we demonstrated that low-frequency components of the organization contribute to decoding and irregularities do not. Do these results generalize over functional organizations for preferred orientation? And do macroscopic vessels and complex spatiotemporal filtering contribute to decoding of orientation? In this chapter, we acquired optical imaging responses from cat area 18 to oriented gratings presented in an event related paradigm. We computed relative changes in deoxy- and total-hemoglobin, which are analogous to BOLD- and CBV-fMRI, respectively. This data-acquisition paradigm allows for the evaluation of contributions of irregularities and low-frequency components of the organization, and for contributions from macroscopic blood-vessels. In addition, it allows the evaluation of overlap and redundancies in information obtained from these components. Lastly, it allows testing whether classification based on the spatiotemporal response yields better decoding accuracies than that based on the spatial pattern of the response averaged over time.

Mechanisms underlying decoding the orientation of grating stimuli investigated by optical imaging of cat area 18

Ze Shan Yao, Martin Villeneuve, Pascal Kropf, Javeed Shaikh, Denis Chaimow, Amir Shmuel

McConnel Brain Imaging Centre, Montreal Neurological Institute,

Departments of Neurology, Neurosurgery, Physiology and Biomedical Engineering

McGill University, Montreal, QC, Canada

Correspondence:
Amir Shmuel, Ph.D.
3801 University, room NW109
Montreal, QC, Canada H3A 2B4
E-mail: amir.shmuel@mcgill.ca

Keywords: High-resolution functional MRI, Blood oxygenation level dependent, BOLD, Optical imaging of intrinsic signals, Cortical columns, Orientation columns, Decoding

Acknowledgements: We thank Drs. Doina Precup, Curtis Baker and Robert Kearney for insightful discussions. This work was supported by grants from the Natural Sciences and Engineering Research Council of Canada (NSERC Discovery grants RGPIN 375457-09 and RGPIN-2015-05103) and the Human Frontier Science Program (RGY0080/2008) awarded to AS.

Abstract

Multivariate machine learning algorithms can decode the orientation of grating stimuli from coarsely (3×3×3 mm3) sampled fMRI data. Six alternative mechanisms have been hypothesized as candidates to contribute to decoding of information encoded in fine scale structures: (I) aliasing of high spatial-frequency components of the columnar organization by the large voxels; (II) random local irregularities in the functional organization; (III) very low spatial frequencies reflecting large-scale components of the organization; (IV) orientation selective responses near the retinotopic edge of the orientation stimuli; (V) selective responses of macroscopic blood vessels, and (VI) fMRI voxel complex spatiotemporal sampling that transforms finely organized neuronal activity to more coarsely organized vessel responses. Here we aimed at evaluating contributions from local irregularities and low spatial-frequency responses from gray matter, from macroscopic vessels and from information conveyed by the spatiotemporal evolution of the hemodynamic response. To this end, we computed total- and deoxy-hemoglobin responses to oriented grating stimuli from optical imaging of cat area 18. We defined voxels homologous in size to those used in fMRI-based decoding in humans, by comparing the main frequency of the orientation map in cat area 18 to that in human V1.

The main frequency of the organization in cat area 18 is 0.84 ± 0.05 cycles/mm. In the frequency domain, the responses around this main frequency of the organization decreased gradually towards lower or higher frequencies, creating a wide Gaussian-like distribution. The voxel size homologous to that used in human studies of orientation decoding is 1.80 mm, making it possible to capture frequencies of 0.278 cycles/mm (or lower), which was within the lower-frequency end of the irregularities domain. Large vessel responses using the homologous voxel size showed decoding accuracies higher than chance level but lower compared to those from gray matter regions. The decoding accuracies using combined responses from large vessels and gray matter were comparable to those obtained exclusively from gray matter regions. The decoding accuracies obtained from total-hemoglobin responses were higher than those obtained from deoxy-hemoglobin responses. Lastly, spatiotemporal time-series does not improve decoding accuracy compared to that obtained from the spatial response averaged over time. Our results show that whether irregularities contribute to decoding depends on features of the area-specific columnar organization. They further show that while responses from macroscopic vessels can be orientation selective, their contributions to decoding are redundant.

Introduction

Functional MRI (fMRI) localizes sites showing increased neuronal activity by measuring metabolic and hemodynamic responses. Since fMRI relies on indirect measures of neuronal activity, with relatively poor specificity to the sites of increased neuronal activity, resolving cortical columns using current fMRI techniques is not trivial. However, several studies have shown that it is possible to probe orientation selective signals in human area V1 using blood-oxygenation level dependent (BOLD) fMRI. These studies employed multivariate analyzes, including the use of a supervised classifier to decode the presented stimuli. Indeed, recent studies have demonstrated that multivariate machine learning algorithms can decode visual stimuli from fMRI data (Haxby et al., 2001; Haynes and Rees, 2005; Kamitani and Tong, 2005). Using gradient-echo (GE) BOLD-fMRI at 3 Tesla (T), these studies decoded information thought to be encoded only in fine-scale structures, i.e. orientation columns (Haynes and Rees, 2005; Kamitani and Tong, 2005). This result is surprising given the large size of the voxels ($3\times3\times3$ mm^3) relative to the expected mean cycle length of the orientation map in human area V1 (~2 mm; see methods section). This result is even more surprising considering the relatively wide point-spread function (PSF) of GE BOLD-fMRI signals at 3T (~3.5 mm, Engel et al., 1997; Parkes et al., 2005) and even that estimated at 7T (~2 mm, Shmuel et al., 2007). The mechanism by which low-resolution imaging decodes information represented at a fine scale relative to the voxel size is unclear. Here we aim to determine the mechanisms that can potentially contribute to decoding oriented grating stimuli based on invasive optical imaging of intrinsic signals in cat area 18.

Six alternative mechanisms have been hypothesized as candidates to contribute to decoding of information encoded in fine scale structures. The first suggested hypothesis posited that aliasing of high spatial-frequency components of the columnar organization by the large voxels gives rise to a decoding rate higher than chance level (Boynton, 2005). This hypothesized "aliasing" mechanism, also termed the "hyperacuity" mechanism (Op de Beeck, 2010) involves components of the columnar organization with frequencies higher than the Nyquist frequency, which were thought to contribute to the sampled voxels. However, we have ruled out this hypothesized mechanism (Chaimow et al., 2011), based on the fact that fMRI samples data in the frequency space, with the highest frequency in the k-space being the highest frequency available to the sampling process. Therefore, there are five remaining hypothesized mechanisms. (I) It was hypothesized that random local variations and irregularities in the functional organization

contribute to decoding (Kamitani and Tong, 2005; Haynes and Rees, 2006; Kriegeskorte and Bandettini, 2007; Swisher et al., 2010) The argument is that due to irregularities in columnar patterns, each voxel overlaps columns with different preferences unequally, resulting in biases towards specific preferences. (II) Very low spatial frequencies reflecting large-scale components of the organization were proposed to play a role as well (Op de Beeck, 2010; Freeman et al., 2011; Freeman et al., 2013; Wang et al., 2014). These include the oblique effect (Furmanski and Engel, 2000; Sun et al., 2013) and the radial bias effect (Sasaki et al., 2006; Clifford et al., 2009; Mannion et al., 2010; Freeman et al., 2011; Freeman et al., 2013; Sun et al., 2013) associated with the representation of orientation. For decoding the stimulated eye, a relevant large scale organization is formed by the higher amplitude response to stimulation of the contra-lateral eye (Tychsen and Burkhalter, 1997). (III) An alternative mechanism to the large-scale organization (item II above) has been recently proposed. Observations made by Carlson (2014) suggest that the edges of oriented grating stimuli elicit responses that are orientation specific. Similarly, Wang et al. (2014) identified a direction-selective response bias in human visual cortex that predicted motion-decoding accuracy. This direction selective responses depended on the shape of the stimulus aperture rather than the absolute direction of motion. The response amplitudes gradually decreased with distance from the stimulus aperture edge corresponding to motion origin in V1, V2, V3, thus explaining the higher motion-decoding accuracies reported previously in early visual cortex.

Alternatively (IV), veins draining regions that cover cortical maps and columns non-homogeneously may cause selective responses of their corresponding blood vessels (Kamitani and Tong, 2005; Gardner et al., 2006; Kamitani and Tong, 2006; Kriegeskorte and Bandettini, 2007; Gardner, 2010; Shmuel et al., 2010; Thompson et al., 2011). In this scenario, selective signals from macroscopic blood vessels can be captured by large voxels; therefore, they can contribute to the decoding of stimuli encoded at the resolution of cortical columns. Evidence in support of this phenomenon was provided by (Gardner et al., 2006; Shmuel et al., 2010; Thompson et al., 2011). Lastly (V), Kriegeskorte et al. (2010) introduced a model in which fMRI voxels sample neuronal activity as complex spatiotemporal filters. Each voxel samples the neuronal activity pattern in its vicinity through a unique fine-grained structure of venous vessels that underlie its blood oxygen level-dependent signal. Temporal properties of the hemodynamics (e.g., the speed of the blood in the capillary bed) can shape spatial properties of a voxel's filter (e.g., how finely structured it is). A voxel, together with its signal-supplying vasculature, may best be thought of as a complex

spatiotemporal filter. Such a filter may have greater sensitivity to high spatial frequencies than the compact kernels, i.e. Gaussian or averaging-box kernels typically used to characterize voxel sampling (both of which would act like anti-aliasing filters that minimize such sensitivity). Kriegeskorte et al. (2010) described how such a model can account for representation of high-frequency components of the cortical maps by the sampled voxels and for decoding of information conveyed by fine structures.

In the current study, we aim to test whether contributions from mechanisms I, II and IV above, namely local irregularities in the organization, low frequencies and/or macroscopic blood vessels contribute to successful decoding. Using BOLD-fMRI, it is not trivial to assess contributions from these proposed mechanisms because cortical fMRI responses are likely the combined contributions of these intertwined mechanisms. Therefore, in order to be able to evaluate these 3 proposed mechanisms together, we imaged cat area 18 using optical imaging of intrinsic signals. This method allows for high-resolution imaging of orientation modules at high SNR (Bonhoeffer and Grinvald, 1993b; Shmuel and Grinvald, 2000). Moreover, it makes it possible to quantify spectrally decomposed deoxy-hemoglobin (HbR) and total-hemoglobin (HbT) responses, which physiologically correspond to BOLD- and cerebral-blood volume (CBV) fMRI, respectively.

Although pial blood vessels do carry information about the presented stimuli, this information is small relative to that conveyed by the gray matter regions. In contrast to our previous results obtained from cat area 17, irregularities in the fine-scale organization of orientation maps in cat area 18 can potentially contribute to decoding of oriented gratings. We conclude that whether irregularities in the fine scale organization contribute to decoding depends on the area-specific features of the orientation map.

Materials and Methods

A detailed description of the animals, anesthesia, data acquisition, selection of frames for averaging the response over time, and spectral decomposition of absorption obtained from multiple wavelength into hemoglobin species can be found in (Chapter 5). Here we analyze the mechanisms underlying decoding the orientation of grating stimuli using HbT and HbR responses, that reflect CBV-fMRI and BOLD-fMRI, respectively. The analysis of HbT responses allows us to relate the current study to a previous study we pursued with MION-based fMRI of CBV (Chapter 3).

Data pre-processing

We sought to determine whether contributions from local irregularities in the organization, low frequencies and/or macroscopic blood vessels contribute to successful decoding of orientation stimuli. To this end, we quantified decoding success rate with different subsets of inputs that represent different isolated contributions. The cortical response maps underwent spatial manipulations in order to isolate the intertwined contributions from gray matter regions and blood vessels. For each of these two compartments, we analyzed contributions as a function of cortical spatial frequency.

Delineation of the ROI

Fig. 4-1A shows the cortical image obtained under illumination wavelength of 530 nm from one hemisphere. We used two maps to delineate a cortical region in area 18 as the ROI for further analysis. These included the average HbT differential response to one pair of orthogonal orientation stimuli (Fig. 4-1B) and the pixels that responded significantly to at least one of the 8 orientation stimuli (two-tail t-test, $p < 0.05$, n=30-40 trial). We then delineated the responding region manually, such that it encompassed the main spatial segments that responded to orientation stimuli (green dashed curve in Fig. 4-1C).

Cortical map manipulation

Within the defined ROI, we first split the cortical image into 3 components: pixels that corresponded to gray matter (GM), pixels that corresponded to large veins with diameter ≥0.15mm (LV), and pixels that belonged to the union of these two classes, i.e. pixels that corresponded to one of these regions (GM&LV). For HbR analysis, we excluded the visible small veins (with diameter smaller than 0.15 mm) from further analysis, in order to clearly differentiate between contributions from gray matter and macroscopic veins. We also excluded contributions from all arteries as they show minimal changes in HbR content and BOLD fMRI signal. For HbT analysis, we kept the same exclusions, in order to compare the 2 types of measurements, HbR and HbT, based on contributions from the exact same tissue. To this end, we first segmented the pial blood vessel regions and determined their respective diameters (Chapter 5). To allow for an artifact-free spatial filtering of only one modality, e.g. GM, we filled the masked regions by means of a smoothing algorithm (Garcia, 2010). We present the process for obtaining the filled in map for GM in Fig. 4-1 D to G. Panel D presents the segmented pial vessels, and panel E demonstrates the

classification of these vessels to arteries (red) and veins (blue). Panel F presents an overlay of classified blood vessels superimposed onto the differential orientation map presented in B. Finally, panel G presents the same map, following the masking out and the filling-in of all blood vessel regions by the smoothing algorithm. This effectively represents the GM filled-in map.

Note that to obtain the filled in map for GM, we filled in the regions belonging to all vessels. To obtain the filled in map for LV, we filled in the regions belonging to GM, all arteries and small veins. To obtain the filled in map for GM&LV, we filled in the regions belonging to all arteries and small veins. Any singularities of the orientation map, such as the pinwheels and fractures were included in the analysis, since they contribute to the irregular organization.

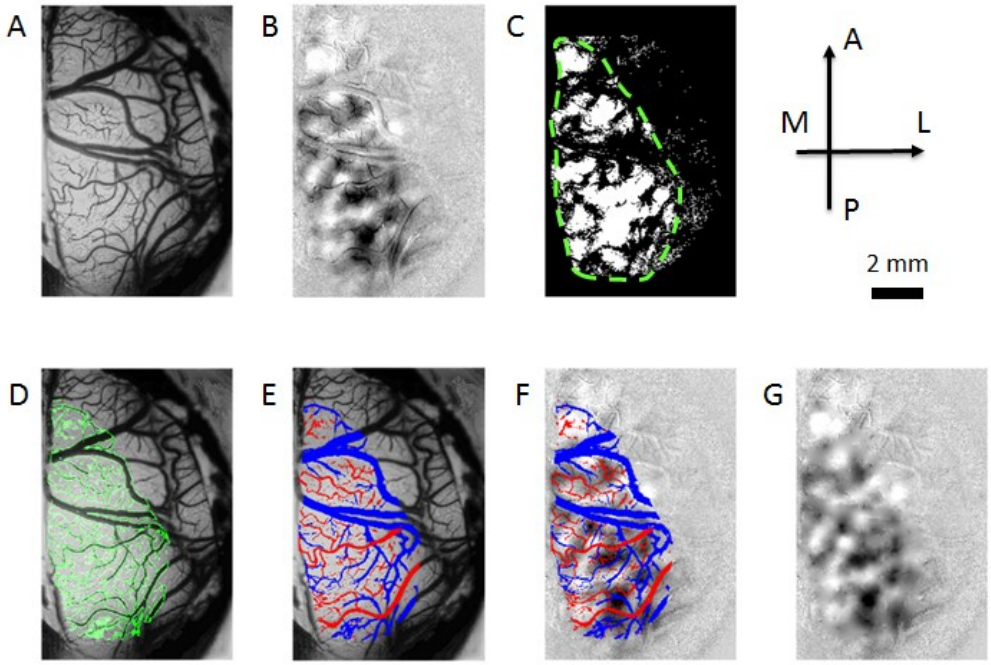

Figure 4-1. Filling in interpolated differential values in spaces occupied by pial blood vessels. **A)** Raw image acquired under illumination of the green LED (530 nm) and used for creating the blood vessel mask. **B)** Differential cortical response to two orthogonal orientation stimuli. **C)** Pixels on cortex that showed statistically significant response to at least one of the orientation stimuli, and the manually delineated ROI that encircled the responding region (green dashed line). **D)** Mask of edges of blood vessels obtained by applying the classification algorithm on the image acquired under green illumination, which is presented in the background (same image as in A). **E)** The blood vessels were further separated into arteries (in red) and veins (in blue) based on their response under green (530 nm) and orange (617 nm) illumination. Under orange illumination, HbR is washed out of veins upon cortical activation (this is the hyper-oxygenated BOLD response); hence, veins appear brighter relative to baseline, whereas arteries remain dark. **F)** Differential orientation map, with the pial vessels masked out. **G)** The missing values in spaces occupied by vessels were filled in according to the algorithm suggested by (Garcia, 2010).

Spectrum of orientation maps, and voxels homologous to those used in human decoding studies

To obtain the spectrum of orientation maps and the voxel size homologous to that used in previous decoding studies in humans, we employed methods similar to those described in (Chapter 3). We computed the differential contrast to two orthogonal orientations, the corresponding noise and contrast-to-noise ratio, CNR (Fig. 4-2A). We defined the voxel-by-voxel differential contrast of one map as the difference in cortical responses to the two orthogonal stimuli. We defined the noise as the standard deviation of differential contrast across trials. We defined the voxel-by-voxel CNR for the map as the ratio of absolute differential contrast to noise.

In order to determine the main cycle length of the orientation map, we computed the mean CNR of the GM filled-in map as a function of spatial cortical frequency. We first computed the 2D fast Fourier transform (FFT) spectrum for each of the normalized response maps in the 4-dimensional normalized data matrix (see previous Chapter). The filtering was performed on the response maps limited within the delineated ROI and zero-padded to have a rectangular output of 20×20 mm. We then masked the FFT for point-pass filtering at center frequencies from 0.05 to 2.40 cycles/mm, with a step size of 0.05 cycles/mm. The masked FFT was transformed back to image space. We then computed the differential contrast map, noise map, and CNR map for each pair of orthogonal orientation stimuli from each animal (Fig. 4-2B presents an example for point-pass filtering with 0.833 cycles/mm). Finally, a mean of absolute CNR was calculated spatially across the CNR map, as a function of center frequency.

Next, in order to determine the peak frequency of the organization separately for each map, we fitted a Gaussian curve to the data points between 0.50 and 2.40 cycles/mm. Fig. 4-2C presents two examples obtained from 2 different animals. Finally, we determined the main frequency of the orientation map as the center of the Gaussian curve. We performed this process separately for each map obtained from a pair of orthogonal orientations for each animal. The average peak was at 0.84 ± 0.06 cycles/mm (Fig. 4-2D; n = 18; 4 differential contrast maps per animal, 5 animals, 2 outliers). As explained in our previous work (Chapter 3), the ratio between the voxel edge used by Kamitani and Tong (2005) and Haynes and Rees (2005) and the cycle of orientation maps in human subjects is ~1.5. We defined the voxel size in cat area 18 which we consider homologous to those used in human decoding studies as 1.5 times the average length of the orientation cycle, i.e. 1.5 × (1 ÷ 0.84 cycles/mm) ≈ 1.80 mm (rounded up from 1.7857 mm). Since the standard deviation of the peak

orientation cycle across animals was small (0.06 cycles/mm), we applied one standard homologous voxel of size of 1.80 mm across all datasets.

Voxel positioning, filtering and binning

Lastly, we placed a rectangular ROI using a group of these large homologous voxels, after determining their loci such that there was a maximal overlap between the homologous voxels matrix and the previously defined ROI (Fig. 4-1C). The orange dots within the homologous voxels matrix in Fig. 4-3A highlight those voxels whose spatial overlap with the ROI was ≥ 75%. These voxels defined the area used for the analysis, including the input to the Support Vector Machine (SVM) decoding.

Following the determination of the homologous voxel size (1.80 mm), we pre-processed the normalized data in two stages: filtering and binning (Chapter 3). We zero-padded the ROI, transforming it into a square with each side equal to 6-homologous-voxel edges (6 × 1.80 mm = 10.8 mm). The lowest frequency obtainable, and the step size (frequency resolution in the FFT), was then: 1 ÷ 10.8 = 0.093 cycles/mm. We then filtered the data using an ideal spatial 2D FFT low-pass or point-pass filter (point-pass: 1 frequency passing band-pass) with the following frequency cut-offs:

[0 (=mean response); 1; 2; 3; 4; 6; 9; 12; 15; 18; 24; 30; 36; 48] ÷ 1.80 ÷ 6 cycle per mm. Note that here we define filtering with 0 frequency as the mean response over the ROI, which represents the global bias towards one orientation or the other.

Fig. 4-3B presents an example of low-pass filtered differential map, with cut-off frequency 0.833 cycles/mm.

In the second stage of data pre-processing, we applied spatial binning: we simulated larger fMRI voxels of several sizes, including the size of the homologous voxel:

[1/16; 1/12; 1/8; 1/6; 1/4; 1/3; 1/2; 1] × 1.80 mm.

Fig. 4-3C presents an example of spatial binning with the side of each bin equal to half of the homologous bin size, following the filtering presented in Fig. 4-3B.

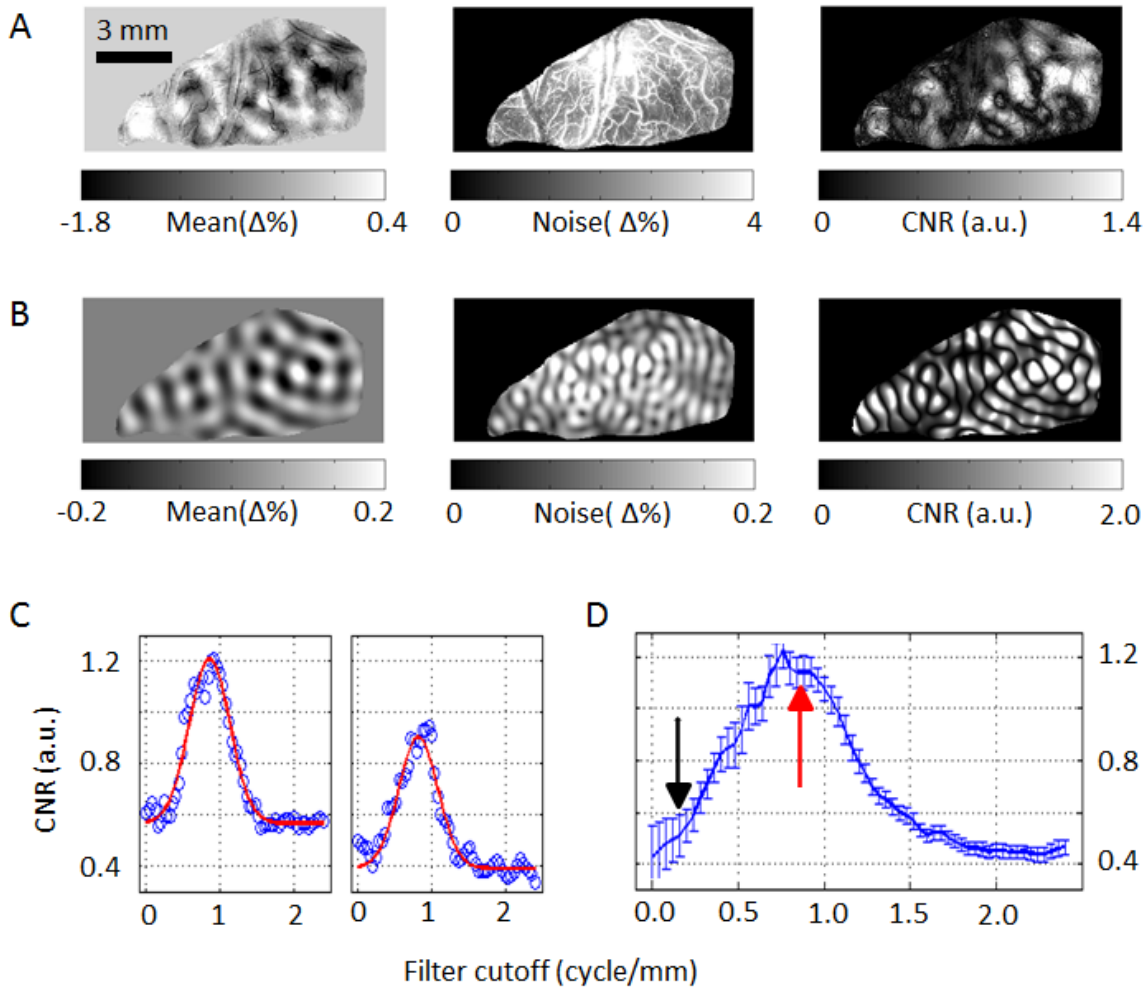

Figure 4-2. Main frequency of the orientation map.
A) Differential orientation map, Noise map, and CNR map within the ROI. **B)** Differential orientation map, Noise map, and CNR map obtained following point-pass filtering of the response maps with center frequency of 0.83 cycles/mm. Prior to filtering, zero-padding completed the image to a 20×20 mm region in order to have a square output. **C)** Two examples from 2 different animals of the CNR as a function of point-pass frequencies. A Gaussian curve was fitted to the segment between 0.5 and 2.40 cycles/mm. **D)** The mean and standard error of the mean (SEM) of the raw CNR values. The average cycle length computed over all 4 pairs of orthogonal orientations and 5 animals (N = 18, 2 outliers) was 0.84 ± 0.06 cycles/mm (red arrow). The black arrow indicates the frequency of 0.278 cycles/mm, which is the highest that can be captured by the homologous voxel.

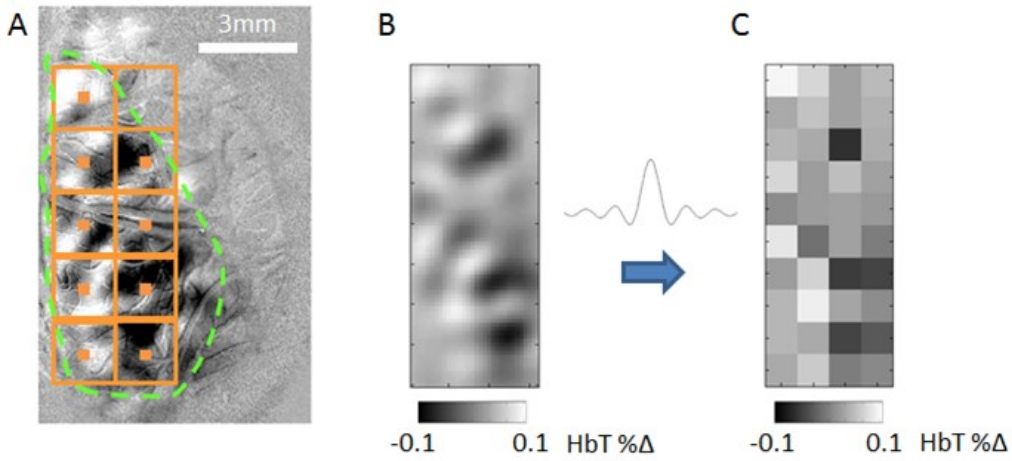

Figure 4-3. Spatial manipulation of cortical maps.
A) Loci of homologous voxels that maximally overlapped with the ROI. The centers of voxels that defined the ROI used for further analysis are marked by a filled orange square. A rectangular region was taken to allow for spatial manipulation (orange squares); however, only voxels whose overlap with the ROI was larger than 75% were taken as part of the input feature for SVM decoding (voxels with filled orange squares inside) **B)** Ideal spatial FFT2 filtering of various cut-offs were applied to the rectangular region determined in A. The example here shows low-pass filtering with cutoff frequency of 0.83 cycles/mm. **C)** Following the filtering, fMRI-like voxel sampling was applied at various binning sizes. To this end, the map was first convolved with a sinc function followed by point sampling with intervals equal to the standard deviation of the sinc function. Pixels that were part of the squares that overlapped with the ROI (green curve in A) with less than 75% of their area were included in the spatial manipulations presented in B and C but were not included as part of the input to the multivariate classifiers.

Classifiers

We performed decoding analysis with 3 classifiers. We used linear SVM as the main classifier. We used another linear classifier, linear discriminant analysis (LDA), as a control. Note that SVM and LDA outperformed other classifiers in a study that compared the performance of various classifiers applied to fMRI data (Misaki et al., 2010). In addition, we applied a sparse logistic regression classifier (SLR), since it has been shown to perform even better on fMRI data (Krishnapuram et al., 2005; Ryali et al., 2010; note that Misaki et al., 2010 did not include sparse logistic regression in their comparison). The inputs to the classifiers were binned pixels of the cortical response maps captured with the high- spatial-resolution optical imaging of intrinsic signal.

Support Vector Machine classifier (SVM)

SVM (Misaki et al., 2010; Vapnik, 2013) uses the notion of largest margin between the separated classes from the decision boundary as its optimization criterion. The support vectors are the data points that are closest to the separating hyperplane; these points are on the boundary margin. Because it is computationally simpler to solve the dual quadratic problem (e.g., a square function always has an extremum), Lagrange multiplier α is applied to the constraints:

$$\text{Maximize } L(\alpha) = \sum_{i=1}^{n} \alpha_i - \frac{1}{2}\sum_{i,j} \alpha_i \alpha_j y_i y_j x_i^T x_j$$

$$\text{Subject to } \sum_i \alpha_i y_i x_i = \omega,\ \sum_i \alpha_i y_i = 0$$

Linear Discriminant Analysis classifier (LDA)

Fisher's LDA (Misaki et al., 2010; Duda et al., 2012) projects the multi-dimensional data onto one warped dimension such that the ratio of the between-class variance and the within-class variance is maximized. The decision boundaries are then placed to discriminate classes. In a two-class problem, one hyperplane exists along the optimal discriminatory dimension of LDA:

$$\boldsymbol{\omega \propto \Sigma^{-1}(\mu_A - \mu_B)}$$

Where ω is the hyperplane, μ are the mean vectors of each distribution, and Σ is the within-class covariance matrix. This covariance matrix, often called the 'scatter matrix' in the context of LDA, is assumed to be equal between the two classes and is estimated from the training samples of both classes.

$$\Sigma_A = \sum_{x \in \omega_A} (x - \mu_A)(x - \mu_A)^T$$

$$\Sigma_B = \sum_{x \in \omega_B} (x - \mu_B)(x - \mu_B)^T$$

$$(\Sigma_A + \Sigma_B) \div 2 = \Sigma$$

Sparse Logistic Regression classifier (SLR)

Logistic regression (Freedman, 2009) starts off by applying the logistic function, which results in values from zero to one:

$$F(x) = \frac{1}{1 + exp\left(-(\omega_0 + \omega^T x)\right)}$$

Because the function F(x) can take any value from negative to positive infinity and the output is confined between 0 and 1, it therefore can be regarded as the probabilistic predictor of success based on the input variable 'x'. Hence, one can classify a two-class problem by simply thresholding this probability to two outputs: Y = [A, B].

For determining the coefficients, the linear regression form is expressed in terms of a log-odds function:

$$g\big(F(x)\big) = \ln \frac{F(x)}{1 - F(x)} = \omega_0 + \omega^T x$$

The coefficients are usually estimated using maximum likelihood estimation. Furthermore, by using L1-regularization the logistic regression forces certain coefficients to be zero, creating sparseness of regression coefficients, i.e. eliminating redundant coefficients. Unlike linear regression, it is not possible to find a closed-form. Hence a numerical iterative process such as Newton's method is applied.

Decoding Paradigm

We performed 2-stimuli decoding across 4 different orthogonal pairs of orientation stimuli. The cross-validation method was used to avoid potential over-fitting of the classifiers (Kohavi, 1995). We randomly split the available trials into 10 groups, and performed the training with 9 groups and the testing with the remaining 1 group. We repeated this process 10 times, leaving each of the 10 groups out once. Although we varied the bin size, thus having more pixels available when smaller bins were employed, we used a fixed number of features (bins) for the input of the classifiers because the number of features influences the overall CNR and the decoding rate (Chaimow et al., 2011). Thus, we defined the lowest number of bins available across all the 5 data-sets at the homologous binning size as our fixed number of bins used across all bin sizes. This fixed number was 8 bins. When using small bins, and thus having more than 8 bins available, we randomly sampled 8 bins for the analysis. We repeated this process 10 times for each of the 4

orthogonal orientation pairs to have an averaged accuracy across data-sets (n = 5 animals × 10 repetitions) at various filtering and binning parameters. The general decoding procedure was as follows:

9. Choose a binning size
10. Randomly sample 8 voxels
11. Choose a frequency cut-off
12. Perform decoding with leave-one-trial-out cross-validation, with each of the 10 blocks left once out
13. Obtain one mean decoding accuracy from the entire 10 validation datasets
14. Do steps 3-5 for each of the defined frequency cut-offs
15. Repeat steps 2-6 ten times (i.e. randomly sample a set of different 8 voxels in each iteration)
16. Do the entire process (steps 1-7) for each of the defined binning sizes

Once the averaged accuracy matrix is obtained, we statistically tested whether the accuracy in each entry (associated with specific filtering and binning parameters) was different than chance level (two-tailed t-test, n = 5 data-sets × 10 repetitions of random sampling; corrected for multiple comparisons by FDR (Chapter 3).

Time-series analysis

We tested whether the concept of complex spatio-temporal sampling could be an important factor in contributing to decoding of information conveyed by the fine scale organization of orientation selectivity. To this end, we focused on the time span for acquiring one volume of fMRI (i.e., 1 TR). In their pioneering decoding studies, Kamitani and Tong (2005) and Haynes and Rees (2005) used TRs of 2 s and 1.3 s, respectively. Haynes and Rees demonstrated a decoding rate of ~80% using single fMRI volumes as the input to the classifier. Hence, if complex spatio-temporal filtering was a main contributor to decoding, then it must play a role in decoding of data obtained from one TR. Therefore, we used a 2 second long time-series from each of 10 acquired OI images as a 3D volume input to the classifier (2 dimensions in space and a third dimension in time). The input to the classifiers had 3 dimensions instead of the 2 dimensional cortical image.

We selected 10 frames of HbR response that were acquired from 1 to 3 seconds following the onset of the stimulus. We performed the time-series analysis using bin sizes of 1.8 mm (the size of voxel homologous to that used in human decoding studies) or 0.6 mm (which was within the range of voxels that gave the highest decoding rates). In contrast to the methods we used for the rest of the study, all the binned pixels within the ROI were used as input features to the

decoding algorithm. The reason for this is that since we test here results that hypothetically can be attributed to spatio-temporal interactions we need to fully cover the space where these interactions may take place. We computed the evolution of decoding rate as a function of time. In addition, we compared decoding rates obtained from averaging all frames into one static image, 3 dimensional (2 dimensions in space, 1 in time) image frames in chronological order, 3 dimensional image frames with the order of frames randomly shuffled, and the averaged static image with additive Gaussian noise. The standard deviation of the Gaussian noise assigned to any pixel was equivalent to that pixel's standard deviation across the 10 frame long measured response.

We expect that, if the spatio-temporal information contributes to decoding using the coarse fMRI voxels, the classifier should pick up extra information from the 3 dimensional volume inputs compared to the 2 dimensional static image. In addition, the decoding rate should be higher for the 3 dimensional volume inputs that has the measured frame order compared to the 3 dimensional input with the order of frames shuffled.

Results

Main cycle of organization

To determine the main frequency of the organization, the differential contrast map, noise map, and CNR map (Fig. 4-2B) were obtained from the normalized data matrix that was subjected to 2D FFT point-pass filtering of different frequencies. For point-pass filtering, the normalized data matrix was zero-padded to a size of 20 mm × 20 mm so that the frequency resolution was 0.05 cycles/mm in the FFT domain. For each of the 20 CNR maps obtained from the 5 animals and 4 stimuli-pairs, we applied point-pass filtering at various frequencies in the FFT domain. The filtered FFT was transformed back to the image domain and the CNR was averaged over the image. This process resulted in an estimate of CNR for each frequency (Fig 4-2C shows two examples from 2 different animals). We then fitted a Gaussian distribution to the curve of CNR within the 0.50 to 2.40 cycles/mm segment (Fig. 4-2C). The mean frequency computed over all peaks of the fitted Gaussians from 18 differential maps was 0.84 ± 0.06 cycles/mm (Table4- I; Fig. 4-2D; n = 18; 4 differential contrast maps per animal × 5 animals, 2 outliers; see Table 4-II for the mean FWHM of the fitted Gaussians). Hence, the voxel size homologous to that used in human studies of orientation decoding was 1.5 × 1 ÷ 0.84 cycles/mm ≈ 1.80 mm (rounded from 1.7857 mm). The highest frequency that can be captured by such a voxel is 0.278 cycles/mm (Fig. 4-2D, black arrow).

Note the monotonous decrease in CNR from the main frequency of the organization towards lower frequencies including 0 frequency (= the mean response). In contrast to our findings from cat area 17 (Chapter 3), here there was no trough observed in CNR anywhere between the main frequency of the organization and the lowest frequency analyzed (mean response).

Table 4-I. Center of the Gaussian fit to the CNR as a function of point-pass center frequency.

Center of fit (mm)	Animal A	Animal B	Animal C	Animal D	Animal E
Orientation-pair 1	0.816	0.560*	0.868	0.697	0.528*
Orientation-pair 2	0.839	0.868	0.885	0.747	0.907
Orientation-pair 3	0.816	0.836	0.940	0.949	0.797
Orientation-pair 4	0.811	0.864	0.788	0.859	0.828

The average of the centers is 0.84(0.06) cycle/mm, n = 18, 2 outliers (denoted by *, with values more than 2 standard deviations away from the mean of the distribution) was not taken into account.

Table 4-II. FWHM of the Gaussian fit to the CNR as a function of point-pass center frequency.

Center of fit (mm)	Animal A	Animal B	Animal C	Animal D	Animal E
Orientation-pair 1	0.629	1.227	0.577	0.886	1.239
Orientation-pair 2	0.870	0.776	0.572	0.819	0.621
Orientation-pair 3	0.923	1.158	0.671	0.571	0.688
Orientation-pair 4	0.851	0.932	0.385*	0.645	0.625

The average of the FWHM is 0.80(0.22) cycle/mm, n = 19, one outlier (denoted by *, with values more than 2 standard deviations away from the mean of the distribution,) was not taken into account.

Decoding accuracy as a function of binning and filtering

To evaluate the potential contributions of GM, LV and spatial frequency components to decoding, we sampled the responses following low-pass filtering, using an fMRI-like K-space sampling at different pixel sizes. Figures 4-4 and 4-5 present the results obtained from HbR and HbT responses, respectively. The white shaded parts of the accuracy matrices depict the combinations of filtering and binning in which the mean of the distribution was not statistically different than chancel level (50%, $p > 0.05$, two-tail t-test, FDR corrected, n = 50). The black dashed lines represent the homologous voxel binning size and the maximal frequency that can be captured by such binning size.

Using HbR responses (Fig. 4-4), the decoding accuracy obtained from GM, LV and GM&LV (upper 3 panels) was significantly higher than chance level for every combination of filtering and binning parameters, except for low-pass filtering with 0 cycles/mm, which represents the mean response ($n = 50$, 2-tailed t-test, corrected according to FDR, $q < 0.05$). The decoding accuracy of GM and GM&LV remained high (GM: range 66.3%-68.7%, mean±SD 68.0±0.5%; GM&LV: 66.6-69.3%, 67.8±0.7%) in an L-shaped region consisting of low-pass filtering with cut-off frequencies from 0.83 to 1.67 cycles/mm and binning sizes from 0.45 to 0.90 mm. In addition, a small region of lower decoding accuracy (GM: range 65.4%-67.1%, mean±SD 66.6±0.5%; GM&LV: 65.2%-68.5%, 67.2±0.9%) was observed for cut-off frequencies 2.22 cycles/mm and higher and binning sizes of 0.30 mm and lower. A monotonous decrease in accuracy (from ~66.5% down to chance level, 50%) was observed with cut-off frequencies decreasing from 0.56 cycles/mm towards 0. The decoding accuracy of LV was higher (LV: range 55.0%-64.5%, mean±SD 61.9±2.2%) than chance level through all combinations of filtering and binning, except for decoding using the mean response. Nevertheless, a monotonous decrease in accuracy was observed for LV responses too, for cut-off frequencies 0.56 cycles/mm and lower. There were no significant differences in decoding accuracies between GM and GM&LV (lower left panel). In contrast, for the majority of filtering and binning parameters, we did observe statistically significant different decoding rate between the LV and GM&LV (lower right panel).

Figure 4-4. HbR Decoding accuracy using a fixed number of pixels, as a function of low-pass filter cutoff frequency and binning. (See next page for figure)
Decoding accuracy using an SVM classifier. The 3 panels in the upper row present decoding using data from gray matter only, large veins (diameter > 0.15mm) only, and GM&LV: gray matter and vessels together (all data are included), as denoted by the label GM, LV and GM&LV, respectively. The bottom-left panel presents the differences between decoding accuracies obtained from gray matter and large vessels data and that obtained using data from gray matter only. The bottom-right panel presents the differences between decoding accuracies obtained from gray matter and large vessels data and that obtained using data from large vessels only. The decoding rates are presented in matrices, as a function of low-pass filter cut-off frequency and bin size along the vertical and horizontal axis, respectively. The vertical and horizontal dashed lines represent the homologous voxel size and the highest frequency that can be captured by the homologous voxel, respectively. The pixels used as input to the classifier were limited to 8 randomly selected pixels. The color look up tables represent decoding accuracy in percent (corresponding to the upper 3 panels) and

decoding accuracy difference (corresponding to the bottom 2 panels). Statistical tests were applied to each of the matrices, in order to test whether the accuracies were significantly higher than chance level (50%, GM, LV, GM&LV) or showing difference (subtraction result different than 0%, GM&LV-GM, GM&LV-LV). Statistically significant results were plotted in color (2 tail t-test, FDR corrected, alpha 0.05, N = 5 data-sets x 10 repetitions).

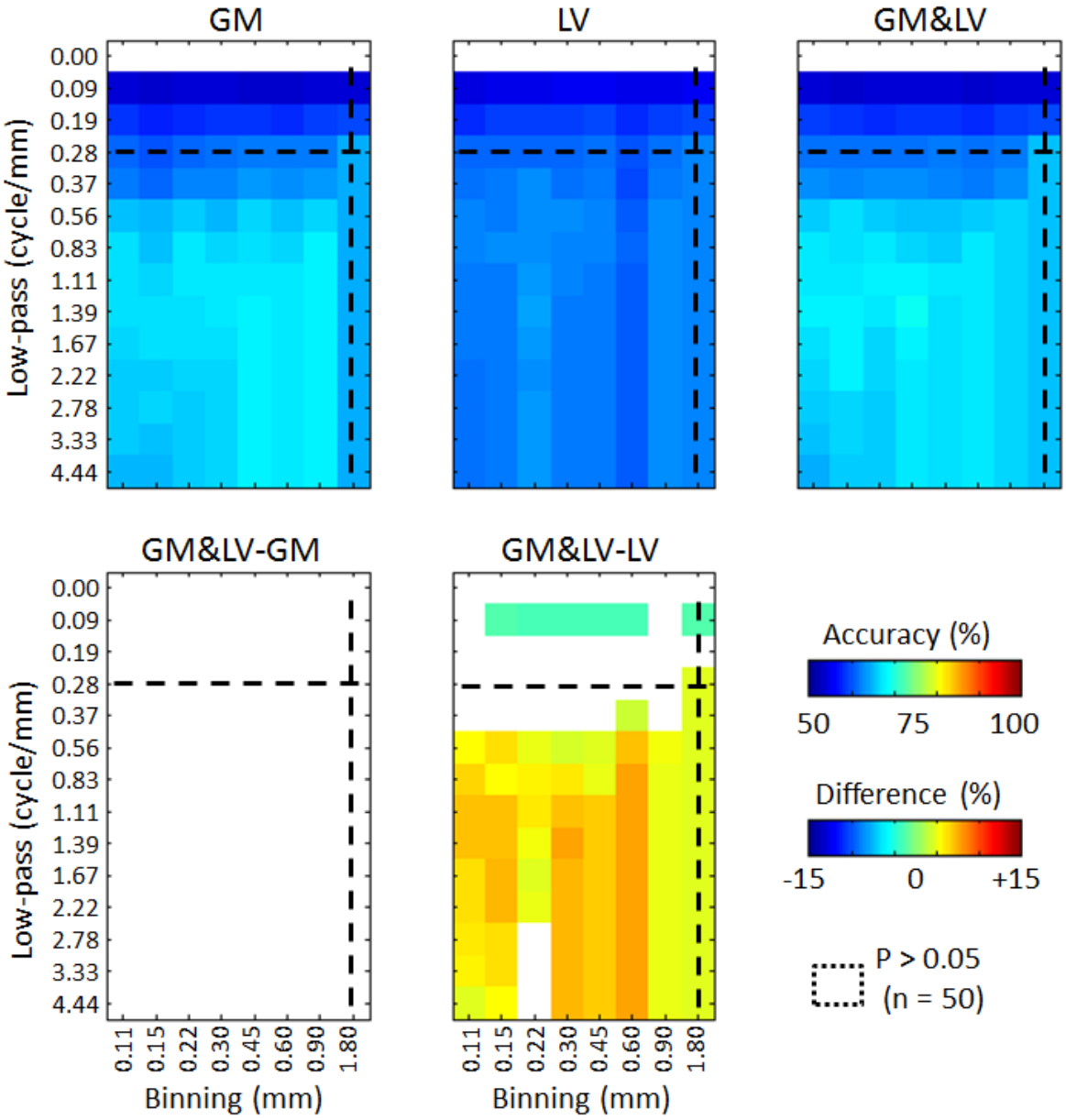

Figure 4-4. HbR Decoding accuracy using a fixed number of pixels, as a function of low-pass filter cutoff frequency and binning. (See previous page for legend)

HbT responses (Fig. 4-5), showed a similar accuracy pattern as a function of filtering and binning parameters to that observed for HbR responses. However, on average, the HbT decoding rate was higher than that of HbR (difference in GM: 12.7 ± 3.5%, LV: 7.5 ± 2.0%, GM&LV: 12.9 ± 3.2%; mean and SD computed over all entries in the matrix except for those showing results with filter cut-off of 0 cycles/mm). The decoding accuracy of GM and GM&LV combined remained high (GM: range 81.6%-86.1%, mean±SD 84.1%±1.5%; GM&LV: 81.6%-85.4%, 83.8%±1.2%) for low-pass filtering with cut-off frequencies from 0.83 to 1.67 cycles/mm and for binning sizes from 0.45 to 0.90 mm. In addition, a region of lower decoding accuracy (GM: 78.9%-81.1%, 80.2±0.8%; GM&LV: 78.2%-81.9%, 80.3%±0.9%) was observed for cut-off frequencies of 2.22 cycles/mm or higher and binning sizes equal to or smaller than 0.30 mm. A monotonous decrease in accuracy (from ~80.2% down to chance level, 50%) was observed with the cut-off frequency decreasing from 0.56 to 0 cycles/mm. The decoding accuracy of LV was higher (LV: 58.1%-74.1%, 69.4±3.7%) than chance level for all combinations of filtering and binning (except for decoding using with the mean response). Nevertheless, a monotonous decrease in accuracy was observed for LV responses too, with cut-off frequencies decreasing from 0.56 to 0 cycles/mm. There were no significant differences in accuracies between GM and GM&LV (lower left panel). In contrast, for all filtering and binning parameters except for cutoff frequency of 0 cycles/mm, we did observe statistically significant different decoding rates between the LV and GM&LV (lower right panel).

Our main findings prevail across 3 decoding algorithms

The results of decoding performance as a function of filtering and binning were qualitatively similar across all three decoding algorithms, i.e. LDA, SLR and SVM (supplementary Figures 4-1 to 4-4). Thus our main findings do not depend on a specific decoding algorithm. However, in the majority of comparisons, LDA performed best and SLR performed worst, with SVM showing an intermediate level of success. For all 3 decoding methods, decoding based on GM was comparable to decoding based on GM&LV. Decoding accuracy based on LV was higher than chance level for all combinations of filtering (except for a cutoff frequency of 0 cycles/mm) and binning. However, consistently over the same range of combinations, it was significantly lower compared to the accuracy obtained from GM or GM&LV. We thus concluded that the findings we presented for decoding based on SVM in Figures 4-4 and 4-5 could be generalized to other decoding methods.

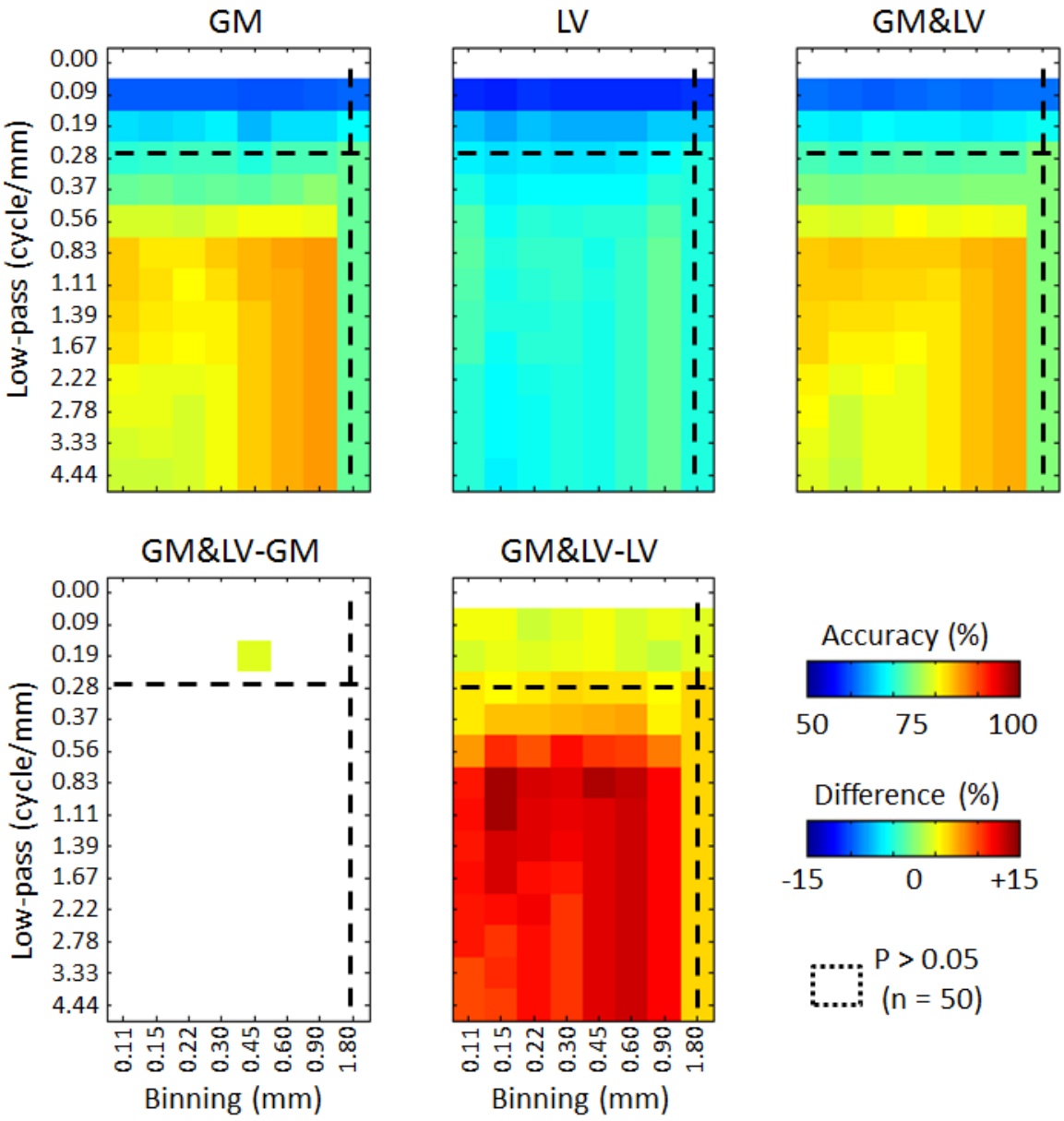

Figure 4-5. HbT Decoding accuracy using a fixed number of pixels, as a function of low-pass filter cutoff frequency and binning.
The analysis and format of presentation are identical to those used for Figure 4-4.

Spatial frequency-dependent contributions to decoding using homologous voxels

In order to better analyze contributions to decoding using the homologous voxels (1.8 mm), we applied SVM to HbR and HbT responses in GM, LV and GM&LV regions following point-pass and low-pass filtering (Fig. 4-6). Here we focus on the response maps following filtering with 4 frequency cut-offs that can be captured with the homologous voxel: 0 (mean response), 0.093, 0.185, and 0.278 cycles/mm (Fig. 4-6; Table 4-III). Note that 0.278 cycles/mm is the highest frequency that can be captured with such large pixels.

A statistically significant difference of 3% was observed between the GM&LV and the LV decoding accuracies to HbR data at the homologous binning size with point-pass and low-pass filtering at the cutoff of 0.278 cycles/mm ($p < 0.05$, two-tail t-test). Statistically significant differences of 3-7% were observed between the GM&LV and the LV decoding accuracies to HbT data at the homologous binning size with point-pass and low-pass filtering at cutoffs of 0.093, 0.185, 0.278 cycles/mm ($p < 0.05$, two-tail t-test). No statistical differences were observed between GM&LV and GM decoding accuracies applied to HbR or HbT data for any filtering cutoffs at the homologous voxel binning size.

We observed a monotonous increase in decoding accuracy as a function of increasing cut-off frequencies from 0 to 0.278 cycles/mm across all our data. For example, the GM&LV decoding using HbR data with point-pass filtering showed 50.5 ± 4.5% at 0, 55 ± 5.1% at 0.093, 63.4 ± 9.3% at 0.185, and 67.4 ± 6.9% at 0.278 cycles/mm. This result is in contrast to our previous observations using MION CBV-fMRI in cat area 17 (Chapter 3), where a trough in decoding rate separated decoding based on point-pass with frequencies in the irregularities and low-frequencies regimes. In other words, in cat area 18, we observe no clear low-frequencies regime. This is corroborated by Figure 4-2D, where the CNR spectrum resembles a Gaussian function with monotonous decreases in CNR from the main frequency of the organization towards both low and high frequencies.

Figure 4-7 compares decoding rate obtained from HbT and HbR responses. HbT decoding accuracy was higher than that obtained from HbR (difference averaged over all bin sizes and frequency cut-offs except for 0 cycles/mm in GM: 12.7 ± 3.5%, in LV: 7.5 ± 2.0%, GM&LV: in 12.9 ± 3.2%). Moreover, consistently for each frequency cut-off and binning size, decoding based on HbT responses gave higher accuracy than that based on HbR response, in GM, LV and GM&LV regions (two-tailed t-test, $p < 0.05$, $n=50$, corrected for FDR).

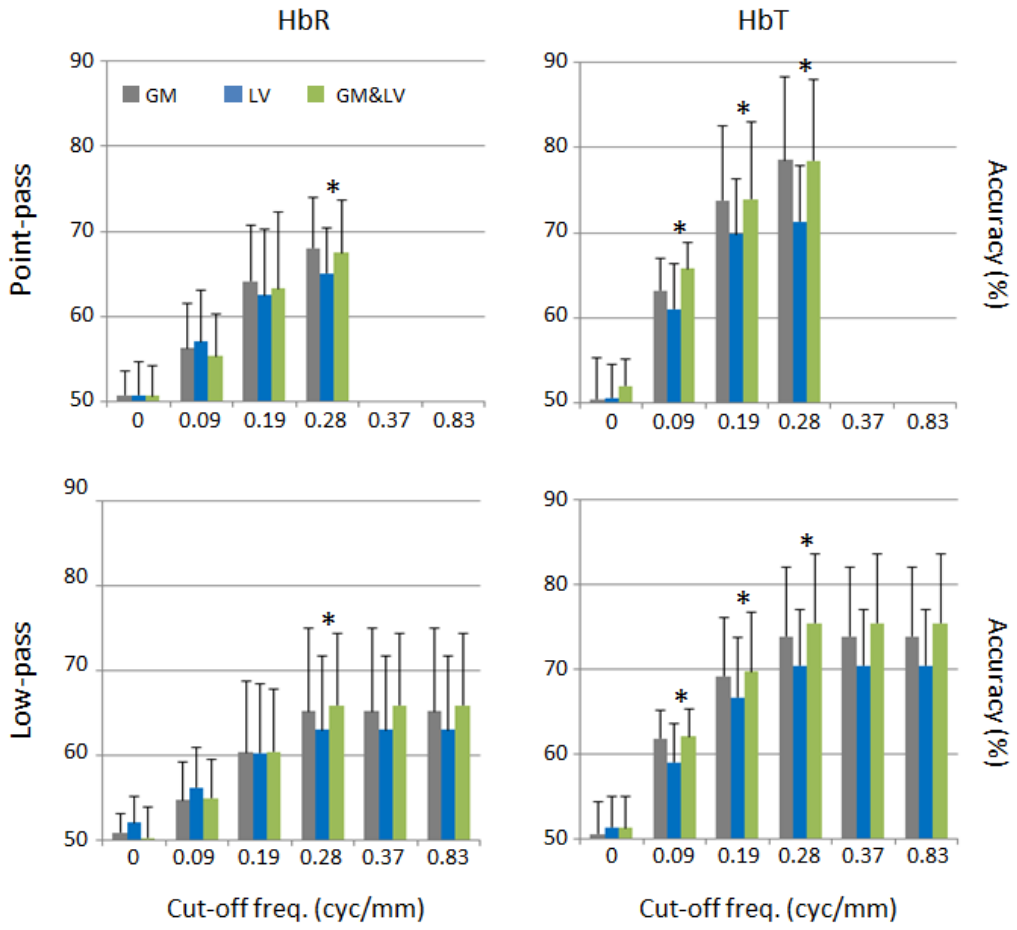

Figure 4-6. Decoding accuracy using pixels homologous in size to those used in human decoding studies.

The decoding accuracy of GM, LV and GM&LV using binning size of 1.8 mm, following low-pass filtering with frequency cutoffs of 0 (mean response computed over the ROI), 0.093, 0.185, and 0.278 cycles/mm. The two panels to the left show results obtained from HbR responses; those to the right present results obtained using HbT responses. The upper and lower rows present results obtained after spatial point-pass and low-pass filtering, respectively. A statistically significant difference of 3% was observed between the GM&LV and the LV decoding accuracies using HbR data with point-pass and low-pass filtering at the cutoff of 0.278 cycles/mm ($p < 0.05$, two-tail t-test). Statistically significant differences of 3-7% were observed between the GM&LV and the LV decoding accuracies using HbT data with point-pass and low-pass filtering at cutoffs of 0.093, 0.185, 0.278 cycles/mm ($p < 0.05$, two-tail t-test). No statistical differences were observed between GM&LV and GM decoding accuracies using either HbR or HbT data for any filtering frequency cutoff at the homologous voxel binning size. Note the monotonous increase in decoding accuracy as a function of increasing cut-off frequencies from 0 to 0.278 cycles/mm across all our data. No change in decoding accuracies were observed following low-pass filtering with frequency cutoffs higher than 0.278 cycles/mm relative to the results obtained with that frequency cutoff.

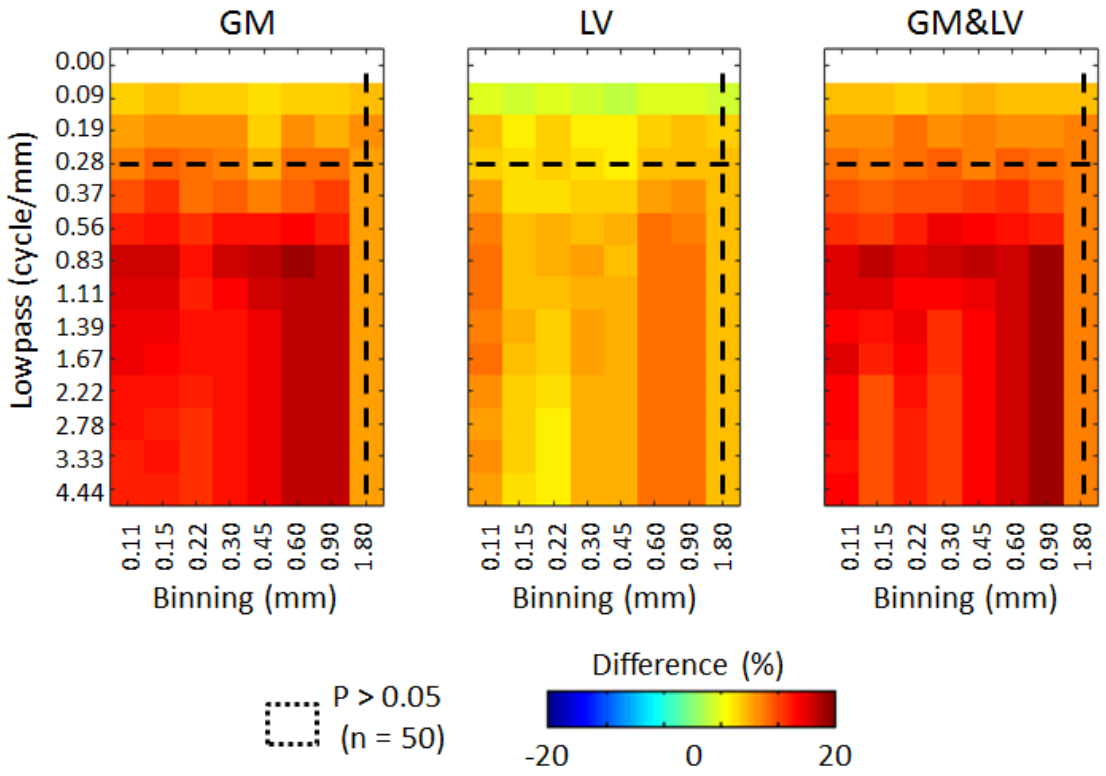

Figure 4-7. Differences in decoding accuracy obtained from HbT and HbR data using a fixed number of pixels, as a function of low-pass filter cutoff frequency and binning.
The analysis and format of presentation are identical to those used for Figures 4 and 5. We present the matrices of differences in mean decoding accuracy obtained from HbT and HbR responses. All colored entries showed results where the null hypothesis of no difference was rejected (two-tailed student t-test, n = 50; 5 animals × 10 groups of selected voxels).

Time-series contributions to decoding

We also tested whether subtle complex-spatiotemporal effects hypothesized by a modeling study (Kriegeskorte et al., 2010) improve the decoding accuracy. To this end, we used 10 frames of HbR responses acquired from 1 to 3 s following the onset of the stimulus. Figure 4-8A presents the average decoding accuracy (n = 5 experiments) obtained when using each of these frames separately. The decoding accuracy increased with increasing time relative to the onset of the stimulus. The decoding accuracies obtained from the frame corresponding to 1.8 second following the stimulus onset and each of the subsequent frames were significantly higher than that of the frame corresponding to the 1 second following the stimulus onset.

We then created 4 different inputs to the classifier, 3 of which had 2 dimension in space and 1 dimension in time: 1) normal frame order, 2) shuffled frame order for each trial, and 3) a time-series in which each of the 10 frames was the average over all 10 original frames plus a Gaussian noise equivalent to the standard deviation across frames. The fourth input was the response image averaged over the 10 frames ('static', Fig. 4-8B). All 3 dimensional spatiotemporal inputs yielded decoding performances that were not statistically different from one to another ($p > 0.05$, two-tail t-test). In addition, none of these 3 inputs reached the decoding performance obtained from the static 2 dimensional averaged response image. The decoding rate obtained from the static pattern of the response was significantly higher than those obtained with each of the 3 the spatiotemporal inputs ($p < 0.05$, two-tail t-test, $n = 5$ animals).

Discussion

Summary of the results

The main frequency of the organization in cat area 18 is 0.84 ± 0.05 cycles/mm (Table 4-I; Fig. 4-2D). In the frequency domain, the responses around the main frequency of the organization decrease gradually towards lower or higher frequencies, creating a wide Gaussian-like distribution. The voxel size homologous to that used in human studies of orientation decoding is 1.80 mm, making it possible to capture frequencies of 0.278 cycles/mm (or lower), which is within the lower frequency end of the irregularities domain. Following low-pass filtering, the successful decoding rate of HbR-based responses (Fig. 4-4) and of HbT-based responses (Fig. 4-5) using the homologous voxels and cut-off frequencies higher than 0.370 cycles/mm are not different from those obtained with the same voxel size and cut-off frequency of 0.278 cycles/mm. Large vessel responses using the homologous voxel size shows decoding accuracies higher than chance level but lower compared to those from gray matter regions (Figures 4-4 to 4-6). The decoding accuracies using combined responses from large vessels and gray matter are comparable to those obtained exclusively from gray matter regions. The decoding accuracies obtained from total-hemoglobin responses are higher than those obtained from HbR responses (Fig. 4-7). Lastly, decoding based on spatiotemporal time-series does not improve accuracy compared to that obtained from the spatial response averaged over time (Fig. 4-8).

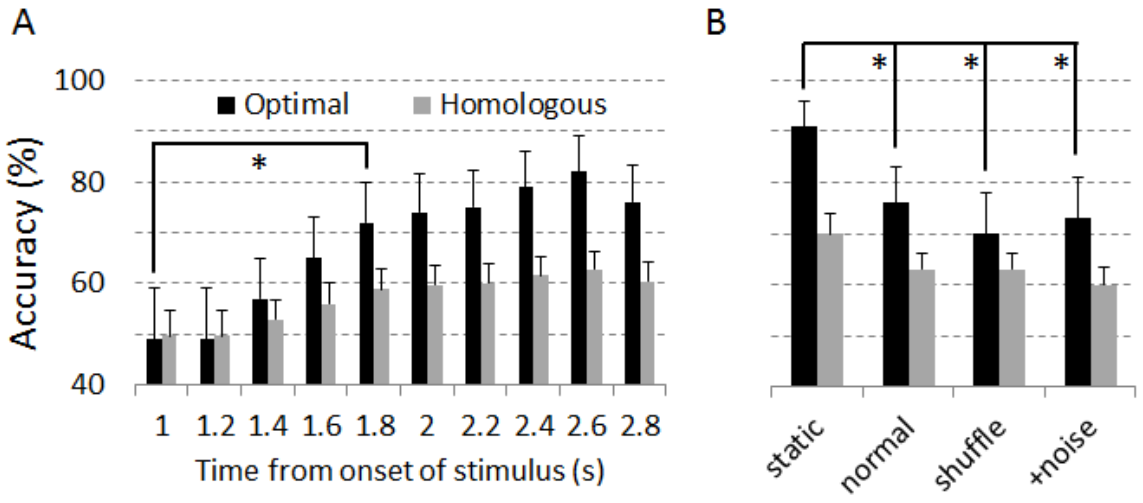

Figure 4-8. Decoding accuracy from spatio-temporal response compare to the spatial pattern of the response.

The input to the classifier consisted of 3D data (2 dimensions in space and one in time) instead of 2D (2 dimensions in space = cortical response image averaged over time). Voxel size of 0.6 mm (which was within the binning range that gave the highest decoding rate using HbR responses from GM&LV, Fig. 4) and 1.8 mm (the homologous voxel size) were selected for this analysis. All binned pixels in the ROI were used as input to the classifier instead of randomly chosen 8 pixels, as in other analyses of the study. **A)** The 10 frames of the HbR response that were acquired from 1 s to 3 s following the stimulus onset were inserted individually into the classifier. The numbers next to the horizontal axis show the time from the onset of the stimulus in which data acquisition over 200 ms for the specific frame started. These 10 frames (2 seconds) also represent 1 volume of fMRI data with TR = 2 s (Kamitani and Tong, 2005). Error bars represent the standard deviation of the mean accuracy across animals (n = 5). The decoding accuracies obtained from each of the 200 ms long frames starting with 1.8 s following the onset of the stimulus were significantly higher than that obtained from the frame obtained 1 s following this onset. **B)** The 3D volume data were modified to several types of inputs. 'Static': the spatial 2D response averaged over the 2 seconds in which the 10 original frames were acquired. 'Normal': the 3D spatio-temporal response as depicted by the 10 frames acquired during the same 2 seconds in normal chronological order. 'Shuffled': a 3D data structure in which the original frame acquisition order was randomly shuffled separately for each trial. '+Noise': noise equivalent to the standard deviation of the response time series was added to 10 copies of the averaged frame. Error bars are the standard deviation of the mean accuracy across animals (n = 5). The decoding accuracy obtained from the static pattern of the response was significantly higher than that obtained from each of the 3 spatiotemporal response datasets.

Do irregularities in the functional organization contribute to decoding using large voxels?

If irregularities in the map did not exist, then the cortical orientation preference map would constitute one single spatial frequency. Therefore, by definition of irregularities, if irregularities exist the columnar organization involves a distribution of frequencies, including frequencies lower than the main frequency of the organization (Rojer and Schwartz, 1990; Chaimow et al., 2011). Indeed, in Fig. 4-2D we show that the CNR of differential orientation maps shows a peak at 0.84±0.06 cycles/mm and a wide Gaussian-like distribution of frequencies around the peak with a FWHM of 0.80±0.22 cycles/mm (Table 4-II). Therefore, irregularities do exist in orientation maps.

However, do irregularities in the organization contribute to orientation decoding using voxels that are 1.5 times larger than the average cycle length of the organization? The critical factor in addressing this question is the width of the distribution of frequencies around the main frequency of the organization. If this Gaussian-like distribution is wide, low-frequencies that still belong to it can possibly be captured by voxels that are 1.5 times larger than the average cycle length of the organization.

For orientation maps in cat area 18, the curve of mean CNR (Fig. 4-2D) shows a maximum at 0.84 cycles/mm, which represents the main cycle of the orientation map. The CNR curve decays slowly in both directions, towards higher and lower frequencies (Fig. 4-3D, red arrow). We defined the size of the voxel homologous to that used by Kamitani and Tong (2005) and Haynes and Rees (2005) in human subjects to be 1.5 times larger than the main cycle of the orientation map in our cat area 18 data (1.5×1.2 mm = 1.8 mm; see Chapter 3 for details on the definition of the homologous voxel size). The largest frequency that can be captured by such a voxel is 0.278 cycles/mm (black arrow in Fig. 4-2D). This frequency shows relatively low CNR, but is still within the lower end of the slow decay (Fig. 4-3D, black arrow) of the Gaussian of CNR values centred on the main frequency of the organization. Thus, this coarse voxel still captures the lower end tail of the elevated amplitude within the frequency regime caused by irregular organization of the orientation columns.

This is in contrast to our previous results with data from cat area 17, where we observed two frequency regimes with elevated power: one associated with the main frequency of the organization, including the irregularities regime, and the other at low-frequencies. In area 17, a trough in amplitude separates the irregularities and the low frequencies regimes. The homologous voxel is too large for capturing frequencies higher than the trough. In contrast, in cat area 18 we

observe a wide band of frequencies with elevated amplitudes that well matches a Gaussian centered on the main frequency of the organization. The amplitudes fall monotonously towards both lower and higher frequencies relative to the main frequency of the organization, and the homologous voxel can capture low-frequencies within this Gaussian.

In addition to these observations that are based on the spectrum of CNR, using the homologous voxel, in cat area 18 we observe a steady increase in decoding accuracy following point-pass filtering with frequencies from 0 to 0.28 cycles/mm (Fig. 4-7). This is in contrast to the trough in decoding accuracy we observed with data from cat area 17. Using the homologous voxel, the decoding accuracy increased monotonously with increasing cut-off frequency from 0 to 0.28 cycle/mm, with no interfering trough or plateau. This indicates that the combined frequencies are not redundant. We therefore conclude that in contrast to their null-contribution in cat area 17, local irregularities in the organization of preferred orientation in cat area 18 make relatively small contribution to the CNR and to successful decoding when sampled using the homologous voxel size.

There are several possible reasons that could account for the difference between our conclusions based on data from cat area 17 (Chapter 3) and area 18 (here) with regard to contributions from local irregularities. The main important difference is in the frequency range that can be captured by the homologous voxels in these two areas. As discussed above, the homologous voxel is determined by the main frequency of the organization. Importantly the Gaussian-like distribution of frequencies around the main frequency is wider in area 18 (FWHM, 0.80 cycles/mm Table 4-II, Figure 4-2) than in area 17 (FWHM, 0.56 cycles/mm; Chapter 3, Table 3-II, Figure 3-3). This allows the homologous voxel to capture contributions in area 18 from frequencies lower than the main frequency of the organization, but within the irregularities regime.

We suggest that the differences we observe in the mechanisms underlying decoding based on data obtained from cat areas 17 and 18 cannot be primarily attributed to methodological differences. In our previous study (Chapter 3) we used MION-based cerebral blood volume (CBV) fMRI. The HbT signals we imaged here are comparable to MION-CBV responses, since both are measurements of cerebral blood volume. Here we added HbR measurements, but the HbT measurements bridge the different methodologies used in these two studies. Moreover, the orientation selectivity of neurons in layers 2/3, where the optical imaging responses originate, is not lower than that of neurons in layer 4 (Ringach et al., 1997), where fMRI sensitized to CBV

receives its main contributions from (Zhao et al., 2006). Hence, differences in results regarding the relative contributions from large scale organization or from local irregularities should be attributed to the visual areas involved rather than to methodology.

Our conclusion, showing contributions from local irregularities in the columnar organization to decoding, are consistent with the conclusion made by Swisher et al. (2010). These authors used high-field, high-resolution (0.3125 mm) BOLD-fMRI and multivariate pattern analysis to determine the spatial scales at which orientation-selective information can be found in cat area 18. They concluded that their results demonstrate a reliable millimeters-scale orientation signal, likely emerging from irregular spatial arrangements of orientation columns and their supporting vasculature. However, although Swisher et al. (2010) applied low-pass and high-pass spatial filtering, they used small voxels that could capture the main frequency of the organization. In contrast, we base our conclusion on voxels homologous in size to those used in human decoding studies. In addition, we simulated fMRI k-space sampling, which eliminates contributions from frequencies higher than its Nyquist frequency (half of the inverse of the sampling interval).

In our previous study, we used MION CBV-based fMRI which is accepted as optimal in terms of spatial specificity of the functional imaging response relative to the site of increased neurophysiological measures (Fukuda et al., 2006). Based on analysis of homologous voxels derived in a manner similar to our derivation here, we concluded that irregularities in the organization of area 17 do not contribute to decoding of oriented gratings. We also reported on elevated power in low frequencies of the organization, which were clearly lower than- and separated from the frequency regime of irregularities. Our current imaging data from cat area 18 shows that irregularities in the organization can potentially contribute to decoding. Thus, whether irregularities contribute to decoding of a fine scale organization depends on the main frequency of the organization, and on the rate of decrease of amplitude from the main frequency of the organization towards lower frequencies.

2.4.1 Selectivity of large vessels and their contributions to decoding

One of the mechanisms proposed to underlie the decoding of information in fine structures by relatively large voxels is the contribution of macroscopic blood vessels. The idea is that draining regions that cover cortical maps and columns non-homogeneously may cause selective responses of their corresponding blood vessels (Kamitani and Tong, 2005; Gardner et al., 2006; Kamitani and Tong, 2006; Kriegeskorte and Bandettini, 2007; Gardner, 2010; Shmuel et al., 2010;

Thompson et al., 2011). However, in our previous work (Chapter 3) we used high-resolution contrast-agent based fMRI data with no contributions from macroscopic blood vessels, and showed that it is possible to achieve successful decoding with no contributions from LV. The OI data we use here at high spatial resolution (better than or equal to 0.016 mm per pixel) allow clear separation of responses from LV and GM. Using these data, we show that decoding accuracies obtained from LV responses following low-pass filtering with all tested parameters and using all pixel sizes are higher than chance level. Thus, LV responses can potentially contribute to decoding. However, LV responses have no incremental contributions (i.e., higher decoding accuracies) when they are combined with the data from the GM regions, relative to the decoding accuracy based on data obtained exclusively from GM regions. The contributions from LV are redundant when they are combined with information from GM (GM&LV decoding). Thus, our current data, where responses from LV are available, shows results consistent with- and complements the findings from- our previous study that analyzed data with no contributions from LV.

In our current analysis, we used as input to the decoders equal numbers of voxels across 3 tested modalities (GM, LV, GM&LV), in order to focus on their relative selectivity. Therefore, the analysis based on separate data from LV and GM does not account for the low abundance of LV relative to GM regions. However, the GM&LV data does represent the realistic situation, in which LV occupy less space, but their amplitudes are higher than those in GM regions. Data from this realistic scenario showed higher decoding accuracies relative to data from LV alone, and comparable decoding accuracies to those obtained from GM regions. Thus, the contributions to decoding from LV are redundant relative to those from GM regions. Therefore, LV responses may be relevant in situations where their amplitudes exceed those obtained from GM, such as when using GE-BOLD at 3 Tesla (and even at 7 Tesla). However, in the general case, the information available from LV is redundant.

Previous fMRI studies suggested that LV carry information for decoding (Gardner et al., 2006; Shmuel et al., 2010; Thompson et al., 2011). However, none of them excluded contributions to decoding from GM regions. Thus, our results are consistent with theirs. The quantitative differences between our current findings and those presented in previous fMRI studies of decoding may be caused by the spatial extent of the draining regions analyzed in each case. For example, it may well be that the veins that carry information on the stimulated eye (Shmuel et al., 2010) drain blood from a large region within V1, that shows higher response to stimulation of the contra- than

to the ipsi-lateral eye (Tychsen and Burkhalter, 1997). Similarly, it is possible that the selective responses in vessels to oriented visual stimuli reflect drainage of large scale organizations such as the oblique effect (Furmanski and Engel, 2000; Sun et al., 2013) and the radial bias effect (Sasaki et al., 2006; Clifford et al., 2009; Mannion et al., 2010; Freeman et al., 2011; Freeman et al., 2013; Sun et al., 2013). This interpretation is consistent with our current results, showing that the cortical frequencies that contributed to decoding based on signals from LV were lower than those of gray matter (Figures 4-4 and 4-5; Suppl. Figures 4-1 to 4-4).

Comparing decoding rates obtained from HbR and HbT responses

The maximal decoding accuracy obtained for HbT responses following point-pass filtering showed a peak at frequencies of 0.56-0.83 cycles/mm. Using HbR, point-pass filtering showed a maximum decoding accuracy at 0.56 cycles/mm. This local maximum was part of a wide band of frequencies showing elevated decoding rates ranging from 0.19 to 0.83 cycles/mm. (Suppl. Figures 4-2 and 4-4). This observation supports the concept that HbT better reflects the approximately cyclic organization of the orientation columns, whereas HbR responses present a smoother version of the organization. Using BOLD-fMRI, which is based on HbR responses, Shmuel et al. (2010) demonstrated ocular dominance selective regions broader than conventional columns, showing a cortical frequency lower than the main frequency of the organization in humans. These regions carried information on the stimulated eye. Of note, it has been suggested that smoothing the pattern obtained in multiple voxels does not degrade multivariate pattern decoding (Kamitani and Tong, 2005). The authors used this observation in order to refute claims against the contributions of irregularities to decoding of fine scale organizations (Op de Beeck, 2010). However, their observation may in fact explain why frequencies of the BOLD response that are lower than the main frequency of the organization but higher than those constituting large scale organizations carry information on the orientation or the stimulated eye (Shmuel et al., 2010; Swisher et al., 2010).

Decoding accuracy obtained from spatiotemporal responses compared to the spatial pattern averaged over time

One of the mechanisms that were proposed as potential contributors to decoding of fine scale organizations using large voxels is complex spatiotemporal filtering of neuronal activity (Kriegeskorte et al., 2010). In part, this concept is based on the notion that a voxel receives spatiotemporal blood flow with origin from its vicinity. It proposes that information on fine-scale functional organizations transforms into signals in larger vessels that can be captured by large voxels. In our previous study (Chapter 3), we used MION-based CBV-fMRI of responses to phase-encoded oriented gratings. We could not detect any responses from macroscopic vessels due to the extreme dephasing conditions and no variation in blood volume during steady-state continuous stimulation. Thus, our measurements and paradigm combined to a scenario in which we could not expect any contributions to decoding from complex spatiotemporal filtering. In spite of this, we were still able to obtain decoding accuracies significantly higher than chance level under all conditions of spatial filtering and voxel sizes. The results we present here (Fig. 8) complement our previous findings. We demonstrate that decoding accuracy based on spatiotemporal responses are not higher than those obtained from appropriate control. Moreover, they are lower than the decoding accuracy obtained from the static pattern of response average over time.

To the best of our knowledge, contributions conceptualized as complex spatiotemporal filtering of neuronal activity have not yet been demonstrated. If this mechanism indeed contributed significantly, we could expect that the spatiotemporal response should yield higher decoding rates than appropriate control data. Here we compare the decoding rates obtained from the spatiotemporal response to those obtained by randomly shuffling the order of imaged frames. A second control we use is the spatial pattern of the response averaged over time, contaminated by additive noise equivalent to the variability of the measured response over time. There is no statistically significant difference between decoding accuracies obtained with the measured- and time-shuffled spatiotemporal responses. Similarly, there is no statistically significant difference between decoding accuracies obtained with the measured response and the response pattern averaged over time and contaminated with noise. Importantly, the number of features available to the decoding algorithm and the overall variability of the data remain unchanged across these 3 data-sets. We therefore conclude that the spatiotemporal evolution of the response does not increment the orientation decoding accuracy compared to appropriate controls.

We acknowledge that our sample was relatively small (5 data-sets). However, if complex spatiotemporal filtering was a major contributor to decoding, we would expect the measured order to show higher success rates than the 2 other tested conditions, even with n = 5 experiments. In addition, we tested whether the spatiotemporal response yields better decoding rates compared to those obtained with the spatial pattern of the response averaged over time. Even with our small sample, the decoding accuracy obtained from the static response pattern averaged over time was significantly higher than those obtained by each of the 3 spatiotemporal time series. These findings corroborate the notion that complex spatiotemporal filtering of neuronal activity by fMRI voxels does not play a major role in decoding of oriented gratings.

We would like to emphasize that we do not refute the concept of complex spatiotemporal sampling. In fact, this concept is possibly a realistic model of fMRI sampling. However, we show here that the spatial pattern of the response averaged over time has a better decoding rate than the spatiotemporal evolution of the response. It is important to note two advantages that the spatial pattern of the response has over the spatiotemporal evolution of the response. Firstly, the averaging over time reduces the noise. In addition, decoding based on the spatial response pattern incorporates a simpler classification based on 10 times fewer features than those used for the decoding based on the spatiotemporal response. Thus, it reduces the dimension and complexity of the input to the classifier. Our findings suggest that it is unlikely that the complex spatiotemporal sampling contributes significantly to the successful decoding of orientation under conventional coarse fMRI voxel sampling.

Here we have analyzed the decoding accuracy obtained from the spatiotemporal response over a duration of two seconds. We chose this duration because it is commonly the TR in fMRI, constituting the sampling rate in conventional fMRI and that used by Kamitani and Tong (2005) decoding study. Thus, our conclusions hold for decoding based on one volume of fMRI response (as demonstrated by Haynes and Rees, 2005). To generalize it to all conditions possible for spatiotemporal responses, in a future study we will pursue similar analyses over various longer durations of the OI response to oriented grating.

Decoding accuracy from cat area 18 relative to that obtained in human fMRI studies

In order to study the mechanisms underlying decoding of orientation, we have compared the performance obtained from GM, LV and GM&LV using a fixed number of pixels (8). This

allows us to compare the decoding accuracy that can be obtained using various pixel sizes, while maintaining the number of pixels constant and equal to the maximal number of the (large) homologous voxels that overlap the orientation map (8). Using 8 voxels, Haynes and Rees (2005) obtained a decoding accuracy of ~73.8±5.8% (average over the data from 4 subjects, estimates from Haynes and Rees, 2005 Figure 1).

The mean decoding accuracy using the homologous pixel size and HbT responses in our study (~75.4±8.1%; Fig. 4-6, Table 4-III) is comparable to that obtained by Haynes and Rees in human subjects. In contrast, the decoding accuracy we obtained from HbR responses (65.9±8.6%) that are homologous to BOLD-fMRI responses, is smaller than that demonstrated by Haynes and Rees. We attribute this difference to the fact that Haynes and Rees made a pre-selection of voxels included as input to their decoding procedure. They first selected the 100 voxels that showed the highest response, then sorted these voxels according to the orientation bias they showed for the pair of decoded orientation stimuli. Thus, Haynes and Rees optimally pre-selected the features they used, from a large pool of voxels in V1. In contrast, the number of homologous voxels available to us when using OI of cat area 18 is limited to 8, due to the small region of this area which occupies the lateral gyrus and can thus be imaged by OI. Therefore, we could not perform feature selection as Haynes and Rees did. Of note, when using the optimal filtering and voxel size and the data from the entire ROI (not limited to 8 pixels), the decoding accuracy reached 100%. Importantly, our aim is to investigate the *mechanisms* underlying decoding by comparing accuracy obtained from several potential contributing mechanisms, rather than reaching the exact decoding accuracy obtained in human studies. Therefore, although using the homologous voxel size we do not reach the decoding accuracy demonstrated by Haynes and Rees (2005), our data and findings are valid for studying the *mechanisms* underlying decoding of oriented grating stimuli.

Table 4-III. Spatial frequency-dependent contributions to decoding using homologous voxels.

Frequency (cycles/mm)		0.00	0.09	0.19	0.28	0.28+
HbR	GM	50.8±2.3	54.7±4.5	60.3±8.4	65.2±9.8	65.2±9.8
	LV	51.8±2.9	56.1±4.8	60.2±8.3	63.0±8.7	63.0±8.7
	GM&LV	50.2±3.3	54.9±4.6	60.4±7.5	65.9±8.6	65.9±8.6
HbT	GM	50.5±4.8	61.8±3.8	69.2±7.9	73.9±8.4	73.9±8.4
	LV	51.3±3.6	59.0±4.6	66.7±7.0	70.4±6.6	70.4±6.6
	GM&LV	51.2±3.8	62.0±3.3	69.7±7.0	75.4±8.1	75.4±8.1

Comparing the performance of SVM, LDA and SLR in our study

SVMs are meant to extract optimal boundaries in data sets where the dimension of the features exceeds the number of available samples (for example, when there are many more fMRI voxels compared to the number of volumes in an experimental session). Hence SVMs are often used in situations where LDA fails because of ill conditioned covariance matrix.

However, in our current study, LDA showed slightly better performance than SVM (Suppl. Figures 4-1 to 4-4), because we deliberately limited the number of features in order to test the mechanisms underlying decoding with the same number of features/pixels independent of the pixel size.

Conclusions

We previously ruled out aliasing contributions to the decoding of fine-scale organizations by large voxels (Chaimow et al., 2011). In addition, we estimated that the contributions from local irregularities in V1 are very small, i.e. insufficient in accounting for the classification performance reported at 3 T using 3×3×3 mm^3 voxels (Chaimow et al., 2011); subsequently, we indeed ruled out contributions from local irregularities in the orientation map of cat area 17 (Chapter 3). Here we show that irregularities in the organization of cat area 18 can make relatively small contributions to decoding. Therefore, contributions from irregularities depend on the features of the organization, e.g. peak frequency and width of the frequencies band around it, and thus may change from one organization to another and across cortical areas.

Here we point to a reduced role of contributions from macroscopic vessels and from complex spatio-temporal filtering. Hypothesized mechanisms that may still contribute to successful decoding using BOLD-fMRI include low-frequency organizations (Chapter 3), stimulus specific edge effects (Carlson, 2014; Wang et al., 2014) and irregularities, depending on the features of the organization.

Appendix

Supplementary Figure 4-1. LDA, SLR and SVM decoding based on HbR following low-pass filtering.
Decoding accuracy using 3 different linear classifiers: linear discriminant analysis classifier, sparse logistic regression classifier, and support vector machine. The decoding rates are presented in a matrix, as a function of low-pass filtering cut-off frequency along the vertical axis and bin size along the horizontal axis. The color look up table represents decoding accuracy in percent.

Supplementary Figure 4-2. LDA, SLR and SVM decoding based on HbR following point-pass filtering.
The format of presentation is identical to that used for presenting Supplementary Figure 4-1.

Supplementary Figure 4-3. LDA, SLR and SVM decoding based on HbT following low-pass filtering.
The format of presentation is identical to that used for presenting Supplementary Figure 4-1.

Supplementary Figure 4-4. LDA, SLR and SVM decoding based HbT following point-pass filtering.
The format of presentation is identical to that used for presenting Supplementary Figure 4-1.

See next four pages for figures

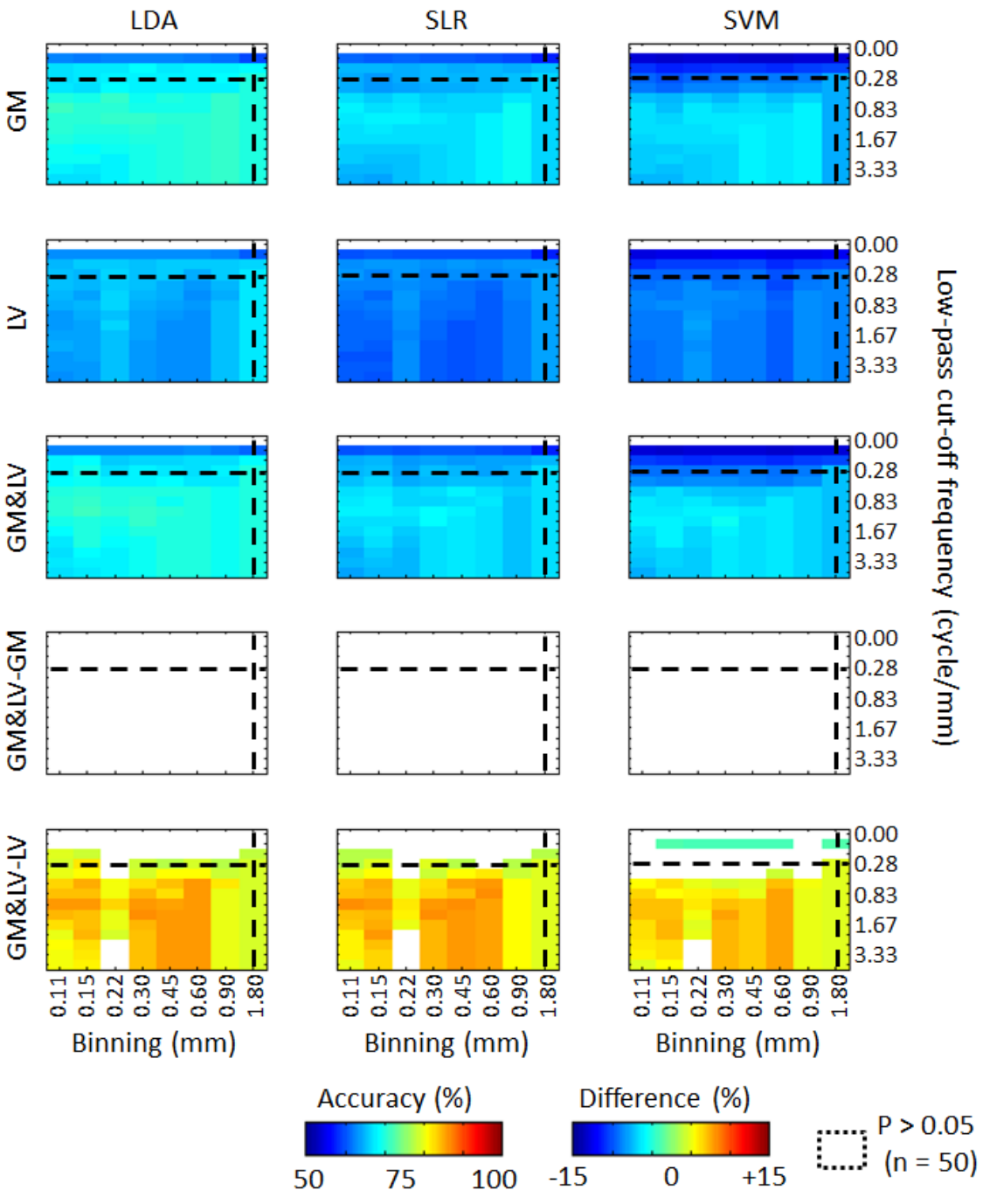

Supplementary Figure 4-1. LDA, SLR and SVM decoding based on HbR following low-pass filtering.

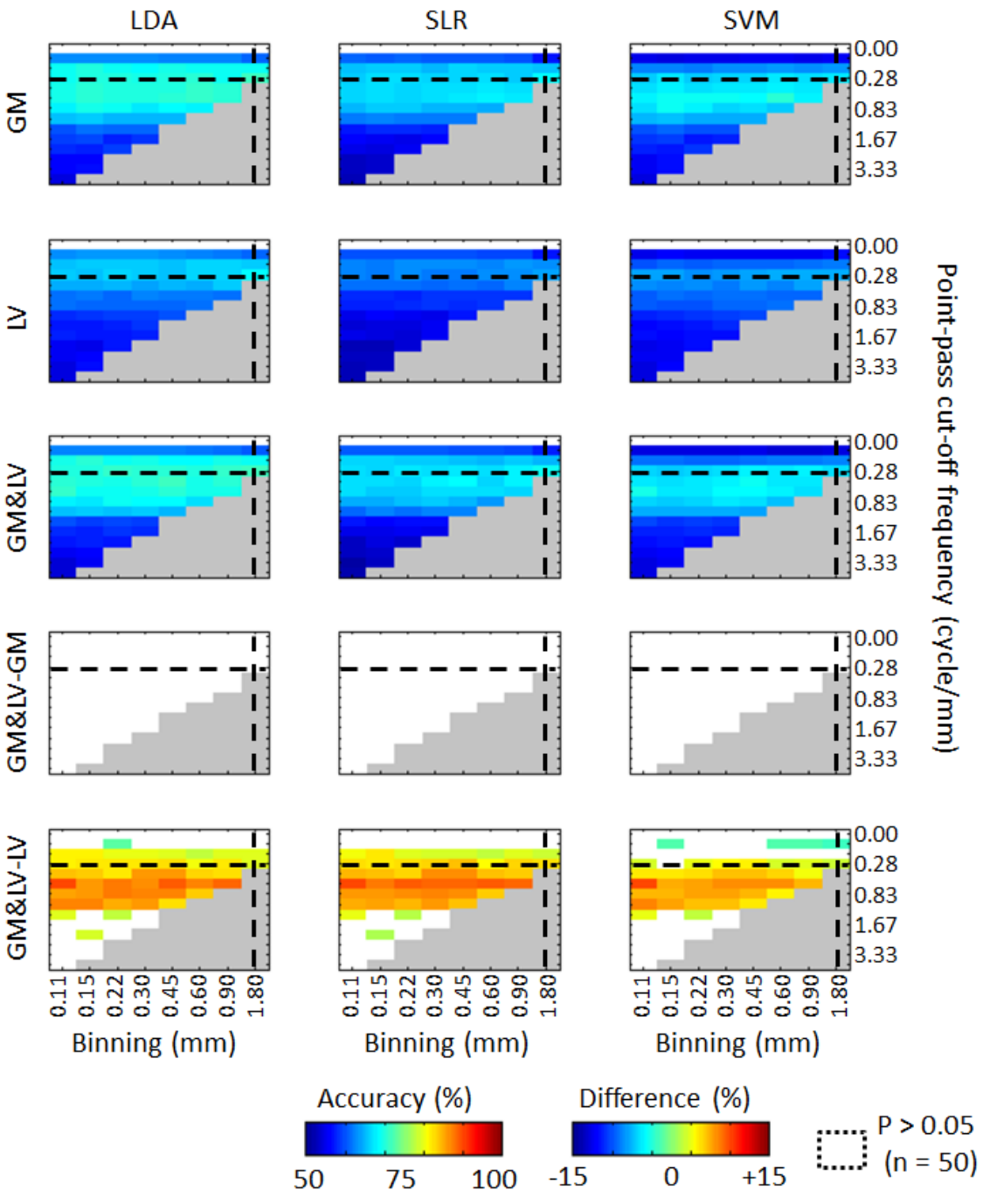

Supplementary Figure 4-2. LDA, SLR and SVM decoding based on HbR following point-pass filtering.

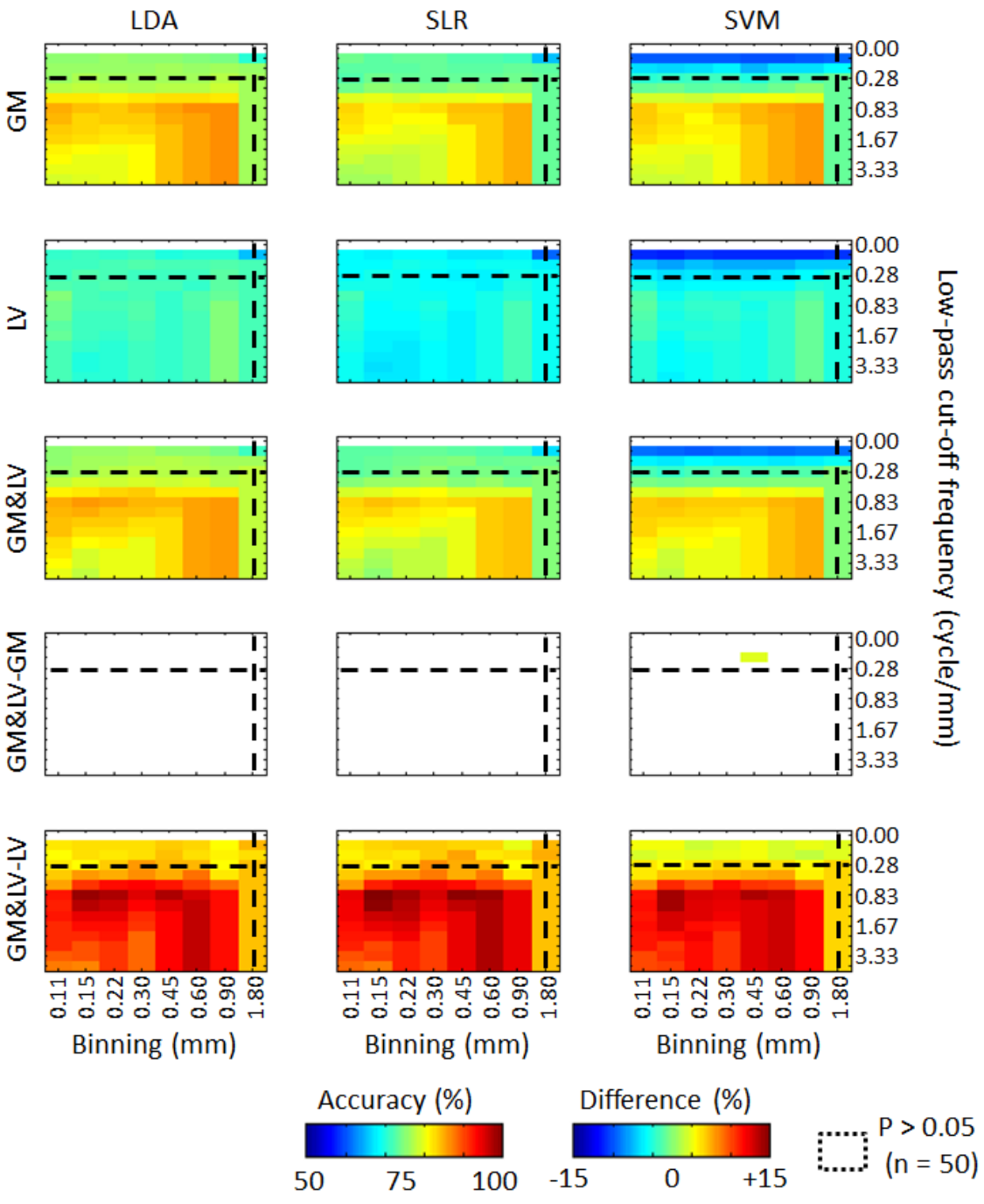

Supplementary Figure 4-3. LDA, SLR and SVM decoding based on HbT following low-pass filtering.

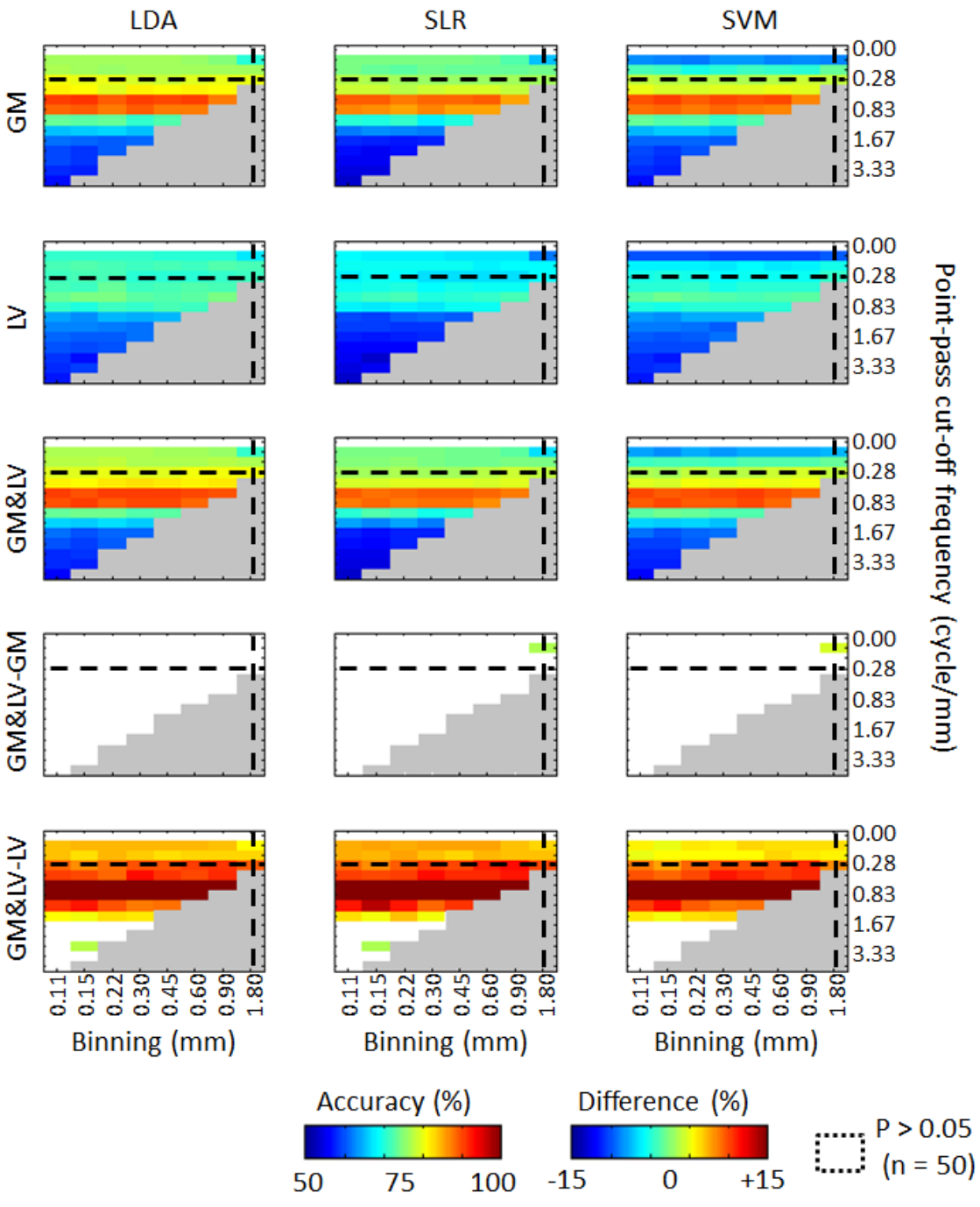

Supplementary Figure 4-4. LDA, SLR and SVM decoding based HbT following point-pass filtering.

Preface to Chapter 5

In Chapter 5, we address aim 2: 'To determine the functional and spatial specificity of deoxy- and total-hemoglobin response in vessels as a function of blood vessel diameter'. In Chapter 4, we demonstrated that macroscopic veins with diameter of 150 micrometer or larger do carry information for decoding oriented gratings, either when total-hemoglobin or deoxy-hemoglobin responses are considered. We arbitrarily selected the diameter of 150 micrometer as the limit for what can be described as 'macroscopic vessels', mentioned in the context of the mechanisms underlying the decoding of orientation. In Chapter 5, we investigate the functional/spatial specificity of deoxy-hemoglobin and total-hemoglobin responses from vessels with diameters in the range of 0.04 to 0.28 mm relative to responses from gray matter regions. The findings can be used for optimizing the data analysis, and to a lesser extent the data acquisition for fMRI-based decoding and high-resolution fMRI.

Spatial specificity of blood-oxygenation and blood volume signals in pial vessels and gray matter: implications for high-resolution fMRI

Ze Shan Yao, Martin Villeneuve, Alexandre Hutton, Pascal Kropf, Alexander Peplowski, Amir Shmuel

McConnel Brain Imaging Centre, Montreal Neurological Institute,
Departments of Neurology and Neurosurgery, Physiology and Biomedical Engineering
McGill University, Montreal, QC, Canada

Correspondence:
Amir Shmuel, Ph.D.
3801 University, room NW109
Montreal, QC, Canada H3A 2B4
E-mail: amir.shmuel@mcgill.ca

Keywords: High-resolution functional MRI, Blood oxygenation level dependent, BOLD, Cerebral blood volume, Cortical columns.

Acknowledgements: We thank Samuel Belanger and Frederic Lesage for the design and implementation of the apparatus for illumination using LEDs. This work was supported by grants from the Human Frontier Science Program (RGY0080/2008) and Natural Sciences and Engineering Research Council of Canada (NSERC Discovery grant RGPIN 375457-09) awarded to AS.

Abstract

Functional MRI (fMRI) detects metabolic and haemodynamic changes that accompany changes in neuronal activity. Therefore, fMRI is an indirect measure of changes in neuronal activity. An accepted, but not yet quantified concept is that the smaller the vessel diameter is the more spatially specific responses it shows relative to the site of changes in neuronal activity. Therefore, fMRI techniques for imaging cortical columns or layers aim to suppress signal contributions from large vessels. This in turn reduces image signal to noise ratio (SNR) and response contrast to noise ratio (CNR), forming a trade-off between these measures and spatial specificity. Suppressing signals exclusively from vessels that reduce spatial specificity and including signals from other vessels, either at the data-acquisition or the data-analysis stage, can maintain the spatial specificity while increasing CNR. Here we compare and quantify the spatial specificity of blood oxygenation and blood volume responses in gray matter and blood vessels as a function of vessel diameter. To this end, we optically imaged responses to oriented gratings in cat area 18. Using the Beer-Lambert law and Monte-Carlo simulations of partial path-length in heterogeneous tissue we computed relative changes of deoxy-Hemoglobin (HbR) and total-Hemoglobin (HbT) in gray matter and pial arteries and veins.

HbR responses in veins with diameter smaller than or equal to 0.12 mm showed selectivity to noise ratio, contrast to noise ratio and decoding accuracy measures comparable to those obtained from gray matter regions. HbT responses in veins and arteries of all tested diameters showed decreased orientation-selectivity measures relative to those obtained from GM regions. These selectivity measures decreased with increasing vessel diameter. For all tested vein and artery diameters, HbR response selectivity measures were lower than their HbT counterparts. HbT responses in veins and arteries showed comparable selectivity measures. The cortical frequency of the orientation maps we imaged is higher than any frequency of maps we expect to exist in the human brain. Therefore, if SNR and CNR are insufficient in high-resolution BOLD-fMRI of human cortical columns, one can integrate contributions from vessels with diameter smaller than or equal to 0.12 mm with no significant decrease in spatial specificity. For high-resolution CBV-fMRI, the smaller the diameter of contributing vessels, the higher the expected spatial specificity.

Introduction

The majority of functional brain imaging studies in humans rely on functional MRI (fMRI), and on imaging the Blood Oxygenation Level Dependent (BOLD) signal (Ogawa et al., 1990; Bandettini et al., 1992; Kwong et al., 1992; Ogawa et al., 1992). The BOLD signal reflects the content of deoxy-Hemoglobin (HbR) in an inverse manner (Ogawa et al., 1990). Increases in neuronal activity induce an increase in the local cerebral blood flow which exceeds the increase in oxygen consumption (Fox and Raichle, 1986; Bandettini et al., 1992), resulting in lowered HbR content and increased BOLD signal (Hoge et al., 1999). Thus, fMRI is an indirect measure of changes in neuronal activity: it detects metabolic and haemodynamic changes in brain areas that respond to a given task or stimulus. Therefore, fMRI responses may not necessarily be spatially specific to the site of increased neuronal activity. For high-resolution fMRI, it is highly desired to acquire data which colocalizes well with the site of increased neuronal activity. The current paper compares the functional/spatial specificity of blood oxygenation and blood volume responses in blood vessels and gray matter regions relative to the site of increased neuronal activity.

Gradient Echo (GE) Blood-oxygen-level-dependent (BOLD) contrast is the most widely used contrast of fMRI. Using GE BOLD-fMRI the oxygenation changes in cortical capillaries, which are expected to show spatially specific responses, generate the weakest response; while the oxygenation changes in draining veins, which are expected to be less spatially specific, give rise to the strongest signals. The draining veins' strong signal contaminates the capillaries' signals within the same voxel or in voxels downstream relative to the site of increased neuronal activity (Turner, 2002). Thus, for maintaining responses that represent the neuronal activity, researchers are often forced to discard the voxels that receive dominant signal contributions from large blood vessels prior to more in-depth analysis.

Imaging fine spatial organizations of the brain, such as orientation maps in the visual cortex, has been of particular interest in the field of fMRI. Over the past 10 years, there has been a growing interest in the research community to image the cortex at high spatial resolution using high magnetic-field fMRI (Shmuel et al., 2007; Yacoub et al., 2007). High resolution imaging enables probing brain responses at the scale of cortical columns, which are considered by many as important building blocks for encoding and decoding sensory information. However, high-resolution fMRI inherently suffers from low image signal to noise ratio (SNR), which in MRI is proportional to the volume of each voxel. Although the temporal SNR increases less rapidly with

increasing field strength relative to the image SNR, it still decreases with decreasing voxel volume too (Triantafyllou et al., 2005). Moreover, the commonly used Gradient-Echo BOLD fMRI response is dominated by contributions from large draining veins, independent of the field strength (Kim et al., 1994; Shmuel et al., 2007; Kim and Ogawa, 2012); therefore, it commonly shows responses downstream of the site of increased neuronal activity.

Although alternative contrasts such as Spin Echo (SE) BOLD-fMRI can suppress contributions from large veins at the data acquisition stage (Ogawa et al., 1993; Kim and Ogawa, 2002; Lee et al., 2002), it is not always practical to apply this sequence due to its significantly low signal-to-noise ratio compared to the GE sequence (Uludag et al., 2009). An alternative to SE BOLD-fMRI, which may allow capturing responses that are more spatially specific than those of GE BOLD-fMRI, is cerebral blood volume (CBV). The first CBV-fMRI studies used contrast agents injected into the blood circulation, e.g. gadolinium diethylene-triamine-penta-acetic acid (Gd-DTPA) in humans (Belliveau et al., 1991). More recently, monocrystalline-iron-oxide-nanoparticles (MION) were injected to the circulation of animal models (Mandeville et al., 1998; Vandueffel et al., 2003). Recently, there have been several advances in CBV-based functional imaging that do not require the injection of a contrast agent (MOTIVE, Kim and Kim, 2005;VASO, Lu and van Zijl, 2012; VERVE, Stefanovic and Pike, 2005). Moreover, MION-CBV functional imaging measured with either GE or SE sequences shows higher relative responses in the capillary-dense layer 4 of the cat visual cortex than BOLD-fMRI measured with the same sequences (Zhao et al., 2006). This finding supports the notion of CBV regulation at a sub-millimeter scale and emphasizes the potential of CBV imaging for high-resolution fMRI in human subjects.

Therefore, by optimizing fMRI for increasing contributions from blood vessels that show spatially specific responses, one can optimize the trade-off between spatial specificity and SNR in high-resolution BOLD- and CBV-fMRI. The asymmetric spin echo (ASE) pulse sequence provides higher partial nullification of contributions from large veins relative to suppression of contributions from capillaries, leading to a middle ground between SE and GE sequences. A key simulation study showed that the more asymmetric the acquisition of the pulse, the closer to GE the resultant signal is (Boxerman et al., 1995). Therefore the asymmetry parameter of ASE controls a trade-off between spatially specific fMRI contrast of low SNR, and fMRI contrast of high SNR but poor spatial specificity. This trade-off can possibly be optimized by setting the level of SE asymmetry. A different way of reducing the non-spatially specific contributions of larger venules

to the SE-BOLD functional signal is by shortening the duration of the readout window (Goense and Logothetis, 2006). Increasing the read out duration to include signals away from the peak increases T2* contributions that emerge from larger vessels, while increasing image SNR. Optimizing the trade-off between long readout for higher SNR and short readout for spatial specificity, or by setting an optimal asymmetry parameter in asymmetric SE, can benefit from information on the spatial specificity of veins and venules of various diameters.

Increasing specificity in functional magnetic resonance imaging can be done in an even more straightforward manner during the data analysis stage. This can be done by combining fMRI with techniques for estimating the vessel size based on changes in blood oxygenation (Jochimsen and Moller, 2008). Voxels that reflect contributions from a range of vessel diameters known to show non-spatially specific responses can be discarded.

Therefore, a direct physiological investigation of the spatial specificity of blood vessels can inform the choice of fMRI data acquisition parameters and data analysis for optimizing the trade-off between spatial specificity and SNR. Based on the cortical surface area supplied or drained by arteries and veins of various diameters, it is a commonly accepted hypothesis that the larger the vessel, the less spatially specific responses it generates. However, to the best of our knowledge, the spatial specificity of cortical and pial draining veins has not been quantified.

Here, we quantify the physiological spatial specificity of responses measured from pial arteries and veins relative to those obtained from gray matter regions. To this end, we applied Optical Imaging of Intrinsic Signals (OI-IS, Grinvald et al., 1999). We spectrally decomposed HbR and total-Hemoglobin (HbT) responses obtained from cortical capillaries, arteries and veins, using the Beer-Lambert law and Monte-Carlo simulations of partial path-length in heterogeneous tissue. Our findings can guide fMRI data-acquisition and data-analysis for optimizing spatially specific responses together with SNR.

Materials and Methods

The methods used for preparing the animals were similar to those used in previous OI-IS studies in anesthetized cats (Grinvald et al., 1999; Shmuel and Grinvald, 2000). These methods are outlined below, whereas differences and new methodological aspects are described in detail. The analysis was performed using code written in MatLab (The MathWorks, Natick, MA), while incorporating utility functions from the MatLab R2013 platform.

Surgical procedures and animal preparation

All procedures were performed according to the guidelines of the Canadian Council on Animal Care (CCAC) and were approved by the animal care committees of the Montreal Neurological Institute and McGill University.

Data were obtained from 10 hemispheres of 8 adult cats, weighing 3.0-4.5 kg. The animals were premedicated with glycopyrrolate (Sandoz Canada, 0.01 mg/kg, I.M.), acepromazine maleate (Atravet®, Boehringer Ingelheim, 0.2 mg/kg, S.C.) and ketamine (20 mg/kg IM). Deep anesthesia was induced by inhalation of 5% of isoflurane (Baxter Medical) mixed with 100% O_2. The level of isoflurane was gradually lowered and maintained at 2% for the duration of the surgery. Blood oxygen saturation and heart rate were monitored using pulse oximetry (Nonin Medical, Inc.; during surgery, the heart rate was kept between 150 and 180 beats/minute). The end tidal CO_2 was monitored using a capnometer (Capnomac Ultima, Datex). Depth of anesthesia was determined by verifying lack of response to clamping the inter-digital web of the posterior paws and by monitoring the heart rate.

Following endotracheal intubation and cephalic vein cannulation for intravenous administration of fluids, the animal was artificially ventilated with a mixture of medical air and O_2 (80%/20%) using a respiratory pump (Ugo Basile, 6025). Lidocaine 2% (Lidocaine Neat, Pfizer) was administered at all points of pressure and incision. The animal was placed in a stereotaxic frame (David Kopf instrument) modified for allowing visual stimulation. End-tidal CO_2 was kept between 30 and 38 mm Hg by adjusting the rate and stroke volume of the respiratory pump. The core temperature was maintained at 38°C by a feedback-controlled heating pad (Homeothermic Blanket Systems, Harvard Apparatus). The animals were continuously infused intravenously with a solution consisting of 5% Dextrose in lactated Ringer's injection solution (Abbott Laboratories) diluted with sterile water and mixed with a muscle relaxant, gallamine triethiodide (Sigma-Aldrich). The mixture was adjusted so that the solution had an osmolality of 310 mOsm with an injection rate of 6ml/kg/h of fluid and 10mg/kg/h of gallamine.

The skull was opened above area 18 by drilling a circular hole with an approximate 18 mm diameter centered on Horsley–Clarke coordinates AP +4 and ML 0. A stainless steel circular chamber with inner diameter of 20 mm was implanted onto the skull. The dura mater was resected, and the chamber was filled with silicon oil and sealed with a round perspex cover.

At the end of the surgical procedures, gas anesthesia was switched from isoflurane to halothane (Sigma-Aldrich). Throughout the imaging sessions, the halothane level was kept at 0.7-1.0% and the heart rate was maintained at 160-180 BPM. The animal was mechanically ventilated at a rate of 25-40 strokes per minute and a volume of 10-15 ml/kg, maintaining the end-tidal CO2 within 32-38 mm Hg. The gas mixture was adjusted within the range of 100% medical air to 80% medical air / 20% O2, in order to keep the oxygen saturation level at ≥ 94%. Finally, the animal's temperature was kept between 37.9 and 38.1 degrees.

The pupils were dilated with local application of phenylephrine hydrochloride 2.5% (Mydfrin®, Aventix Animal Health). The eyes were protected using contact lenses with zero power; they were focused on a tangent screen at a distance of 30 cm using external lenses with power determined by retinoscopy. The retinal vessels, blind spot and area centralis of each eye were back projected onto the screen (Bishop et al., 1962).

Optical imaging

Cortical images were obtained using a differential data acquisition system (VDAQ Imager 3001, Optical Imaging Ltd., Rehovot, Israel) equipped with a 12-bit depth Pantera 1M60 camera (Teledyne Dalsa, Waterloo, Ontario, Canada) and a macro lens (Nikon, AF Micro Nikkor, 60 mm, 1:2.8 D). The camera was mounted above the optical chamber and was aimed such that its optical axis was perpendicular to the cortical surface. The camera was focused on the surface of the cortical region of interest (ROI), ensuring that the surface of the gray matter and the cortical pial blood vessel were in focus. The ROI was limited to area 18 in one hemisphere; we imaged this ROI with a matrix of approximately 1000-by-500 pixels, 70-80 pixels/mm and 50μm depth of field). The camera frame rate was set at 20Hz, binned every 2 frames to yield a data frame rate of 10Hz. We imaged the cortex at this high frame rate, under illumination of 2 LEDs with centre wavelengths of 530 nm and 617 nm, respectively (Fig. 5-1A). The power to these 2 LEDs alternated at every other frame, based on the camera's frame toggle signal. Hence, the frame rate obtained under the illumination of each of the 2 LEDs was 5Hz. Green and orange LEDs were then used to compute changes in content of HbR and HbT (see section on spectral decomposition below), where HbR and HbT are analogous to BOLD-fMRI and CBV-fMRI, respectively. At the end of each imaging session, a high-resolution image of a ruler was taken without changing the camera lens' magnification. The ruler image served as a scaling reference, in order to compute the precise number of pixels/10 mm, and from this measure further extract the resolution in mm/pixel.

Visual stimuli

The visual stimuli were generated using the Matlab R2010a platform (The MathWorks, Natick, MA) and Psychophysics toolbox 3.0.8 (Brainard, 1997), run on a Quad-CPU MacBook Pro 6.2 (Mac OS 10.6.7) with a NVIDIA GeForce GT 330M graphic card. The stimuli were presented on a 19 inch Dell 1908FPt monitor set at 60Hz refresh rate. The luminance was gamma corrected using Eye-one display II (X-rite, Grand Rapids, MI). The mean across all pixels of the maximum luminance of the monitor was set at 33 cd/m^2. The monitor was positioned at a distance of 30 cm from the animal's eyes, subtending 60° × 45° of the visual field. It was shifted contralateral to the imaged hemisphere by approximately 15°.

The animals were stimulated binocularly, using drifting high contrast rectangular-wave gratings with a spatial frequency of 0.15 cycles per degree, a duty cycle of 50%, and a temporal frequency of 4 Hz. The main set of stimuli included 17 conditions. In one control/baseline condition, the screen remained gray and no stimulus was presented. Each of the remaining 16 conditions presented one of eight differently oriented gratings, drifting in a direction orthogonal to the orientation. The main set of stimuli spanned both direction and orientation spaces at a resolution of 22.5°.

Stimulation paradigm

From each of the hemispheres, we obtained 30-50 trials of data, where each trial consisted of acquiring 17 time-series, each of which associated with one of the 17 conditions. All 17 conditions were presented once in each trial with a randomized order of presentation, in order to average out any systematic effects of stimulus presentation order. During each presentation, we acquired data over a period of 12 second: 2 seconds in which the gratings were static, 5 seconds of moving gratings, followed by 5 seconds of static gratings. To allow for the relaxation of activity-dependent vascular changes, each 12 seconds period of data-acquisition was followed by 8-second inter-stimulus interval (ISI). The stimulus was switched to the static grating of the next condition at the beginning of the ISI.

Data preprocessing

(1) All data frames were inspected, in order to verify that there were no large discontinuities in image intensity due to failure of the illumination system. (2) The two image time-series obtained from stimuli of the same orientation but opposite directions of motion were averaged together,

obtaining the image series associated with orientation. This was done separately for images obtained under illumination at 530 nm and 617 nm. (3) In order to separate arteries from veins, we first computed the average over 5 trials of all frames acquired from 2 to 7 seconds following the stimulus onset. We divided the result by the average of the baseline frames acquired over the 2 sec before stimulus onset, thus obtaining the two average cortical activation maps obtained under illumination at 530 nm and 617 nm. (4) In order to compensate for the slight LED illumination decay over time, we then pursued the exact same procedure for the control baseline condition, and divided the two response maps described in (3) by the corresponding maps obtained under the control condition. (5) The two corrected response maps were averaged over all 8 orientations, and then inspected in order to make a preliminary differentiation of arteries and the veins (Fig. 5-1B). (6) We then designated 3 representative pixels in regions of an approximately 0.1 mm wide vein appearing as white under 617 nm, an artery with approximately the same diameter appearing as black under 617 nm, and gray matter. We computed the HbR and HbT activation time courses from these 3 pixels using spectral decomposition methods (see next section). (7) Next, taking into account that the HbT response in arteries is early relative to the HbR response in veins (Moon et al., 2013), we computed the average of the normalized relative to peak time courses of the HbT response from the artery and HbR response from the vein (Fig. 5-1C, purple-colored curve). We defined the response duration as the range of frames that showed a response higher than 50% peak response in this combined time course (Fig. 5-1C, black dotted lines). In order to compute the response maps in each of the HbR and HbT modalities, we integrated the response over the response duration. (8) The orientation response maps obtained under each of the two illumination conditions were separately concatenated in order to create a global data matrix for further analysis: [Y X O T], where Y and X denote the pixels in the ROI, O denotes the orientations and T represents the number of trials. (9) Finally, the data matrices were converted to HbR and HbT data matrices using the spectral decomposition method described below.

Masks of segmented blood vessels

From the raw images and from the averaged activation map, we created separate masks of arteries and veins with corresponding vessel diameter at each point (Fig. 5-3C). To this end, the raw image obtained under illumination at 530 nm image (Fig. 5-2A) was first convolved with 1-dimensional Difference of Gaussians (DOG) wavelets of 10 different scales ([3 5 7 9 13 19 27 39 55 81] pixels) horizontally and vertically (Fig. 5-2B). The different wavelet scales capture blood

vessels of different diameters; i.e. a small blood vessel of diameter of 3 pixels would show high amplitude in an image convolved by a wavelet of 5 pixels but would show zero amplitude in an image convolved by a wavelet of 81 pixels. Each convolution created one additional parameter at each pixel; hence we added 20 coefficients to the one parameter of intensity value. Then a normalization was performed for each of the coefficient map so that the coefficient's range in the parameter space is scaled between 0 and 1. The end result of this convolution stage were 21 images, each consisting of normalized values between 0 and 1. We then performed the segmentation of the image to pial vessels and gray matter in a pixel-wise manner, using a nearest-neighbour algorithm (Hong et al., 2012) with the 21 parameters as its feature space. The schematic representation of how this algorithm works in a 2-parameter situation is explained in Figure 5-2B (right panel). The user initially assigns a blood vessel class or gray matter class to each of 20 reference pixels from the raw image. In the schematic example, the squares represent reference gray matter pixels and the triangles represent reference blood vessel pixels. The algorithm then uses the Euclidian distance in the feature space (dashed lines) to classify the non-referenced pixels, according to the assigned class of the closest reference point.

Figure 5-1. High resolution OI-IS of HbR and HbT. (See next page for figure)
A) Raw images acquired under illumination using a green LED (530 nm) and orange LED (617 nm). **B)** Activation map of cortex under illumination with the 2 wavelengths (average of 5 trials and all 8 orientations from one hemisphere). The frames from 2 to 7 seconds after the onset of stimulus were averaged and divided by the average of frames from 2 to 0 seconds before the onset of stimulus. The gray-level bar represents the change in photons captured by the camera sensor during the response relative to the pre-activation baseline state. C) Typical time courses of HbT and HbR responses relative to their respective baseline concentrations (Table 5-I). The time-courses were sampled from a 3x3 pixels area within gray matter, small artery and small vein indicated by the gray, red and blue arrows in B, respectively. For computing these time courses, we averaged over responses of 5 trials and all 8 orientations. The panel to the right demonstrates the range of frames that were used for the computation of the main cortical response maps. This range was determined by averaging the normalized time-courses of change in HbR content in vein and change in HbT content in artery (thick purple curve in the panel to the right). Each of these 2 time courses was first normalized by dividing it by its own peak. Then the two normalized time courses were averaged, and the response duration was determined as the range of frames for which the averaged time course showed amplitude higher than 50% of its own peak (black dashed line).

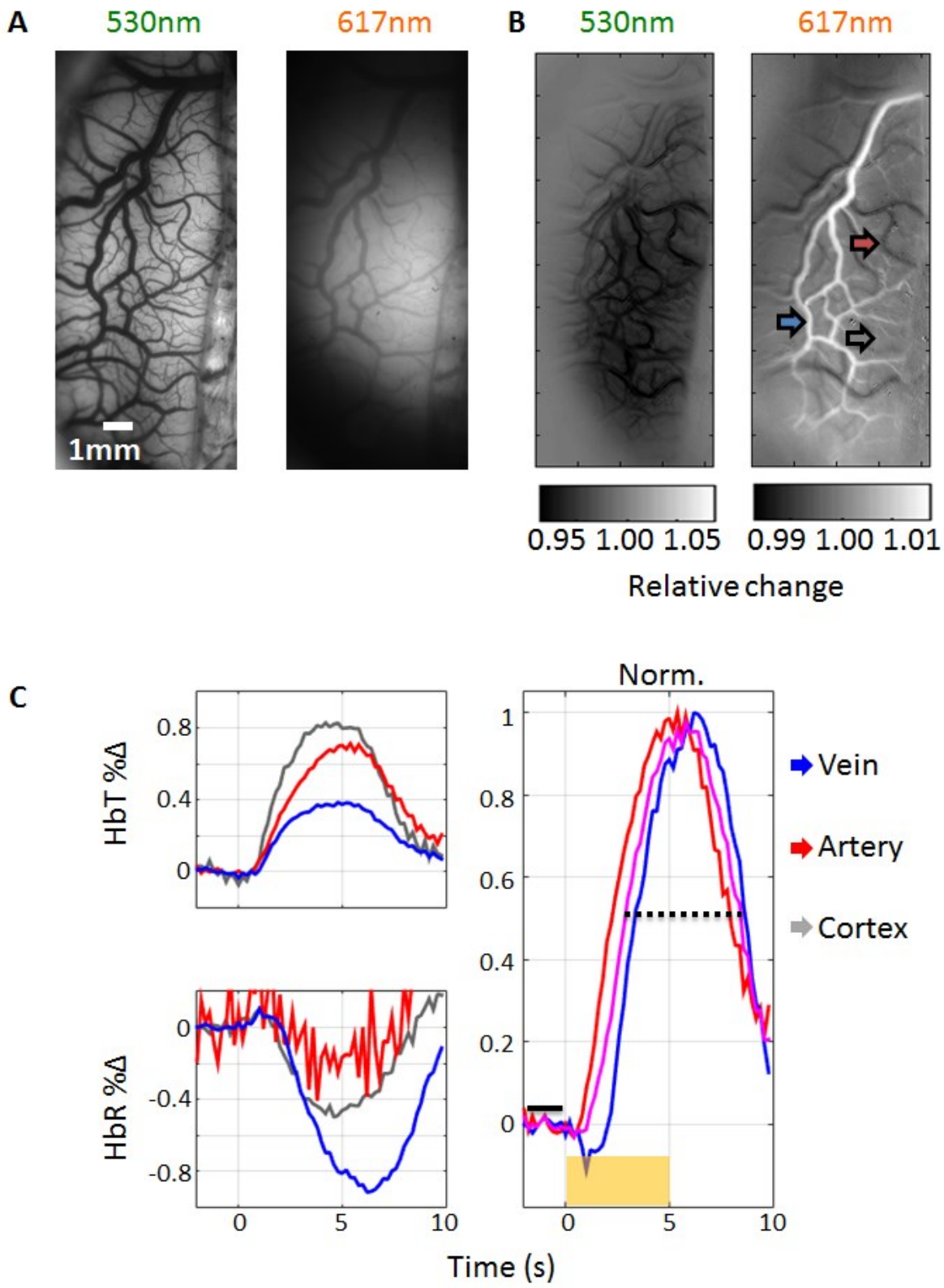

Figure 5-1. High resolution OI-IS of HbR and HbT responses. (See previous page for legend)

Figure 5-2. Segmentation of an image of the cortical surface to gray matter, pial veins and pial arteries.
A) The raw image taken under green illumination used for creating the mask of veins and arteries. Based on this image, we assigned pixels to the blood vessels or gray matter classes using a nearest-neighbor classification algorithm. **B left)** 1D Difference of Gaussians (DOG) wavelets of 10 different scales (ranging from 3 pixels to 80 pixels, ≈ 0.045 to 1.2 mm for the overall DOG, including the positive center and negative peripheral troughs) were convolved horizontally and vertically with the raw image. Each convolution created one parameter at each pixel. Hence we added 20 coefficients at each pixel to the original gray scale intensity value. **B right)** Schematic 2D representation of nearest-neighbor algorithm using the resultant 21 parameters as its feature space. We first manually assigned 20-30 reference points (blood vessel pixels or gray matter pixels) from the raw image to one of the blood vessels or gray matter classes. In the schematic description, squares represent gray matter reference pixels and triangles represent blood vessel reference pixels. For the remaining, non-reference pixels, the algorithm used the Euclidian distance in the 21 dimensions feature space to determine whether they were closest to a blood vessel reference pixel or to a gray matter reference pixel of those initially selected by the user. Based on the Euclidean distance, the algorithm assigned the pixel of interest accordingly. In this schematic example, the black dot represents a pixel which was classified as a gray matter (square) pixel, based on its shortest distance to the reference point (square) marked with orange arrow. **C)** Resultant blood vessel mask from the application of the classification algorithm on the image acquired under green illumination. **D)** The blood vessel mask is further separated into arteries and veins by first identifying large veins and arteries based on their respective responses under 617 nm and the smoothness of the arteries. Smaller vessels were then classified by tracking the vessels connected to the identified seed large vessels (small arteries connected to the large arteries; small veins connected to the large veins) and verifying the classification based on their response under 617 nm.

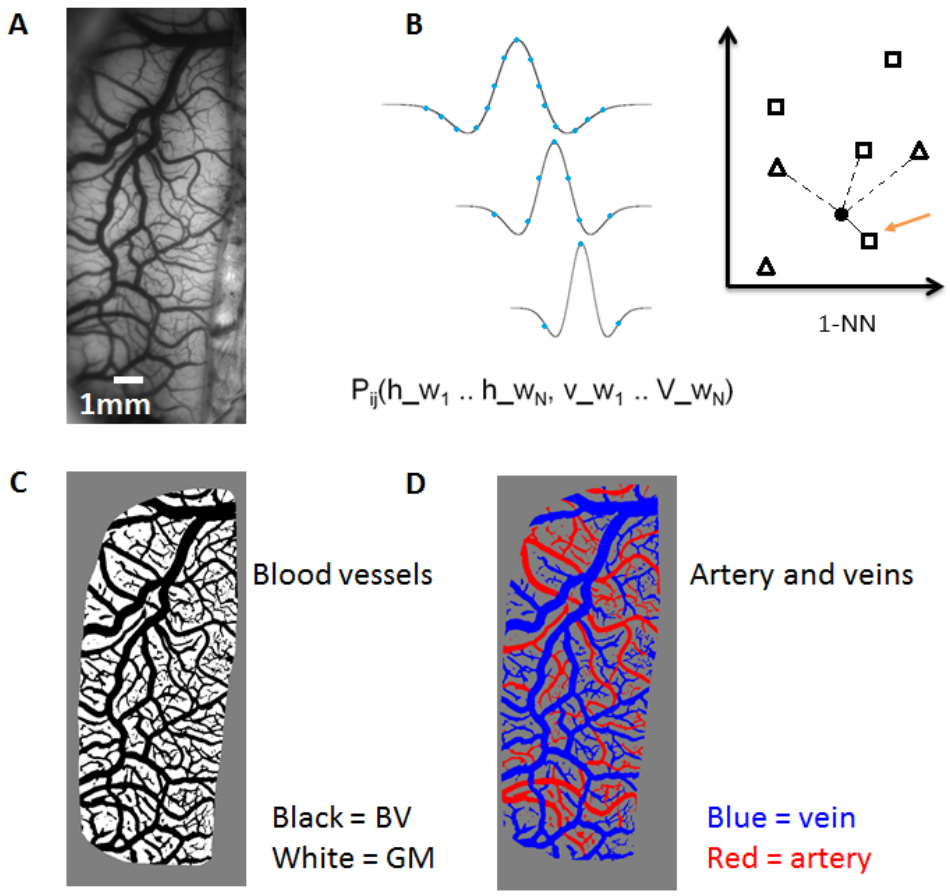

In the schematic example, the black circle represents a non-referenced pixel which will be classified as a gray matter pixel (square). We then obtained two separate masks for arteries and veins (Fig. 5-2D) by further segmenting the blood vessel mask (Fig. 5-2C). This separation was based on identifying large diameter veins and arteries (diameter ≈ 0.1 mm or wider), based on the smoothness of arteries (Hillman et al., 2007) and the different response of these large vessels under illumination of 617 nm (whitening in large veins, darkening in large arteries; Fig. 5-1B). We then classified smaller vessels as arteries or veins by tracking the vessels connected to the identified seed large vessels (small arteries connected to the large arteries; small veins connected to the large veins) and verifying the classification based on their response under 617 nm.

Once the blood-vessel mask was created, the approximate local diameter of each blood vessel was computed using an algorithm we developed as follows. We first identified all pixels which were part of the skeleton of a vessel (Fig. 5-3A, red pixels; we employed Matlab's function bwmorph). For each of these skeleton pixels, we then computed the shortest line segment of all lines that passed through the pixels' coordinates at different angles and reached the edges of the blood vessel (Fig. 5-3A, thin blue lines). The thin line that passed through the skeleton pixel represented the diameter of the blood vessel at that location. The non-skeleton pixels that had one blue line crossing them took a value equivalent to the diameter of the corresponding skeleton pixel. The pixels that had multiple blue lines overlapping them took the average diameter of the corresponding skeleton pixels. The pixels that had no blue lines overlapping them were assigned with the average value computed over the neighboring pixels. Because the diameter tends to be overestimated near branching points, we set an upper threshold to the diameter of the pixels near the branching point (pixels within the dotted black circle, which is the smallest circle centered on the branching of the skeleton and reaching at least one edge; Fig. 5-3B). They were assigned with diameters no larger than the maximal diameter computed for pixels between the dotted circle and the solid circle (the solid circle was the smallest circle centered on the branching of the skeleton and reaching all 3 edges associated with the branching). We then obtained maps of artery diameter and vein diameter, based on our previous delineation to veins and arteries (Fig. 5-2D).

Finally, we chose 8 partially-overlapping masks as representative spatial distributions of the blood vessel segments with various diameters (Fig. 5-3D). Each image shows a mask of pial veins or arteries whose diameters fell within the range indicated on top of the image in micrometers. These 8 masks were used for calculating the blood vessel response selectivity as a function of vessel diameter (Figs. 5-5 to 5-8, green asterisks).

Figure 5-3. Assigning diameter to the blood vessels. (See next page for figure)
A) The diameter of the blood vessels at each pixel that belonged to a skeleton of a vessel was estimated by finding the minimal line segment that crossed the pixel and reached the edge of blood vessels (thin blue lines). The non-skeleton pixels that overlapped with one blue line took the value that was equivalent to the diameter of the corresponding skeleton pixel. The pixels that overlapped with multiple blue lines took the average diameter associated with the corresponding skeleton pixels. The pixels that did not overlap with blue lines were assigned the average diameter of their neighboring values. **B)** Because the diameter tends to be overestimated near branching points, we set an upper threshold of diameter assigned to the pixels near the branching point (pixels within the dotted black circle, which is the smallest circle centered on the branching of the skeleton and reaching at least one edge). They were assigned with diameters no larger than the maximal diameter computed for pixels between the dotted circle and the solid circle (the solid circle was the smallest circle centered on the branching of the skeleton and reaching all 3 edges associated with the branching. **C)** Resultant diameter maps of the veins and arteries. **D)** Eight partially-overlapping masks that show representative spatial distributions of the blood vessel segments with various diameters. Each image shows a mask of pial blood vessels whose diameters fell within the range indicated on top of the image in microns. For example, the upper right mask represents pixels that lie within veins whose diameter was larger than 280 and smaller than 627 micrometers. These 8 masks were used for calculating the blood vessel response selectivity as a function of vessel diameter (data points in Figures 5-5 to 5-8).

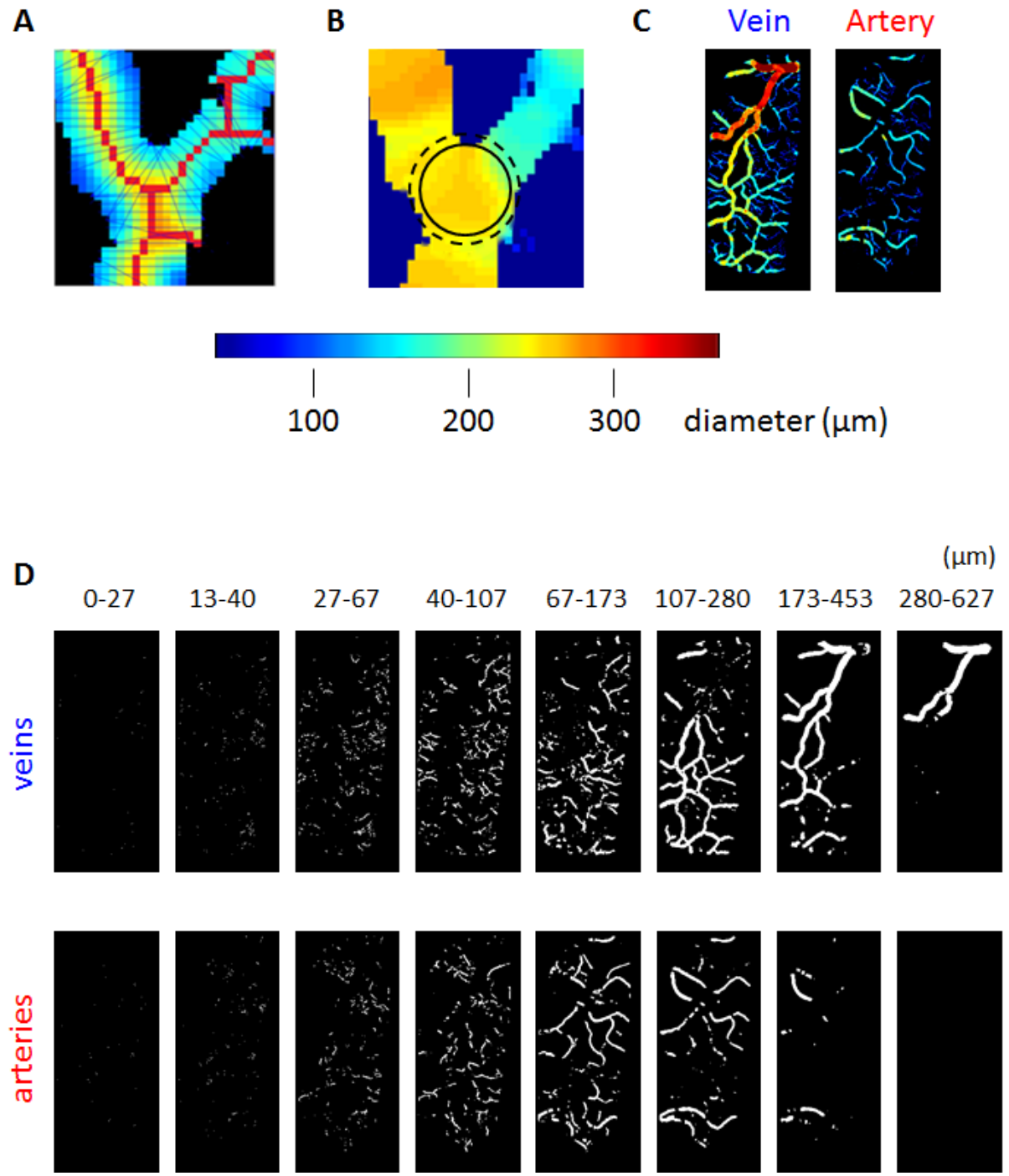

Figure 5-3. Assigning diameter to the blood vessels. (See previous page for legend)

Spectral decomposition and path-length correction

Data obtained under an illumination of 530 nm and 617 nm were transformed into HbR and HbT time series using the modified Beer-Lambert law. The Beer-Lambert law describes the change in light absorption as the sum of changes in concentration of various chromophores with different absorptions at each wavelength. In equation 1-10 (Appendix) we separated the contributions of oxyHb and deoxyHb as a function of light absorption in order to transform the total change in light absorption into changes in concentrations of these chromophores. The Modified Beer-Lambert law also takes into account the dependence of path-length on illumination wavelength, denoted by $1/p_\lambda$ in the equation, which affects the calculation when one's interest is to measure the reflected light from the specimen (see Suppl. Fig. 5-1 and Appendix). Given the LED illumination we used at 530 nm and 617 nm, the respective path-length ratio in gray matter regions would be ~1:5 (Brieu et al., 2010; Dunn et al., 2005; Kohl et al., 2000). Table 5-I shows approximate baseline concentrations of total hemoglobin, hemoglobin saturation and path-lengths that we used for the decomposition. The oxygen saturation level is the average value we measured in our experiments over data-acquisition periods and hemispheres (95.0±3.6%), whereas the oxygen saturation in capillaries and veins was obtained from (Edwards and Mayall, 1998; Dunn et al., 2005; Baetge and Matthews, 2012). Note that the lower saturation in capillaries relative to vein was also demonstrated by Vovenko (1999). The baseline HbT value in GM was based on Dunn et al. (2005), while those in arteries and veins were estimated by Hines (2013). We estimated the path lengths by first computing absorbance based on the baseline concentrations of HbO and HbR and their respective absorption coefficients under illumination of 530 nm and 617 nm. We then mapped the absorbance to path length based on Fig. 1B in Kohl et al. (2000).

Table 5-I. Baseline concentrations and Path lengths of Hb species.

	Saturation [HbO]/[HbT]	Baseline [HbT]	Baseline [HbO]	Baseline [HbR]	Path length under 530nm	Path length under 617nm
Capillaries	60%	100 μM	60 μM	40 μM	0.534 mm	2.54 mm
Artery	95.0%	2000 μM	1900 μM	100 μM	0.0775 mm	0.717 mm
Vein	70%	2000 μM	1300 μM	700 μM	0.0778 mm	0.393 mm

According to Table 5-I, under illumination wavelength of 617 nm, photons that emerge out of veins with diameter larger than 0.197 mm (= 0.393/2) are expected in the majority of cases to have their origin within the vessel, while photons that emerge out of veins with diameter smaller than 0.197 mm are expected to have mixed origin: photons that pass within the vessel and also within the gray matter nearby and beneath, before passing within the vessel. Note that we refer here to 0.197 mm = 0.393 / 2, taking into account that a photon needs to first penetrate the tissue, then emerge out of it in order to be detected by the camera. These heterogeneous sources were corrected according to relative path-length travelled within and out of the vessel in order to estimate the HbR and HbO concentration changes separately within the vessel and the underlying gray matter (see Appendix 1).

High-pass filtering of individual components within the ROI

From each hemisphere, we computed a 4D response data matrix M = [I J O T] where I and J are 2D pixel indices, O is an orientation index, and T is a trial index. We then defined our region of interest as the region that showed the most prominent orientation modules (Fig. 5-4B; yellow dotted curve). We then applied a high-pass filter with cut-off threshold of 0.2 cycle/mm (signal associated with cycles longer than 5 mm were filtered out) separately for gray matter, veins, and arteries. This step was performed in order to remove any differences in the global cortical response to certain orientations, in order to focus our study on the fine scale structure of the orientation map. To this end, we separately selected regions corresponding to gray matter, veins or arteries, thus creating 3 rectangular ROI matrices of the same size. We then filled in the missing values with a robust spline smoothing algorithm (Garcia, 2010), separately for each of the matrices corresponding to gray matter, veins and arteries. The 2D filling in was followed by the 2D spatial high-pass filtering. Lastly, we reapplied the masks of GM, arteries, and veins to the filtered response maps, which yielded separate response maps of GM, arteries and veins, now consisting of only high frequencies underlying the columnar organiaztion.

Evaluation of functional/spatial specificity

We computed quantitative measures of differential contrast of orientation, orientation selectivity, and decoding accuracy analyzes within the ROI. For the orientation selectivity analysis, we defined the Selectivity Index (SI) as the magnitude of the vectorial sum of responses across all orientations, normalized (divided) by the sum of absolute responses to all orientations. Because

the stimuli we used are mapped to cortex in a fine scale organization, this ratio represents how spatially specific the responses from blood vessels are relative to the underlying columnar arrangement of the orientation modules over the cortical surface. We defined the selectivity index map as the map of the pixel-wise SI averaged across trials. We defined the noise map as the pixel-wise standard deviation of the trial-by-trial SI, and the SI to Noise (SINR) map as the SI map divided by noise map.

$$SI_{i,j} = \frac{\sum_{o=1}^{8}\left[\frac{1}{T}\sum_{t=1}^{T}\left(M_{i,j,o,t}\times e^{-i\frac{\pi}{4}o}\right)\right]}{\sum_{o=1}^{8}\left[\frac{1}{T}\sum_{t=1}^{T}\left(M_{i,j,o,t}\right)\right]} \quad (1)$$

$$SINoise_{i,j} = stdev_t\left(SI_{i,j,t}\right) \quad (2)$$

$$SINR_{i,j} = \frac{SI_{i,j}}{SINoise_{i,j}} \quad (3)$$

From the selectivity index map, we obtained the selectivity index range by computing the standard deviation across the map's pixels. The same operations were performed for the selectivity index noise map and the SiNR map.

$$SIRange = stdev_{i,j}\left(SI_{i,j}\right) \quad (4)$$

$$SINoiseRange = stdev_{i,j}\left(SINoise_{i,j}\right) \quad (5)$$

$$SINRRange = stdev_{i,j}\left(SINR_{i,j}\right) \quad (6)$$

The differential contrast measures the difference in the amplitude of cortical responses to 2 orthogonally oriented grating stimuli (Fig. 5-4A). We defined the contrast map for each pair of orthogonal orientations as the pixel-wise difference of cortical responses to orthogonally oriented gratings averaged across trials. We defined the noise map as the pixel-wise standard deviation of the trial-by-trial contrast. Finally we defined the contrast-to-noise ratio map as the absolute value of the contrast map divided by the noise map (Fig. 5-4B). We then separately obtained the contrast map, noise map, and contrast-to-noise map for each of the 4 pairs of orientations.

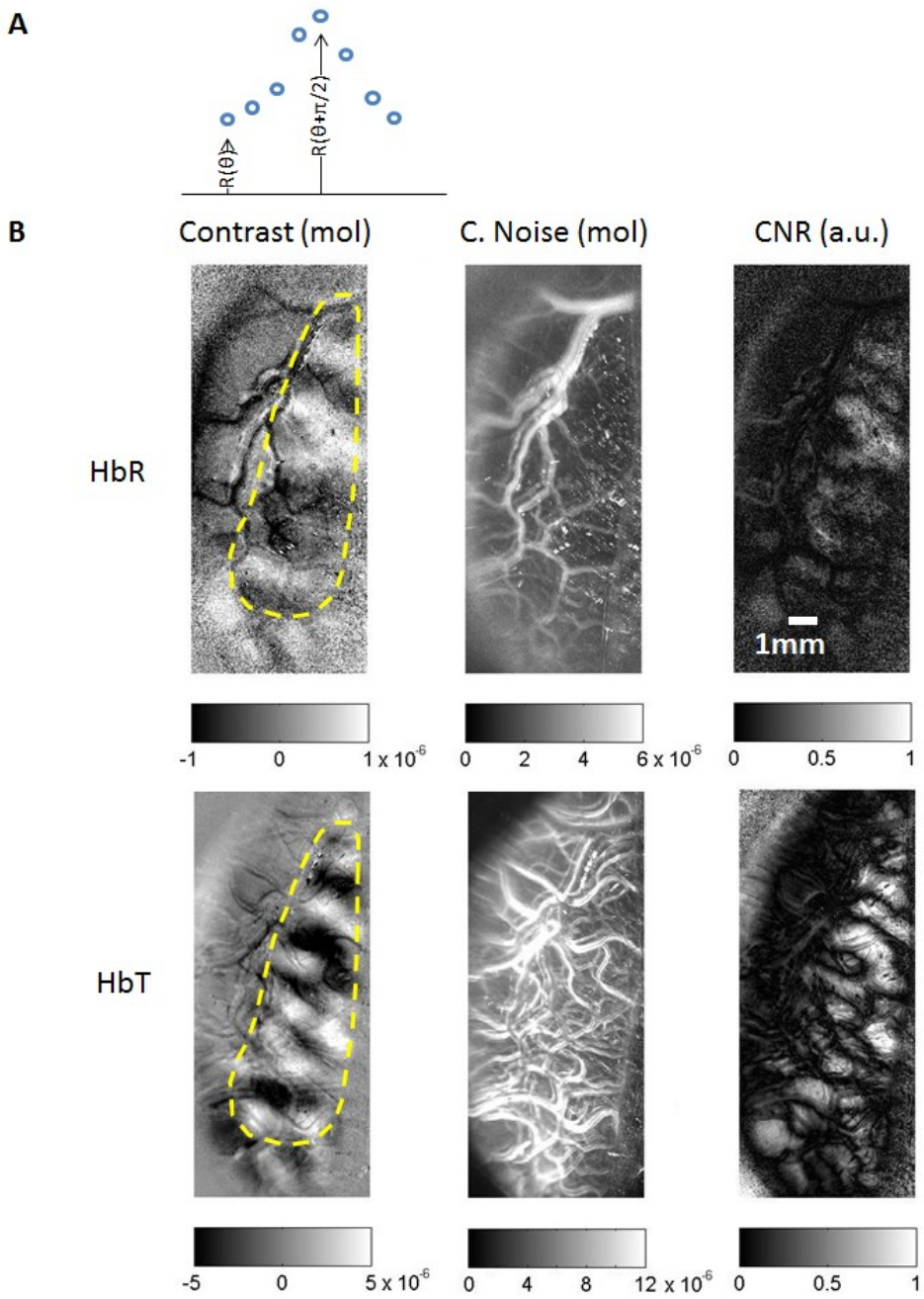

Figure 5-4. Differential analysis maps.
A) Typical responses to 8 oriented gratings from one pixel. We defined the contrast as the averaged difference over 4 pairs of orthogonal orientations (here, 1 pair is shown as θ and θ+90°). **B)** Differential contrast: the mean difference between cortical response maps of 2 orthogonal stimuli computed across trials. Noise: standard deviation of the difference across trials. CNR: absolute value of the mean difference divided by the noise. **Top)** Maps of the above defined values from HbR response. **Bottom)** Maps of above defined values from HbT response. The manually selected region enclosed by the dotted yellow line indicates the most responsive area with clear orientation modules, which was used for statistical evaluation of functional/spatial specificity in gray matter, vein, and artery.

$$Contrast_{i,j,o} = \frac{1}{T}\sum_{t=1}^{T}\left(M_{i,j,o,t} - M_{i,j,o+4,t}\right) \quad (7)$$

$$CNoise_{i,j,o} = stdev_t\left(Contrast_{i,j,o,t}\right) \quad (8)$$

$$CNR_{i,j,o} = \frac{|Contrast_{i,j,o}|}{CNoise_{i,j,o}} \quad (9)$$

From the CNR map, we obtained the contrast range by computing the standard deviation across the map's pixels and then averaging the standard deviation across the 4 orientation pairs.

$$CNRRange = \frac{1}{4}\sum_{o=1}^{4} stdev_{i,j}\left(CNR_{i,j,o}\right) \quad (10)$$

Lastly the decoding analysis evaluates the information about the orientation stimulus that can be extracted from the functional response. We used a linear support vector machine (SVM) classifier for pair-wise decoding of orthogonal orientation stimuli (Kamitani and Tong, 2005). During the training process, the classifier assigns weights at each pixel from the cortical response map that best separates one orientation condition from the other. Then a trained classifier will predict what were the presented stimuli associated with new inputs, such as the response map $M_{i,j}$ below, that were not used during the training process.

$$if \quad \sum_i \sum_j \omega_{i,j} M_{i,j} + \omega_0 = \begin{cases} \geq 0 \\ \\ < 0 \end{cases} \quad then \quad \begin{matrix} Orientation\ A \\ \\ Orientation\ B \end{matrix} \quad (11)$$

where ωi,j are the trained weights of pixel i,j and ω0 is the bias term computed during training. There is a sigmoidal relationship between the CNR and the decoding accuracy (Chaimow et al., 2011). Therefore, decoding accuracy is expected to monotonously (but not necessary linearly) increase with increasing CNR.

To obtain a fair evaluation when comparing the different regions of gray matter and pial blood vessels, for the feature space of the SVM we randomly chose a fixed number of pixels from each of the compared modalities. We used a cross-validation method in order to avoid potential over-fitting of the classifier (Kohavi, 1995). We randomly picked half the trials for training the classifier and the remaining trials for testing/validating. The decoding accuracy was marked based on the validation dataset, by comparing the classifier's output to the presented stimulus.

Statistical tests (Student *t*-test & FDR correction)

The contrast maps (Fig. 5-4B) were multiplied point by point with the 8 blood vessels maps (Fig. 5-3D), yielding separate contrast maps from GM, artery and vein regions. We computed the standard deviation of the differential contrast values across pixels within each of these partial maps. We term this standard deviation 'contrast range': it assigns a quantitative value of functional/spatial specificity. The rationale is that differential cortical responses to orthogonal stimuli are distributed approximately as a Gaussian distribution, and more selective responses are associated with a larger contrast range (Chaimow et al., 2011). We then linearly interpolated in-between the measured values, in order to present the mean in the range of 40 µm to 280 µm at a resolution of 10 µm (Fig. 5-5 to 5-8; see the next paragraph for the rationale of limiting the range). In addition, we applied paired two-tailed Student-t statistical tests within this range to compare the functional specificity measures for each vessel diameter relative to a constant (unity) or to a distribution of values in GM (in the specific case of decoding accuracy). For clarity, we report within the text only 2 classes of p-values, smaller than 0.05 or smaller than 0.001. The detailed numerical values are summarized in Table 5-II. In addition to the paired t-tests, we applied non-parametric rank-sum tests to the same comparisons, and obtained similar p-values (not shown).

The number of samples for each t-test was 10 hemispheres for gray matter and small to medium size blood vessels. For larger vessels, where the number of available samples decreased, we limited the t-test to vessels diameters smaller than or equal to 280 micrometers, for which we had data from 7 hemispheres. Thus, any reference we make to 'all *tested* blood vessel diameters' refers to vessels with diameter between 40 and 280 micrometers. In contrast, references we make to 'all vein diameters in our sample', refer to N = 73 measurements, each representing an average selectivity measure obtained for one diameter range (Fig. 5-3) from one hemisphere, pulled together from all 10 hemispheres and 8 diameter ranges (in some of the hemispheres, not all diameter ranges existed) . 'All artery diameters in our sample', refers to N = 68 measurements pulled together from 10 hemispheres and 8 diameter ranges.

Because we deal with multiple t-tests with several points along the dimension of different diameters of the blood vessels, we applied the FDR correction to multiple comparisons, thus obtaining the Q-values from our P-value distribution (Benjamini and Hochberg, 1995).We then used a Q-threshold of 0.05 as our threshold of statistical significance. The same procedures were repeated for noise, CNR, selectivity index, SI noise, SiNR, and decoding accuracy maps.

Results

Response time course

We first compared the time-courses of cortical HbR and HbT content responses. We sampled the time-courses from 3 locations: an artery and a vein of approximately 0.1 mm diameter and a gray matter region (Fig. 5-1B arrows). The highest relative change in HbR occurred within the vein (1.5%); in contrast, the highest relative changes in HbT occurred within the gray matter (1.0%) (Fig. 5-1C).

Functional selectivity of responses in blood vessels relative to gray matter

Selectivity Index, Noise and SiNR of HbR and HbT responses in veins and arteries

Figure 5-5 compares the tuning curve's response selectivity index obtained from blood vessels of various diameters relative to that obtained from gray matter. The detailed numerical values are summarized in Table 5-II.

In veins, the SI obtained from HbR responses was on average smaller than that obtained from GM regions (the ratio averaged over all vein diameters was 0.78±0.13 mm, see green asterisks for specific *tested* diameters, two-tailed t-test, FDR corrected, $q < 0.05$). It decreased with increasing vessel diameter (slope = -0.39/mm, $p < 0.05$, F test). For all *tested* vein diameters, the SiNoise did not show significant differences relative to that in GM. However, the changes in SiNoise with increasing diameter were on average opposite to those in SI. Therefore, the SiNR showed steep decreases with increasing vein diameter (slope = -1.21/mm, $p < 0.001$). The SiNR obtained from veins with diameter ≥ 0.14 mm within the range of our *tested* diameters ($0.04 \leq d \leq 0.28$ mm) was smaller than that obtained from GM.

In arteries, the HbR-based selectivity index was approximately constant and significantly lower than that obtained in GM regions for all *tested* artery diameters (two-tailed t-test, FDR corrected, $q < 0.05$, ratio averaged over all artery diameters pulled together: 0.67±0.16, $p < 0.001$). The noise remained approximately constant and comparable to that obtained from GM. Thus, with increasing artery diameter, the SiNR across all *tested* diameters remained approximately constant and significantly lower than that obtained from GM.

The HbT-based SI from both veins and arteries were lower than those obtained from GM throughout all *tested* vessel diameters (two-tailed t-test, FDR corrected, $q < 0.05$, the averaged ratios over all diameters pulled together were 0.63±0.15 mm for veins and 0.61±0.17 mm for

arteries. With increasing vein and artery diameter, the SI further decreased (slope = -1.37/mm and -1.51/mm, respectively, $p < 0.001$, F-test). In contrast, the noise remained approximately constant and comparable to that obtained from GM regions. Thus, for all tested vessel diameters, the SiNR was lower than that obtained from GM regions, and further decreased with increasing vein and artery diameter (slope = -1.36/mm and -1.63/mm, respectively, $p < 0.001$, F-test

In summary, in both arteries and veins and for both HbR and HbT, the selectivity indices obtained from all *tested* blood vessel diameters were lower than those obtained from GM. The noise from all *tested* blood vessel diameters remained comparable to that obtained from GM. The HbR-based SiNR obtained from veins was not significantly different than that in GM for vein diameters smaller than or equal to 0.14 mm. The HbR-based SiNR in arteries was significantly lower than those in GM for all *tested* blood vessel diameters. The HbT-based SiNRs in veins and in arteries were significantly lower than those in GM for all *tested* blood vessel diameters, and decreased with increasing vessel diameter.

Figure 5-5. Selectivity indices of veins and arteries relative to gray matter. (See next page for figure)
Statistical testing of the null hypothesis that Selectivity Index, SiNoise, and SiNR in veins and arteries are not different than those in gray matter ('GM' on the horizontal axis). Each blue and red asterisk represents the mean of the selectivity measure for the corresponding vessel diameter. The dark curve within each panel represents the interpolated average selectivity measures with distance between two adjacent interpolated values equal 10 μm. To this end, we linearly interpolated between the measured values from the 8 different groups of vessel diameters, and the slightly different diameters obtained from different hemispheres due to slight sampling resolution differences. The dashed line represents a linear regression of the response as a function of the blood vessel diameter computed over the data points. The green asterisks indicate vessels diameters showing responses with statistically significant different selectivity than that observed in gray matter (2 tail t-test, FDR correction, $q < 0.05$). The average measure curve and the statistical tests were computed and plotted for vessel diameters in the range of 0.04-0.28 mm.

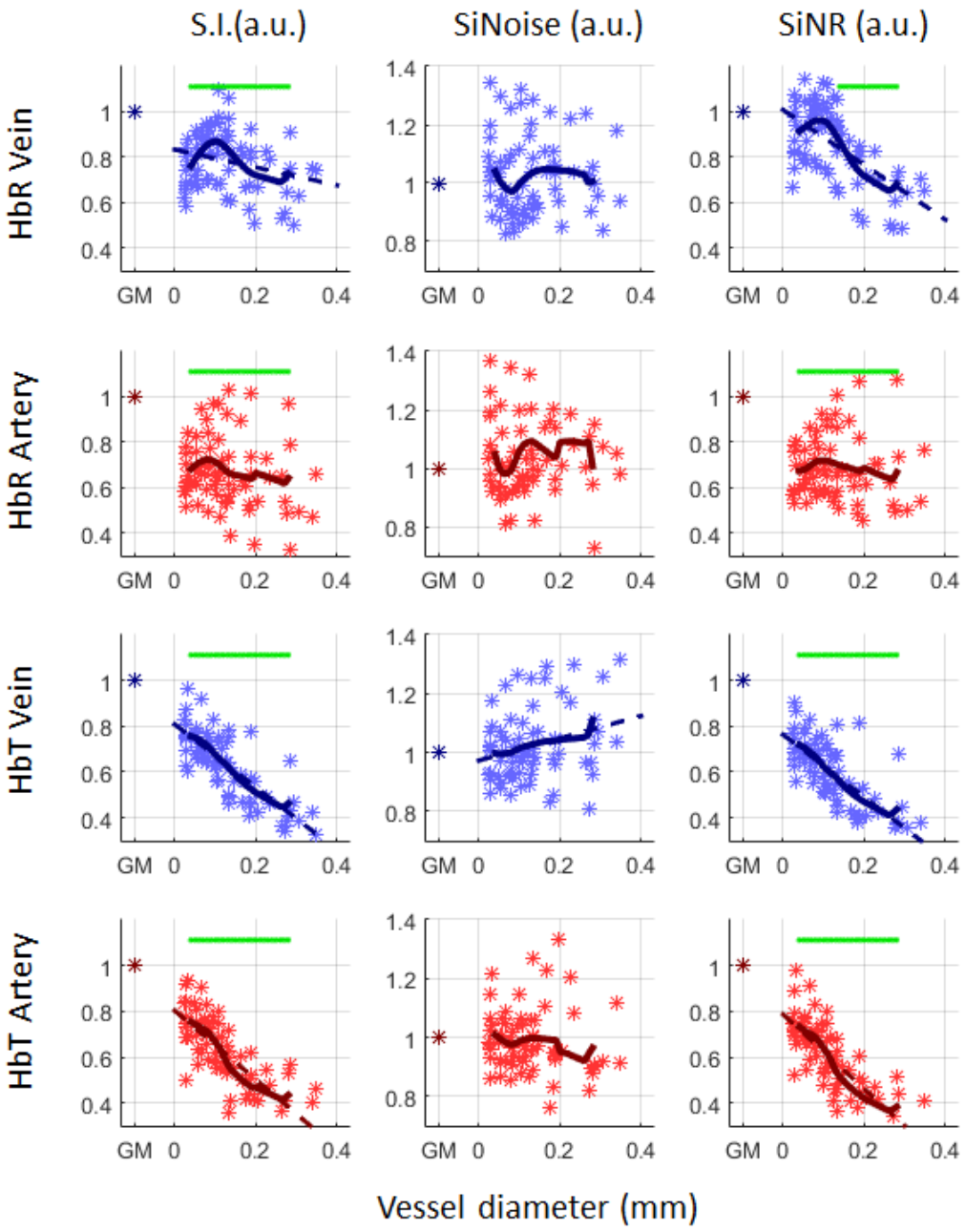

Figure 5-5. Selectivity indices of veins and arteries relative to gray matter. (See previous page for legend)

Contrast to noise ratio and Decoding accuracy of HbR and HbT responses in veins and arteries

Figure 5-6 compares the difference in responses to orthogonal stimuli (CNR), and the information these responses convey (decoding accuracy), obtained from blood vessels relative to those obtained from gray matter. The detailed numerical values are summarized in Table II.

In veins, the CNR of HbR responses averaged over the vein diameters pulled together across our sample was smaller than that obtained from GM region (0.91±0.12 mm, $p < 0.001$, two-tailed t-test). Moreover, with increasing vein diameter, the CNR measure of functional specificity decreased (slope = -0.78/mm, $p < 0.001$, F-test). Statistically significant decreases in CNR were obtained for *tested* vein diameter of 0.16 mm or larger (green asterisks, two-tailed t-test, FDR corrected, $q < 0.05$). The mean decoding accuracy averaged across all vein diameters pulled together was 77±12% ($p < 0.001$, two-tailed t-test). Decoding accuracy decreased with increasing vessel diameter (slope -75%/mm ($p < 0.001$, F-test), respectively.

In arteries, the CNR of HbR responses averaged over all artery diameters in our sample was smaller than that obtained from GM region (0.83±0.14, $p < 0.001$, two-tailed t-test). The HbR-based CNR was lower than that obtained from GM and remained approximately unchanged across all *tested* blood vessel diameters (see green stars, $q < 0.05$, two-tailed t-test, FDR corrected). The mean decoding accuracy computed across all artery diameters in our sample was not different than chance level (51±6%) and significantly lower than that obtained from GM ($p < 0.001$, two-tailed t-test). It decreased moderately with increasing artery diameter (slope -23%/mm, $p < 0.01$, F-test).

In veins and arteries, the HbT-based CNR averaged across blood vessel diameters in our sample was lower than that obtained in GM (0.69±0.15 and 0.68±0.16, respectively, $p < 0.001$, two-tailed t-test). The CNR decreased with increasing vein and artery diameters (slopes of -1.13/mm and -1.23/mm, respectively, $p < 0.001$, F-test). Statistically significant decreases in CNR were obtained for all *tested* vein and artery diameters (green asterisks, two-tailed t-test, FDR corrected, $q < 0.05$). The mean decoding accuracies averaged over all vein and artery diameters in our sample were 89±12% and 86±16%, respectively, lower than that obtained from GM ($p < 0.001$, two-tailed t-test). It decreased with increasing vein and artery diameters (-96%/mm and -132%/mm, respectively, $p < 0.001$, F-test).

In summary, the CNR obtained from HbR-based responses in veins and arteries was significantly lower than that obtained from GM for vein diameter of 0.16 mm and larger and across all *tested* artery diameters. Although the decoding accuracy was higher than chance level, it was lower than that obtained in GM regions for vein diameters larger or equal to 0.13 mm. The decoding accuracy in arteries with each of the diameters within the range we tested was lower than that obtained in GM. The CNR and decoding accuracy obtained from HbT responses across all *tested* vein and artery diameters were lower than the corresponding measures obtained in GM. The CNR and decoding accuracy of HbT responses in veins and arteries decreased with increasing vessel diameter.

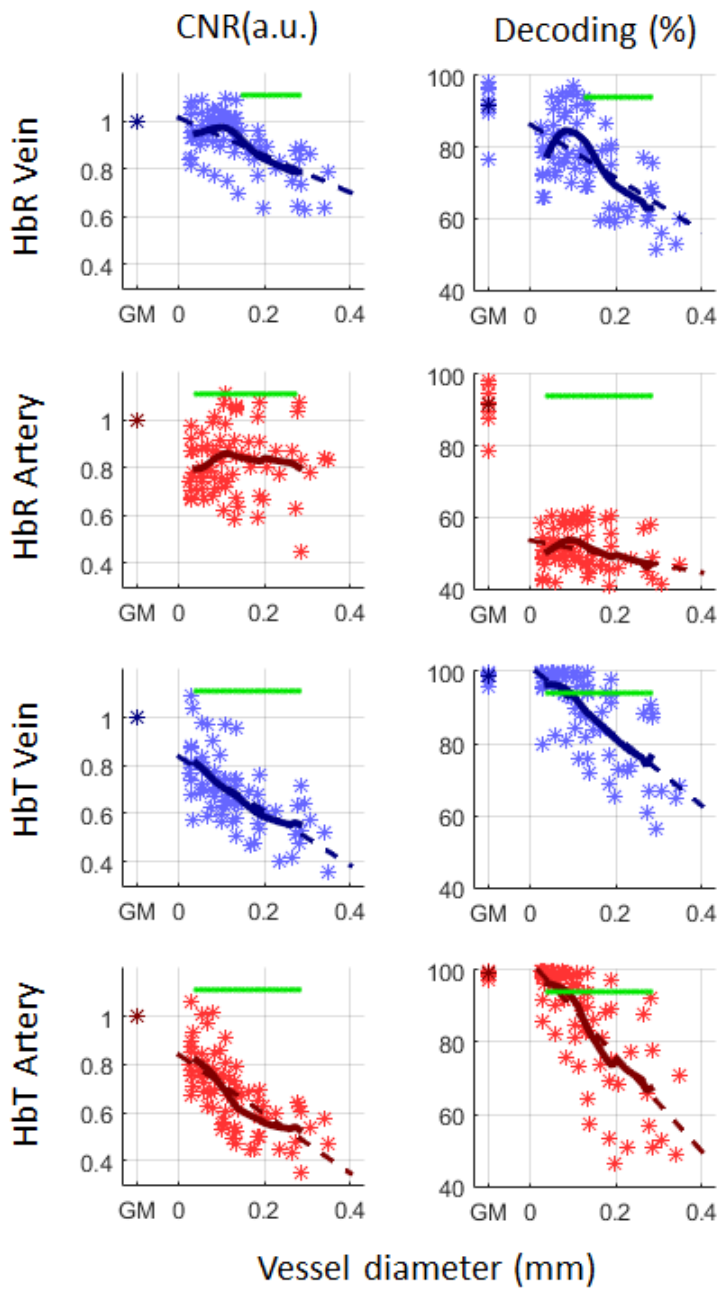

Figure 5-6. CNR and Decoding accuracy obtained from veins and arteries relative to gray matter. Statistical testing of the null hypothesis suggesting that CNR and Decoding accuracy in veins and arteries are not different than those in gray matter ('GM' on the horizontal axis). The format of presentation is similar to that used for Fig. 5-5.

Table 5-II. Comparison of response selectivities in blood vessels relative to gray matter.

	μ	σ	p_μ	α	β	p_ α	min	max
Ve-HbR-SI	0.78	0.13	E-20	-0.39	0.83	0.03	0.04-	0.28+
Ve-HbR-SiN	1.03	0.13	0.11	-0.05	1.03	0.79		
Ve-HbR-SiNR	0.85	0.17	E-9	-1.21	1.01	E-8	0.14	0.28+
Ve-HbR-CNR	0.91	0.12	E-7	-0.78	1.02	E-6	0.16	0.28+
Ve-HbR-Acc	77	12	E-57	-75	86	E-6	0.13	0.28+
Ar-HbR-SI	0.67	0.16	E-26	-0.37	0.72	0.10	0.04-	0.28+
Ar-HbR-SiN	1.05	0.18	0.02	0.04	1.05	0.87		
Ar-HbR-SiNR	0.68	0.15	E-26	-0.21	0.71	0.33	0.04-	0.28+
Ar-HbR-CNR	0.83	0.14	E-14	0.05	0.82	0.80	0.04-	0.28+
Ar-HbR-Acc	51	6	E-62	-23	54	0.01	0.04-	0.28+
GM-HbR-Acc	92	5						
Ve-HbT-SI	0.63	0.15	E-30	-1.37	0.81	E-15	0.04-	0.28+
Ve-HbT-SiN	1.02	0.12	0.14	0.38	0.97	0.03		
Ve-HbT-SiNR	0.59	0.15	E-32	-1.36	0.76	E-13	0.04-	0.28+
Ve-HbT-CNR	0.69	0.15	E-25	-1.13	0.84	E-8	0.04-	0.28+
Ve-HbT-Acc	89	12	E-61	-96	101	E-10	0.04-	0.28+
Ar-HbT-SI	0.61	0.17	E-28	-1.51	0.80	E-13	0.04-	0.28+
Ar-HbT-SiN	0.98	0.11	0.24	-0.21	1.01	0.19		
Ar-HbT-SiNR	0.58	0.17	E-29	-1.63	0.79	E-15	0.04-	0.28+
Ar-HbT-CNR	0.68	0.16	E-25	-1.23	0.84	E-9	0.04-	0.28+
Ar-HbT-Acc	86	16	E-51	-132	102	E-11	0.04-	0.28+
GM-HbT-Acc	99	1						

μ: mean computed over all pulled measured data points
σ: standard deviation computed over all pulled measured data points
p_μ: p-value associated with the statistical significance of difference of the mean relative to unity, or, for decoding accuracy, relative to the mean obtained from GM regions
α: slope of the regression line
β: intercept of the regression line
p_α: p-value associated with the statistical significance of the regression

min/max: smallest/largest BV diameter (within the tested range, 0.04-0.28 mm) that showed mean value significantly different than 1, or, for decoding accuracy, different than the mean obtained from GM regions

Note that the smallest and largest vessel diameters we tested were 0.04 and 0.28 mm, respectively; the entries mention '0.04-' or '0.28+', since the min diameter is likely to be narrower and the max diameter is likely to be wider in a more complete and larger data-set.

Functional selectivity of HbR compared to HbT

Selectivity Index, Noise and SiNR of HbR and HbT responses in veins and arteries

Figure 5-7 (top half) compares the tuning curve response selectivity index obtained from HbR vs. HbT responses, in blood vessels of various diameters and gray matter. The detailed numerical values are summarized in the Table 5-III.

In veins, the SI obtained from HbR was lower than that obtained from HbT responses across all *tested* diameters (green asterisks, $q < 0.05$, two-tailed t-test, FDR corrected; average ratio across diameters pulled together 0.62±0.16, $p < 0.001$, two-tailed t-test). The SI obtained from HbR relative to HbT increased with increasing vein diameter (slope = 1.05/mm; $p < 0.001$, F-test). Across all *tested* diameters, the SiNoise from venous HbR and HbT responses showed no significant differences. The SiNR obtained from HbR relative to HbT responses showed a profile similar to that observed for SI.

In arteries, the SI obtained from HbR was lower than that obtained from HbT responses across all *tested* diameters (green asterisks, $q < 0.05$, two-tailed t-test, FDR corrected; average ratio across all diameters pulled together 0.55±0.15, $p < 0.001$, two-tailed t-test). The SI obtained from HbR relative to HbT increased with increasing vein diameter (slope = 0.98/mm; $p < 0.001$, F-test). The SiNoise from HbR and HbT responses showed no significant differences, but their ratio (Hbr/HbT) increased with increasing artery diameter (slope = 0.50, $p < 0.05$). The SiNR obtained from HbR relative to HbT responses showed a profile similar to that observed for SI.

Figure 5-7. Relative selectivity indices obtained from HbR and HbT responses in veins and arteries. (See next page for figure)
Top half: statistical testing of the null hypothesis that the ratios of Selectivity Index, SiNoise, and SiNR of HbR responses relative to HbT responses in veins and arteries (cyan and purple asterisks, respectively) are not different than unity. **Bottom half:** statistical testing of the null hypothesis that Selectivity Index, SiNoise, and SiNR of HbR and HbT responses (blue and amber asterisks, respectively) in veins relative to arteries are not different than unity. The dark curve within each panel represents the interpolated average ratio of the selectivity measures. The dashed line represents a linear regression of the ratio as a function of blood vessel diameter computed over the data points. The green asterisks indicate vessels diameters showing ratio significantly different than unity (2 tail t-test, FDR correction, $q < 0.05$). The average ratio curve and the statistical tests were computed and plotted for vessel diameters in the range of 0.04-0.28 mm. Each colored asterisk represents the mean ratio measured (not interpolated) for the corresponding vessel diameter. The format of presentation is similar to that used for Fig. 5-5.

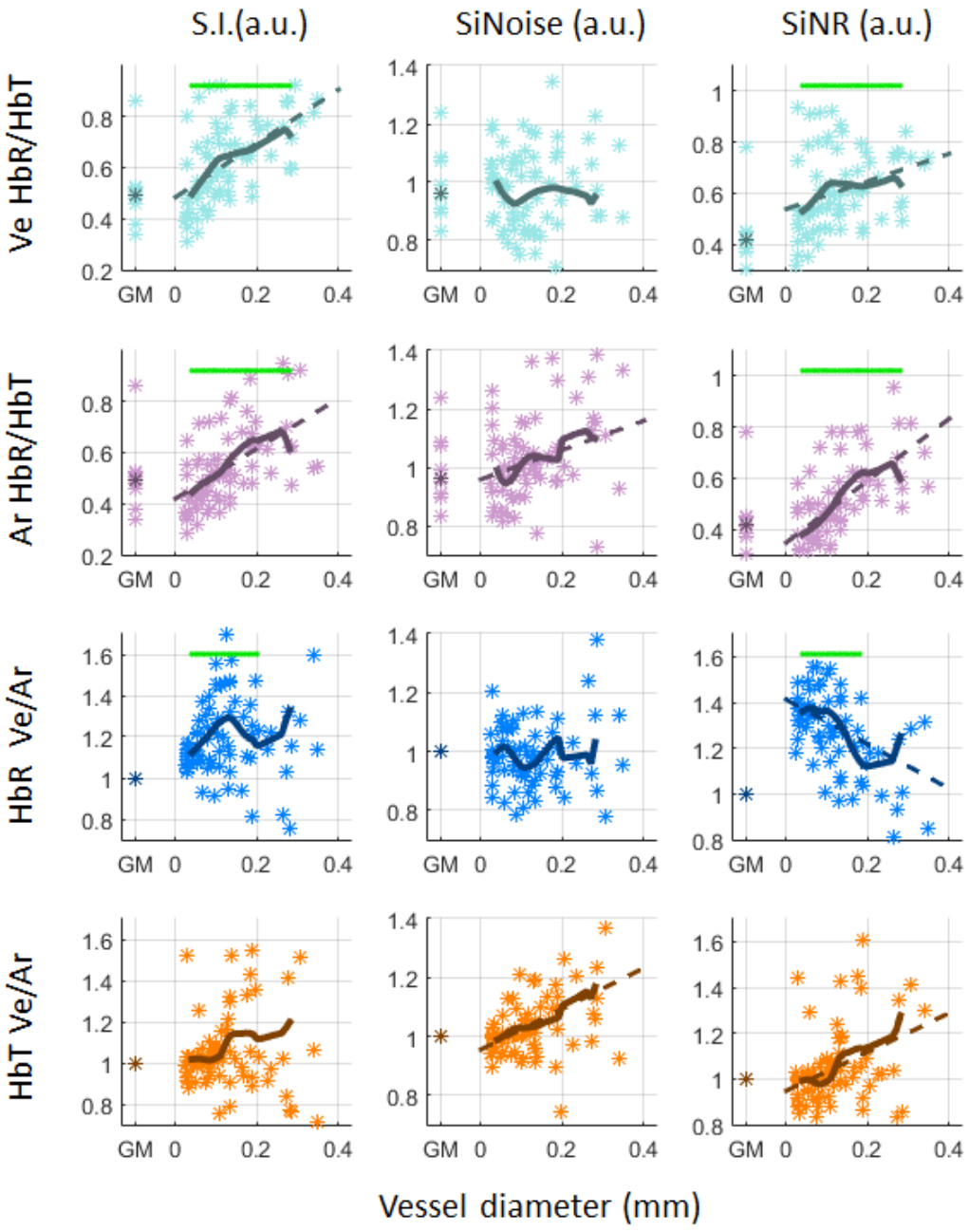

Figure 5-7. Relative selectivity indices obtained from HbR and HbT responses in veins and arteries. (See previous page for legend)

Contrast to noise ratio and Decoding accuracy of HbR and HbT responses in veins and arteries

Figure 5-8 (top half) compares the difference in responses to- and information conveyed on each of 2 stimuli with orthogonal orientations obtained from HbR vs. HbT responses, veins, arteries and GM. The detailed numerical values are summarized in Table III.

In veins, the CNR obtained from HbR was lower than that obtained from HbT responses across all *tested* diameters (green asterisks, $q < 0.05$, two-tailed t-test, FDR corrected; average ratio across all diameters pulled together 0.73±0.16, $p < 0.001$, two-tailed t-test). The CNR obtained from HbR relative to HbT increased with increasing vein diameter (slope = 0.48/mm; $p < 0.05$, F-test). In veins, the decoding accuracy obtained from HbR responses was lower than that obtained from HbT responses across all *tested* diameters (green asterisks, $q < 0.05$, two-tailed t-test, FDR corrected; average ratio computed over all diameters pulled together 0.86±0.08, $p < 0.001$, two-tailed t-test). The ratio of decoding accuracy obtained from HbR relative to HbT did not change significantly with increasing vein diameter.

In arteries, the CNR obtained from HbR was lower than that obtained from HbT responses across all *tested* diameters (green asterisks, $q < 0.05$, two-tailed t-test, FDR corrected; average ratio across all diameters pulled together 0.67±0.16, $p < 0.001$, two-tailed t-test). The CNR obtained from HbR relative to HbT increased with increasing artery diameter (slope = 1.05/mm; $p < 0.001$, F-test). In arteries, the decoding accuracy obtained from HbR responses was lower than that obtained from HbT responses across all *tested* diameters (green asterisks, $q < 0.05$, two-tailed t-test, FDR corrected; average ratio across diameters pulled together 0.61±0.09, $p < 0.001$, two-tailed t-test). The ratio of decoding accuracy obtained from HbR relative to HbT increased with increasing vessel diameter (slope 0.79, $p < 0.001$).

Functional selectivity in veins compared to arteries

Selectivity Index, Noise and SiNR of HbR and HbT responses in veins and arteries

Figure 5-7 (bottom half) compares the tuning curve response selectivities obtained from veins and arteries of various diameters. The detailed numerical values are summarized in the Table 5-IV.

HbR responses in veins showed higher SI than those obtained in arteries for all diameters equal to or smaller than 0.2 mm (green asterisks, two-tailed t-test, FDR corrected, $q < 0.05$; the

ratio averaged over all diameters pulled together was 1.21±0.23, $p < 0.001$, two-tailed t-test). The SiNoise obtained for HbR responses was approximately equal in veins and arteries; the ratio did not change significantly with vessel diameter. The SiNR of HbR responses in veins was significantly higher than that in arteries for vessel diameters equal to or smaller than 0.18 mm (the ratio averaged over all vessel diameters pulled together was 1.29±0.27). The ratio decreased with increasing vessel diameter (slope = -0.97/mm; $p < 0.01$, F-test).

HbT responses in veins showed SIs that were not significantly different than those obtained from arteries across all *tested* diameters. The SiNoise obtained for HbT responses in veins was not significantly different than that in arteries for each our *tested* diameters; however the average ratio over all diameters pulled together showed higher noise in veins relative to arteries (average 1.04±0.12, $p < 0.05$, two-tailed t-test). The ratio of HbT-based SiNoise in veins relative to arteries increased with increasing vein diameter (slope = 0.69/mm, $p < 0.001$, F-test). For each of the diameters we tested, the SiNR of HbT responses in veins was not significantly different than that in arteries; however, their ratio did increase with increasing vessel diameter (slope = 0.85/mm; $p < 0.05$, F-test).

Contrast to noise ratio and decoding accuracy of HbR and HbT responses in veins and arteries

Figure 5-8 (bottom half) compares the difference in responses to- and information conveyed about each of 2 stimuli with orthogonal orientations obtained from veins vs. arteries. The detailed numerical values are summarized in Table 5-IV.

The CNR obtained from HbR responses in veins was higher than that obtained from arteries for vessels diameters equal to or smaller than 0.09 mm (green asterisks, $q < 0.05$, two-tailed t-test, FDR corrected; average ratio across all diameters pulled together 1.14±0.22, $p < 0.001$, two-tailed t-test). The ratio of CNRs obtained from HbR responses in veins relative to arteries decreased with increasing vessel diameters (slope = -0.73/mm; $p < 0.05$, F-test). The decoding accuracy obtained from HbR responses in veins was higher than that obtained in arteries across all *tested* diameters (green asterisks, two-tailed t-test, FDR corrected, $q < 0.05$; average ratio across all diameters pulled together 1.52±0.14, $p < 0.001$, two-tailed t-test). The ratio of decoding accuracy obtained from HbR responses in veins relative to arteries decreased with increasing vessel diameter (slope = -0.72, $p < 0.001$, F-test).

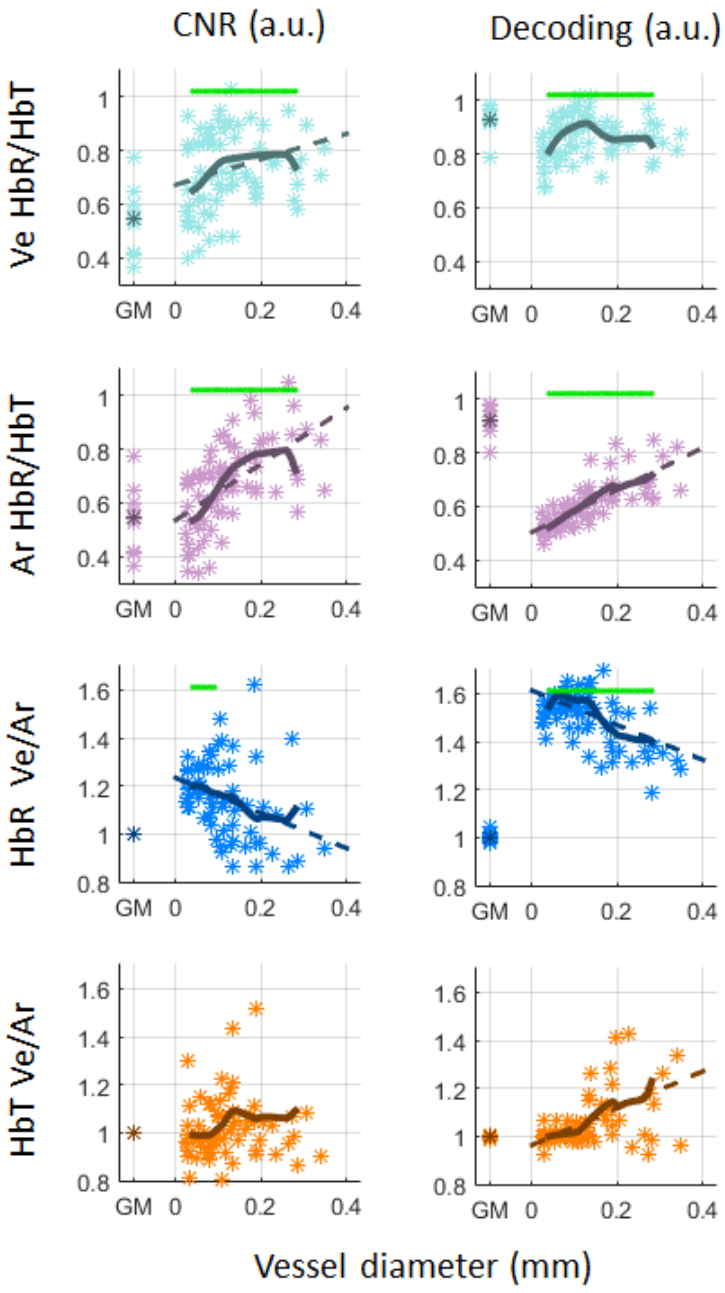

Figure 5-8. Relative CNR and Decoding accuracy obtained from HbR and HbT responses in veins and arteries.

Top half: statistical testing of the null hypothesis suggesting that the ratios of CNR and decoding accuracy of HbR response relative to HbT response in veins and arteries (cyan and purple asterisks, respectively) are not different than unity. Bottom half: statistical testing of the null hypothesis suggesting that the ratios of CNR and decoding accuracy of HbR and HbT responses (blue and amber asterisks, respectively) in veins relative to arteries are not different than unity. The format of presentation is similar to that used for Fig. 5-5

For each of the tested diameters, the CNR obtained from HbT responses in veins was not different than that obtained from arteries. The decoding accuracy obtained from HbT responses in veins was not significantly different than that obtained from arteries for any of the *tested* diameters; however, the data pulled over all diameters showed higher decoding rate in veins than in arteries (ratio 1.06±0.13, $p < 0.001$, two-tailed t-test). The ratio increased with increasing vessel diameter (slope = 0.77/mm; $p < 0.001$, F-test).

Table 5-III. Comparison of response selectivities obtained from HbR relative to HbT.

	μ	σ	p_μ	α	β	p_ α	min	Max
Ve-SI	0.62	0.16	E-29	1.05	0.48	E-6	0.04	0.28+
Ve-SiNoise	0.97	0.15	0.06	-0.16	0.99	0.45		
Ve-SiNR	0.61	0.16	E-31	0.54	0.54	0.01	0.04	0.28+
Ve-CNR	0.73	0.16	E-21	0.48	0.67	0.03	0.04	0.28+
Ve-Acc	0.86	0.08	E-22	0.10	0.85	0.38	0.04	0.28+
Ar-SI	0.55	0.15	E-35	0.98	0.42	E-5	0.04	0.28+
Ar-SiNoise	1.02	0.16	0.25	0.50	0.96	0.03		
Ar-SiNR	0.50	0.16	E-36	1.21	0.35	E-8	0.04	0.28+
Ar-CNR	0.67	0.16	E-25	1.05	0.54	E-6	0.04	0.28+
Ar-Acc	0.61	0.09	E-46	0.79	0.50	E-13	0.04	0.28+

See Table 5-II for the definition of notations.

Table 5-IV. Comparison of response selectivities in veins relative to arteries.

	μ	σ	p_μ	α	β	p_ α	min	Max
HbR-SI	1.21	0.23	E-9	0.49	1.15	0.14	0.04	0.20
HbR-SiNoise	0.99	0.15	0.66	0.07	0.98	0.74		
HbR-SiNR	1.29	0.27	E-12	-0.97	1.41	0.01	0.04	0.18
HbR-CNR	1.14	0.22	E-5	-0.73	1.23	0.02	0.04	0.09
HbR-Acc	1.52	0.14	E-41	-0.72	1.61	E-3	0.04	0.28+
HbT-SI	1.07	0.25	0.02	0.58	1.00	0.11		
HbT-SiNoise	1.04	0.12	E-02	0.69	0.96	E-4		
HbT-SiNR	1.06	0.28	0.10	0.85	0.95	0.03		
HbT-CNR	1.03	0.18	0.21	0.20	1.00	0.44		
HbT-Acc	1.06	0.13	E-3	0.77	0.96	E-4		

See Table 5-II for the definition of notations.

Discussion

Summary of results

We have quantitatively characterized the functional and spatial specificity of HbR and HbT responses in pial veins and arteries relative to GM and relative to each other. HbR responses in veins showed decreased SiNR, CNR and decoding accuracy for vein diameters of 0.13-0.16 mm relative to those obtained in GM regions (Figs. 5-5 and 5-6). These selectivity measures further decreased with increasing vein diameter. HbT responses in veins and arteries of all *tested* diameters showed decreased SiNR, CNR and decoding accuracy relative to those obtained from GM regions (Figs. 5-5 and 5-6). Moreover, these selectivity measures decreased with increasing vessel diameter. For all *tested* vein and artery diameters, HbR response selectivity measures were lower than their HbT counterparts (Figs. 5-7 and 5-8). HbT responses in veins and arteries showed comparable selectivity measures (Figs. 5-7 and 5-8).

As expected, consistently over all selectivity measures and all tested artery diameters, HbR responses in arteries are significantly less selective than those in GM regions (Figs. 5-5 and 5-6). The decoding accuracy obtained from these responses is at or very close to chance level (Fig. 5-6). Thus, although oxygen transfer seems to take place in arteries (Vovenko, 1999), the response is of low SNR and functional/spatial selectivity. Therefore, the larger part of the discussion is on HbR responses in GM and veins (but not in arteries), and HbT responses in arteries, GM and veins.

Spatial specificity of HbT and HbR responses as a function of vessel diameter

Although it is an accepted assumption that the larger the diameter of an artery/vein the less spatially specific the response it registers, to the best of our knowledge, the functional and spatial specificity of BOLD, HbR CBV and HbT responses have not been quantified as a function of vessel diameter. This is certainly true for vessels within a cortical map organized in multiple cortical columns, such as ocular dominance or orientation columns. Our results show a clear and sharp decrease in the spatial specificity of HbT response relative to that obtained in gray matter even for the smallest vessel diameters in the range we tested. Moreover, the spatial specificity of HbT responses decreases as a function of pial vessel diameter (Figs. 5-5 and 5-6). This is consistent with previous anatomical studies that demonstrated that the wider the diameter of a pial vein, the larger the overall cortical region that its ramifications drain (Duvernoy et al., 1981, Fig. 26). In contrast, HbR spatial specificity in veins of diameter smaller than or equal to 0.12 mm was not

significantly different than that in gray matter regions. We attribute this phenomenon to the lower selectivity of HbR response relative to HbT response, already at the gray matter itself (Fig. 5-7, first row). This poor selectivity in gray matter propagates to the veins. Therefore, the increase in selectivity of HbR relative to HbT with increasing vein diameter (Fig. 5-7, first row) can be attributed to the decrease in selectivity of HbT responses with increasing vein diameter (Fig. 5-5, third row) rather than to increase in HbR selectivity (note that HbR selectivity decreases with vein diameter too, Fig. 5-5, first row). In addition, we attribute this phenomenon to the gradual dilution of changes in HbR and HbO in veins with increasing distance from the site of increased neuronal response (Turner, 2002). In contrast, hypercapnia studies showed that the diameters of small arteries and venules increases relatively more than those of large vessels (Lee et al., 2001), suggesting that small vessels can accommodate a larger increase in CBV.

Selectivity of vessels with diameters not within the range we tested

While in principle, no conclusion can be made with no measurements, we believe that it is safe to assume that the selectivity measures of veins with diameter smaller than 0.04 mm should not be different than those in GM regions. We limited our analysis to the range of diameters of 0.04-0.28 mm, in order to have sufficient data for statistical testing. However, it is an accepted assumption that the draining region area of veins (and similarly, the region supplied by an artery) increases with increasing vein diameter. This implies that the wider a vein is, the more cortical columns, with more diverse preferred orientations it drains. Our measurements showed that the selectivity measures obtained from veins with diameters of 0.04-0.14 mm (SiNR), 0.04-0.16 mm (CNR) and 0.04-0.13 mm (decoding accuracy) were not significantly different than those in GM regions. Therefore, we can safely conclude that the veins with diameter smaller than 0.04 mm would follow and have selectivity at least as high as that shown by veins with diameter of 0.04 mm and not different than that in GM.

In addition, the HbR responses in veins (and arteries) and those of HbT in veins and arteries with diameters between 0.16-0.28 mm were significantly lower than those in GM. Furthermore, they decreased with increasing vessel diameter. Therefore, for similar reasons, we can safely assume that the functional selectivity measures of HbR responses in veins (and arteries) and those of HbT in veins and arteries with diameters larger than 0.28 mm (which were not in the diameter range we tested) are less selective than those in GM regions.

Increasing spatial specificity of fMRI during data-acquisition and by informed selection of voxels according to vessel diameter

Our results show that the functional/spatial specificity of HbR responses in veins and HbT responses in veins and arteries decreases with increasing vessel diameter. Certain data-acquisition parameters, such as the readout duration in SE fMRI and the level of asymmetry in ASE fMRI can limit the signal contribution to vessels along draining propagation. ASE-fMRI provides higher partial nullification of contributions from large veins relative to suppression of contributions from capillaries. The more asymmetric the refocusing pulse is, the closer to GE the resultant signal (Boxerman et al., 1995). Thus, ASE-FMRI enables a continuum of contrasts between the two extremes, T2 and T2* contrasts. In SE-BOLD fMRI, controlling the T_2* contributions can be done by varying the duration of the readout window (Goense and Logothetis, 2006). The signal acquired at the peak of the echo reflects mainly T_2 contributions. Increasing the read out duration to include signal away from the peak increases T_2* contributions that emerge from larger vessels, while increasing image SNR. In the study by Goense and Logothetis, varying the duration of the readout window in SE resulted in different response profiles across layers. The longer the readout, the closer was the SE functional response across layers to that of GE sequence; i.e. more signals originating from superficial layers. Optimizing the trade-off between long readout for higher SNR and short readout for spatial specificity can benefit from information on the spatial specificity of veins and venules of various diameters. Thus, indirectly, ASE-fMRI and SE-fMRI can weigh contributions from vessels of certain diameters more than those of others, in order to increase the spatial specificity of responses to the sites of increased neuronal activity.

Whereas limiting the data-acquisition to contributions from vessels within a certain range of diameters may not be straightforward, MRI methods exist for estimating the average vessel radius in a voxel. Thus, contributions from voxels containing vessels with large diameters can be excluded during the analysis stage. Typically, the mean vessel size, or vessel caliber index (VCI), is calculated from the ratio of the change in R2* and R2 following the injection of a contrast agent (Tropres et al., 2001; Kiselev et al., 2005; Germuska et al., 2013) However, the majority of these methods require injection of either gadolinium diethylenetriaminepenta-acetic acid (Gd-DTPA) or superparamagnetic iron oxide particles as the contrast agent. An alternative method which does not require injection of a contrast agent, relies on the blood oxygenation level-dependent (BOLD) effect that can be used as the source of this contrast (Prinster et al., 1997; Jochimsen et al., 2010;

Shen et al., 2013). The blood oxygenation is modulated with either hypoxic, hyperoxic, or hypercapnic gas challenges, probing the venous vasculature. However, these gas challenges may similarly be inconvenient for use in conjunction with fMRI. Likely, the most convenient method for use in the context of improving the spatial specificity of the fMRI response, is the one proposed by Jochimsen and Moller (2008). The method derives the mean vessel diameter in a voxel from the change in transverse relaxation rates upon activation which can be measured by multi-gradient-echo sampling of the spin echo sequence (Jochimsen and Moller, 2008). Thus, our findings can be combined with fMRI-based estimation of the average vessel diameter (Jochimsen and Moller, 2008) to exclude contributions from vessels with low spatial specificity.

Our study is different than that by Jochimsen and Moller (2008) in several ways. First, rather than estimating the mean vessel size within a voxel, we measure, in a more direct manner, the diameters of all vessels. In addition, Jochimsen and Moller (2008) provide a method for estimating the mean vessel size within a voxel, and the amplitude or significance of the BOLD response as a function of the mean vessel diameter, but no information on which vessel size contributes spatially specific responses. In contrast, our study quantifies the functional/spatial specificity of vessels according to their respective diameters: we measure the specificity of blood vessels at a scale that cannot be achieved with MRI or fMRI. Therefore, our study complements the one by Jochimsen and Moller (2008), and the results of the two studies together can be combined for improving the spatial specificity of the BOLD response.

Conclusions about spatial specificity based on functional selectivity

In this work, we measured the blood vessel and gray matter response selectivity to a group of stimuli. Hence the selectivity measures can be classified as "functional", as they quantify the differences between the functional responses to these stimuli. However, the specific group of stimuli we used is that of oriented gratings that span the orientation space. Orientation selective neurons in cat area 18 are clustered together, forming orientation selective columns orthogonal to cortical surface and an orientation preference map parallel to the surface (Bonhoeffer and Grinvald, 1993b; Hubel, 1995; Shmuel and Grinvald, 2000). This organization is not arranged in a purely cyclic manner involving one single frequency (Chapter 4). However, the cortical spatial frequencies showing significant amplitudes are organized in an approximate Gaussian shape, including a Gaussian center and peak of ~0.84 cycles per mm and local irregularities (Chapter 3,

4). Hence, the functional selectivity is mapped to space, and therefore, in our current study it is justified to use the term functional specificity interchangeably with spatial specificity.

Another way to view it, is via the well accepted concept that the larger the diameter of a vein the larger cortical area it drains. Since orientation columns are organized as a mosaic with a main cortical spatial frequency, the larger the vein diameter, the larger number of columns with a variety of orientation preferences it drains. Therefore, although we measured functional selectivity, our conclusion can be directly extended to terms of spatial specificity.

Several studies have demonstrated that across the cortical surface, the orientation preference can also vary in cortical spatial frequencies substantially lower that the main frequency of the columnar organization (Furmanski and Engel, 2000; Sasaki et al., 2006; Clifford et al., 2009; Mannion et al., 2010; Freeman et al., 2011; Freeman et al., 2013; Sun et al., 2013; Wang et al., 2014). This could in principle have a confounding effect on our measurements that are aimed to quantify the spatial specificity of vessels for high-resolution functional imaging of cortical columns. In particular, the radial bias is retinotopically organized, and includes components other than a global constant change in response. Therefore, in order to avoid this confound, we spatially high-pass filtered our data in the pre-processing stage with a cut-off frequency of 0.2 cycles/mm. This filtering leaves only frequencies associated with the main frequency and the irregularities of the organization (Yao et al., Chapter 4). Importantly, we performed this high-pass separately for arteries, veins and gray matter regions, in order to avoid cross-interference due to abrupt changes in response between modalities.

Implications of our conclusions for high-resolution fMRI in humans

We have made our measurements in the cat visual cortex. However, our findings and conclusions can be extended to high-resolution fMRI of human cortex. As discussed above, the functional selectivity of blood vessels measured in our work can be regarded as spatial specificity. Importantly, the vascular architecture is essentially similar across mammalian species at the capillary level. The mean capillary diameter changes only slightly with brain volume (~4.6 μm in rat, Laursen and Diemer, 1977; ~4.8 μm in cat, Auen et al., 1979; ~6.5 μm in human, Lauwers et al., 2008). The capillary volume fraction (ratio of total capillaries volume to brain volume) and the capillary length per neuron are invariant across mammalian species, including mouse, rat, rabbit, pig, cat, dog, primate and humans (Karbowski, 2011). This could be expected, since single neurons or small volumes within brains need to be maintained by supply of oxygen and glucose,

independent of the size of brains they belong to. For this reason, we can expect that the vascular statistics of arterioles, small arteries, venules and small veins with diameter smaller than or equal to 0.12 mm is essentially similar across species. In other words, the functionality of vessels of similar diameter is invariant across mammalian brains. The vascular network structure and diameter does vary with the brain's volume only in the infrastructure of large vessels (Gillilan, 1976), which is irrelevant in the context of high-resolution functional imaging.

Hence, in absolute terms, the vessel diameter limit we report here is applicable to any cortical functional organization arranged around a peak frequency of 0.84 cycles/mm or lower frequency. The cortical maps with the highest spatial frequency known in the macaque cortex are those of ocular dominance columns (~1.25 cycles/mm, Ts'o et al., 1990) and orientation columns (~1.25 cycles/mm, Bartfeld and Grinvald, 1992) in V1. All anatomical and functional studies in humans have demonstrated that the organization of the human visual cortex is similar to that of the macaque monkey. We can therefore assume that the cortical maps with the highest spatial frequency in humans are those of ocular dominance (~0.5 cycles/mm, Adams et al., 2007; Yacoub et al., 2007) and orientation (~0.56 cycles/mm,Yacoub et al., 2008). These 2 organizations in humans have main frequencies that are lower than that in cat area 18, where we obtained our measurements from. We can therefore safely conclude that the vessels with diameter smaller or equal to the limit we report here can contribute to fMRI of human cortical columns if the signal to noise ratio (SNR) justifies inclusions of contributions other than those from capillaries.

The periodicity of this organization constitutes higher cortical frequencies than any of the cortical maps that can be expected to exist in the human cerebral cortex. In addition, as discussed above, the functionality of vessels of similar diameter is invariant across mammalian brains. Therefore, all vessels with diameter smaller than or equal to the limit we propose can be included in data-acquisition and not excluded in data analysis for increasing CNR of high-resolution fMRI.

Extension of our conclusions to intra-cortical vessels

The physiological phenomenon measured by OI-IS of HbR and HbT is the same physiological phenomenon measured by BOLD-fMRI and CBV-fMRI, respectively. What differs between the two methods is the principle of measurement, i.e. changes in local absorption of light in the case of OI-IS and of relative magnetism in the case of fMRI. Therefore, an fMRI slice aligned to the cortical surface should in principle, barring issues such as extra-vascular BOLD in GE fMRI, come up with findings similar to those we present here with OI-IS. However, unlike

fMRI, OI-IS acquires signals limited to the superficial layers of cortex. We have imaged the OI-IS response in gray matter and pial blood vessels. Therefore we cannot extend our conclusions in a straight-forward manner to intra-cortical vessels. However, pial vessels drain cortex, and the vessels in cortex have diameters that are smaller than that of the pial vessel they connect to, or, in the minority of cases, equal to that diameter (Duvernoy et al., 1981, Fig. 25-26). The largest diameters of vessels in cortex are 0.12-0.125 mm, associated with veins of class 5 (Duvernoy et al., 1981). These veins have a vertical path, draining venous blood from all cortical layers, starting with layer 6. All venous branches that connect to veins of class 5 have diameters smaller than 0.12 mm. The branches that drain blood to class 5 veins from relatively distant sites are those in layer 6 and below it. However, the laminar profile of the BOLD response shows significantly lower amplitude in layer 6 than in superficial layers (Koopmans et al., 2010). Thus, the spatially non-specific contributions of these veins has lower amplitude than those from the veins in superficial layers, with smaller draining regions. We conclude that our measurements of spatial specificity demonstrated by pial veins is consistent with what one can expect based on draining regions within cortex. If the CNR obtained from BOLD responses does not limit the measurement, it is clear from the significant regression slope of SiNR obtained from HbR responses that veins of all diameters should be excluded, and data acquisition and/or analysis should be based exclusively on BOLD responses from the gray matter. However, since high-resolution BOLD fMRI has low CNR in the majority of cases, veins with diameter up to 0.12 mm can contribute with non-significantly degraded spatial specificity.

We have based our findings on functional imaging of cortical columns. Thus, our findings and recommendations apply to high-resolution functional imaging of cortical columns that by definition show similar neurophysiological preference to the feature they map (e.g., ocular dominance and orientation in visual cortex, frequency in the auditory cortex, specific finger and phalanx in the somatosensory cortex) across all cortical depths. Our findings do not apply to high resolution functional imaging of cortical layers. The relatively large intra-cortical arteries and veins are oriented orthogonally to the cortical manifold. Therefore, any consideration of vessel sizes for optimizing laminar specific functional imaging is going to be different than our consideration here, and is likely to end up in exclusion of all vessels except for capillaries.

Conclusion

We conclude that if SNR and CNR are insufficient in high-resolution BOLD-fMRI of human cortical columns, one can integrate contributions from vessels with diameter smaller than or equal to 0.12 mm with no significant decrease in spatial specificity. For high-resolution CBV-fMRI, the smaller the diameter of contributing vessels, the higher the expected spatial specificity.

Appendix

Monte-Carlo simulations

In the first part, we used Monte-Carlo simulations with heterogeneous media in order to estimate the distribution of path lengths of all photons emerging from one location at the top of a pial vessel (Suppl. Fig. 5-1A). Specifically, we estiamted the path lengths of each photon within the blood vessel and gray matter . Intuitively, if the vessel's diameter is large, the only photons that will emerge from its top are those whose entire path length was within the vessel. In contrast, if the diameter is small, a large proportion of photns that emerge from its top have part of their path length in the surrounding gray matter.

We first applied our Monte Carlo simulations to a homegeneous gray matter tissue and separately, a homegenous volume of blood. Monte Carlo simulations uses the medium properties such as the absortion coefficient and the scattering coefficient as the input parameters, and outputs the disitribution of the photon path-lengths. The simulation itself does not depend on the incident light's wavelength; however, the absorption and scttering coefficients of a biological tissue do depend on the light's wavleength. Hence we need to consider the tissue's absorption and scaterring coefficients as a function of wavelength when using either monocrome light or light with a certain band of wavelengths.

For the simulation associated with gray matter, we calculated the medium's absorption based on the HbR and HbO contents within the gray matter and their extinction coefficients at 530 nm and 617 nm. For each medium's absorption parameter used as input, the software computed a distribution of path lengths obtained from millions of photons. We confirmed that the estimated mean path lengths in gray matter for illumination of 530 nm and 617 nm agreed with the previously reported values (approximately 0.5 mm and 2.5 mm, respectively, Dunn et al. (2005), with extrapolation from Kohl et al. (2000)). Then, we estimated the vessel absorptions for 530 nm and 617 nm based on the typical HbR and HbO contents reported in animals (Table 5-I in the main text). These allowed us to estimate the mean path lengths obtained for a blood vessel with infinite diameter (namely homogeneous blood volume) via the simulation (Suppl. Table 5-I).

The estimated path lengths in infinite blood vessels and gray matter were obtained by first computing absorbance based on the baseline concentrations of HbO and HbR and their respective absorption coefficients under illumination of 530 nm and 617 nm.

Supplementary Figure 5-1. Estimation of path-lengths of photons emerging from blood vessels as a function of blood vessel diameter.

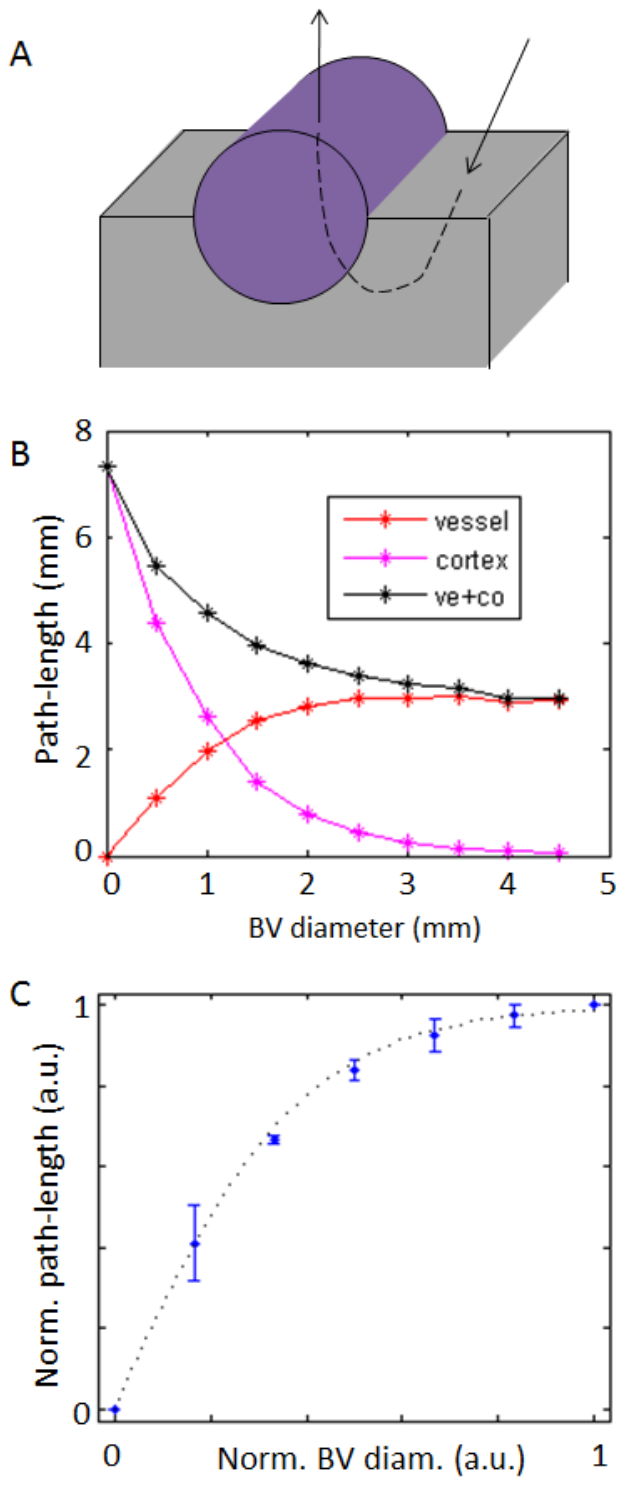

When a blood vessel has diameter of 0 mm, the entire photon trajectory is within the gray matter. However, a photon may travel partially in the gray matter and partially in the blood vessel. **A)** A scheme of a trajectory of a photon that goes through gray matter, then through a blood vessel in the generated mesh. **B)** Mean photon path-length for photons emerging from blood vessels as a function of blood vessel diameter. In this particular simulation, the mean photon path-length in homogenous gray matter medium was 7.3 mm and that in homogeneous blood vessel medium was 3 mm. The vessel curve (red) was cut at 3 mm (the mean photon path-length in homogeneous blood vessel medium) and normalized in both the x and y axes to [0 1]. The cut-off of 3 mm on the x-axis was chosen because, as expected, that's where the curve plateaued. Similarly, the cortex curve (pink) was cut according to the blood vessel cut-off (3 mm), inversed vertically and normalized along both the x and y axes to [0 1]. We simulated this process for 2 additional simulation parameter sets. For these simulations, the x-axis cut-off was similarly chosen to be the mean photon path-length in a homogeneous medium with blood vessel tissue parameters. **C)** The mean and SEM of the 6 normalized function curves obtained from the 3 simulation parameter sets. We found that $1-(1-x)^{4.1}$ fitted the data well (n = 3 simulations x 2 curves, $R^2 > 0.98$). Then this equation, which describes the ratio of the partial path length in GM or vessel relative to their pathlengths in their respective homogeneous tissue as a function of blood vessel diameter, was used to approximate and separate photon partial path-lengths in a heterogeneous media in the following section and Suppl. Fig. 5-2, steps 4 and 6.

For example, the baseline concentrations of HbO and HbR in the gray matter are 60 μM and 40 μM, respectively (Table 5-I in the main text). The absorption (extinction) coefficients of HbO and HbR under illumination of 600 nm are 320/mm·M and 1470/mm·M, respectively. Then the total gray matter absorption is 2.303×(3.2E2 ×6E-5 + 1.47E3×4E-5) = 0.18 (note that 2.303 is a normalization factor based on the Beer-Lambert law). The absorbance of 0.18/mm on the horizontal axis of Fig. 1B in Kohl et al. (2000) yields a mean path length of 1.52 mm on the vertical axis of the same figure. This simple calculation also matches with the simulated results in Fig. 1C of Dunn et al. (2005) under illumination of 600 nm on the horizontal axis. We performed similar calculations as described above for homogeneous gray matter tissue under illumination of 600 nm, to our current interest in gray matter, arteries, and veins (assuming infinite vessel volume) under illumination wavelengths of 530 nm and 617 nm.

Then, to estimate path length in the heterogenous setting we inserted a cylindrical mesh buried half-way into the cortical surface to represent the pial blood vessel (Suppl. Fig. 5-1A). We estimated the distribution of path lengths as a function of the pial blood vessel's diameter. Using realistic blood vessel radii required the generation of high-resolution cylindrical meshes that were too fine for our custom written simulation software. Specifically, the meshes that our system could manage were too coarse, thus we could not depict vessels them as cylinders. Because of this limitation in precision, we simulated heterogeneous media with large vessels and gray matter thicker than in reality. To this end, we adjusted the absorption properties of the gray matter and blood vessels to values smaller than realistic values, so that we could simulate heterogeneous tissue of gray matter and veseels with relatively large vessels. For this, we carried out 3 simulations, each with different combinations of absorption parameters.(Suppl. Table 5-I).

Supplemantary Table 5-I: absorption coefficients used for gray matter and blood vessels in our 3 simulations.

	Gray matter absorption	Blood vessel absorption
Simulation A	0.017 mm-1	0.062 mm-1
Simulation B	0.049 mm-1	0.180 mm-1
Simulation C	0.017 mm-1	0.180 mm-1

When used in a simulation with homogeneous tissue, the absorption coefficients we used [0.017 0.049 0.062 0.180] mm^{-1} yield mean path lengths of [7.0 3.5 3.0 1.5] mm, respectively (Kohl 2000). We selected these values, for simulating the condition of path-lengths of 7 mm in cortex and 3 mm in blood vessel.

For the simulation presented in Suppl. Fig. 5-1B, the absorption properties of gray matter and blood vessels were set with apriori knowledge from Kohl et al. (2000) so that the mean photon path length within their respective homogenous media were approximately 7.0 mm and 3.0 mm. We then obtained the distribution of partial photon path lengths within the gray matter and the blood vessel as a function of increasing blood vessel diameter from 0.0 mm to 9.0 mm. With increasing blood vessel diameter, the path-length of photons within the blood vessel increased monotonously up to approximately 3.0 mm. As expected, for photons emerging at the top of the vessel, the average partial path lenth in gray matter decreased with increasing blood vessel diameter.

We then normalized each of the 2 resultant curves of partial path length as a function of blood vessel diameter, by limiting it to radii equal to or smaller than 3 mm (where the partial pathlength within the blood vessel plateaued), and dividing both the x and y values by their max value. Thus, the curve of the partial path length in the vessel (red) was cut at 3 mm and normalized along both the x and y axes to [0 1]. The cut-off of 3 mm on the x-axis was chosen here because that's where the curve plateaued. Similarly, the curve describing the partial path length in gray matter as a function of vessel diameter (pink) was also cut at 3 mm, inverted vertically (flipped around the horizontal axis) and normalized along both the x and y axes to [0 1].

We repeated this process for 3 combinations of hypothetical absorption properties of gray matter and blood vessel (Suppl. Fig. 5-1C). For each simulation, the x-axis cut-off was chosen to be the diameter in which the average partial path length in blood vessel reached 99.5% of the mean photon path length in a homogeneous blood vessel medium. The 99.5% cutoff on the x-axis corresponded to the diameter of blood vessel that matched the mean photon path length in a homogeneous blood volume. An inverse power function, $1-(1-x)^{a}$, was fitted to the curve averaged over the 6 normalized simulated curves (3 simulations x [BV GM] curves, fitting was done using Matlab's 'fit' function). Based on the similarity of the normalized curves, we concluded that the function with $\alpha = 4.1$ ($1-(1-x)^{4.1}$, $R^2 > 0.98$) fits well the normalized curves within the range of absorption spectra we used (Suppl. Fig. 5-1C). We assumed that we can extrapolate and use the same function also for gray matter and vessels with realistic thickness and diamaters, respectively, and with realistic absorption parameters under 530 nm and 617 nm (Table 5-I in the main text). We therefore applied this equation, which describes the path length as a function of

blood vessel diameter, to approximate and separate photon path-lengths of heterogeneous media in the following section.

Correction of path length in heterogeneous media

Next, we corrected the absorption change associated with a pial blood vessel region according to the absorption change in its surrounding gray matter regions (Suppl. Fig. 5-2).

To this end, we first masked out all blood vessels, and filled in their regions by interpolating the response values from the surrounding gray matter regions, separately under illumination with 530 nm and 617 nm (Suppl. Fig. 5-2, step 2). Then, we computed the change in HbR, HbO and HbT for each pixel in the imaged region, including the gray matter (GM) and the filled in (GM') blood vessel regions. For this, we applied a standard procedure for decomposing LED illumination absorption changes to the underlying hemoglobin content changes (Suppl. Fig. 5-2, step 3):

$$\triangle A = P\Delta\mu = P(\Delta c_{HbO}\alpha_{HbO} + \Delta c_{HbR}\alpha_{HbR}) \quad (1)$$

$$\Delta c_{HbR}^{\lambda 1,\lambda 2} = \frac{\alpha_{HbR}^{\lambda 1} \triangle A^{\lambda 2} \frac{1}{p_{\lambda 2}} - \alpha_{HbR}^{\lambda 2} \triangle A^{\lambda 1} \frac{1}{p_{\lambda 1}}}{\alpha_{HbR}^{\lambda 1}\alpha_{HbO}^{\lambda 2} - \alpha_{HbO}^{\lambda 1}\alpha_{HbR}^{\lambda 2}} \quad (2)$$

$$\Delta c_{HbO}^{\lambda 1,\lambda 2} = \frac{\alpha_{HbO}^{\lambda 1} \triangle A^{\lambda 2} \frac{1}{p_{\lambda 2}} - \alpha_{HbO}^{\lambda 2} \triangle A^{\lambda 1} \frac{1}{p_{\lambda 1}}}{-\alpha_{HbR}^{\lambda 1}\alpha_{HbO}^{\lambda 2} + \alpha_{HbO}^{\lambda 1}\alpha_{HbR}^{\lambda 2}} \quad (3)$$

$$\Delta c_{HbT}^{\lambda 1,\lambda 2} = \Delta c_{HbR}^{\lambda 1,\lambda 2} + \Delta c_{HbO}^{\lambda 1,\lambda 2} \quad (4)$$

Where:

λ_1 = 530 nm wavelength illumination (green)

λ_2 = 617 nm wavelength illumination (orange)

$P_{\lambda 1,2}$ = mean pathlength of photons at 530/617 nm

$\Delta A_{\lambda 1,2}$ = change in absorption of the gray matter relative to the baseline under 530/617 nm

$\alpha^{\lambda 1,2}{}_{HbO}$ = absorption coefficient of HbO in gray matter under illumination at 530/617 nm

$\alpha^{\lambda 1,2}{}_{HbR}$ = absorption coefficient of HbR in gray matter under illumination at 530/617 nm

Δc_{HbO} = change in oxy-hemoglobin concentration

Δc_{HbR} = change in deoxy-hemoglobin concentration

Δc_{HbT} = change in total-hemoglobin concentration

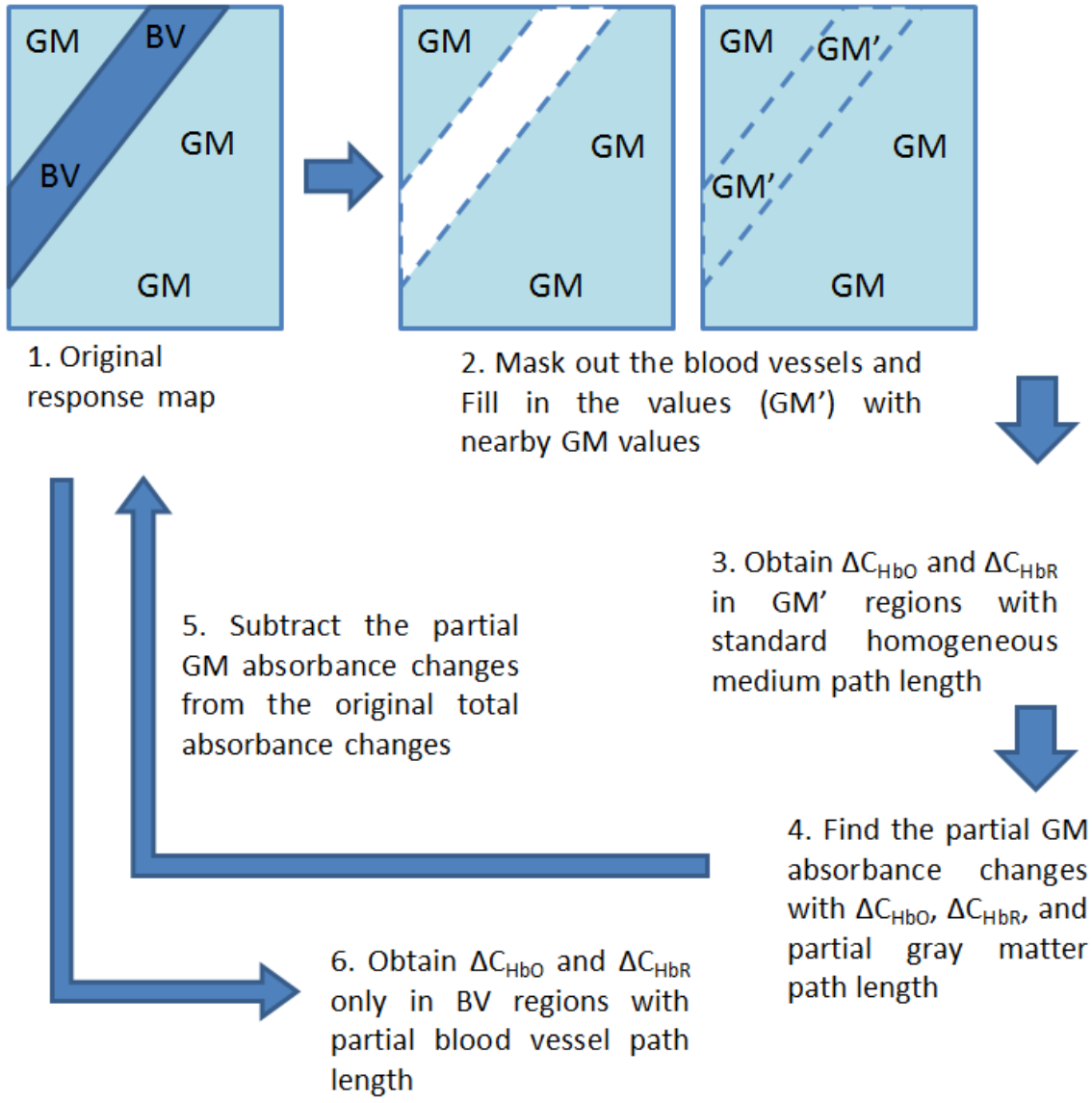

Supplementary Figure 5-2. Path-length correction of pixels depicting blood vessel regions. **1.** The original cortical map contains both blood vessel and gray matter pixels. **2.** The blood vessel pixels were first masked out from the cortical response map. The missing values were filled using a robust smoothing algorithm (Garcia, 2010), by interpolation of the values from adjacent GM regions. **3.** Spectral decomposition was performed on the filled-in region using the path-length of homogeneous gray matter medium. The obtained values correspond to the gray matter hemoglobin molar concentration changes hidden underneath the blood vessels. **4.** The obtained molar concentration changes were converted back to photon absorption; however, with the shorter (= partial) path-length in GM which was a fraction of the path length in the homogeneous GM medium and depended on the diameter of vessel above the corresponding gray matter tissue. **5.** The partial absorbance computed for the GM underneath the vessel was subtracted from the original response map. **6.** The final spectral decomposition is carried out with adjusted path-length that accounts for the part traveled through the blood vessel part only.

Because the light emitted from LEDs have a certain spectral diameter (it is not composed of a single wavelength) and, in adition, the camera sensor has different sensitivity over the spectrum, we employed an effective path-length model that takes into account the integrals over the distribution of the light and camera sensitivity spectra (Brieu et al., 2010).

Once the spectral decomposition was performed for all pixels in the imaged region, including the filled in BV regions, we performed adjusted spectral decomposition for the pixels within the vessel regions. The measured absorption in blood vessel regions is the combination of partial blood vessel and gray matter absorption changes. Therefore, for all blood vessel pixels, we need to separate the partial blood vessel absorption change from the overall absorption change which we measured. The decomposed gray matter molar concentration changes ($\Delta c_{HbR}^{\lambda 1,\lambda 2}$ and $\Delta c_{HbO}^{\lambda 1,\lambda 2}$) in the blood vessel regions were converted back to absorption changes with partial path lengths (Suppl. Fig. 5-2, step 4).

$$\triangle A = \triangle A_{bv} + \triangle A_{gm} = P_{vb}\Delta\mu_{vb} + P_{gm}\Delta\mu_{gm} \quad (5)$$

$$P_{vb}\Delta\mu_{vb} = \triangle A - P_{gm}\Delta\mu_{gm} \quad (6)$$

Where:

ΔA = change in total absorbance constituting ΔA_{gm} and ΔA_{vb}, i.e. the partial absobances of GM and BV, respectiviely

ΔA_{gm} =change in partial absorbance of the underlying gray matter

ΔA_{vb} = change in partial absorbance of the overlying pial blood vessel

$\Delta\mu_{gm}$ = change in absorption coefficient of the gray matter underneath the blood vessel

$\Delta\mu_{bv}$ = change in absorption coefficient of the blood vessel

P_{vb} = mean partial pathlength of photons travelled within blood vessel

P_{gm} = mean partial pathlength of photons travelled within cortex

The partial path lengths of the blood vessels regions varied according to the radii of the overlying vessels (Suppl. Fig. 5-1). Since we established that the normalized curves are well represented by the inverse power function, $1-(1-x)^{4.1}$, we can de-normalize it (i.e., multiply the values along the x-axis by the path length within the homogeneous medium of the considered blood vessel (vein or artery) for 617 nm or 530 nm illuminations. Following the de-normalization, we computed the ratio of the partial path length relative to the path length of the homogeneous blood volume for every diameter range of blood vessels.

For example, looking at a vein under illumination of 617 nm, the path length in a homogeneous vein volume is 0.393 mm (Table 5-I in the main text); this is the factor with which we de-normalize the horizontal axis. Then, if the vein of interest has a diameter of 0.393 mm or wider, we check for the value along the vertical axis that the function yields at the maximal value (1, de-normalized to 0.393 mm) along the horizontal axis. The result is 1, the maximal value along the normalized vertical axis. The meaning of this, is that the mean combined path length for a vein with diameter 0.393 mm under illumination of 617 nm is composed of photons that travelled exclusively (100%, 0.393 mm) through the vessel and none (0%) through the gray matter. On the other hand, if the vein of interest has a diameter of 0.197 mm (half of the path length under 617 nm in a homogeneous vein volume), the mean combined path length is composed of partial path length in vein which is 85% (0.334 mm) of the mean path length in homogeneous vein volume (0.393 mm) and of partial path length in gray matter which is 15% (0.381 mm) of the mean path length in homogenous gray matter medium (2.54 mm) under 617nm.

The final decomposition was obtained from changes of chromophores within blood vessel only (Suppl. Figures 4-2, steps 5 and 6). First, the molar concentration change of HbR and HbO in gray matter, calculated previously, was multiplied by the gray matter partial path length to yield the partial gray matter absorption changes. Then the partial blood vessel absorption changes were separated from the mixed absorption changes by subtracting the partial gray matter absorption changes from the total absorption under the wavelength we consider.

$$\Delta A_{bv\lambda 1} = \Delta A_{\lambda 1} - P_{gm\lambda 1}\left(\alpha_{HbO}^{\lambda 1}\Delta c_{gmHbO} + \alpha_{HbR}^{\lambda 1}\Delta c_{gmHbR}\right) \quad (7)$$

$$\Delta A_{bv\lambda 2} = \Delta A_{\lambda 2} - P_{gm\lambda 2}\left(\alpha_{HbO}^{\lambda 2}\Delta c_{gmHbO} + \alpha_{HbR}^{\lambda 2}\Delta c_{gmHbR}\right) \quad (8)$$

Where $P_{gm\lambda}$ = partial path length of gray matter underneath the pial blood vessel

Finally, the isolated hemoglobin content changes in blood vessels were obtained from the partial blood vessel absorption changes and from the partial blood vessel path lengths (Suppl. Fig. 5-1)

$$\Delta c_{bv\_HbR}^{\lambda 1,\lambda 2} = \frac{\alpha_{HbR}^{\lambda 1}\,\Delta A^{bv\lambda 2}\frac{1}{p_{\lambda 2}} - \alpha_{HbR}^{\lambda 2}\,\Delta A^{bv\lambda 1}\frac{1}{p_{\lambda 1}}}{\alpha_{HbR}^{\lambda 1}\alpha_{HbO}^{\lambda 2} - \alpha_{HbO}^{\lambda 1}\alpha_{HbR}^{\lambda 2}} \quad (9)$$

$$\Delta c_{bv\_HbO}^{\lambda 1,\lambda 2} = \frac{\alpha_{HbO}^{\lambda 1}\,\Delta A^{bv\lambda 2}\frac{1}{p_{\lambda 2}} - \alpha_{HbO}^{\lambda 2}\,\Delta A^{bv\lambda 1}\frac{1}{p_{\lambda 1}}}{-\alpha_{HbR}^{\lambda 1}\alpha_{HbO}^{\lambda 2} + \alpha_{HbO}^{\lambda 1}\alpha_{HbR}^{\lambda 2}} \quad (10)$$

The symbols are similar to those used in the previously defined equations.

Preface to Chapter 6

In Chapter 6, we address aim 3: 'to quantify the spatial specificity of aggregates of capillaries within the gray matter relative to that of neurophysiological responses'. An important aspect that challenges successful decoding of orientation stimuli is the spatial spread of the hemodynamic response. This spread has been modeled as a hemodynamic point spread function (PSF) which is thought to represent the upper bound on how spatially precise fMRI response is to a point-like or a line-like increase in neuronal activity. However, except for one study that applied stimulation to a single cortical site in mouse area S1 (Vazquez et al., 2014), all previous studies that estimated the spatial specificity of the hemodynamic response did not consider the spread of the neurophysiological response. Thus the reported hemodynamic PSFs include the component of the spatial spread of neural activity, including the size of receptive fields, the spatial extent of the scatter of receptive-fields and integration by the dendritic fields. In this chapter we use optical imaging simultaneously with neurophysiological recordings to demonstrate that the PSF of the hemodynamic response relative to the spread of neurophysiological responses to retinotopic stimuli is smaller than the absolute PSF. Our findings predict that the PSF of BOLD responses in humans are expected to be smaller than what has been reported thus far, consistent with the feasibility of fMRI at the resolution scale of cortical columns.

Spatial specificity of the hemodynamic response relative to neuronal response in cat area 18: implication for high-resolution fMRI

Zeshan Yao, Niladri Mohanty, Victor Mocanu, Amir Shmuel

McConnel Brain Imaging Centre, Montreal Neurological Institute,

Departments of Neurology, Neurosurgery, Physiology and Biomedical Engineering

McGill University, Montreal, QC, Canada

Correspondence:

Amir Shmuel, Ph.D.

3801 University, room NW109

Montreal, QC, Canada H3A 2B4

E-mail: amir.shmuel@mcgill.ca

Keywords: High-resolution functional MRI, Optical imaging of intrinsic signals, Blood oxygenation level dependent, BOLD, Cerebral blood volume, CBV, Cortical columns, Point-spread function.

Acknowledgements: We thank Drs. Doina Precup, Curtis Baker and Robert Kearney for very helpful discussions, and Kelly Hennegan for her scientific English editing. This work was supported by grants from the Natural Sciences and Engineering Research Council of Canada (NSERC Discovery grants RGPIN 375457-09 and RGPIN-2015-05103) and the Human Frontier Science Program (RGY0080/2008) awarded to AS.

Abstract

The spatial spread of functional MRI (fMRI) responses relative to the site of increased neurophysiological activity is an important measure for correctly planning and interpreting high-resolution fMRI and fMRI-based decoding of fine-scale organizations. Previous studies that quantified the point spread function (PSF) of the blood oxygenation level dependent (BOLD) response implicitly assumed that the neurophysiological response is point-like, with no spread. However, neurophysiological responses to stimulation of part of the visual field, commonly used for estimating the spread of the BOLD response, are expected to show spatial spread too. Here we used optical imaging of hemodynamic signals: changes in content of oxy- (HbO) deoxy- (HbR) and total (HbT) hemoglobin, simultaneously with neurophysiological recordings to measure the response of cat area 18 to visual stimulation of parts of the visual field, with edges at various eccentricities. We modeled the hemodynamic and neurophysiological spreads as Gaussians. The mean absolute full-width-at-half-max (FWHM) of HbO and HbT responses in cat area 18 were 3.26 and 2.83 mm, respectively. The mean absolute FWHM of the HbR responses was larger than that of HbT responses. The mean absolute FWHMs of PSFs of low-gamma, high-gamma and spiking responses in cat area 18 were 3.73, 3.25 and 2.07, respectively. The PSF of HbT and HbO responses relative to spiking activities were 2.52 mm and 1.93 mm, respectively, using a convolution model and 1.19 mm and 0.76 mm using an additive model. We conclude that the spatial spreads of low-gamma and high-gamma neurophysiological responses are comparable to that of HbT responses. Thus, Cerebral Blood Volume (CBV) responses reflect fine scale organization at high fidelity. Our findings predict that the PSF of BOLD responses in humans are expected to be smaller than what has been reported thus far, consistent with the feasibility of fMRI at the resolution scale of cortical columns.

Introduction

Functional magnetic resonance imaging (fMRI) is the most commonly used non-invasive method for investigating brain activity. fMRI can measure changes in blood-oxygenation-level-dependent (BOLD) contrast (Bandettini et al., 1992; Kwong et al., 1992; Ogawa et al., 1992), and in cerebral-blood-volume (CBV) (Belliveau et al., 1991; Kim and Kim, 2005; Stefanovic and Pike, 2005; Lu and van Zijl, 2012). fMRI infers the brain's neurophysiological activity indirectly by measuring hemodynamic responses coupled closely with neural activity (Mathiesen et al., 1998; Logothetis et al., 2001; Shmuel et al., 2006; Shmuel and Leopold, 2008). In order to infer the neurophysiological responses from fMRI, one needs to quantify the transformation between the evoked neuronal activities and the subsequent hemodynamic responses. Progress has been made towards quantifying the temporal relationship between the two responses, revealing of a linear relationship with long stimulus durations, and nonlinear features that appear when comparing responses to short and long stimuli (Boynton et al., 1996; Vazquez and Noll, 1998).

Several investigations have been also made towards quantifying the spatial specificity of fMRI responses relative to the area where increased neurophysiological activity was expected. The first study that quantified the spatial specificity of hemodynamic response showed that the BOLD-fMRI at 1.5T can be modeled as a Gaussian with full-width-at-half-max (FWHM) of 3.5mm (Engel et al., 1997). Subsequent fMRI studies estimated FWHM of 3.9 mm for gradient echo BOLD at 3 Tesla, 3.4 mm for spin echo BOLD at 3 Tesla, and ~2 mm for gradient echo BOLD at 7 Tesla (Parkes et al., 2005; Shmuel et al., 2007). Using optical imaging of intrinsic signal (OI-IS) Sirotin and Das estimated a FWHM of 3.06 mm and 2.74 mm for measurements equivalent to BOLD- and CBV-fMRI, respectively (Sirotin et al., 2009).

The studies mentioned above, that quantitatively estimated the spatial specificity of the fMRI response, did not account for the spread of the neurophysiological response. In other words, they implicitly assumed that the neurophysiological response in V1 to stimulation of part of the visual field ends in a sharp transition, with no spread between the retinotopically stimulated and non-stimulated regions. Here we aimed to demonstrate that the spatial spread of the hemodynamic response relative to the neurophysiological response is smaller than the absolute spread estimated for the hemodynamic response. To this end, we applied optical imaging of intrinsic signals measured simultaneously with neurophysiological recordings in cat area 18. We presented a group of stimuli that covered parts of the visual field, with horizontal boundaries that were positioned

along the vertical meridian. We estimated the spatial spread of the neurophysiological as well as the hemodynamic responses. Our results show that when accounting for the spatial spread of neurophysiological responses, the relative point spread function (PSF) of hemodynamic responses is smaller than the absolute, measured hemodynamic spread.

Materials and Methods

Experiments

10 data sets were obtained from 5 hemispheres of 4 animals, weighting 3.2 to 3.5kg. All procedures were pursued according to the guidelines of the Canadian Council on Animal Care (CCAC) and were approved by the animal care committees of the Montreal Neurological Institute and McGill University. The methods used for preparing and maintaining the animals were similar to those used in previous OI-IS studies using anesthetized cats (Shmuel and Grinvald, 1996, 2000). The methods are outlined below, whereas differences and new methodological aspects are described in detail. Data analysis was performed using code written in MATLAB (MATLAB 2013; The MathWorks, Natick, MA).

Visual stimuli

The stimuli were generated using Psychophysics toolbox (Brainard, 1997) running on the Matlab platform (the MathWorks, Natick, MA). They were displayed on an LCD monitor operating at 60 Hz refresh rate. The monitor was positioned at a distance of 30cm from the animal's eyes, subtending 60º × 45º of the visual field. It was shifted laterally by 1/3 of the monitor width, contralateral to the imaged hemisphere. The animals were stimulated monocularly through the eye contra-lateral to the exposed cortical hemisphere, using high-contrast black and white checker-patterns with a spatial frequency of 0.15 cycles per degree and a duty cycle of 50%. The stimulus drifted with a speed of 4 cycles per seconds, changing its shifting direction to a randomly selected new direction every 1 second. The main set of stimuli included 27 conditions. In one control/baseline condition, the screen remained gray and no stimulus was presented. The remaining 26 conditions formed 13 pairs of stimuli. Each pair included two stimuli that abutted along a horizontal line in the visual space. Each of the horizontal lines that corresponded to the 13 pairs was located at a position defined by a scalar (from the vector [-4 -3 -2 -1.5 -1 -0.5 0 0.5 1 1.5 2 3 4]) multiplied by the width of receptive fields near the electrode insertion site. The electrode

insertion site, in the middle of the exposed part of area 18, corresponded to a typical receptive field size of 2.4 degrees (Tusa et al., 1979) Each pair of stimuli included a stimulus that stimulated the visual space from the corresponding horizontal line and up, and a stimulus covering the visual space from the horizontal line and below. Thus, the upper or bottom part of the stimulation monitor showed moving checker-patterns (Fig. 6-1). The height of the monitor was adjusted so that the horizontal line corresponding to 0 degrees approximately overlapped with the aggregate receptive fields of neurons close to the recording probe. In the point spread function analysis, the top and bottom sets of stimuli were treated as 2 different groups of stimuli.

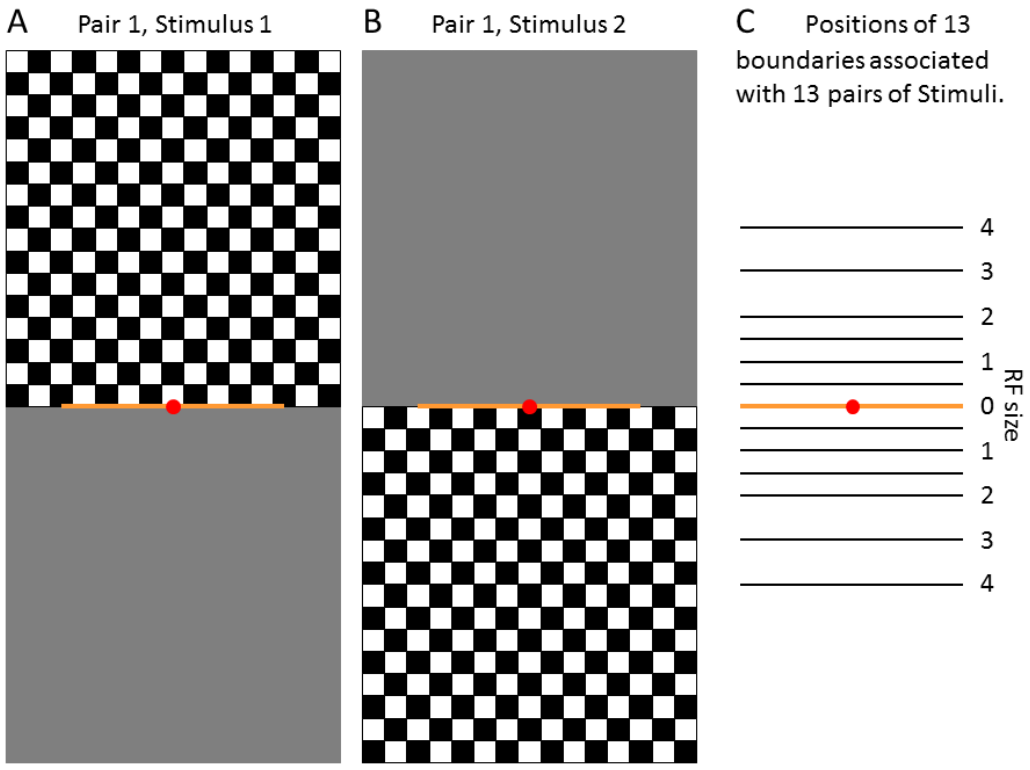

Figure 6-1. Visual stimuli.
A) Pattern of stimulus 1 of a pair of stimuli: moving high-contrast checkers stimulated the upper part of the visual field. B) Pattern of stimulus 2 of a pair of stimuli: moving checkers stimulated the lower part of the visual field. Note that stimuli 1 and 2 abutted along a horizontal line in the visual field. C) The complete set of 13 horizontal lines, each of which was associated with one of 13 pairs of stimuli. The two stimuli belonging to each pair abutted along the horizontal line corresponding to the pair. The vertical distances between the horizontal lines were defined according to visual angles that corresponded to the size of receptive fields at the electrode insertion site.

Data acquisition

From each of the hemispheres, we obtained 30-40 trials of data, where each trial consisted of acquiring 27 time-series, each of which associated with one of the 27 conditions. All 27 conditions were presented in each trial, with a randomized order of presentation. During each presentation, we acquired data over a period of 12 seconds: 2 seconds in which the stimulus pattern was static, 5 seconds during which the pattern moved, followed by 5 seconds with a static stimulus pattern. To allow for the relaxation of activity-dependent vascular changes, each 12 second period of data-acquisition was followed by an 8-second inter-stimulus interval. The stimulus was switched to the static checkers of the next condition during this interval.

Surgical procedures

The animal was first intubated and anesthetized with isoflurane in 100% O_2. During the surgery, the level of isoflurane was adjusted within 1-3%, and the animal's temperature and heart rate were kept between 36-37 degrees Celsius and 130-160 beats per minute, respectively. Cannulas were inserted into the cephalic veins, for intravenous administration of fluids (Villeneuve and Casanova, 2003). The animal was then placed in a stereotaxic frame. The skull of the cat was opened above area 18 by drilling a circular hole with an approximate 18 mm diameter centered at Horsley–Clark coordinate A4. The imaged area extended from the midline to the lateral sulcus. The dura was removed from above area 18 in one hemisphere. A stainless steel chamber was cemented onto the skull. The chamber was filled with silicone oil and sealed with a round perspex cover. We then projected the retinal blood vessels, including the regions of the blind spot and the area centralis, onto a screen positioned 30 cm from the animal's eyes, in order to appropriately position the stimulation monitor. The nictitating membranes were retracted with local application of Mydfrin and the eyes were protected using contact lenses with zero power. The eyes were focused on a screen at a distance of 30 cm using appropriate external lenses, as determined by retinoscopy. External lens with appropriate power was placed in front of the stimulated eye. The height of the stimulating screen was adjusted so that the pair of stimuli with the edge at the middle of the screen would also activate hemodynamic responses that show a boundary in the middle of the exposed cortex. Once the height of the screen was determined, the perspex cover was removed and an electrode was inserted. 1% agar was poured to fill the chamber and to reduce the physiological movement artifact. Finally, simultaneous recordings of OI-IS and extracellular EP were then pursed for 8 – 10 hours (see following sections).

Animal monitoring

Following the surgery, gas anesthesia was reduced and kept at 0.8-1.0%, and the heart rate was maintained at 160-180 BPM. A paralytic agent (gallamine, 10mg/kg/h) was infused via the I.V. line, dissolved in a sterile lactated Ringer solution. The animal was mechanically ventilated at a rate of 25-40 strokes per minute and a volume of 10-15 ml/kg, in order to keep the end-tidal CO2 at 32-38 mm Hg. The gas mixture was adjusted within the range of 100% medical air to 70% medical air / 30% O2, in order to keep the oxygen saturation level at 93-98%. Finally, the animal's temperature was kept at 37.9-38.1 degrees.

Optical imaging

Cortical images were obtained using a 12-bit differential data acquisition system (Imager 3001, Optical Imaging Ltd., Rehovot, Israel) with a Pantera 1M60 camera (Teledyne Dalsa, Waterloo, Ontario, Canada) and a 60 mm lens. The camera was mounted above the optical chamber such that its optical axis was approximately perpendicular to the cortical surface. The camera was focused on the surface of the cortical region of interest (ROI), ensuring that the surface of the gray matter and the cortical pial blood vessels were in focus. The ROI was limited to area 18 in one hemisphere; we imaged this ROI with a matrix of approximately 800 by 300 pixels, at a sampling resolution of 40-55 pixels/mm). The camera frame rate was set at 10Hz. We imaged the cortex at this high frame rate, under illumination of 2 light emitting diodes (LEDs) with center wavelengths of 530 nm and 617 nm, respectively. The power to these 2 LEDs alternated at each data frame, based on the camera's frame toggle signal. Hence, the frame rate obtained considering the illumination of each of the 2 LEDs was 5Hz. Green and orange LEDs were used to compute changes in content of oxy- (HbO) deoxy- (HbR) and total (HbT) hemoglobin (Chapter 5), where HbR and HbT are analogous to BOLD-fMRI and CBV-fMRI, respectively.

Neurophysiological recordings

Neurophysiological recordings were performed using recording probes with 32 electrode contacts (A32, intervals between adjacent contacts 100 μm, impedance 1-2 MΩ, contact surface area of 177 or 413 μm^2 (NeuroNexus Technologies). We used a multi-channel neurophysiology recording system (RZ2, Tucker-Davis Technologies). The probes were inserted perpendicularly to the surface of the cortex, approximately at the center of the exposed part of area 18 (Fig. 6-2A). The data were acquired at a sampling rate of 24,414 Hz.

Optical imaging data preprocessing

The preprocessing of the data, including the integration of response and definition of response time relative to the onset of the stimulus, was carried out similarly to our previously published work (Chapter 5). Data acquired under 530 nm and 617 nm were subject to artifact removal (Chapter 5). They were transformed into changes in HbR and HbT, followed by masking out of blood vessel regions and filling in the space occupied by pial vessels with nearby GM values (Chapter 5). The average values within each of nine 0.7 × 0.7 mm squares arranged in a 3 × 3 array centered on the electrode were taken for further analysis (Figures 6-2B and 6-2C). The averaging ensured stability of data.

Estimation of retinotopic boundaries

The estimation of the boundaries between representations of abutting stimuli on cortex was important, as it served to transform the edges of stimuli from visual space to distance along the cortical surface. We determined the boundaries by first fitting the differential maps of each pair of abutting stimuli with sigmoid functions, one along each vertical line (Fig. 6-3A). All differential maps across all edges were then summed together to create the overall gradient map (Fig. 6-3B). Similar procedure was performed on the fitted differential maps as well (Fig. 6-3C). Partial derivatives along the X and Y directions were computed to create a 2D gradient vector map. Then from the electrode insertion point, a gradient vector curve was created, extending to the positive maximum with gradient ascent and to the negative minimum with gradient descent (Figures 6-3B and 6-3C, white curve). The gradient ascent is superior to just drawing a line, because it is capable of capturing nonlinear mapping features (such as the log-polar) of the retinotopic mapping. Finally, the points of intersection between the gradient vector curve and the edge boundaries were marked (Fig. 6-3D). The total distances along the curve from the electrode to the intersections were used as the reference for fitting of Gauss error functions (erf; see Fitting section below).

Neurophysiology Data preprocessing

Data recorded extracellularly was first split into 3 categories: 1) peristimulus time histogram (PSTH) of spike counts using custom made spike detection algorithm binned in 10ms long bins, 2) band limited power (BLP) of low gamma (30-50 Hz) and high gamma (50-100 Hz). The BLP was computed based on Fourier Transform of 100 ms long time segment rolling at a step size of 10ms. Then, the average of the spike count or of the BLP value was averaged over the

period of 1 to 5 seconds following the onset of the stimulus (sustained response). This measure of the response was divided by the average of the baseline activity acquired over the 2 seconds before the beginning of the stimulus, in order to determine the response in each trial for each condition (Fig. 6-4A). We determined the contacts that overlapped with layer 4 based on the CSD profile (Fig. 6-4B, black dashed line). The neurophysiological response was averaged over the 7 contacts from the 4th contact above to the 2nd contact below the center of layer 4 (Fig. 6-4C white dashed line). These average responses were used for further analysis

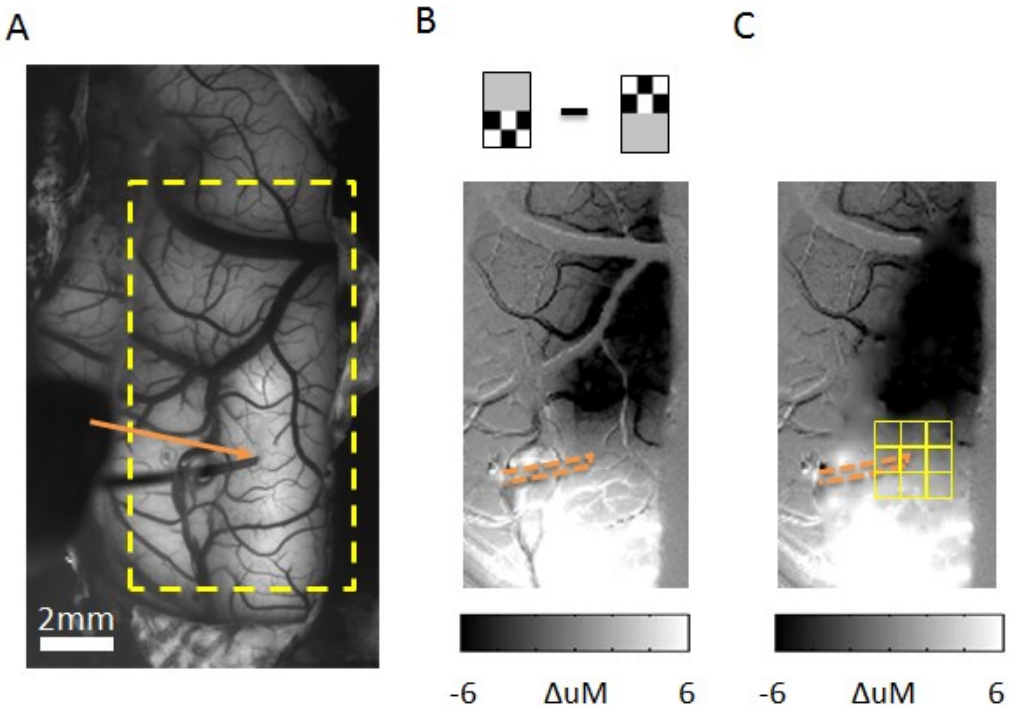

Figure 6-2. Optical Imaging.
A) Image of light reflected under 530 nm illumination. The electrode, marked by an orange arrow, was inserted perpendicularly to the cortical surface and approximately in the middle of the part of area 18 residing on the cortical surface. B) Differential cortical map of the two responses elicited by the pair of stimuli sharing their boundary at the middle of the screen (this is the boundary marked as 'Size RF' 0 in Figure 1C. The orange dotted curve depicts the electrode. The gray level colorbar presents the change in HbT in units of micro-mole. C) The pixels in B that correspond to blood vessels or to the electrode were masked out and filled in with values interpolated based on responses from nearby gray matter pixels. The yellow squares mark a 3x3 array of 0.7 x 0.7mm squares centered on the insertion point of the probe. The optical imaging responses to each of the 27 conditions were averaged over all pixels in each square in preparation for further analysis.

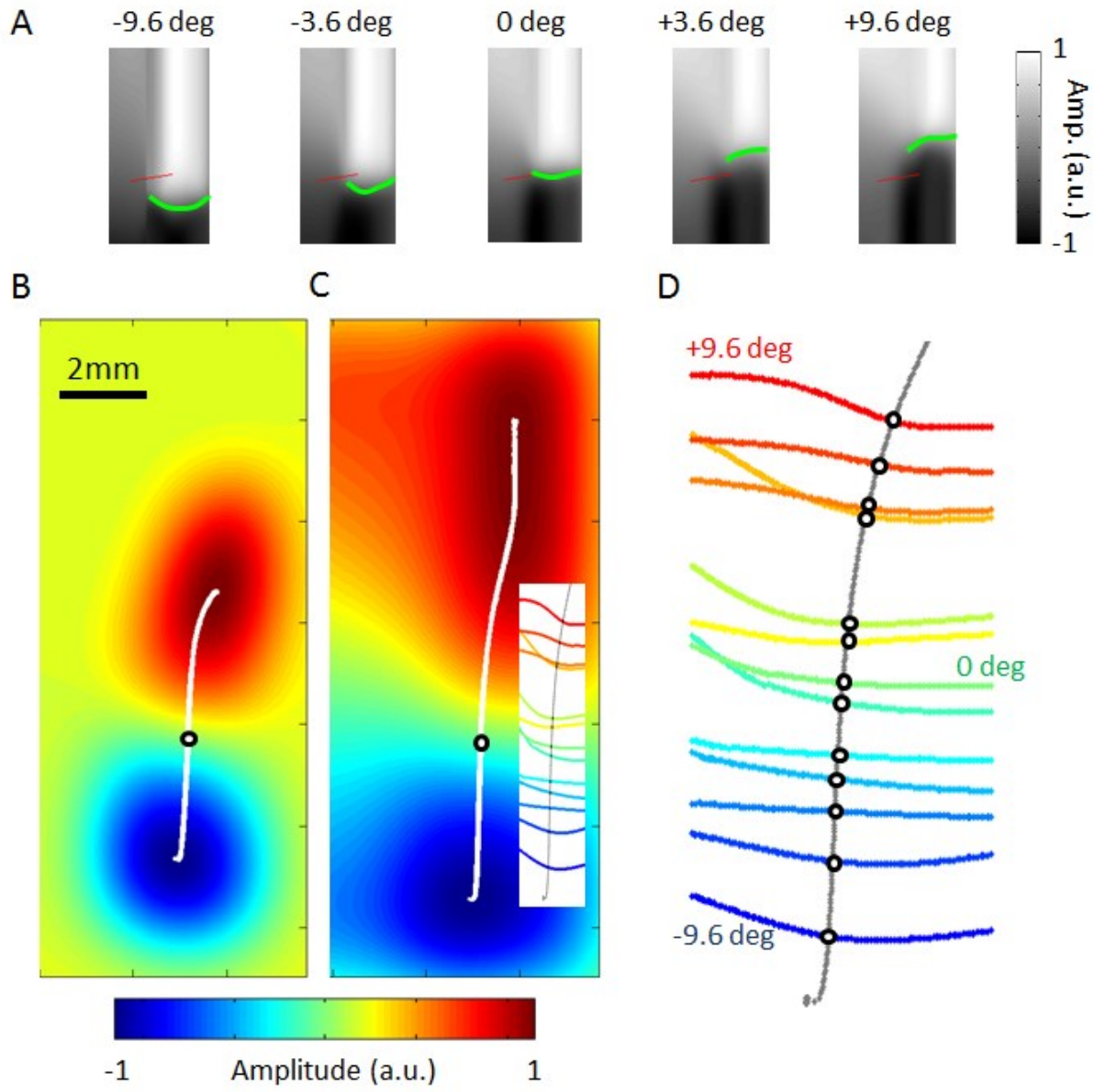

Figure 6-3. Retinotopic boundaries.
A) Differential cortical response maps obtained from each of the pairs of stimuli were fitted with a sigmoidal function along each vertical column. The 5 images present the sigmoid fitted maps obtained from 5 pairs. The boundary associated with each pair was then defined as the curve formed by the group of zero values (green curve). The site where the electrode penetrated cortex is marked by the red line. B) The differential images were summed together to create an overall differential map. C) The fitted sigmoidal images were summed together to create an overall sigmoid fitted differential map. From the electrode insertion point (circle), a gradient vector curve was extended to both the positive and negative extrema. D) Zoomed view of the intersections of the vector curve and the retinotopic boundaries (marked as circles). Each circle depicts the mapping of a point on the corresponding stimuli pair's horizontal boundary from the visual space to the cortical surface space. The actual size of this map of retinotopic boundaries and intersections relative to the overall differential map can be seen in panel C.

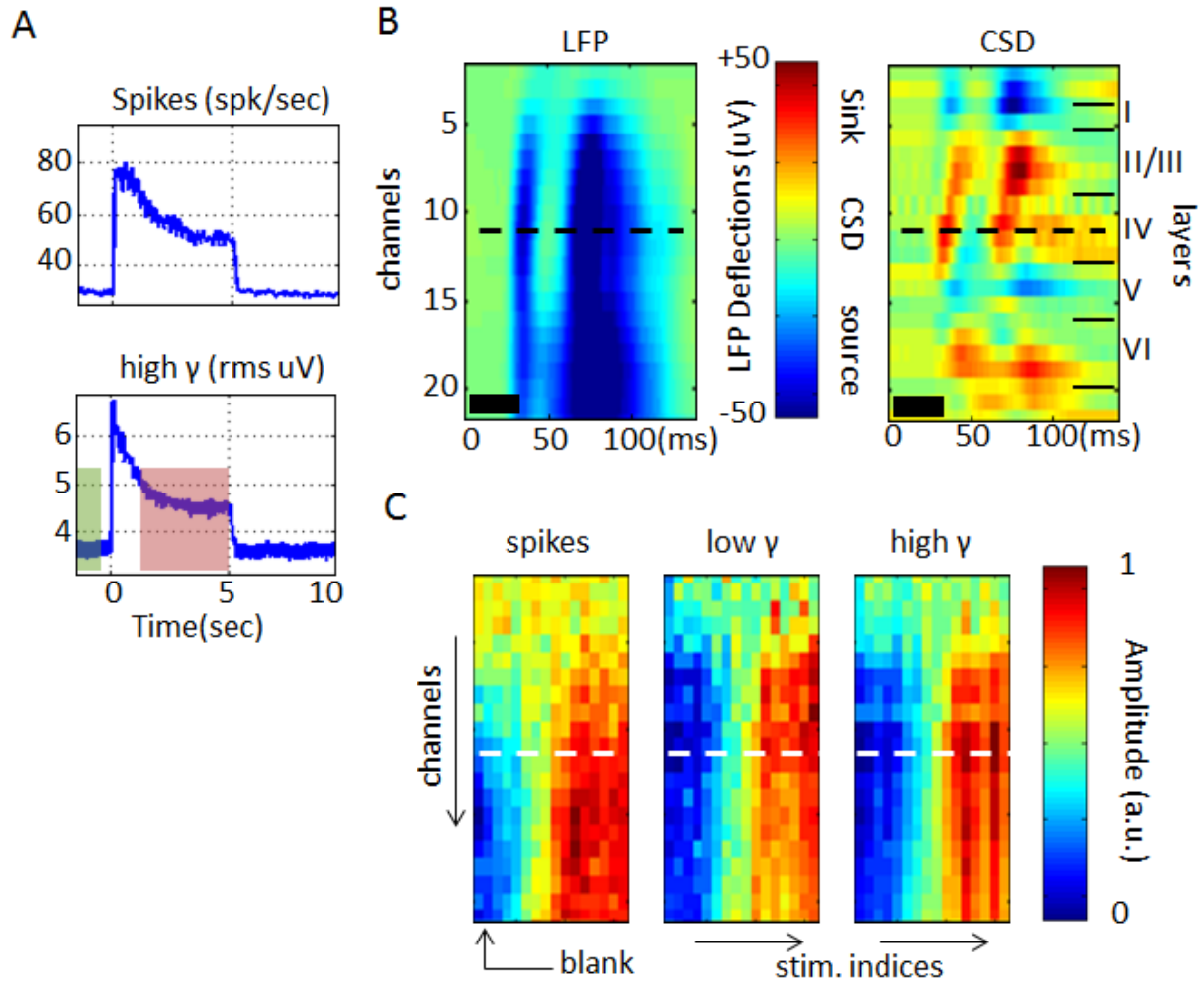

Figure 6-4. Electrophysiology.
A) Temporal dynamics of electrophysiological responses. The time-courses first show a transient response followed by a gradually decreasing response and a sustained response for the stimulus duration of 5 seconds. The average activity from 1 to 5 seconds from the onset of the stimulus (pink shade) was divided by the activity averaged over the baseline period from -2 to -0.5 seconds (green shade). Time-courses of spiking activity and RMS of high gamma are presented. B) Estimation of depth. The panel to the left presents the average LFP response to 33 millisecond long full-field 33 white flash stimuli. Standard CSD analysis was applied to the LFP in order to determine the contacts showing the main sink response (in red) expected in layer 4. C) Cortical depth-wise responses as a function of the different stimuli sorted according to the part of visual field they covered. The vertical axis represents the electrode contacts according to their order and depth. Four contacts above and 2 contacts below the center of the layer 4 (white dotted line) were considered for further analysis.

Fitting Gauss error functions (erf) to the data

The processed OI-IS and EP data were subjected to an outlier removal process. First, for each stimulus condition, the cortical response of a single trial that exceeded 3 standard deviations from the mean response to the corresponding stimulus was removed. Then the ensemble data of all trials and all stimulus conditions was scaled so that the mean of cortical responses to blank stimulus (gray screen) was 0 and the mean of cortical responses to the stimulus that elicited the highest response was 1. We then manually removed trials that showed weak or no response compared to the mean response over trials. We re-scaled the data so that the mean of blank and mean of the strongest responses are again 0 and 1; and re-performed outlier removal, with any single trial with response that exceeded 3 standard deviations away from the mean of all trials was removed. Finally, we removed average responses to any stimulus lower than -2 or higher than 3. These responses were considered outliers relative to the expected normalized responses in the range of 0 to 1.

A Gaussian distribution function can be formulated as follows. An important parameter is the standard deviation, σ, which denotes how wide the function is.

$$f_{gauss}(x) = Aexp\left(-\frac{1}{2}\left(\frac{x-B}{\sigma}\right)^2\right) + C$$

Previous studies that quantified the spatial specificity of BOLD-fMRI used the FWHM of a Gaussian as their specificity measure. The standard deviation of a Gaussian function can be related to the FWHM using the following relationship.

$$FWHM = 2\sqrt{2\ln 2}\,\sigma \approx 2.355\sigma$$

Since we used a step-like edge stimulus, if the hemodynamic or neuronal responses were not smoothed versions of the cortical representation of the stimulus we could expect a step-like response. Since we did expect smoothed responses, we fitted the responses with a step function convolved with a Gaussian, i.e. a Gauss error function. The error function is the cumulative density of the Gaussian function and is also equal to a step function smoothed with a Gaussian kernel. In Figure 6-5, we demonstrate that linearly arranged aggregate receptive fields, modeled as Gaussians respond as a smoothed version of the edge stimulus. This response is identical to a Gauss error function, also known as cumulative Gaussian distribution.

$$f_{error}(x) = Aerf\left\{\frac{x-B}{\sqrt{2}\sigma}\right\} + C$$

In this work, we measured the FWHM of absolute EP PSF (electrophysiological responses relative to unsmoothed stimulus representation), of absolute OI-IS PSF (hemodynamic responses relative to the unsmoothed stimulus representation), and of the relative PSF (hemodynamic responses relative to electrophysiological responses). The relative PSF FWHM was obtained based on two different methods, the Gaussian identity and direct subtraction. The Gaussian identity methods is based on the observation that convolution of two Gaussian functions is also a Gaussian function with resultant standard deviation which is the quadratic sum of the standard deviations of the convolved Gaussians;

$$\sigma_N^2 + \sigma_{HrN}^2 = \sigma_H^2$$

$$f_{gauss}(x, \sigma_N) * f_{gauss}(x, \sigma_{HrN}) = f_{gauss}(x, \sigma_H) = f_{gauss}\left(x, \sqrt{\sigma_N^2 + \sigma_{HrN}^2}\right)$$

where the subscripts refer to:

N = neuronal responses

H = hemodynamic responses

HrN = hemodynamic relative to neuronal responses

Using this relationship, we can estimate the hemodynamic PSF relative to neuronal responses by subtracting the squared neuronal PSF from the squared absolute hemodynamic response, and taking the square root of the result. This method (Gaussian convolution model) for obtaining relative PSF is commonly used (Xing et al., 2009).

$$\sigma_{HrN} = \sqrt{\sigma_H^2 - \sigma_N^2}$$

In addition, we have considered the subtraction method (additive model for PSF of neurophysiology and hemodynamic responses) for quantifying the hemodynamic PSF relative to the neuronal PSF, so that we can compare our results to those presented by Vazquez et al. (2014).

$$\sigma_{HrN} = \sigma_H - \sigma_N$$

Statistics

We computed the statistical significance of testing whether the mean FWHMs of OI-IS and EP modalities were different using 2-tail paired t-test with $n \leq 11$. Part of the data sets did not include FWHMs of all the measured modalities (HbR, HbO, HbT, spikes count, power of low- and high-gamma), since the confidence interval obtained during the fitting was too wide (95% confidence interval of FWHM is > 2 mm). These data-sets were excluded from the corresponding comparisons, leaving only data-sets that had measures of FWHM of the two compared modalities, thus allowing paired statistical testing.

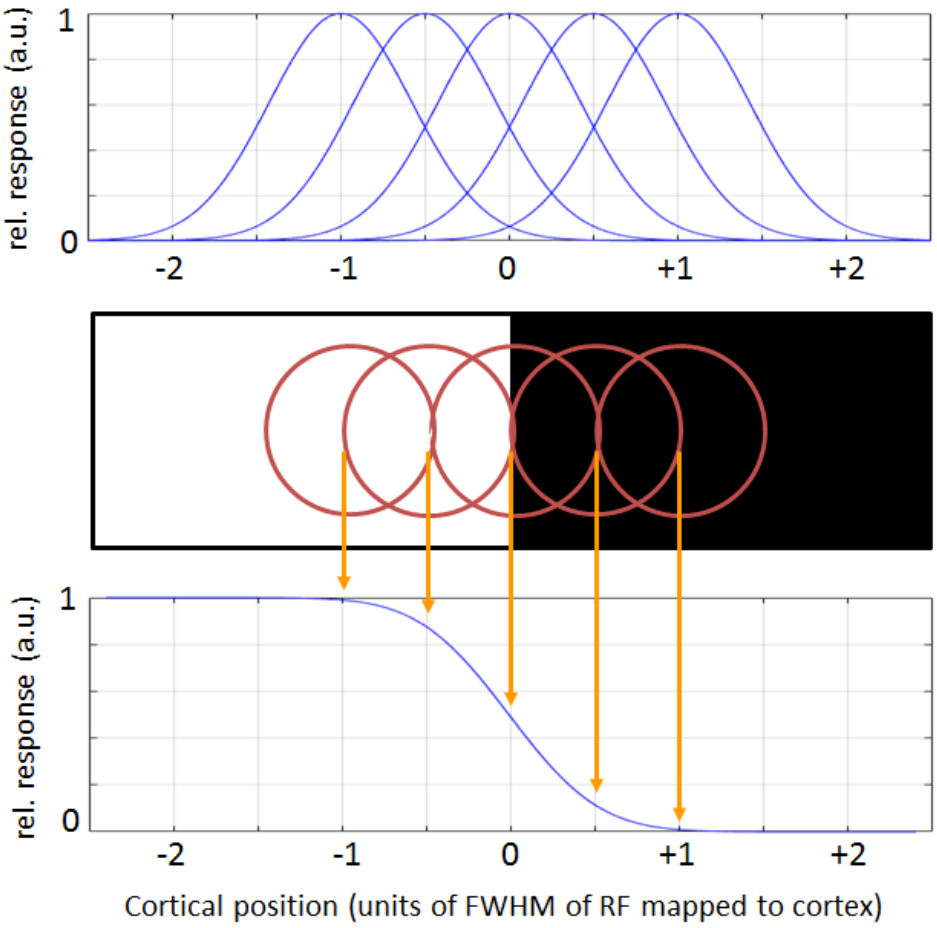

Figure 6-5. Gauss error function as a model for the visual cortex response to edge-like stimulus.
Top) Gaussian-like aggregate receptive fields with a FWHM of 1 unit. Middle) Schematic representation of edge stimulus stimulating part of the visual field and part of the aggregate receptive fields. Bottom) Summed response of all neurons in response to the presented edge stimulus. The transition from maximal to minimal responses extends approximately over 2 units of FWHM.

Results

Fitting with Gauss error functions

In this work, we found an approximate linear relationship between the presented edges' eccentricity in the visual field and the actual loci found on the cortical surface (Fig. 6-6). The expected non-linear relationship based on previous retinotopic mappings (Tusa et al., 1979) was not found in our study (see Discussion). We then used this approximate linear mapping of the edges (mm/◦) as a function of space in area 18 to serve as a spatial grid for fitting the measured hemodynamic and neurophysiological responses to our stimuli. In other words, determining the mapping of the edges of stimuli, allowed us to estimate the spreads of neurophysiological and hemodynamic responses as a function of cortical distance (mm) instead of visual eccentricity in degrees.

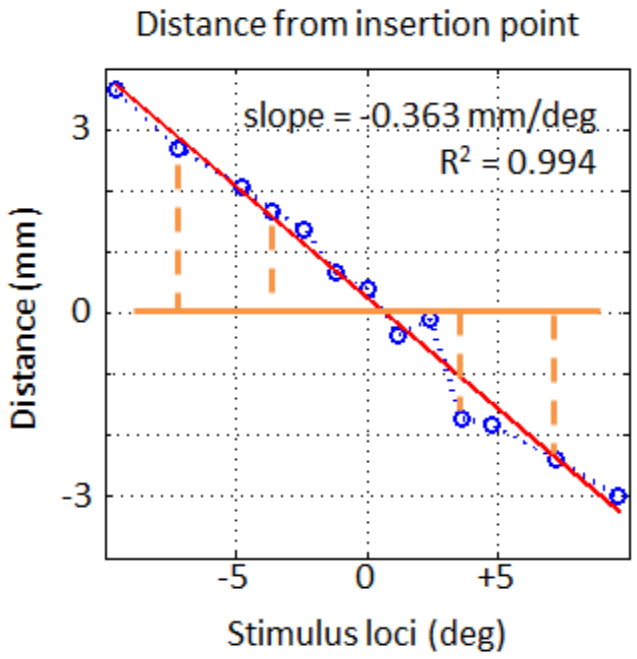

Figure 6-6. Regression of boundaries in visual space to cortical surface.
The loci on the cortical surface along the gradient vector curve (circle in Figure 3D) were plotted as a function of the pair-wise boundary between visual stimuli in the visual space. The insertion of the electrode is assigned 0 degrees on the x-axis (orange horizontal line) and 0 distance on the y-axis. The distance from the electrode's penetration to the corresponding boundary point on the cortical surface is presented on the y-axis (vertical dotted lines). The example shown here shows a linear regression with R^2 = 0.994. The slope parameter was used to transform the loci of the boundaries in the visual space expressed in degrees to their corresponding cortical surface loci in millimeters.

The responses were fitted using the Gauss error function. We first performed individual error function fitting across the 9 binned pixels (3x3 squares) on the OI-IS map and 7 channels (from -2 to +4 channels of the center of layer IV) in EP recording (not shown). We then averaged, for each hemisphere, raw data of ROIs or Channels that showed reliable fitting. Finally we refitted the error function for the averaged ROIs and Channels. Outliers with FWHM higher than 10mm or lower than 0.1mm were removed from the statistics. Here we show an example of cleaned hemodynamic responses and EP responses across stimuli averaged across trials and the corresponding fitted curve (Fig. 6-7).

Absolute PSF

We report the summary of absolute FWHMs from 10 datasets (Table. 6-I). The average FWHM of HbT and HbO responses were 2.83 mm and 3.26 mm, respectively. The FWHM values computed from HbR responses had confidence intervals wider than 2 mm in 3 of the 10 data sets, due to low-quality fits compared to HbT/HbO and hence part of the HbR PSF data could not be estimated. However, the average pair-wise ratio of HbR/HbO/HbT from those data sets where the HbR PSF fit was acceptable was 1.17/1.06/1.00 respectively. The EP FWHM for spiking activity was 2.07 mm. The FWHM widened with decreasing frequency content (3.25 mm for high gamma and 3.73 mm for low gamma).

We compared whether these values were significantly different from each other. Paired two-tailed t-test showed that the FWHM of the spiking response was statistically different from that of the low gamma band and the HbO responses ($p < 0.05$, Table 6-II). In addition, the FWHM measures of HbR and HbT responses were statistically different ($p < 0.05$, Table 6-II).

Relative PSF

We computed the relative FWHM using two methods: 1) Gaussian identity and 2) simple subtraction (Table 6-III). Using the Gaussian convolution model, the relative PSFs of HbO and HbT responses in reference to spike activity responses were 2.52 mm and 1.93 mm, respectively. Using the additive model, the relative PSFs of HbO and HbT in reference to spiking activity response were 1.19 mm and 0.76 mm, respectively. The gamma bands were not considered for this part of the analysis because the FWHM of low gamma's absolute PSF was larger than that of HbO and HbT; and similarly the FWHM of high gamma was larger than that of HbT.

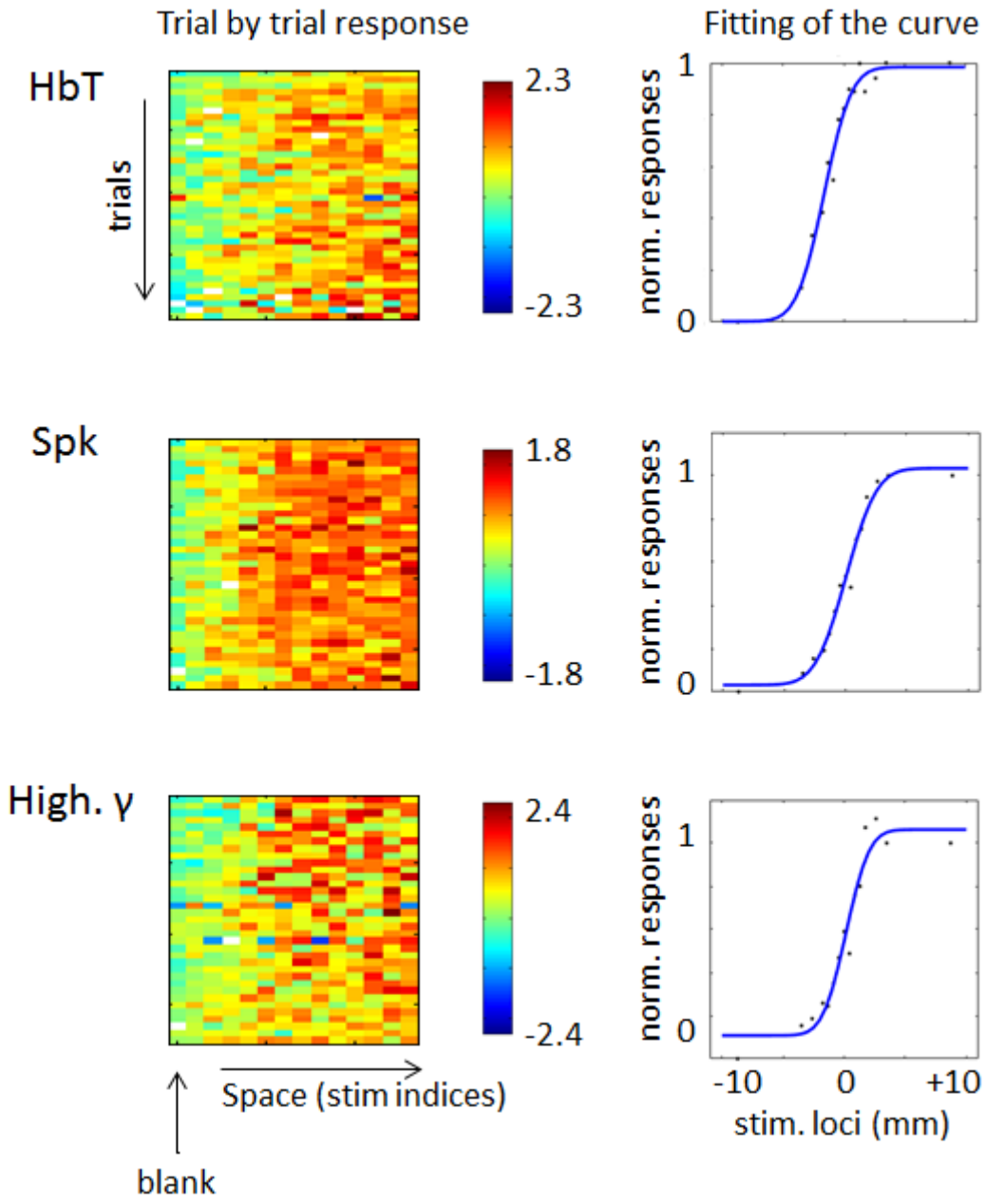

Figure 6-7. Fitting of Gauss error function.
An example of OI-IS responses (HbT) and EP responses (Spike count; high-gamma) across stimuli and across trials. The ensemble data in each row and each matrix was normalized such that the average (over trials) response to blank (gray screen) condition is 0 and the average response to the stimulus with the largest area of moving checkers is 1. An error function was then fitted to the ensemble responses (the average responses to stimuli across trials are plotted as black dots). In this particular example, the FWHM of the error function were 3.30, 3.40 and 3.18 for HbT, Spike count and high-gamma, respectively.

Table 6-I. Point spread function of physiological responses to the checker-pattern stimuli

		HbR	HbO	HbT	L.gam	H.gam	Spk
Top	hemi. A	3.44	3.21	3.30		3.11	3.40
	hemi. B		4.85	4.47	2.63	1.79	1.58
	hemi. C		3.30	1.15	4.33		0.71
	hemi. D	2.88	2.43	2.41	2.67		1.22
	hemi. E	1.22	1.21	0.84	3.12	2.69	2.23
Bottom	hemi. A	3.01	3.02	3.10	4.20	3.28	3.36
	hemi. B		5.78	5.08	6.66	5.28	2.64
	hemi. C	2.51	2.61	1.61			0.87
	hemi. D	2.85	2.60	2.65	2.92	3.05	1.24
	hemi. E	4.61	3.60	3.69	3.33	3.58	3.48
Mean		- - -	3.26	2.83	3.73	3.25	2.07
St-Dev		- - -	1.28	1.39	1.35	1.06	1.09
p-value ($\mu = 0$)		- - -	1_E-5	5_E-5	5_E-5	1_E-4	1_E-4

The FWHMs of the fitted error function are presented here for each of the reliable OI-IS and EP measures from the 5 hemispheres and 2 stimulus groups. FWHM values in empty entries had 95% confidence interval > 2.0 mm and were therefore excluded from further analysis. The global mean of the HbR was not computed due to too many missing values. The bottom row shows the p-value for testing the hypothesis that the mean is not wider than 0 (one-tailed t-test).

Table 6-II. Paired t-test for comparing the FWHM of OI-IS and EP responses

	HbO	HbT	L. Gamma	H. Gamma	Spike
HbR	0.12	0.03	0.58	0.79	0.16
HbO		0.09	0.41	0.70	0.04
HbT			0.19	0.92	0.09
L. Gamma				0.10	0.01
H. Gamma					0.15

Results of testing differences between the means of FWHM associated with the different modalities (paired two-tailed t-test). The matrix of p-values shows the comparisons for all possible pairs of measured modalities, including the comparisons of each of the neurophysiology measures against each of the OI-IS measures. All tests were done using pairs of available FWHMs from the same animal and set of stimuli (top or bottom stimuli).

Table 6-III. Point spread function of hemodynamic responses relative to neurophysiological response (using Gaussian convolution and additive models)

FWHM (mm)	Gaussian		Additive	
	HbO	HbT	HbO	HbT
Spike	2.52	1.93	1.19	0.76

The root-subtraction-square and subtraction were computed from the averaged FWHM of HbO/HbT and FWHM of spiking activities to yield the PSF of the hemodynamic responses relative to neurophysiological responses.

Discussion

Summary of the results

In this work, Gauss error functions are fitted to the cortical responses to retinotopic stimuli with edges at various eccentricities in the visual field (Figures 6-3 and 6-7). The FWHM of each of the measured responses is based on this fitting. The mean absolute FWHMs of HbO and HbT responses in cat area 18 are 3.26 and 2.83 mm, respectively. The FWHM of the average HbO is 1.15 times wider than that of HbT responses (Table 6-I). The mean FWHM of HbR responses is significantly larger than that of HbT responses. The mean absolute FWHMs of PSFs of low-gamma, high-gamma and spiking responses in cat area 18 are 3.73, 3.25 and 2.07, respectively (Table 6-I). The FWHM of HbO and low gamma responses are significantly larger than that of spiking responses (Table 6-II). Lastly, the PSF of HbO and HbT responses relative to spiking activities are 2.52 mm and 1.93 mm, respectively, using the Gaussian convolution model; and 1.19 mm and 0.76 mm using the additive model (Table 6-III).

Wide absolute FWHM of hemodynamic and neurophysiological responses in cat area 18

In this work, we modeled the spatially mapped hemodynamic and neurophysiological responses as error functions. This corresponds to stimulation of part of the visual space and cortex with a sharp edge between the stimulated and non-stimulated regions, combined with a convolution of this edge-like retinotopic representation with a Gaussian PSF (Figure 6-5).

Modeling the spread of the BOLD response as Gaussian has been previously used in the fMRI literature (Engel et al., 1997; Parkes et al., 2005; Shmuel et al., 2007). The RFs of single neurons in cat areas 17 and 18 were previously mapped subjectively as rectangles (or, taking into account the response magnitude, as boxes; Hubel and Wiesel, 1959, 1962, 1965) or cylinders (Tusa et al., 1979). Similarly, the RFs in macaque V1 were previously mapped as rectangles/boxes (Hubel and Wiesel, 1974). However, in that same area (macaque V1), the spread of aggregate receptive fields of multi-unit activity (MUA), that accounts for both the receptive fields and their scatter (Hubel and Wiesel, 1974) fits well a Gaussian model (Xing et al., 2009). Consistent with the results demonstrated by Xing et al. (2009), the spread measured through population neurophysiological action potential responses to edge-like stimuli fits well Gauss error functions in our data too (Fig. 6-5). Similarly, a Gaussian model fits well the spread of the LFP in macaque area V1 (Xing et al., 2009) and in our own data (Fig. 6-7).

Here, we have obtained absolute FWHMs of 3.73, 3.25 and 2.07 mm for low-gamma, high-gamma and spike responses, that are large relative to those reported by Xing et al. (2009). These authors reported σ values of .622 mm and .573 mm that correspond to FWHM of 1.46 mm for the LFP and 1.35 mm for MUA. However, we believe that the difference in MUA spread can be explained by differences in the size of RFs and magnification factor in monkey V1 and cat area 18. The mean width of receptive fields of neurons in the region where we inserted the electrode is approximately 2.4° of visual field (RFs modeled with cylindrical response; Tusa et al., 1979). In the same region, the cortical magnification factor is approximately 4 mm per 10° of visual field (Tusa et al., 1979). Indeed, our regression curve on the representative hemisphere shows a slope of 0.393 mm/degree of visual eccentricity (Fig. 6-6). The mean slope of the regression computed over data-sets is 0.434 ± 0.060 mm/degree, n = 5 hemispheres. We can infer that the average cylindrical-like receptive field of single neurons in the part of area 18 we recorded from is approximately mapped to 2.4º×0.434 mm/° = 1.04 mm. In macaque V1 at an eccentricity of 5°, where Xing et al. (2009) obtained their results, the mean size of RFs is approximately 0.4º, and the magnification factor is approximately 2°/mm (Hubel and Wiesel, 1974). We can infer that the average cylindrical-like receptive field of single neurons' diameter is mapped to 0.8 mm. The ratio between this measure in monkey V1 and the one in the cat brains' region we recorded from is then 0.8/1.04 = 0.77. Therefore, to directly compare our results to Xing et al.'s, we need to multiply the FWHM we obtained by 0.77: 2.07*0.77 = 1.59 mm. This value is comparable to the FWHM reported by Xing et al. (2009) (1.35 mm for MUA). Our result, showing substantially wider FWHM for the gamma-band responses compared to that of spiking activity is at odds with the report by Xing et al. (2009). However it is in agreement to those reported in several previous studies (Mitzdorf, 1987; Kruse and Eckhorn, 1996; Kreiman et al., 2006; Liu and Newsome, 2006; Berens et al., 2008; Nauhaus et al., 2009; Kajikawa and Schroeder, 2011).

Here, we have obtained large absolute FWHM of 2.83 and 3.26 mm for HbT and HbO responses, respectively, in comparison to the FWHM observed in fMRI of the human visual cortex at 7 Tesla (~2.34 mm; Shmuel et al., 2007). All post-mortem anatomical studies and fMRI studies in humans indicate that the human visual cortex is highly similar to that of the macaque. Therefore, we expect that the difference between the PSF of fMRI response at 7 Tesla (2.34 mm, Shmuel et al., 2007) and the one we report here can be accounted for, in part, by the likely smaller RFs and spread of neurophysiological responses in humans than in cats.

A confounding factor that increases the absolute FWHM we estimate for HbT responses can possibly be the light scattering effect. The PSF as measured by OI-IS includes a contribution of light scattering, which does not affect the PSF measured by BOLD-fMRI. The additional PSF component due to light scattering was measured in the order of 250 µm (234 µm, Orbach and Cohen, 1983; 280 µm, Polimeni et al., 2005). This additional PSF from light scattering is part of the absolute OI-IS PSFs we estimate here. It adds up to the relatively wide PSF of EP responses as factors determining the wide PSF of HbT responses.

In principle, it is possible that the wide point spreads we measured are caused in part by drifts or fluctuations in gaze in spite of our use of a paralytic agent (Forte et al., 2002). However, we measured the center of the Gauss error function across trials, and we did not observe any systematic drift in the gaze of the paralyzed animal (Fig. 6-8A). The fit of the Gauss error functions as a function of time was based on data from only two consecutive trials, and was therefore noisy (Fig. 6-8). However, no obvious systematic drift could be observed.

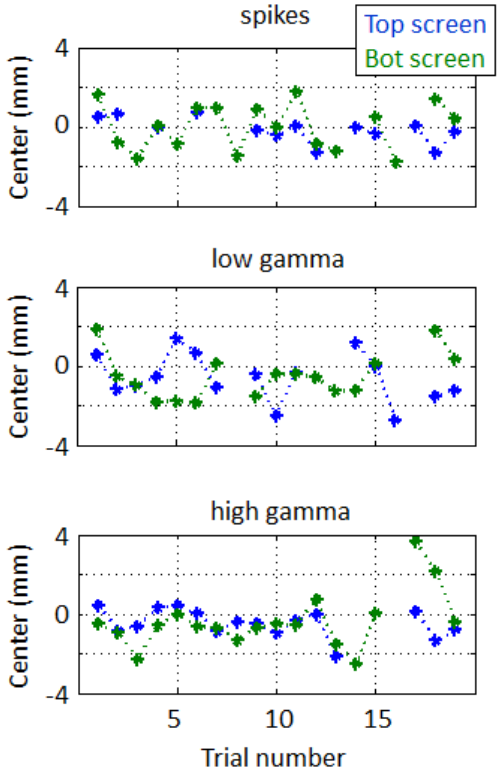

Figure 6-8. Center of cortical responses as a function of trial number.
Center of error function as a function of trial number. An error function was fitted to EP responses on trial-by-trial basis. For each trial, the center parameter was computed. The figure presents an example of spiking, low- and high-gamma responses to the top and bottom screen checker stimuli from one hemisphere.

Spatial specificity of Hemoglobin species

Based on several fMRI studies that compared CBV and BOLD responses, the CBV response is more spatially specific compared to BOLD and better reflects the spatial pattern of neuronal responses (Kim and Kim, 2005; Zhao et al., 2006; Smirnakis et al., 2007; Kim et al., 2013; Poplawsky and Kim, 2014). The hypothesized mechanism constitutes only gradual dilution of increased HbR in draining veins. Therefore, since in regions non-overlapping with the site of increased neurophysiological activity undiluted HbR can still be observed, it must be accompanied with decreases in HbO, since the HbT does not change. In these regions, although the absolute change in HbO is equivalent to that of HbR, the relative change of HbO should be smaller than that of HbR because the concentration of HbR is inherently smaller in cortical blood vessels, including veins, compared to HbO (Chapter 5; Vovenko, 1999). Thus the overall hemodynamic specificity should follow the following ranking: HbT > HbO > HbR. Our findings are consistent with this expectation, i.e. HbT is more specific than HbO, which in turn is more specific than HbR.

Spatial specificity of neurophysiological responses

In this work, we show that the absolute FWHM of neurophysiological responses decreases as we go higher in LFP frequency bands: from low gamma (30-50 Hz), to high gamma (50-100 Hz), and spiking response. This finding agrees with the concept that cortex acts as a low-pass filter, which can be described as capacitive filter, allowing lower frequencies to travel further than higher frequency signals (Bedard et al., 2006). These authors proposed a possible biophysical mechanism for the low-pass filtering properties of LFPs. They suggested that passive cellular membranes around current sources, such as those of glial cells, may polarize under the influence of the electric source field. Because of the finite velocity of ionic charge movements, this polarization will not be instantaneous. Consequently, the induced electric field will be frequency-dependent, and much reduced for high frequencies.

Calculation of relative FWHM

The FWHMs we computed relative to neurophysiological activity are larger than the values reported by (Vazquez et al., 2014). However, the way we calculate the relative PSF is different. Simple subtraction (additive model) of the EP FWHM from the OI-IS FWHM, similar to that used by Vazquez and colleagues, yields results more similar to those reported by them (Table III). However, we believe that the method we use here (Gaussian convolution model) fits the problem

better. It allows for the extraction of FWHMs of two signals from their convolution. Convolution fits the modeling of neurophysiological and hemodynamic spread, because the hemodynamic spread is influenced by more than neuronal responses in one site.

The model used by Vazquez et al. (2014) suggests that the FWHM of the HbT PSF relative to the neurophysiological response in mouse area S1, including LFP and MUA, ranges between 103 and 175 μm with an upper bound of 525 μm. However, their stimulus duration was very short (up to 30 ms), not allowing the full development of the CBV response, which explains the difference in spatial extent of the HbT response measured by their study and ours.

Spatial specificity of hemodynamic relative to neurophysiological responses: implications for fMRI-based decoding

Our findings reemphasize that the neurophysiological response to point like stimulation is not point-like: it is scattered (Hubel and Wiesel, 1974). We show that stimulation of part of the visual field elicits a neurophysiological response with a spread near the edge of the stimulated region. Therefore previous studies that have quantified the PSF of the fMRI response (Engel et al., 1997; Parkes et al., 2005; Shmuel et al., 2007) in fact reported on the spatial specificity of the BOLD response convolved with the spread of neurophysiological activity. Therefore, the PSF of BOLD responses in humans are expected to be smaller than what has been reported thus far, consistent with the feasibility of fMRI at the resolution scale of cortical columns (Cheng et al., 2001a; Goodyear and Menon, 2001; Yacoub et al., 2007; Shmuel et al., 2010).

Linear relationship of the retinotopic map

We found in our data a linear relationship between the projected stimulus in degrees of visual field and the corresponding area of response on the exposed brain (Fig. 6-6). This is unexpected since retinotopic mapping of the visual field in cat area 18 is non-linear with eccentricity in the visual space (Tusa et al., 1979). However, the part of cortex we image is small (~1cm anterior to posterior) and the eccentricity range of stimuli we employed is only within 20 degrees of visual field. The anatomical distance from -10 to -20 degrees of visual eccentricity is 5 mm and that from -20 to -30 degrees is 4mm (Tusa et al., 1979). With such small difference in non-linearity it is very reasonable that a linear fit works very well (Fig. 6-6).

Conclusion

We have modeled the spatial spread of neurophysiological and hemodynamic responses to stimulation of part of the visual field as Gaussians. The spatial spread of HbR responses is larger than that of HbT responses. The spatial spreads of low-gamma and high-gamma neurophysiological responses are comparable to that of HbT responses. The spatial spread of low-gamma responses is larger than that of spiking responses. Our findings predict that the PSF of BOLD responses in humans are expected to be smaller than what has been reported thus far, consistent with the feasibility of fMRI at the resolution scale of cortical columns.

Chapter 7. General Discussion

This Chapter summarizes the findings and discussions of individual chapters into one coherent message. It first explains why OI-IS is a valid method for studying mechanism of fMRI. The second part of the general discussion revolves around the assessment of the mechanisms underlying decoding of orientation stimuli using coarse fMRI voxels. The third part focuses on the mechanisms and limits of high-resolution fMRI, as reflected by my thesis' evaluation of the functional/spatial specificity of blood vessels and the spatial specificity of the hemodynamic response relative to neurophysiological activity.

7.1 OI-IS as a 2D model for studying the mechanisms underlying fMRI-based decoding

In Chapters 4-6 we have employed OI-IS in order to study the mechanisms underlying fMRI-based decoding and high-resolution fMRI. Here we advocate the use of OI-IS for studying such mechanisms.

Both OI-IS and fMRI capture the same physiological phenomena, i.e. the hemodynamic and metabolic responses. The main difference between the HbR and HbT OI-IS and BOLD- and CBV-fMRI, respectively is in the principles of measurement. OI-IS is based on differences in absorption spectra of deoxy- and oxy-hemoglobin as a function of illumination wavelength. In contrast, BOLD-fMRI is based on the magnetic properties of deoxy-hemoglobin, and MION-CBV-fMRI is based on the magnetic properties of the MION contrast agent.

Indeed, it is common to use OI-IS to investigate HbR and HbT changes, which are homologous to BOLD and CBV respectively, in order to validate fMRI-based phenomena. OI-IS has been commonly used as surrogate to fMRI, making it possible to study hemodynamic responses that may improve high-resolution fMRI (Malonek and Grinvald, 1996) and the neurophysiological mechanisms underlying fMRI in the lab environment (Devor et al., 2003). Examples of validating fMRI by using OI-IS include the phenomena of the initial dip (Grinvald et al., 2000; Sirotin et al., 2009) and negative BOLD responses (Kennerley et al., 2012).

OI-IS has been also used for validating high-resolution fMRI of cortical columns. The visual cortex constitutes arrangements of neurons organized in cortical columns. For example, the neurons' preferred orientation changes gradually across the cortical surface but is approximately unchanged as a function of cortical depth (Hubel and Wiesel, 1962; Shmuel and Grinvald, 1996). It can therefore be assumed that the responses of the aggregates of neurons to the presented oriented grating stimuli do not change across cortical depth. Hence, it is common to align high-resolution fMRI's slices (or, a single slice) parallel to the surface of the ROI and use one slice for analysis of the underlying columnar structure (Fukuda et al., 2006; Shmuel et al., 2007; Yacoub et al., 2007; Shmuel et al., 2010). This procedure speaks to the applicability of data obtained from OI-IS experiments as analogous to high-resolution fMRI of cortical columns. The origin of cortical responses measured by OI-IS is mainly from layers 1-2/3 and pial blood vessels. However, since the preferred orientation does not change with increasing cortical depth, the pattern observed by

OI-IS reflects the preferred orientation measured by high-resolution fMRI. Indeed, studies that performed both high-resolution fMRI and OI-IS showed that the HbT OI-IS orientation selective response pattern is similar to changes measured in MION-based CBV-fMRI (Fukuda et al., 2006) and BOLD-fMRI (Moon et al., 2007).

For these reasons, OI-IS can be used for investigating the mechanisms of fMRI-based decoding of information conveyed by fine-scale organizations. It can be regarded as analogous and complementary to fMRI, adding high-resolution, high SNR directly visualized responses from gray matter and pial vessels, not available to fMRI.

7.2 Mechanism of fMRI-based decoding of information conveyed by fine-scale organizations

In Chapters 3 and 4 we analyzed the mechanisms underlying decoding of orientation stimuli. FMRI reflects the neuronal activations through indirect measurements of changes in hemodynamic responses (Ogawa et al., 1993; Logothetis et al., 2001). Hence it is expected that fMRI cannot easily differentiate responses in two cortical loci separated by only a few hundreds of micrometers (Shmuel et al., 2007; Chaimow et al., 2011), such as the difference in neuronal response due to drifting gratings of orthogonal orientations. However, several studies have shown that it is possible to demonstrate orientation selectivity from BOLD-fMRI responses in human V1 using multivariate analysis that employs supervised learning. The mechanisms underlying such decoding have been under continuous and fierce debate. The input to the multivariate algorithms is based on conventional coarse voxels of 3×3×3 mm. The edge of each voxel is more than 1.5 times longer than the projected cycle of orientation columns. It has been hypothesized that the mechanisms include contributions from aliasing of fine scale organization by the coarse fMRI voxels (Boynton, 2005), local irregularities in the orientation maps (Kamitani and Tong, 2005; Haynes and Rees, 2006; Kriegeskorte and Bandettini, 2007; Swisher et al., 2010), large-scale organizations (Furmanski and Engel, 2000; Sasaki et al., 2006; Clifford et al., 2009; Mannion et al., 2010; Op de Beeck, 2010; Freeman et al., 2011; Freeman et al., 2013; Sun et al., 2013), orientation or direction selective responses near the edge of the stimuli (Carlson, 2014; Wang et al., 2014; Wardle et al., 2015), macroscopic draining vessels (Gardner et al., 2006; Gardner, 2010;

Shmuel et al., 2010), and complex spatiotemporal filtering of neuronal activity by fMRI voxels' sampling (Kriegeskorte et al., 2010).

Of these six hypothesized mechanisms, we did not evaluate contributions due to aliasing and contributions due to orientation selective responses near the edges of the visual stimuli. Chaimow et al. (2011) previously ruled out contributions to decoding due to aliasing effect, based on the fact that fMRI samples data in the frequency domain, discarding any contributions beyond the highest frequency of sampling. The possible contributions from edge effects have been introduced by Carlson (2014), Wang et al. (2014) and Wardle et al. (2015) after we completed data acquisition for this thesis. Future experiments employing CBV-fMRI and optical imaging will be able to evaluate such contributions in our cat model.

7.2.1 Do macroscopic blood vessels contribute to decoding information conveyed by fine-scale organizations?

In Chapter 3, we employed MION-based CBV-fMRI data and a phase encoding paradigm, with continuous stimulation with gradually changing orientations. By employing MION-based CBV-fMRI, we can rule out any contribution of macroscopic vessels to our data. MION-CBV reflects responses from tissue, and to a lesser extent from arterioles and venules, all belonging to fine scale vasculature. The decoding rate using a voxel size (1.5 mm) homologous to that used in human studies (3.0 mm) was higher than chance level. Therefore, we provide evidence showing that MION-based CBV-fMRI enables orientation decoding with no contributions from large blood vessels.

In Chapter 4, our OI-IS data allows us to directly evaluate contributions from all 4 possible mechanisms (aliasing and edge effects excluded), including contributions from macroscopic blood vessels. We demonstrate that contributions from gray matter regions exceed those from macroscopic blood vessels (Figures 4-4, 4-5, and 4-6). We find that decoding based on responses from macroscopic blood vessels results in accuracy higher than chance level. However, the decoding accuracy based on data from large blood vessels was lower than that obtained from gray matter regions. Importantly, we find that decoding accuracy based on combined blood vessel and gray matter contributions is not higher than that obtained from gray matter contributions alone (Figures 4-4 to 4-6). In other words, although contributions from macroscopic vessels can be used

for decoding with success rate higher than chance level, they are redundant when the data from the gray matter is used for decoding.

We therefore conclude that the contributions of macroscopic blood vessels are unimportant for decoding information conveyed in fine scale organizations.

7.2.2 Does complex spatiotemporal filtering of neuronal activity by fMRI voxels contribute to decoding information conveyed by fine scale organizations?

In Chapter 3, we employed MION-based CBV-fMRI data and a phase encoding paradigm, with continuous stimulation with gradually changing orientations. Similarly to our explanation regarding contribution of macroscopic blood vessels, by employing MION-based CBV-fMRI, we can rule out any contribution of macroscopic vessels to our data. In addition, the steady-state response to the continuous stimulation can be expected to keep the CBV in large arteries and large draining veins constant throughout each scan. This, in practice eliminates any contributions of spatiotemporal responses. The decoding rate using a voxel size (1.5 mm) homologous to that used in human studies (3.0 mm) was higher than chance level. Therefore, we provide evidence showing that MION-based CBV-fMRI enables orientation decoding with no contributions from complex spatiotemporal filtering of neuronal activity by fMRI voxels.

Using OI-IS in cat area 18 (Chapter 4), the spatiotemporal response yields lower decoding accuracy compared to the decoding accuracy obtained from the spatial pattern of the response averaged over time (Fig. 4-8). For analyzing decoding accuracy based on the spatiotemporal response, we made sure to also evaluate success rate with control inputs that constituted the exact same number of features available for decoding while manipulating the normal order of the measured spatiotemporal response. Our results show that considering the spatiotemporal evolution of the hemodynamic response results in lower decoding accuracy compared to that obtained by the spatial pattern of the response averaged over time.

Over all, our evaluations show redundancy of contributions from macroscopic vessels and lower decoding accuracy obtained by spatiotemporal responses compared to that obtained by the spatial response patterns averaged over time. Our finding show that the hypothesized complex spatiotemporal filtering mechanism is unlikely to contribute to decoding of information conveyed by fine scale organizations.

7.2.3 Do local irregularities in the arrangement of cortical columns contribute to decoding of oriented gratings?

Our findings of small and redundant information conveyed by macroscopic blood vessels and complex spatiotemporal filtering, leaves only contributions from gray matter regions as viable candidates to underlie decoding information conveyed by fine-scale organizations. Contributions of responses from gray matter can be classified according to the cortical frequencies.

It has been hypothesized that irregularities in the fine-scale organization of orientation preference underlie decoding of oriented grating stimuli (Kamitani and Tong, 2005). By definition, if irregularities exist, the columnar organization involves a distribution of frequencies, including frequencies lower than the main frequency of the organization (Rojer and Schwartz, 1990; Chaimow et al., 2011). In Figure 3-3 we show that the CNR of differential orientation maps in cat area 17 shows a peak at 0.99±0.05 cycles/mm and a distribution of frequencies around the peak with FWHM of 0.56±0.14 cycles/mm. Therefore, irregularities of the organization do exist in cat area 17. With an appropriate voxel size, irregularities in the orientation map in cat area 17 may contribute to decoding. Indeed, using voxels with 0.5 mm edges, Shmuel et al. (2010) demonstrated contributions to decoding of the stimulated eye in human subjects from frequency components lower than the main frequency of the organization (~0.5 cycle/mm).

However, in order to address the question whether irregularities in the organization contribute to decoding, one needs to use voxel size homologous to 3×3×3 mm previously used in human studies. Based on the main frequency projected for the organization in humans, the homologous voxel size is 1.5 times the cycle length associated with the main frequency of the organization. For orientation maps in cat area 17, the curve of mean CNR (Fig. 3-3D) shows a local maximum at 0.99 cycle/mm that represents the main cycle of orientation map. We define the size of the voxel homologous to that used by Kamitani and Tong (2005) and Haynes and Rees (2005) in human subjects to be 1.5 times larger than the main cycle of the orientation map in our cat area 17 data (1.5×1 mm = 1.5 mm). The largest frequency that can be captured by such a voxel is 0.33 cycle/mm.

Then, the determining factors of whether irregularities contribute to decoding is the highest frequency that can be captured by such voxels (0.33 cycle/mm), and the width of the power spectra around the main frequency of the organization. If the distribution of power around the main frequency of the organization is sufficiently wide, low frequencies that still belong to the

irregularities regime can possibly be captured by voxels that are 1.5 times larger than the average cycle length of the organization.

The power spectrum of CNR in cat area 17 showed a local minimum at 0.36 cycle/mm. It is reasonable to define this trough as the frequency that separates the distribution of frequencies that underlie local irregularities in the organization (frequencies higher than the trough frequency) and lower-frequencies. We consider this trough frequency or a frequency slightly higher to be the lowest frequency belonging to the distribution of frequencies that constitute the local irregularities. However, in cat area 17, the homologous voxel captures frequencies of 0.33 cycle/mm or lower, all lower than the frequency at the trough (0.36 cycle/mm). We therefore conclude that the local irregularities in the organization do not contribute to the CNR and to successful decoding when sampled with the homologous voxel size. Indeed, our computation of CNR and decoding accuracy as a function of point pass and low-pass filtering shows no contributions of frequencies within the irregularities domain when using the homologous voxel (Figures 3-5, 3-6, and-3-7). Both the CNR and the decoding success rates obtained with the homologous voxel size and cut-off frequencies higher than 0.36 cycle/mm (the "irregularities" frequency regime) are not different than those obtained with the same voxel-size and cut-off frequency 0.333 cycle/mm. These results further support our conclusion that when sampling with the homologous voxel size the low-frequency regime contributes to successful decoding, whereas irregularities in the organization do not.

As discussed in Chapter 3, our MION CBV-fMRI measurements reflect the neuronal orientation preference map better than BOLD measurements do (Mandeville et al., 2001; Keilholz et al., 2006; Zhao et al., 2006; Smirnakis et al., 2007; Kim and Kim, 2011; Poplawsky and Kim, 2014). Our CBV MION measurements show no contributions of irregularities in the organization to decoding. Therefore, taking into account that the BOLD response is expected to be less spatially specific than the MION CBV-fMRI response, BOLD imaging is even less likely to reflect direct contributions of irregularities in the fine-scale organization to decoding.

For data confined to responses from the gray matter in cat area 18, we provide evidence that irregularities that reflect frequencies lower than main frequency of the organization contribute to decoding when using voxels smaller than the homologous voxel (Figures 4-4 and 4-5). In contrast to our findings from cat are 17, when using homologous voxels the data from the irregularities domain showed decoding accuracy higher than chance level (Fig. 4-6). In cat area 18, we found that the decoding accuracy following either point-pass or low-pass filtering gradually

increases when moving from very low frequencies (starting with the mean response over space) to the highest frequency that can still be captured by the homologous voxel. This path also parallels the path taken from low frequencies to getting closer and closer to- and within the irregularities regime. Similarly, the power spectra of the response CNR (Fig. 4-2) showed neither distinct increase in power in very low frequencies, nor a trough between the irregularities regime and the low frequency regime similar to those shown in our data from cat area 17 (Fig. 3-3). In other words, our data does not show distinct low-frequency components of the organization in cat area 18 similar to those we observed in cat area 17.

Therefore, our results presented in Chapter 4 show apparent inconsistency with our own results presented in Chapter 3. The discrepancy between our conclusions based on Chapters 3 and 4 is that in area 17 we find the very low frequency components of the organization to be the main contributor to orientation decoding; whereas in cat area 18 we find no distinct, high-amplitude low-frequency components of the organization. Instead, the low frequency end within the local irregularities domain is the main contributor to orientation decoding. As discussed above, it is unlikely that the use of HbT-based OI-IS (Chapter 4) or MION-based CBV-FMRI (Chapter 3) causes the difference. The reason is that HbT-based OI-IS captures the same physiological hemodynamic responses as MION-based CBV-fMRI does.

Our results, demonstrating contributions from irregularities in cat area 18 (Chapter 4) are consistent with those demonstrated by Swisher et al. (2010) with data from the same area. These authors used high-field, high-resolution (0.3125 mm) BOLD-fMRI and multivariate pattern analysis to determine the spatial scales at which orientation-selective information can be found in cat area 18. Similarly to our results, using small voxels they showed orientation selective signal at the scale of irregularities and reliable orientation bias at spatial scales of several millimeters. They concluded that their results demonstrate a reliable millimeters-scale orientation signal, likely emerging from irregular spatial arrangements of orientation columns and their supporting vasculature. Our own study of responses in cat area 18 adds to the findings demonstrated by Swisher and colleagues, by showing only minor contributions from low-frequencies, redundant information conveyed by macroscopic blood vessels, and no improved decoding accuracy when the spatiotemporal response is considered rather than the spatial response.

Therefore, we show no contributions from irregularities in cat area 17 using the homologous voxel size. In contrast, using the homologous voxel size, irregularities contribute to

decoding of oriented grating based on responses in cat area 18. As explained above, this difference cannot be attributed to differences in methodology. We conclude that whether irregularities contribute to decoding depends on the features of the specific organization being probed. Specifically, it depends on the main frequency of the organization, and the width of elevated power of frequencies around the main frequency of the organization. It also depends on the voxel size used for functional imaging.

7.2.4 Do low-frequency components of the organization contribute to decoding of oriented gratings?

Our findings of small and redundant information conveyed by macroscopic blood vessels and complex spatiotemporal filtering, leaves only contributions from gray matter regions as viable candidates to underlie decoding information conveyed by fine-scale organizations. Contributions of responses from gray matter can be classified according to the cortical frequencies.

It has been hypothesized that large scale organizations of orientation preference underlie decoding of oriented grating stimuli (Furmanski and Engel, 2000; Sasaki et al., 2006; Clifford et al., 2009; Mannion et al., 2010; Op de Beeck, 2010; Freeman et al., 2011; Freeman et al., 2013; Sun et al., 2013). In Fig. 3-3 we show that the power spectrum of CNR in cat area 17 shows a local minimum at 0.36 cycle/mm. There is a significant increase in power in frequencies lower than 0.36 cycle/mm. It is reasonable to define this trough as the frequency that separates the distribution of frequencies that underlie local irregularities in the organization (frequencies higher than the trough frequency) and lower-frequencies. We consider this trough frequency or a frequency slightly higher to be the lowest frequency belonging to the distribution of frequencies that constitute the local irregularities. In cat area 17, the homologous voxel captures frequencies of 0.33 cycle/mm or lower, all lower than the frequency at the trough (0.36 cycle/mm). Indeed, our computation of CNR and decoding accuracy as a function of point pass and low-pass filtering when using the homologous voxel size shows contributions of frequencies lower than the trough (Figures 3-5, 3-6, and 3-7). Both the CNR and the decoding success rates obtained with the homologous voxel size and cut-off frequencies higher than 0.36 cycle/mm (the "irregularities" frequency regime) are not different than those obtained with the same voxel-size and cut-off frequency 0.333 cycle/mm. These results support our conclusion that when sampling with the

homologous voxel size the low-frequency regime contributes to successful decoding, whereas irregularities in the organization do not.

For data confined to responses from the gray matter in cat area 18, the decoding accuracy following either point-pass or low-pass filtering gradually increases when moving from very low frequencies (starting with the mean response over space) to the highest frequency that can still be captured by the homologous voxel. Similarly, the power spectra of the response CNR (Fig. 4-2) shows neither distinct increase in power in very low frequencies, nor a trough between the irregularities regime and the low frequency regime similar to those shown in our data from cat area 17 (Fig. 3-3). In other words, our data does not show distinct low-frequency components of the organization in cat area 18 similar to those we observed in cat area 17.

Therefore, our results presented in Chapter 4 show apparent inconsistency with our own results presented in Chapter 3. In area 17 we find the very low frequency components of the organization to be the main contributor to orientation decoding; whereas in cat area 18 we find no distinct, high-amplitude low-frequency components of the organization. We conclude that whether low-frequency components contribute to decoding depends on the features of the specific organization being probed.

We acknowledge that we have analyzed here contributions from low-frequency components without identifying the specific organization involved. In other words, we have not determined whether these low-frequencies are the results of the oblique effect (Furmanski and Engel, 2000; Sun et al., 2013) or the radial bias effect (Sasaki et al., 2006; Clifford et al., 2009; Mannion et al., 2010; Freeman et al., 2011; Freeman et al., 2013; Sun et al., 2013). This could be the subject of a future study, which should involve fMRI of retinotopy and orientation selective responses in cat area 17 using more than just one fMRI slice, not necessarily at high resolution.

While our work focused on deciphering the mechanism of decoding via CBV-fMRI and OI-IS, other studies have developed stimuli that are less sensitive to large-scale bias. The majority of these studies agree that large-scale biases contribute to decoding of orientation stimuli (Sasaki et al., 2006; Clifford et al., 2009; Mannion et al., 2010; Freeman et al., 2011; Freeman et al., 2013) in human V1, the area homologous to cat area 17. To remove the confounding effect of radial-bias, several studies have used spiral gratings as stimuli (Mannion et al., 2010; Seymour et al., 2010; Alink et al., 2013; Freeman et al., 2013). Nevertheless, the elimination of one mechanism does not

guarantee or express the relative contribution of the other mechanism. Here, based on functional imaging of cat area 17 and 18, we addressed four of the proposed mechanisms.

7.2.5 Conclusions: mechanisms underlying decoding the orientation of grating stimuli

Previously in Chapter 3, we find orientation decoding to be possible without contribution from macroscopic blood vessels or complex-spatiotemporal kernel. In Chapter 4, contributions from macroscopic blood vessels or from the spatiotemporal responses are redundant if gray matter responses are considered. Thus, based on our findings from both Chapters 3 and 4, we can conclude that successful decoding relies primarily on the functional organization of neurons according to their orientation preference, i.e. on the local irregularities or large scale organizations. However, the relative contributions of irregularities and low-frequency components of the organization depend on the probed orientation map: we found these relative contributions to be different between areas 17 and 18.

One may argue that the optical imaging results from A18 show smaller contributions from the low frequency regime compared to A17 due to the restricted craniotomy opening for the optical imaging ROI as opposed to the large tangential slice in the fMRI. However, in our work, a typical optical imaging ROI was approximately 9 mm in length whereas a typical fMRI ROI was approximately 13.5 mm in length. This difference cannot account for the trough observed in A17 at 0.36 cycles / mm, which translates to a cycle length of 2.8 mm. In addition, all probed frequencies lower than 0.36 cycles / mm in area 17 showed elevated power, which cannot be explained by the relatively small difference in ROI lengths.

One may also argue that differences in the retinotopic eccentricity of the ROIs in A17 and A18 cause the differences in contributions of local irregularities and large scale organizations in these areas. In other words, if the ROI in A17 was more off-centered from the fovea, then the low frequencies could be expected to contribute more due to increased radial bias effects. However, the ROI we used for the data from A18 (-5˚ relative to the vertical meridian, -5˚ to -15˚ relative to the horizontal meridian) was more off-centered from the fovea compared to the ROI used for A17 (near the vertical and horizontal meridians). Therefore, such argument would only strengthen our conclusion that A18 shows higher contributions of fine-scale irregularities and lower contributions of low frequencies than A17.

We conclude that the mechanism that accounts for successful decoding of orientation columns depends on the specific functional organization of the underlying neurons in the frequency domain. Thus, it may vary across visual areas. Moreover, the relative contributions of different frequency components depends on the relative size of the voxel as well.

7.3 Functional and spatial specificity of blood vessels as a function of vessel diameter

In Chapter 3 we conclude that the large blood vessels contributions were not necessary for successful decoding of orientation. In Chapter 4 we show that although decoding accuracy based on responses from macroscopic vessels is higher than chance level, the contributions of vessels to decoding is redundant if data from gray matter responses are available. This is true for both decoding based on HbR (homologous to BOLD-fMRI) and HbT (homologous to CBV-fMRI decoding) responses. However, the contribution to decoding from different sizes of fine blood vessels were not analyzed. In Chapter 5 we assessed the selectivity of HbR and HbT responses in fine arteries and veins relative to that of cortical gray matter.

ASE pulse sequence provides partial nullification of contributions from veins, leading to a middle ground of spatial specificity and SNR between SE and GE sequences. A key simulation study showed that with increasing asymmetry of the refocusing pulse, the more similar the SE signal is to GE signal (Boxerman et al., 1995). Therefore, the asymmetry parameter of ASE controls a trade-off between spatially specific fMRI contrast of low SNR, and fMRI contrast of high SNR but poor spatial specificity. This trade-off can possibly be optimized by setting the level of SE asymmetry.

In Chapter 5, we measured the spatial specificity of blood vessels using OI-IS. Based on the statistical results we provide evidence that for CBV-fMRI, cortical regions show more spatially specific responses than the smallest vessels we tested. In contrast, owing to reduced spatial specificity and CNR of blood oxygenation responses, the optimal targets for BOLD-fMRI studies are blood vessels of size up to 0.12 mm for mapping an organization with a main frequency of 0.83 cycle/mm, i.e. the orientation modules in A18. Thus, ASE-BOLD-fMRI may alleviate the low SNR of SE-BOLD-fMRI while maintain the spatial specificity. There exists a set of data-

acquisition parameters in fMRI experiments that optimally balances the signal strength relative to noise and the signal selectivity, both of which are important for high-resolution fMRI.

Whereas limiting the data-acquisition to contributions from vessels within a certain range of diameters may not be straightforward, MRI methods exist for estimating the average vessel radius in a voxel (Prinster et al., 1997; Jochimsen et al., 2010; Shen et al., 2013). Likely, the most convenient method for use in the context of improving the spatial specificity of the fMRI response, is the one proposed by Jochimsen and Moller (2008). This method derives the mean vessel diameter in a voxel from the change in transverse relaxation rates upon activation which can be measured by multi-gradient-echo sampling of spin echo sequence. Thus, our findings can be combined with fMRI-based estimation of the average vessels diameter to exclude contributions from vessels with low spatial specificity.

Here we have measured the spatial specificity of HbR and HbT responses by applying OI-IS for imaging a cortical map with peak frequency of 0.83 cycle/mm. Since the periodicity of this organization constitutes higher cortical frequencies than any of the cortical maps that can be expected to exist in the human cerebral cortex, all vessels with diameter smaller than or equal to the limit we propose can be included in data-acquisition and not excluded in data analysis for the purpose of increasing CNR of high-resolution fMRI. However, the diameter of pial blood vessels whose spatial specificity is significantly different from gray matter is likely to be proportional to the underlying columnar cycle. Finding the exact relationship between the columnar organization and the critical blood vessel diameter at which the contributed signals degrades significantly will allow us to obtain precise optimization parameters to studies conducted in human.

To conclude, the information presented in Chapter 5 is especially useful for future studies that employ high-resolution 7T BOLD-fMRI. These can improve the voxel SNR by relaxing the SE to integrating more blood vessels without over-integrating and thus degrading the spatial selectivity. Moreover, we have assessed here the profile of blood vessels of width smaller than conventional size of fMRI voxels in the interest of suggesting the optimal parameters for extracting the highest spatial specificity of the hemodynamic response. Multivariate pattern analysis studies rely on the global pattern across different voxels in order to mine data that are otherwise too subtle for conventional mass-univariate analyzes. Despite its advantage, this technique, like any other, will always benefit by high-quality, spatially specific responses. Hence, the findings we show here

are not only beneficial for high-resolution fMRI, but also for multivariate fMRI analysis aimed at decoding information conveyed by fine-scale organizations.

7.4 Spatial specificity of hemodynamic response relative to neuronal activities

In Chapters 3 - 5, we assessed the selectivity of gray matter and blood vessels based on CBV-fMRI and OI-IS signals that can represent CBV-fMRI (Belliveau et al., 1991) or BOLD-fMRI (Ogawa et al., 1993). However, fMRI infers the brain activities indirectly through hemodynamic responses, which are believed to be coupled closely with certain components of neural activity (Logothetis et al., 2001). Therefore, it is also of important interest to quantify the extent of coupling between the evoked neuronal activities and the subsequent hemodynamic responses (Boynton et al., 1996; Vazquez and Noll, 1998). Knowing quantitatively the coupling between the neuronal activities and the hemodynamic responses enables in-depth understanding of the hemodynamic limitations and better planning of the sequences related to higher-magnetic-field (e.g. 7.0-9.4 Tesla) super-resolution fMRIs.

In Chapter 6, we measure the extent of hemodynamic specificity relative to the underlying neuronal activity using controlled retinotopic stimuli. Previous fMRI studies that measured the FWHM of a hemodynamic PSF implicitly assumed that the neuronal response is point-like (Engel et al., 1997; Parkes et al., 2005; Shmuel et al., 2007; Sirotin et al., 2009). Other studies measured optical imaging with electrophysiology but with no controlled visual stimuli (Malonek and Grinvald, 1996; Berwick et al., 2008; Vazquez et al., 2014).

In Chapter 6, Gauss error functions are fitted to the cortical responses to retinotopic stimuli with edges at various eccentricities of the visual field (Figures 6-3 and 6-7). The PSF of HbT and HbO responses relative to spiking activities are 1.93 and 2.52 mm, respectively, using the Gaussian convolution model, smaller than the mean absolute FWHMs of HbT and HbO responses (2.83 and 3.26 mm, respectively).

Our findings reemphasize that the neurophysiological response to point like stimulation is not point-like: it is scattered (Hubel and Wiesel, 1974). We show that stimulation of part of the visual field elicits a neurophysiological response with a spread near the edge of the stimulated region. Therefore previous studies that have quantified the PSF of the fMRI response (Engel et al.,

1997; Parkes et al., 2005; Shmuel et al., 2007) in fact reported on the spatial specificity of the BOLD response convolved with the spread of neurophysiological activity. Therefore, the PSF of BOLD responses in humans are expected to be smaller than what has been reported thus far, consistent with the feasibility of fMRI at the resolution scale of cortical columns (Cheng et al., 2001a; Goodyear and Menon, 2001; Yacoub et al., 2007; Shmuel et al., 2010).

7.5 HbT responses are more spatially specific than HbR responses

A common finding across Chapters 4-6 is that HbT-based responses are more spatially specific than HbR-based responses. In Chapter 4, the decoding rate of HbT-based responses are higher than those from HbR-based responses. In Chapter 5, the relative selectivity of gray matter and blood vessels across different diameters is higher for HbT compared to that of HbR. Finally in Chapter 6, the pair-wise ratio of HbR-based FWHM to that of HbT is significantly higher than one. These results clearly demonstrate that the spatial specificity of CBV-fMRI relative to the site of increased neurophysiological activity is higher that of BOLD-fMRI. Although developing fMRI pulse sequences that estimate CBV dynamically is a challenge, the clear advantage of CBV-fMRI should motivate such developments.

7.6 Validity of experiments in anesthetized animals

The work presented in this thesis provides results obtained from anesthetized animals in which both of the neuronal and hemodynamic responses are expected to be altered due to the anesthesia effects. However, our work deals with fundamental, mechanistic features of the neuronal system (e.g., orientation columns, point-spread functions) and the vascular system (e.g., spatial specificity of blood oxygenation and blood volume responses). Moreover, we obtained our data in lower visual areas, where neurophysiological responses are influenced by anesthesia to a lesser extent than responses in higher visual areas. In addition, the conclusions made in the thesis rely on comparisons of measures, such as the spatial specificity of hemodynamic responses in gray matter compared to that of blood vessels, or the spatial spread of hemodynamic responses compared to that of neuronal responses. Lastly, our observations are not confounded by attention

effects that can be expected in the alert state. Hence, we believe that our results of mechanistic nature hold qualitatively for the alert state.

7.7 Closing remarks and future development

The work presented in this thesis assessed mechanisms of decoding of orientation stimuli, as well as the biological limitation of hemodynamic responses using CBV-fMRI, intrinsic optical imaging and multichannel extracellular potential recording. Our novel OI-IS and EP approach provided high resolution data that allow in-depth analysis of fMRI-based decoding and mechanisms of high-resolution fMRI.

Although we have added insight into the ongoing debate on mechanisms underlying decoding of orientation stimuli based on our invasive studies, the debate has progressed onto another level. We did not address the concept of orientation selective edge effects (Carlson, 2014; Wardle et al., 2015) because this has been suggested as a possible mechanism only after we completed data acquisition. The use of spiral stimuli (Mannion et al., 2009; Seymour et al., 2010; Alink et al., 2013; Freeman et al., 2013) is beyond the scope of this thesis. Future studies can incorporate or extend the results presented here to including these two new developments.

In addition, the concept of spatiotemporal filtering was discussed in great detail in Chapter 4. Here we took a "top-down" approach in which we assumed that the spatiotemporal sampling should increase decoding accuracy compared to the static image averaged over time. Since we did not observe such an effect, we concluded that the spatiotemporal response does not add information for decoding of orientation stimuli. Our study does not refute the concept of complex spatiotemporal filtering. However, our results do show that this concept is unlikely to add significant contributions to decoding of information conveyed by fine scale organizations. We note that we did not analyze these contributions in a "bottom-up" approach to fully explore the function of individual elements (such as a model of blood vessels irrigation of orientation columns) that would constitute the complex spatiotemporal filtering of neuronal activity by fMRI voxels.

7.8 Significance of our work

We have implemented novel approaches for studying the mechanisms underlying fMRI-based decoding of information conveyed by fine-scale organizations. These include (1) MION-

based CBV-fMRI, with no contributions from macroscopic blood vessels and complex spatiotemporal filtering of neuronal activity by fMRI voxels, and (2) direct visualization of gray matter and vessel responses using OI-IS of HbR and HbT responses. The latter allows for investigating the contributions of all suggested mechanisms. We have introduced the concept of a voxel size homologous to that used in human studies, based on the ratio of the main frequencies of the fine-scale organization in humans and an animal model.

Since the MION contrast agent-based fMRI shows better spatial specificity than BOLD-fMRI does, and since it excludes contributions from blood vessels, our study is the first to test whether the functional anatomy of orientation selective columns with no blood vessel contributions enables decoding of oriented grating stimuli. Our findings from this work clearly rule out, for the first time, any contributions from irregularities in the organization of orientation preference to decoding in a primary visual area (Chapter 3).

Our work is also the first to demonstrate that contributions from macroscopic vessels to decoding orientation are lower than those from gray matter regions, and redundant when contributions from gray matter regions are considered (Chapter 4). It is the first work that shows that whether irregularities contribute to the decoding of the fine scale organization for orientation depends on the features of the organization, including the main frequency of the organization and the width of elevated amplitudes in the frequency domain around the main frequency (Chapters 3 and 4).

Our work is the first to measure the functional (and, indirectly spatial) specificity of metabolic (deoxy-hemoglobin) and hemodynamic (total hemoglobin) responses in arteries and veins as a function of blood vessel' diameter (Chapter 5). To date, the functional/spatial specificities of responses of veins or arteries relative to the site of increased neurophysiological responses have not been quantified. This study will allow for informed data-acquisition and data-analysis of high-resolution fMRI and fMRI-based decoding for improving the SNR while not degrading the spatial specificity.

Lastly, our work is the first to measure the spatial specificity of hemodynamic responses relative to the neuronal responses using well controlled retinotopic stimuli (Chapter 6). Our findings indicate that the spatial specificity of high-resolution fMRI in humans should be better than has been reported, consistent with the functional imaging of cortical columns in human subjects.

References

Adams DL, Sincich LC, Horton JC (2007) Complete pattern of ocular dominance columns in human primary visual cortex. J Neurosci 27:10391-10403.10.1523/JNEUROSCI.2923-07.2007.

Alink A, Krugliak A, Walther A, Kriegeskorte N (2013) fMRI orientation decoding in V1 does not require global maps or globally coherent orientation stimuli. Front Psychol 4:493.10.3389/fpsyg.2013.00493.

Attwell D, Buchan AM, Charpak S, Lauritzen M, Macvicar BA, Newman EA (2010) Glial and neuronal control of brain blood flow. Nature 468:232-243.10.1038/nature09613.

Auen EL, Bourke RS, Barron KD, San Filippo BD, Waldman JB (1979) Alterations in cat cerebrocortical capillary morphometrical parameters following K+-induced cerebrocortical swelling. Acta Neuropathol 47:175-181.

Baetge CL, Matthews NS (2012) Anesthesia and analgesia for geriatric veterinary patients. Vet Clin North Am Small Anim Pract 42:643-653, v.10.1016/j.cvsm.2012.05.001.

Bandettini PA, Jesmanowicz A, Wong EC, Hyde JS (1993) Processing strategies for time-course data sets in functional MRI of the human brain. Magnetic resonance in medicine 30:161-173.

Bandettini PA, Wong EC, Hinks RS, Tikofsky RS, Hyde JS (1992) Time course EPI of human brain function during task activation. Magn Reson Med 25:390-397.

Bartfeld E, Grinvald A (1992) Relationships between orientation-preference pinwheels, cytochrome oxidase blobs, and ocular-dominance columns in primate striate cortex. Proc Natl Acad Sci U S A 89:11905-11909.

Beckett A, Peirce JW, Sanchez-Panchuelo RM, Francis S, Schluppeck D (2012) Contribution of large scale biases in decoding of direction-of-motion from high-resolution fMRI data in human early visual cortex. Neuroimage 63:1623-1632.10.1016/j.neuroimage.2012.07.066.

Bedard C, Kroger H, Destexhe A (2006) Model of low-pass filtering of local field potentials in brain tissue. Phys Rev E Stat Nonlin Soft Matter Phys 73:051911.10.1103/PhysRevE.73.051911.

Belliveau JW, Kennedy DN, Jr., McKinstry RC, Buchbinder BR, Weisskoff RM, Cohen MS, Vevea JM, Brady TJ, Rosen BR (1991) Functional mapping of the human visual cortex by magnetic resonance imaging. Science 254:716-719.

Benjamini Y, Hochberg Y (1995) Controlling the False Discovery Rate: A Practical and Powerful Approach to Multiple Testing. Journal of the Royal Statistical Society Series B (Methodological) 57:289-300.

Berens P, Keliris GA, Ecker AS, Logothetis NK, Tolias AS (2008) Feature selectivity of the gamma-band of the local field potential in primate primary visual cortex. Front Neurosci 2:199-207.10.3389/neuro.01.037.2008.

Berwick J, Johnston D, Jones M, Martindale J, Martin C, Kennerley AJ, Redgrave P, Mayhew JE (2008) Fine detail of neurovascular coupling revealed by spatiotemporal analysis of the hemodynamic response to single whisker stimulation in rat barrel cortex. J Neurophysiol 99:787-798.10.1152/jn.00658.2007.

Bishop PO, Kozak W, Vakkur GJ (1962) Some quantitative aspects of the cat's eye: axis and plane of reference, visual field co-ordinates and optics. J Physiol 163:466-502.

Biswal B, Yetkin FZ, Haughton VM, Hyde JS (1995) Functional connectivity in the motor cortex of resting human brain using echo-planar MRI. Magn Reson Med 34:537-541.

Blasdel G (1997) Strategies of visual perception suggested by optically imaged patterns of functional architecture in monkey visual cortex. Ann N Y Acad Sci 820:170-195.

Bonhoeffer T, Grinvald A (1991) Iso-orientation domains in cat visual cortex are arranged in pinwheel-like patterns. Nature 353:429-431.10.1038/353429a0.

Bonhoeffer T, Grinvald A (1993a) The layout of iso-orientation domains in area 18 of cat visual cortex: optical imaging reveals a pinwheel-like organization. J Neurosci 13:4157-4180.

Bonhoeffer T, Grinvald A (1993b) Optical imaging of the functional architecture in cat visual cortex: the layout of direction and orientation domains. Adv Exp Med Biol 333:57-69.

Bouchard MB, Chen BR, Burgess SA, Hillman E (2009) Ultra-fast multispectral optical imaging of cortical oxygenation, blood flow, and intracellular calcium dynamics. Optics express 17:15670-15678.

Boxerman JL, Hamberg LM, Rosen BR, Weisskoff RM (1995) MR contrast due to intravascular magnetic susceptibility perturbations. Magn Reson Med 34:555-566.

Boynton GM (2005) Imaging orientation selectivity: decoding conscious perception in V1. Nat Neurosci 8:541-542.nn0505-541.

Boynton GM, Engel SA, Glover GH, Heeger DJ (1996) Linear systems analysis of functional magnetic resonance imaging in human V1. J Neurosci 16:4207-4221.

Brainard DH (1997) The Psychophysics Toolbox. Spat Vis 10:433-436.

Brewer KD, Rioux JA, D'Arcy RC, Bowen CV, Beyea SD (2009) Asymmetric spin-echo (ASE) spiral improves BOLD fMRI in inhomogeneous regions. NMR Biomed 22:654-662.10.1002/nbm.1380.

Brieu N, Beaumont E, Dubeau S, Cohen-Adad J, Lesage F (2010) Characterization of the hemodynamic response in the rat lumbar spinal cord using intrinsic optical imaging and laser speckle. J Neurosci Methods 191:151-157.10.1016/j.jneumeth.2010.06.012.

Buxton RB (2009) Introduction to functional magnetic resonance imaging: principles and techniques: Cambridge university press.

Carlson TA (2014) Orientation decoding in human visual cortex: new insights from an unbiased perspective. J Neurosci 34:8373-8383.10.1523/JNEUROSCI.0548-14.2014.

Cauli B, Hamel E (2010) Revisiting the role of neurons in neurovascular coupling. Front Neuroenergetics 2:9.10.3389/fnene.2010.00009.

Chaimow D, Yacoub E, Ugurbil K, Shmuel A (2011) Modeling and analysis of mechanisms underlying fMRI-based decoding of information conveyed in cortical columns. Neuroimage.S1053-8119(10)01218-8.

Chaimow D, Yacoub E, Ugurbil K, Shmuel A (2015) Spatial specificity of the functional MRI blood oxygenation response relative to metabolic activity. In: Society for Neuroscience Chicago.

Cheng K, Waggoner RA, Tanaka K (2001a) Human ocular dominance columns as revealed by high-field functional magnetic resonance imaging. Neuron 32:359-374.

Cheng K, Waggoner RA, Tanaka K (2001b) Human Ocular Dominance Columns as Revealed by High-Field Functional Magnetic Resonance Imaging. Neuron 32:359-374.http://dx.doi.org/10.1016/S0896-6273(01)00477-9.

Clare S, Humberstone M, Hykin J, D Blumhardt L, Bowtell R, Morris P (1999) Detecting activations in event-related fMRI using analysis of variance. Magnetic Resonance in Medicine 42:1117-1122.

Clarke E, Jacyna LS (1988) "Nineteenth-century origins of neuroscientific concepts". By Edwin Clarke and L. S. Jacyna. Essay review. Med Hist 32:211-213.

Clifford CW, Mannion DJ, McDonald JS (2009) Radial biases in the processing of motion and motion-defined contours by human visual cortex. J Neurophysiol 102:2974-2981.10.1152/jn.00411.2009.

Damadian R (1971) Tumor detection by nuclear magnetic resonance. Science 171:1151-1153.

Damadian R (1977) Nuclear magnetic resonance: a noninvasive approach to cancer. Hosp Pract 12:63-70.

Das A, Gilbert CD (1995) Long-range horizontal connections and their role in cortical reorganization revealed by optical recording of cat primary visual cortex. Nature 375:780-784.

Das A, Gilbert CD (1997) Distortions of visuotopic map match orientation singularities in primary visual cortex. Nature 387:594-597.

Devor A, Dunn AK, Andermann ML, Ulbert I, Boas DA, Dale AM (2003) Coupling of total hemoglobin concentration, oxygenation, and neural activity in rat somatosensory cortex. Neuron 39:353-359.

Devor A, Sakadzic S, Srinivasan VJ, Yaseen MA, Nizar K, Saisan PA, Tian P, Dale AM, Vinogradov SA, Franceschini MA, Boas DA (2012) Frontiers in optical imaging of cerebral blood flow and metabolism. J Cereb Blood Flow Metab 32:1259-1276.10.1038/jcbfm.2011.195.

Devor A, Ulbert I, Dunn AK, Narayanan SN, Jones SR, Andermann ML, Boas DA, Dale AM (2005) Coupling of the cortical hemodynamic response to cortical and thalamic neuronal activity. Proc Natl Acad Sci U S A 102:3822-3827.10.1073/pnas.0407789102.

Duda RO, Hart PE, Stork DG (2012) Pattern classification: John Wiley & Sons.

Dunn AK, Devor A, Dale AM, Boas DA (2005) Spatial extent of oxygen metabolism and hemodynamic changes during functional activation of the rat somatosensory cortex. Neuroimage 27:279-290.10.1016/j.neuroimage.2005.04.024.

Duvernoy HM, Delon S, Vannson JL (1981) Cortical blood vessels of the human brain. Brain Res Bull 7:519-579.

Edwards JD, Mayall RM (1998) Importance of the sampling site for measurement of mixed venous oxygen saturation in shock. Crit Care Med 26:1356-1360.

Engel SA, Glover GH, Wandell BA (1997) Retinotopic organization in human visual cortex and the spatial precision of functional MRI. Cereb Cortex 7:181-192.

Forte J, Peirce JW, Kraft JM, Krauskopf J, Lennie P (2002) Residual eye-movements in macaque and their effects on visual responses of neurons. Vis Neurosci 19:31-38.

Fox MD, Raichle ME (2007) Spontaneous fluctuations in brain activity observed with functional magnetic resonance imaging. Nat Rev Neurosci 8:700-711.10.1038/nrn2201.

Fox PT, Raichle ME (1986) Focal physiological uncoupling of cerebral blood flow and oxidative metabolism during somatosensory stimulation in human subjects. Proc Natl Acad Sci U S A 83:1140-1144.

Freedman DA (2009) Statistical models: theory and practice: cambridge university press.

Freeman J, Brouwer GJ, Heeger DJ, Merriam EP (2011) Orientation decoding depends on maps, not columns. J Neurosci 31:4792-4804.31/13/4792.

Freeman J, Heeger DJ, Merriam EP (2013) Coarse-scale biases for spirals and orientation in human visual cortex. J Neurosci 33:19695-19703.10.1523/JNEUROSCI.0889-13.2013.

Friston KJ, Holmes AP, Poline JB, Grasby PJ, Williams SC, Frackowiak RS, Turner R (1995) Analysis of fMRI time-series revisited. Neuroimage 2:45-53.10.1006/nimg.1995.1007.

Friston KJ, Jezzard P, Turner R (1994) Analysis of functional MRI time‐series. Human brain mapping 1:153-171.

Frostig RD, Lieke EE, Ts'o DY, Grinvald A (1990) Cortical functional architecture and local coupling between neuronal activity and the microcirculation revealed by in vivo high-resolution optical imaging of intrinsic signals. Proc Natl Acad Sci U S A 87:6082-6086.

Fukuda M, Moon CH, Wang P, Kim SG (2006) Mapping iso-orientation columns by contrast agent-enhanced functional magnetic resonance imaging: reproducibility, specificity, and evaluation by optical imaging of intrinsic signal. J Neurosci 26:11821-11832.26/46/11821.

Furmanski CS, Engel SA (2000) An oblique effect in human primary visual cortex. Nat Neurosci 3:535-536.10.1038/75702.

Garcia D (2010) Robust smoothing of gridded data in one and higher dimensions with missing values. Comput Stat Data Anal 54:1167-1178.10.1016/j.csda.2009.09.020.

Gardner JL (2010) Is cortical vasculature functionally organized? Neuroimage 49:1953-1956.S1053-8119(09)00768-X.

Gardner JL, Sun P, Tanaka K, Heeger DJ, Cheng K (2006) Classification analysis with high spatial resolution fMRI reveals large draining veins with orientation specific responses. In: Society for Neuroscience Annual Meeting.

Germuska MA, Meakin JA, Bulte DP (2013) The influence of noise on BOLD-mediated vessel size imaging analysis methods. J Cereb Blood Flow Metab 33:1857-1863.10.1038/jcbfm.2013.141.

Gias C, Hewson-Stoate N, Jones M, Johnston D, Mayhew JE, Coffey PJ (2005) Retinotopy within rat primary visual cortex using optical imaging. Neuroimage 24:200-206.10.1016/j.neuroimage.2004.08.015.

Gillilan LA (1976) Extra- and intra-cranial blood supply to brains of dog and cat. Am J Anat 146:237-253.10.1002/aja.1001460303.

Goense JB, Logothetis NK (2006) Laminar specificity in monkey V1 using high-resolution SE-fMRI. Magn Reson Imaging 24:381-392.10.1016/j.mri.2005.12.032.

Goodyear BG, Menon RS (2001) Brief visual stimulation allows mapping of ocular dominance in visual cortex using fMRI. Hum Brain Mapp 14:210-217.

Grinvald A, Shoham D, Shmuel A, Glaser D, Vanzetta I, Shtoyerman E, Slovin H, Wijnbergen C, Hildesheim R, Arieli A (1999) In-vivo optical imaging of cortical architecture and dynamics. In: Modern techniques in neuroscience research, pp 893-969: Springer.

Grinvald A, Slovin H, Vanzetta I (2000) Non-invasive visualization of cortical columns by fMRI. Nat Neurosci 3:105-107.10.1038/72045.

Haxby JV, Gobbini MI, Furey ML, Ishai A, Schouten JL, Pietrini P (2001) Distributed and overlapping representations of faces and objects in ventral temporal cortex. Science 293:2425-2430.10.1126/science.1063736.

Haynes JD, Rees G (2005) Predicting the orientation of invisible stimuli from activity in human primary visual cortex. Nat Neurosci 8:686-691.nn1445.

Haynes JD, Rees G (2006) Decoding mental states from brain activity in humans. Nat Rev Neurosci 7:523-534.nrn1931.

Hillman EM, Devor A, Bouchard MB, Dunn AK, Krauss GW, Skoch J, Bacskai BJ, Dale AM, Boas DA (2007) Depth-resolved optical imaging and microscopy of vascular compartment dynamics during somatosensory stimulation. Neuroimage 35:89-104.10.1016/j.neuroimage.2006.11.032.

Hines R (2013) Normal Feline & Canine Blood Chemistry Values.

Hodgkin AL, Huxley AF (1952) Propagation of electrical signals along giant nerve fibers. Proc R Soc Lond B Biol Sci 140:177-183.

Hoge RD, Atkinson J, Gill B, Crelier GR, Marrett S, Pike GB (1999) Linear coupling between cerebral blood flow and oxygen consumption in activated human cortex. Proc Natl Acad Sci U S A 96:9403-9408.

Hong L, Cai SM, Zhang J, Zhuo Z, Fu ZQ, Zhou PL (2012) Synchronization-based approach for detecting functional activation of brain. Chaos 22:033128.10.1063/1.4747710.

Hubel D (1995) Brain, Eye and Vision.

Hubel DH, Wiesel TN (1959) Receptive fields of single neurones in the cat's striate cortex. J Physiol 148:574-591.

Hubel DH, Wiesel TN (1962) Receptive fields, binocular interaction and functional architecture in the cat's visual cortex. J Physiol 160:106-154.

Hubel DH, Wiesel TN (1965) Receptive Fields and Functional Architecture in Two Nonstriate Visual Areas (18 and 19) of the Cat. J Neurophysiol 28:229-289.

Hubel DH, Wiesel TN (1974) Uniformity of monkey striate cortex: a parallel relationship between field size, scatter, and magnification factor. J Comp Neurol 158:295-305.10.1002/cne.901580305.

Jochimsen TH, Ivanov D, Ott DV, Heinke W, Turner R, Moller HE, Reichenbach JR (2010) Whole-brain mapping of venous vessel size in humans using the hypercapnia-induced BOLD effect. Neuroimage 51:765-774.S1053-8119(10)00205-3.

Jochimsen TH, Moller HE (2008) Increasing specificity in functional magnetic resonance imaging by estimation of vessel size based on changes in blood oxygenation. Neuroimage 40:228-236.10.1016/j.neuroimage.2007.10.050.

Kajikawa Y, Schroeder CE (2011) How local is the local field potential? Neuron 72:847-858.10.1016/j.neuron.2011.09.029.

Kamitani Y, Sawahata Y (2010) Spatial smoothing hurts localization but not information: pitfalls for brain mappers. Neuroimage 49:1949-1952.S1053-8119(09)00672-7 [pii]

10.1016/j.neuroimage.2009.06.040.

Kamitani Y, Tong F (2005) Decoding the visual and subjective contents of the human brain. Nat Neurosci 8:679-685.nn1444.

Kamitani Y, Tong F (2006) Decoding seen and attended motion directions from activity in the human visual cortex. Curr Biol 16:1096-1102.S0960-9822(06)01464-3.

Karbowski J (2011) Scaling of brain metabolism and blood flow in relation to capillary and neural scaling. PLoS One 6:e26709.10.1371/journal.pone.0026709.

Keilholz SD, Silva AC, Raman M, Merkle H, Koretsky AP (2006) BOLD and CBV-weighted functional magnetic resonance imaging of the rat somatosensory system. Magn Reson Med 55:316-324.10.1002/mrm.20744.

Kennan RP, Scanley BE, Innis RB, Gore JC (1998) Physiological basis for BOLD MR signal changes due to neuronal stimulation: separation of blood volume and magnetic susceptibility effects. Magn Reson Med 40:840-846.

Kennerley AJ, Berwick J, Martindale J, Johnston D, Papadakis N, Mayhew JE (2005) Concurrent fMRI and optical measures for the investigation of the hemodynamic response function. Magn Reson Med 54:354-365.10.1002/mrm.20511.

Kennerley AJ, Mayhew JE, Boorman L, Zheng Y, Berwick J (2012) Is optical imaging spectroscopy a viable measurement technique for the investigation of the negative BOLD phenomenon? A concurrent optical imaging spectroscopy and fMRI study at high field (7 T). Neuroimage 61:10-20.10.1016/j.neuroimage.2012.03.015.

Kim DS, Ronen I, Olman C, Kim SG, Ugurbil K, Toth LJ (2004) Spatial relationship between neuronal activity and BOLD functional MRI. Neuroimage 21:876-885.10.1016/j.neuroimage.2003.10.018.

Kim SG, Harel N, Jin T, Kim T, Lee P, Zhao F (2013) Cerebral blood volume MRI with intravascular superparamagnetic iron oxide nanoparticles. NMR Biomed 26:949-962.10.1002/nbm.2885.

Kim SG, Hendrich K, Hu X, Merkle H, Ugurbil K (1994) Potential pitfalls of functional MRI using conventional gradient-recalled echo techniques. NMR Biomed 7:69-74.

Kim SG, Ogawa S (2002) Insights into new techniques for high resolution functional MRI. Curr Opin Neurobiol 12:607-615.

Kim SG, Ogawa S (2012) Biophysical and physiological origins of blood oxygenation level-dependent fMRI signals. J Cereb Blood Flow Metab 32:1188-1206.10.1038/jcbfm.2012.23.

Kim T, Kim SG (2005) Quantification of cerebral arterial blood volume and cerebral blood flow using MRI with modulation of tissue and vessel (MOTIVE) signals. Magn Reson Med 54:333-342.10.1002/mrm.20550.

Kim T, Kim SG (2011) Temporal dynamics and spatial specificity of arterial and venous blood volume changes during visual stimulation: implication for BOLD quantification. J Cereb Blood Flow Metab 31:1211-1222.10.1038/jcbfm.2010.226.

Kiselev VG, Strecker R, Ziyeh S, Speck O, Hennig J (2005) Vessel size imaging in humans. Magn Reson Med 53:553-563.10.1002/mrm.20383.

Kohavi R (1995) A study of cross-validation and bootstrap for accuracy estimation and model selection. In: Proceedings of the 14th international joint conference on Artificial intelligence - Volume 2, pp 1137-1143 Montreal, Quebec, Canada: Morgan Kaufmann Publishers Inc.

Kohl M, Lindauer U, Royl G, Kuhl M, Gold L, Villringer A, Dirnagl U (2000) Physical model for the spectroscopic analysis of cortical intrinsic optical signals. Phys Med Biol 45:3749-3764.

Koopmans PJ, Barth M, Norris DG (2010) Layer-specific BOLD activation in human V1. Hum Brain Mapp 31:1297-1304.10.1002/hbm.20936.

Kreiman G, Hung CP, Kraskov A, Quiroga RQ, Poggio T, DiCarlo JJ (2006) Object selectivity of local field potentials and spikes in the macaque inferior temporal cortex. Neuron 49:433-445.10.1016/j.neuron.2005.12.019.

Kriegeskorte N, Bandettini P (2007) Analyzing for information, not activation, to exploit high-resolution fMRI. Neuroimage 38:649-662.10.1016/j.neuroimage.2007.02.022.

Kriegeskorte N, Cusack R, Bandettini P (2010) How does an fMRI voxel sample the neuronal activity pattern: compact-kernel or complex spatiotemporal filter? Neuroimage 49:1965-1976.S1053-8119(09)01058-1.

Krishnapuram B, Carin L, Figueiredo MA, Hartemink AJ (2005) Sparse multinomial logistic regression: fast algorithms and generalization bounds. IEEE Trans Pattern Anal Mach Intell 27:957-968.10.1109/TPAMI.2005.127.

Kruse W, Eckhorn R (1996) Inhibition of sustained gamma oscillations (35-80 Hz) by fast transient responses in cat visual cortex. Proc Natl Acad Sci U S A 93:6112-6117.

Kwong KK, Belliveau JW, Chesler DA, Goldberg IE, Weisskoff RM, Poncelet BP, Kennedy DN, Hoppel BE, Cohen MS, Turner R, et al. (1992) Dynamic magnetic resonance imaging of human brain activity during primary sensory stimulation. Proc Natl Acad Sci U S A 89:5675-5679.

Laursen H, Diemer NH (1977) Capillary size and density in the cerebral cortex of rats with a porto-caval anastomosis. Acta Neuropathol 40:117-122.

Lauwers F, Cassot F, Lauwers-Cances V, Puwanarajah P, Duvernoy H (2008) Morphometry of the human cerebral cortex microcirculation: general characteristics and space-related profiles. Neuroimage 39:936-948.10.1016/j.neuroimage.2007.09.024.

Lee SP, Duong TQ, Yang G, Iadecola C, Kim SG (2001) Relative changes of cerebral arterial and venous blood volumes during increased cerebral blood flow: implications for BOLD fMRI. Magn Reson Med 45:791-800.

Lee SP, Silva AC, Kim SG (2002) Comparison of diffusion-weighted high-resolution CBF and spin-echo BOLD fMRI at 9.4 T. Magn Reson Med 47:736-741.

LeVay S, Nelson SB (1991) Columnar organization of the visual cortex. The neural basis of visual function 266-315.

Liu J, Newsome WT (2006) Local field potential in cortical area MT: stimulus tuning and behavioral correlations. J Neurosci 26:7779-7790.10.1523/JNEUROSCI.5052-05.2006.

Logothetis NK (2002) The neural basis of the blood–oxygen–level–dependent functional magnetic resonance imaging signal. Philosophical Transactions of the Royal Society B: Biological Sciences 357:1003-1037.

Logothetis NK, Pauls J, Augath M, Trinath T, Oeltermann A (2001) Neurophysiological investigation of the basis of the fMRI signal. Nature 412:150-157.10.1038/35084005.

Lorente de Nó R (1938) Architectonics and structure of the cerebral cortex. Physiology of the nervous system 291-330.

Lu H, van Zijl PC (2012) A review of the development of Vascular-Space-Occupancy (VASO) fMRI. Neuroimage 62:736-742.10.1016/j.neuroimage.2012.01.013.

Magri C, Schridde U, Murayama Y, Panzeri S, Logothetis NK (2012) The amplitude and timing of the BOLD signal reflects the relationship between local field potential power at different frequencies. J Neurosci 32:1395-1407.10.1523/JNEUROSCI.3985-11.2012.

Malonek D, Grinvald A (1996) Interactions between electrical activity and cortical microcirculation revealed by imaging spectroscopy: implications for functional brain mapping. Science 272:551-554.

Mandeville JB, Jenkins BG, Kosofsky BE, Moskowitz MA, Rosen BR, Marota JJ (2001) Regional sensitivity and coupling of BOLD and CBV changes during stimulation of rat brain. Magn Reson Med 45:443-447.

Mandeville JB, Marota JJ (1999) Vascular filters of functional MRI: spatial localization using BOLD and CBV contrast. Magn Reson Med 42:591-598.

Mandeville JB, Marota JJ, Kosofsky BE, Keltner JR, Weissleder R, Rosen BR, Weisskoff RM (1998) Dynamic functional imaging of relative cerebral blood volume during rat forepaw stimulation. Magn Reson Med 39:615-624.

Mannion DJ, McDonald JS, Clifford CW (2009) Discrimination of the local orientation structure of spiral Glass patterns early in human visual cortex. Neuroimage 46:511-515.

Mannion DJ, McDonald JS, Clifford CW (2010) Orientation anisotropies in human visual cortex. J Neurophysiol 103:3465-3471.10.1152/jn.00190.2010.

Mansfield RJ, Ronner SF (1978) Orientation anistropy in monkey visual cortex. Brain Res 149:229-234.

Mathiesen C, Caesar K, Akgoren N, Lauritzen M (1998) Modification of activity-dependent increases of cerebral blood flow by excitatory synaptic activity and spikes in rat cerebellar cortex. J Physiol 512 (Pt 2):555-566.

Misaki M, Kim Y, Bandettini PA, Kriegeskorte N (2010) Comparison of multivariate classifiers and response normalizations for pattern-information fMRI. Neuroimage 53:103-118.S1053-8119(10)00783-4.

Misaki M, Luh WM, Bandettini PA (2013a) Accurate decoding of sub-TR timing differences in stimulations of sub-voxel regions from multi-voxel response patterns. Neuroimage 66:623-633.10.1016/j.neuroimage.2012.10.069.

Misaki M, Luh WM, Bandettini PA (2013b) The effect of spatial smoothing on fMRI decoding of columnar-level organization with linear support vector machine. J Neurosci Methods 212:355-361.10.1016/j.jneumeth.2012.11.004.

Mitzdorf U (1987) Properties of the evoked potential generators: current source-density analysis of visually evoked potentials in the cat cortex. Int J Neurosci 33:33-59.

Moon CH, Fukuda M, Kim SG (2013) Spatiotemporal characteristics and vascular sources of neural-specific and -nonspecific fMRI signals at submillimeter columnar resolution. Neuroimage 64:91-103.10.1016/j.neuroimage.2012.08.064.

Moon CH, Fukuda M, Park SH, Kim SG (2007) Neural interpretation of blood oxygenation level-dependent fMRI maps at submillimeter columnar resolution. J Neurosci 27:6892-6902.10.1523/JNEUROSCI.0445-07.2007.

Nauhaus I, Benucci A, Carandini M, Ringach DL (2008) Neuronal selectivity and local map structure in visual cortex. Neuron 57:673-679.10.1016/j.neuron.2008.01.020.

Nauhaus I, Busse L, Carandini M, Ringach DL (2009) Stimulus contrast modulates functional connectivity in visual cortex. Nat Neurosci 12:70-76.10.1038/nn.2232.

Nencka AS, Rowe DB (2007) Reducing the unwanted draining vein BOLD contribution in fMRI with statistical post-processing methods. Neuroimage 37:177-188.10.1016/j.neuroimage.2007.03.075.

Ogawa S, Lee TM, Kay AR, Tank DW (1990) Brain magnetic resonance imaging with contrast dependent on blood oxygenation. Proc Natl Acad Sci U S A 87:9868-9872.

Ogawa S, Menon RS, Tank DW, Kim SG, Merkle H, Ellermann JM, Ugurbil K (1993) Functional brain mapping by blood oxygenation level-dependent contrast magnetic resonance imaging. A comparison of signal characteristics with a biophysical model. Biophys J 64:803-812.10.1016/S0006-3495(93)81441-3.

Ogawa S, Tank DW, Menon R, Ellermann JM, Kim SG, Merkle H, Ugurbil K (1992) Intrinsic signal changes accompanying sensory stimulation: functional brain mapping with magnetic resonance imaging. Proc Natl Acad Sci U S A 89:5951-5955.

Olman C, Ronen I, Ugurbil K, Kim DS (2003) Retinotopic mapping in cat visual cortex using high-field functional magnetic resonance imaging. J Neurosci Methods 131:161-170.S0165027003002735.

Op de Beeck HP (2010) Against hyperacuity in brain reading: spatial smoothing does not hurt multivariate fMRI analyses? Neuroimage 49:1943-1948.S1053-8119(09)00202-X.

Orbach HS, Cohen LB (1983) Optical monitoring of activity from many areas of the in vitro and in vivo salamander olfactory bulb: a new method for studying functional organization in the vertebrate central nervous system. J Neurosci 3:2251-2262.

Park S, Kim S (2005) MR venography using BOLD contrast at 9.4 T. In: Proc Int Soc Magn Res Med, vol. 13, p 1718.

Parkes LM, Schwarzbach JV, Bouts AA, Deckers RH, Pullens P, Kerskens CM, Norris DG (2005) Quantifying the spatial resolution of the gradient echo and spin echo BOLD response at 3 Tesla. Magn Reson Med 54:1465-1472.10.1002/mrm.20712.

Polimeni JR, Granquist-Fraser D, Wood RJ, Schwartz EL (2005) Physical limits to spatial resolution of optical recording: clarifying the spatial structure of cortical hypercolumns. Proc Natl Acad Sci U S A 102:4158-4163.10.1073/pnas.0500291102.

Poplawsky AJ, Kim SG (2014) Layer-dependent BOLD and CBV-weighted fMRI responses in the rat olfactory bulb. Neuroimage 91:237-251.10.1016/j.neuroimage.2013.12.067.

Prinster A, Pierpaoli C, Turner R, Jezzard P (1997) Simultaneous measurement of DeltaR2 and DeltaR2* in cat brain during hypoxia and hypercapnia. Neuroimage 6:191-200.10.1006/nimg.1997.0288.

Ringach DL, Hawken MJ, Shapley R (1997) Dynamics of orientation tuning in macaque primary visual cortex. Nature 387:281-284.10.1038/387281a0.

Rojer AS, Schwartz EL (1990) Cat and monkey cortical columnar patterns modeled by bandpass-filtered 2D white noise. Biol Cybern 62:381-391.

Roy CS, Sherrington CS (1890) On the Regulation of the Blood-supply of the Brain. J Physiol 11:85-158 117.

Ryali S, Supekar K, Abrams DA, Menon V (2010) Sparse logistic regression for whole-brain classification of fMRI data. Neuroimage 51:752-764.10.1016/j.neuroimage.2010.02.040.

Sasaki Y, Rajimehr R, Kim BW, Ekstrom LB, Vanduffel W, Tootell RB (2006) The radial bias: a different slant on visual orientation sensitivity in human and nonhuman primates. Neuron 51:661-670.S0896-6273(06)00586-1.

Schummers J, Marino J, Sur M (2002) Synaptic integration by V1 neurons depends on location within the orientation map. Neuron 36:969-978.S0896627302010127 [pii].

Schummers J, Marino J, Sur M (2004) Local networks in visual cortex and their influence on neuronal responses and dynamics. J Physiol Paris 98:429-441.10.1016/j.jphysparis.2005.09.017.

Seymour K, Clifford CW, Logothetis NK, Bartels A (2010) Coding and binding of color and form in visual cortex. Cereb Cortex 20:1946-1954.10.1093/cercor/bhp265.

Shen Y, Pu IM, Ahearn T, Clemence M, Schwarzbauer C (2013) Quantification of venous vessel size in human brain in response to hypercapnia and hyperoxia using magnetic resonance imaging. Magn Reson Med 69:1541-1552.10.1002/mrm.24258.

Sheth SA, Nemoto M, Guiou M, Walker M, Pouratian N, Hageman N, Toga AW (2004) Columnar specificity of microvascular oxygenation and volume responses: implications for functional brain mapping. J Neurosci 24:634-641.10.1523/JNEUROSCI.4526-03.2004.

Shmuel A, Augath M, Oeltermann A, Logothetis NK (2006) Negative functional MRI response correlates with decreases in neuronal activity in monkey visual area V1. Nat Neurosci 9:569-577.nn1675.

Shmuel A, Chaimow D, Raddatz G, Ugurbil K, Yacoub E (2010) Mechanisms underlying decoding at 7 T: ocular dominance columns, broad structures, and macroscopic blood vessels in V1 convey information on the stimulated eye. Neuroimage 49:1957-1964.S1053-8119(09)00950-1.

Shmuel A, Grinvald A (1996) Functional organization for direction of motion and its relationship to orientation maps in cat area 18. J Neurosci 16:6945-6964.

Shmuel A, Grinvald A (2000) Coexistence of linear zones and pinwheels within orientation maps in cat visual cortex. Proc Natl Acad Sci U S A 97:5568-5573.97/10/5568 [pii].

Shmuel A, Leopold DA (2008) Neuronal correlates of spontaneous fluctuations in fMRI signals in monkey visual cortex: Implications for functional connectivity at rest. Hum Brain Mapp 29:751-761.10.1002/hbm.20580.

Shmuel A, Yacoub E, Chaimow D, Logothetis NK, Ugurbil K (2007) Spatio-temporal point-spread function of fMRI signal in human gray matter at 7 Tesla. Neuroimage 35:539-552.S1053-8119(06)01244-4.

Sirotin YB, Cardoso M, Lima B, Das A (2012) Spatial homogeneity and task-synchrony of the trial-related hemodynamic signal. Neuroimage 59:2783-2797.10.1016/j.neuroimage.2011.10.019.

Sirotin YB, Das A (2009) Anticipatory haemodynamic signals in sensory cortex not predicted by local neuronal activity. Nature 457:475-479.10.1038/nature07664.

Sirotin YB, Hillman EM, Bordier C, Das A (2009) Spatiotemporal precision and hemodynamic mechanism of optical point spreads in alert primates. Proc Natl Acad Sci U S A 106:18390-18395.0905509106.

Smirnakis SM, Schmid MC, Weber B, Tolias AS, Augath M, Logothetis NK (2007) Spatial specificity of BOLD versus cerebral blood volume fMRI for mapping cortical organization. J Cereb Blood Flow Metab 27:1248-1261.10.1038/sj.jcbfm.9600434.

Sokoloff L (1981) Relationships among local functional activity, energy metabolism, and blood flow in the central nervous system. Fed Proc 40:2311-2316.

Sotero RC, Bortel AB, Naaman S, Mocanu VM, Kropf P, Villeneuve M, Shmuel A (2015) Laminar distribution of phase-amplitude coupling of spontaneous current sources and sinks. Frontiers in Neuroscience 9.10.3389/fnins.2015.00454.

Spaak E, Bonnefond M, Maier A, Leopold DA, Jensen O (2012) Layer-specific entrainment of gamma-band neural activity by the alpha rhythm in monkey visual cortex. Curr Biol 22:2313-2318.10.1016/j.cub.2012.10.020.

Stefanovic B, Pike GB (2005) Venous refocusing for volume estimation: VERVE functional magnetic resonance imaging. Magn Reson Med 53:339-347.10.1002/mrm.20352.

Sun P, Gardner JL, Costagli M, Ueno K, Waggoner RA, Tanaka K, Cheng K (2013) Demonstration of tuning to stimulus orientation in the human visual cortex: a high-resolution fMRI study with a novel continuous and periodic stimulation paradigm. Cereb Cortex 23:1618-1629.10.1093/cercor/bhs149.

Swindale NV, Grinvald A, Shmuel A (2003) The spatial pattern of response magnitude and selectivity for orientation and direction in cat visual cortex. Cereb Cortex 13:225-238.

Swindale NV, Matsubara JA, Cynader MS (1987) Surface organization of orientation and direction selectivity in cat area 18. J Neurosci 7:1414-1427.

Swisher JD, Gatenby JC, Gore JC, Wolfe BA, Moon CH, Kim SG, Tong F (2010) Multiscale pattern analysis of orientation-selective activity in the primary visual cortex. J Neurosci 30:325-330.30/1/325.

Thompson R, Correia M, Cusack R (2011) Vascular contributions to pattern analysis: comparing gradient and spin echo fMRI at 3T. Neuroimage 56:643-650.10.1016/j.neuroimage.2010.03.061.

Triantafyllou C, Hoge RD, Krueger G, Wiggins CJ, Potthast A, Wiggins GC, Wald LL (2005) Comparison of physiological noise at 1.5 T, 3 T and 7 T and optimization of fMRI acquisition parameters. Neuroimage 26:243-250.S1053-8119(05)00033-9.

Tropres I, Grimault S, Vaeth A, Grillon E, Julien C, Payen JF, Lamalle L, Decorps M (2001) Vessel size imaging. Magn Reson Med 45:397-408.

Tropres I, Pannetier N, Grand S, Lemasson B, Moisan A, Peoc'h M, Remy C, Barbier EL (2015) Imaging the microvessel caliber and density: Principles and applications of microvascular MRI. Magn Reson Med 73:325-341.10.1002/mrm.25396.

Ts'o DY, Frostig RD, Lieke EE, Grinvald A (1990) Functional organization of primate visual cortex revealed by high resolution optical imaging. Science 249:417-420.

Turner R (2002) How Much Cortex Can a Vein Drain? Downstream Dilution of Activation-Related Cerebral Blood Oxygenation Changes. Neuroimage 16:1062-1067.10.1006/nimg.2002.1082.

Tusa RJ, Rosenquist AC, Palmer LA (1979) Retinotopic organization of areas 18 and 19 in the cat. J Comp Neurol 185:657-678.10.1002/cne.901850405.

Tychsen L, Burkhalter A (1997) Nasotemporal asymmetries in V1: ocular dominance columns of infant, adult, and strabismic macaque monkeys. J Comp Neurol 388:32-46.

Uludag K, Muller-Bierl B, Ugurbil K (2009) An integrative model for neuronal activity-induced signal changes for gradient and spin echo functional imaging. Neuroimage 48:150-165.10.1016/j.neuroimage.2009.05.051.

van Bruggen N, Busch E, Palmer JT, Williams SP, de Crespigny AJ (1998) High-resolution functional magnetic resonance imaging of the rat brain: mapping changes in cerebral blood volume using iron oxide contrast media. J Cereb Blood Flow Metab 18:1178-1183.10.1097/00004647-199811000-00003.

Vanduffel W, Fize D, Mandeville JB, Nelissen K, Van Hecke P, Rosen BR, Tootell RB, Orban GA (2001) Visual motion processing investigated using contrast agent-enhanced fMRI in awake behaving monkeys. Neuron 32:565-577.

Vanzetta I, Slovin H, Omer DB, Grinvald A (2004) Columnar resolution of blood volume and oximetry functional maps in the behaving monkey; implications for FMRI. Neuron 42:843-854.10.1016/j.neuron.2004.04.004.

Vapnik V (2013) The nature of statistical learning theory: Springer Science & Business Media.

Vazquez AL, Fukuda M, Crowley JC, Kim SG (2014) Neural and hemodynamic responses elicited by forelimb- and photo-stimulation in channelrhodopsin-2 mice: insights into the hemodynamic point spread function. Cereb Cortex 24:2908-2919.10.1093/cercor/bht147.

Vazquez AL, Noll DC (1998) Nonlinear aspects of the BOLD response in functional MRI. Neuroimage 7:108-118.10.1006/nimg.1997.0316.

Villeneuve MY, Casanova C (2003) On the use of isoflurane versus halothane in the study of visual response properties of single cells in the primary visual cortex. Journal of Neuroscience Methods 129:19-31.10.1016/s0165-0270(03)00198-5.

Vovenko E (1999) Distribution of oxygen tension on the surface of arterioles, capillaries and venules of brain cortex and in tissue in normoxia: an experimental study on rats. Pflugers Arch 437:617-623.10.1007/s004240050825.

Wang HX, Merriam EP, Freeman J, Heeger DJ (2014) Motion direction biases and decoding in human visual cortex. J Neurosci 34:12601-12615.10.1523/JNEUROSCI.1034-14.2014.

Wardle S, Ritchie JB, Seymour K, Carlson T (2015) What information is 'decoded' from stimulus orientation with fMRI and MVPA? J Vis 15:993.10.1167/15.12.993.

Weston J, Watkins C (1998) Multi-class support vector machines. Citeseer.

Xing D, Yeh CI, Shapley RM (2009) Spatial spread of the local field potential and its laminar variation in visual cortex. J Neurosci 29:11540-11549.10.1523/JNEUROSCI.2573-09.2009.

Yacoub E, Harel N, Ugurbil K (2008) High-field fMRI unveils orientation columns in humans. Proc Natl Acad Sci U S A 105:10607-10612.0804110105.

Yacoub E, Shmuel A, Logothetis N, Ugurbil K (2007) Robust detection of ocular dominance columns in humans using Hahn Spin Echo BOLD functional MRI at 7 Tesla. Neuroimage 37:1161-1177.S1053-8119(07)00461-2.

Zhan CA, Ledgeway T, Baker CL, Jr. (2005) Contrast response in visual cortex: quantitative assessment with intrinsic optical signal imaging and neural firing. Neuroimage 26:330-346.10.1016/j.neuroimage.2005.01.043.

Zhao F, Wang P, Hendrich K, Ugurbil K, Kim SG (2006) Cortical layer-dependent BOLD and CBV responses measured by spin-echo and gradient-echo fMRI: insights into hemodynamic regulation. Neuroimage 30:1149-1160.10.1016/j.neuroimage.2005.11.013.